OCRWM	MODEL COVER SHEET	1. QA: QA Page 1 of 144

2. Type of Mathematical Model:

☒ Process Model ☐ Abstraction Model ☐ System Model

Describe Intended Use of Model:

Development and implementation of a conceptual model, and alternative conceptual model for preclosure ventilation of a waste emplacement drift. This model and analysis report predicts the preclosure temperatures of the waste package, drift wall, and ventilation air, and the ventilation efficiency.

3. Title:

Ventilation Model and Analysis Report

4. DI (including Rev. No. and Change No., if applicable):

ANL-EBS-MD-000030 REV 03

5. Total Attachments:	6. Attachment Numbers - No. of Pages in Each:
Seventeen (17)	I-4, II-8, III-6, IV-4, V-4, VI-6, VII-6, VIII-4, VIII-4, IX-74, X-4, XI-4, XII-2, XIII-10, XIV-4, XV-4, XVI-4, XVII-4

	Printed Name	Signature	Date
7. Originator:	Veraun Chipman (lead)		7/18/03
8. CSO:	Bruce Kirstein		7/18/03
9. Checker:	Jim Kam (lead)		7/18/03
10. QER:	Ajulena Barnes		7/18/03
11. Responsible Manager/Lead:	~~Daniel A.~~ Thomas		7/18/03
12. Responsible Manager:	Thomas W. Doering		7.18.03

13. Remarks:

Other Originators: John Case, Sandra Dunn, Bob Walsh, Bruce Kirstein, Zane Walton, Junghun Leem, and Bill Lowry.

This revision addresses TER-02-0037, which deals with the validation of the model for its intended use.

2. Title:

Ventilation Model and Analysis Report

3. DI (including Rev. No. and Change No., if applicable):

ANL-EBS-MD-000030 REV 03

4. Revision / Change Number:	5. Description of Revision/Change:
00	Initial issue
01	Complete Revision
01 ICN 01	Issued for checking...for clarification purposes ICN 01 adds definitions for the ventilation heat removal efficiency (Section 6.1.3) and energy balance checks on the downstream use of the heat removal efficiencies to deliver the right amount of energy to the host rock (Section 6.6.2.1 through 6.6.2.3)
02	The use of MULTIFLUX v.2.2 (STN 10485-2.2-10/29/02) software in ANL-EBS-MD-000030 REV 01 ICN 01, correctly characterized as an unqualified code was issued after the exemption for the interim use of unqualified software (Section 5.10) had expired in August, 2002. Work with the MULTIFLUX v2.2 software had actually been performed in March 2002 when the exemption was in effect and full qualification/baselining of the code was in progress. However, a Project-level business decision was made to discontinue efforts to qualify the code. The significance of this decision with regard to the inclusion of the MULTIFLUX work in the Report was not fully appreciated until the ANL-EBS-MD-000030 REV 01 ICN 01 was approved and issued on 10/29/02. A noncompliance was identified as Quality Observation BSC(B)-03-0-029 for the following reasons: 1) The noncompliance is not a significant condition adverse to quality. MULTIFLUX v2.2 was used in the corroboration of the ventilation model; 2) The noncompliance appears to be isolated and attributable to the unusual situation in which a business, not technical, decision resulted in abandoning software qualification activities; 3) The noncompliance requires only remedial action applicable to the ANL-EBS-MD-000030 REV 01 ICN 01; 4) The noncompliance has no impact or residual impact upon completion of the remedial action. Since Multiflux v2.2 was used for corroboration, software output will not be used as input/feeds to downstream analyses; 5) The noncompliance does not require a cause determination; the cause is known, and the uniqueness of the circumstances which led to the noncompliance suggest that specific actions to preclude are not needed. Revised to remove the discussion of the corroborative model using MULTIFLUX v2.2, and other approaches that were used to corroborate the ventilation model and assess the impacts of moisture on the ventilation efficiency.
03	Complete revision in which ventilation model inputs were updated to reflect the current design for License Application. DRIFTFLOW v.1.0 ventilation calculations were replaced with an analytical model for ventilation which is implemented using the standard (built-in) functions of Microsoft Excel. A mixed convection heat transfer correlation is also developed and implemented in the ventilation models.

EXECUTIVE SUMMARY

The understanding and control of heat generated by the radionuclide decay is critical to the design of the Yucca Mountain Project repository. The thermal environment generated by the decay heat affects the performance of the surrounding drift. A key feature of the engineered barrier system design is the preclosure ventilation process, where air is forced through the emplacement drifts to remove heat. Ventilation delays the onset of the peak temperatures of the drift wall and engineered barrier system components, as well as decreasing their magnitude. Ventilation also removes moisture from the surrounding rock mass.

The effectiveness of the ventilation is described by the *ventilation efficiency*, or the fraction of total decay heat that is removed from the repository by the vent air. The ventilation efficiency is predicted by analyzing the thermal radiation, convection, and conduction which occur simultaneously in the drift and the surrounding rock mass.

The Ventilation Model simulates the heat transfer processes in and around a waste emplacement drift to predict the ventilation efficiency. The heat removed by ventilation is temporally and spatially dependent, so the model described in this report incorporates numerical and analytical methods to predict the transient response of the system for the duration of the ventilating or preclosure period. The results of this modeling effort support downstream total system performance assessment models (such as the Multiscale Thermohydrologic Model, the Unsaturated Zone Coupled Processes Models, and the Drift Degradation Model) that do not explicitly simulate the preclosure period.

The Ventilation Model and Analysis Report:

- Develops a conceptual model and the governing mathematical relationships for preclosure ventilation heat transfer in and around an emplacement drift (Section 6.3).
- Numerically and analytically implements the governing equations of the conceptual model to predict the efficiency of the ventilation to remove heat generated by the waste package during the preclosure period (Section 6.4 through 6.6).
- Develops and implements an alternative conceptual model evaluating the influence of water and water vapor mass transport on the preclosure ventilation heat transfer processes (Section 6.7).
- Performs a sensitivity analysis of the ventilation efficiency given uncertainties in key input parameters (Section 6.11).
- Validates the conceptual model for the specified conditions and limitations by applying it to the results of the Ventilation Test series performed in the engineered barrier system test facility at the North Las Vegas complex (Section 7.1.3).

In addition, the Ventilation Model and Analysis Report addresses the following Key Technical Issue agreements:

- RDTME 3.01 (Reamer and Williams 2001a): The impacts of moisture on the ventilation efficiency is detailed by presenting an alternative conceptual model and its analytical implementations for heat and mass transfer in and around a ventilated emplacement drift (Sections 6.7 through 6.9).

- RDTME 3.14 (Reamer and Williams 2001a): The adequacy of the discretization of the drift along its axis in the ANSYS implementation of the conceptual model is addressed (Section 6.6.1).

- RDTME 3.14 (Reamer and Williams 2001a): The applicability of the ventilation efficiency as a means to initialize downstream postclosure thermal models is addressed (Section 6.10).

- TEF 2.07 (Reamer and Williams 2001b): The post-test modeling of the engineered barrier system ventilation tests using the ANSYS methodology is addressed (Section 7.1.3).

License Application design inputs and parameters are compiled to describe the thermal source term and the adjacent environment. The model is implemented with a combination of numerical and analytical approaches, incorporating radiation, conduction, and mixed convection heat transfer to predict the temporal and spatial response. For the specified inputs, conditions, limitations, and assumptions (including an inlet air temperature of 23°C), the model predicts the integrated ventilation efficiency over a 50-year preclosure period to be 88% with a standard deviation of ±3% for a drift length of 600 meters, and 86% with a standard deviation of ±3% for a drift length of 800 meters. The preclosure temperatures of the waste package surface does not exceed 105°C, and the drift wall surface and in-drift air do not exceed the boiling point of water. Neither the preclosure temperatures, nor the ventilation efficiency, are largely affected by the presence of moisture.

CONTENTS

Page

CONTENTS (Continued)

Page

CONTENTS (Continued)

Page

INTENTIONALLY LEFT BLANK

FIGURES

Page

FIGURES (Continued)

Page

TABLES

Page

TABLES (Continued)

Page

TABLES (Continued)

Page

INTENTIONALLY LEFT BLANK

LIST OF ACRONYMS

AC	Acceptance Criteria
ANSI	American National Standards Institute
ASME	The American Society of Mechanical Engineers
CFR	Code of Federal Regulations
DOE	U.S. Department of Energy
DTN	Data Tracking Number
ECRB	Enhanced Characterization of the Repository Block
EBS	engineered barrier system
FEPs	features, events, and processes
GFM	Geologic Framework Model
NC1	Natural Convection Test 1
NC2	Natural Convection Test 2
PTC	Performance Test Code
PWR	Pressurized Water Reactor
TSPA	total system performance assessment
TSPA-LA	Total System Performance Assessment-License Application
UZ	Unsaturated Zone
WP	waste package
YMP	Yucca Mountain Project

LIST OF SYMBOLS

a	radius of the drift wall
A_s	area of the waste package surface
A_{us}	waste package area per unit length of drift
A_{uw}	drift wall area per unit length of drift
A_w	drift wall surface area
B_s	coefficient
B_w	coefficient
c_i	coefficient in the Kuehn and Goldstein correlations for natural convection
c_o	coefficient in the Kuehn and Goldstein correlations for natural convection
$\overline{C_i}$	coefficient in the Kuehn and Goldstein correlations for natural convection
$\overline{C_o}$	coefficient in the Kuehn and Goldstein correlations for natural convection
C_p	heat capacity of air at constant pressure
D	determinant of a 2×2 matrix
ε	dimensionless variable
d_h	hydraulic diameter
d_s	waste package diameter
d_w	drift diameter
e_s	surface emissivity of waste package
e_w	surface emissivity of drift wall
f	arbitrary energy flux
$f(\tau)$	arbitrary function for the flux rate
F_0	step heat flux applied at x = 0
h_{rad}	radiation heat transfer coefficient
h_s	waste package surface convection heat transfer coefficient
h_w	drift wall convection heat transfer coefficient
L	drift segment length
m	coefficient in the Kuehn and Goldstein correlations for natural convection
$\dot{m}$	ventilation mass flow rate
Nu	Nusselt number
P_b	scale factor depending on system of units
p_s	waste package power
Pr	Prandtl number
Q_{air}	heat convected to the air from the waste package and drift wall surfaces
Q_s	heat generated by the waste package
Q_w	heat conducted into the rock
$Q_{conv\text{-}s}$	heat convected from the waste package to the air
$Q_{conv\text{-}w}$	heat convected from the drift wall to the air
Q_{rad}	heat radiated from the waste package to the drift wall
r	radius
Re	Reynold number
S	generalized temperature response
T	air temperature
t	time

$T_{air\text{-}bulk}$	average air temperature
T_{in}	ventilation air temperature at the drift segment inlet
T_{out}	ventilation air temperature at the drift segment outlet
T_s or T_{wp}	waste package surface temperature
T_w or T_{dw}	drift wall temperature
u	temporary integration symbol
$w_\tau(x,\tau)$	time derivative of the constant heat flux function for a unit loading.
x	distance from the drift entrance

LIST OF GREEK SYMBOLS

κ	thermal diffusivity
$\nu(t)$	temperature change
ρ	density
σ	Stefan-Boltzmann constant
$\eta(t,x)$	instantaneous ventilation efficiency
$\eta_{integrated}$	integrated ventilation efficiency
μ	viscosity
θ	dimensionless temperature
τ	dimensionless time

LIST OF CONVERSIONS

(From Incropera and DeWitt 1996, Backcover; Perry and Green 1984, Table 1-5)

Heat transfer rate	1 W	= 3.4123 Btu/h
Heat flux	1 W/m^2	= 0.3171 $Btu/h\cdot ft^2$
Heat transfer coefficient	1 $W/m^2\cdot K$	= 0.17612 $Btu/h\cdot ft^2\cdot °F$
Temperature difference	1 K	= (9/5)°R = (9/5)°F
Mass flow rate	1 kg/s	= 7936.6 lb_m/h
Specific heat	1 $kJ/kg\cdot K$	= 0.2389 $Btu/lb_m\cdot °F$
Mass	1 kg	= 2.2046 lb_m
Mass	1 grain	= 6.479891×10^{-5} kg

INTENTIONALLY LEFT BLANK

1. PURPOSE

1.1 BACKGROUND

Yucca Mountain, approximately 100 miles northwest of Las Vegas, Nevada, has been selected as the site for the nation's geologic repository for high-level nuclear waste. The Yucca Mountain Project (YMP) is currently developing the design for the underground facilities. The design includes a network of parallel drifts that will hold the waste (emplacement drifts), branching from a main drift. There are two distinct phases considered in the repository operation. The first phase, or preclosure phase, includes emplacement of the waste and a period where heat generated from the decay of radionuclides contained in waste packages is actively removed from the repository by ventilating the emplacement drifts. In the second phase, or postclosure phase, forced ventilation of the drifts is stopped and the repository is closed.

A prerequisite for designing the YMP repository is the ability to both understand and control the heat generated from the decay of the radionuclides. The decay heat affects the performance of both the waste packages and the emplacement drift. During the preclosure period, heat transfer from the waste packages occurs through mixed convection (a combination of forced and natural convection), conduction through the waste package supports, and thermal radiation to the invert and drift walls. In the postclosure phase, heat is transferred from the waste package by natural convection (as opposed to mixed convection before closure), conduction, and thermal radiation.

The purpose of the Ventilation Model, described in this report, is to simulate the heat transfer processes in and around a waste emplacement drift and predict the heat removal by ventilation during the preclosure period. The heat removal by ventilation is temporally and spatially dependent, and is expressed as the fraction or percentage of the heat produced by radionuclide decay that is carried away by the ventilation air. The heat removal by ventilation is also referred to as the ventilation efficiency.

1.2 SCOPE

Technical Work Plan for: Engineered Barrier System Department Modeling and Testing FY03 Work Activities (BSC 2003a) describes work to be performed to provide the technical basis for describing and predicting the preclosure and postclosure performance of the repository. To fulfill this responsibility, the Engineered Barrier System (EBS) Department develops and refines models that describe the repository over time. One of these models, the Ventilation Model, is documented in this report. The work presented in this report is consistent with, and contains no deviations from, the previously mentioned technical work plan.

The objectives of this model report are to:

1. Develop and validate a conceptual model for preclosure ventilation of an emplacement drift (Sections 6.3 and 7).

2. Implement the ventilation conceptual model using numerical and analytical methods, and the License Application design basis inputs and parameters to predict the preclosure ventilation efficiency (Section 6.4).

3. Verify the results of the numerical and analytical implementations of the ventilation conceptual model through comparative analyses (Section 6.6).

4. Develop an alternate conceptual model for preclosure ventilation which includes the impacts of water and water vapor mass transfer on the heat transfer (Section 6.7).

5. Implement the alternative conceptual model using analytical calculations to assess the impacts of moisture on the ventilation efficiency (Sections 6.8 and 6.9).

6. Demonstrate the applicability of the use of the ventilation efficiency as an abstraction method for downstream postclosure models to account for the preclosure heat removal (Section 6.10).

7. Demonstrate the sensitivity of the ventilation efficiency to discretization and uncertainties in key input parameters associated with the host rock and engineered components including thermal conductivity, matrix and lithophysal porosity, specific heat, emissivity, and convection heat transfer coefficient (Sections 6.6.1 and 6.11).

This report conforms to the prescribed outline of AP-SIII.10Q, *Models*, as described in Table 1-1.

Table 1-1. Outline of the Ventilation Model Documentation

Section	Content
1. Purpose	Purpose and introduction to the model report.
2. QUALITY ASSURANCE	Identifies the applicability of the YMP Quality Assurance program.
3. USE OF SOFTWARE	Lists controlled and exempt software used in the development, implementation, and validation of the model.
4. INPUTS	Lists data, parameters, and other inputs used in the development, implementation, and validation of the model. Also lists the appropriate criteria, codes, and standards.
5. ASSUMPTIONS	Lists assumptions and the rationale for their use in the development, implementation, and validation of the model.
6. MODEL DISCUSSION	Describes the conceptual model, the mathematical implementations of the conceptual model and the results, the alternative conceptual model, the mathematical implementation of the alternative conceptual model and the results, the appropriate use of the model output (i.e., ventilation efficiency), and the sensitivity of the ventilation efficiency to uncertainties in key model inputs and parameters.
7. VALIDATION	Presents the analyses that validate the conceptual model, which includes corroboration of the EBS Ventilation Test Phase I results with modeling results.
8. CONCLUSIONS	Summarizes the modeling activities and describes the appropriate use of the model output (i.e., ventilation efficiency) in downstream models.
9. INPUTS AND REFERENCES	Lists input and output data tracking numbers (DTNs) and cited references.
10. ATTACHMENTS	Documents supporting analyses.

1.3 LIMITATIONS

Applicability of the ventilation model documented in this report is limited to:

- Configurations in which the waste packages are spaced in the drift such that the heat generation per unit length will be nearly uniform throughout the drift.
- Conditions in which conduction heat transfer from the waste package to the invert or drift wall is small compared to the heat transfer to the invert and drift wall via thermal radiation.
- Repository average waste package heat loads (or waste streams) that produce sub-boiling temperature conditions in the host rock during the ventilation period.
- Single drift analyses where the repository edges do not significantly affect the near field host rock thermal conduction.
- Simultaneous emplacement of the waste packages at the start of the preclosure period which is conservative with respect to the total heat load applied to the system.

1.4 DOWNSTREAM USE OF THE RESULTS

The main output of the Ventilation Model is the ventilation efficiency. Downstream models that do not explicitly model the preclosure period rely on the ventilation efficiency as a means of initializing their postclosure analyses. Such models include the Multiscale Thermohydrologic Model, the Drift Degradation Model, and the UZ coupled processes models.

2. QUALITY ASSURANCE

The Quality Assurance program applies to the development of this document. This document was prepared in accordance with *Technical Work Plan for: Engineered Barrier System Department Modeling and Testing FY03 Work Activities* (BSC 2003a), which directs the work identified in work package P451224EF2. The technical work plan was prepared in accordance with AP-2.27Q, *Planning for Science Activities*. The methods used to control the electronic management of data as required by AP-SV.1Q, *Control of the Electronic Management of Information*, were accomplished in accordance with the technical work plan. As directed in the technical work plan, this document was prepared in accordance with AP-SIII.10Q, *Models,* AP-SI.1Q, *Software Management*, AP-3.15Q, *Managing Technical Product Inputs*, and reviewed in accordance with AP-2.14Q, *Review of Technical Products and Data*.

3. USE OF SOFTWARE

Table 3-1 lists the software used to perform the analyses as well as the software tracking numbers (where appropriate), CPU(s), operating systems, and physical location where the software was installed. All software listed in Table 3-1 was obtained from Software Configuration Management, was appropriate for the applications used, and was used within the

range of validation in accordance with AP-SI.1Q, *Software Management*. Use of software has been documented in accordance with AP-SI.1Q.

Table 3-1. Software

Code	Software Tracking Number	CPU	Physical Location	Operating System
ANSYS v5.6.2	10145-5.6.2-00 10145-5.6.2-01	SGI Octane, M&O #114441 Sun Microsystems UltraSPARC, M&O #117683	Las Vegas, NV	IRIX 6.5 Solaris 2.7
rme6 v1.2	10617-1.2-00	Sun Microsystems Blade 100, 6878182	Livermore, CA	Solaris 8
YMESH v1.54	10172-1.54-00	Sun Microsystems Blade 100, 6878182	Livermore, CA	Solaris 8
Mathcad 2001i Professional	Exempt	Dell Pentium Workstation, M&O #151635	Las Vegas, NV	Windows 2000
Microsoft Excel 97	Exempt	Various YMP M&O Computers	Las Vegas, NV	Windows 95, Windows 2000

3.1 ANSYS v5.6.2

ANSYS v5.6.2 is a commercially available computer program and is classified as qualified software (per AP-SI.1Q, *Software Management*). ANSYS v5.6.2 is used to implement the ventilation conceptual model. ANSYS v5.6.2 is a general purpose finite element analysis code, and is used in many disciplines of engineering that deal with topics including structural, geotechnical, mechanical, thermal, and fluids. ANSYS was used to predict the ventilation efficiency for the License Application design.

3.2 rme6 v1.2

rme6 v1.2 is a developed computer program and is classified as Level B qualified software (per AP-SI.1Q). rme6 v1.2 is used to convert the numerical grid from the 3-D Site Scale UZ Flow and Transport Model to a format that is readable by YMESH v1.54.

3.3 YMESH v1.54

YMESH v1.54 is a developed computer program and is classified as Level B qualified software (per AP-SI.1Q). YMESH v1.54 is used to generate the thickness of the geologic layers for a stratigraphic column given by some easting and northing coordinates.

3.4 MATHCAD 2001i PROFESSIONAL

Mathcad 2001i Professional is a commercially available software package. The Mathcad software provides a technical computing environment using standard mathematical notation for equations and operations. The use of the Mathcad software in this report is exempt from AP-SI.1Q per AP-SIII.10Q. The formulas, inputs and outputs of those formulas, and additional

information required for an independent technically qualified person to verify the results of these Mathcad analyses are provided in Section 6 and Attachments III and XIII.

3.5 MICROSOFT EXCEL 97

Microsoft Excel 97 is a commercially available spreadsheet software package. Excel 97 is used in conjunction with the ANSYS v5.6.2 software to predict the ventilation efficiency, and as a stand alone implementation of the ventilation conceptual model to predict ventilation efficiency. Each of these applications uses only standard or built in functions. It is also used to make plots of data and perform other computations using standard functions. The use of Excel 97 in this report is exempt from AP-SI.1Q, per AP-SIII.10Q. The formulas, inputs and outputs of those formulas, and additional information required for an independent technically qualified person to verify the results of these Excel analyses are provided in Section 6, Attachments I, II, IV, V, VI, VII, VIII, X, XI, XII, XIV, XV, and the DTNs listed in Table 8-1.

4. INPUTS

4.1 DATA, PARAMETERS, AND OTHER INPUTS

4.1.1 Data

The following data were used as inputs to develop and validate the models and analyses described in Sections 6 and 7.

4.1.1.1 Ventilation Test Phase I and Phase II Input Parameters

Tables 4-1 through 4-5 list measured temperatures for the outer insulation and airstream at Station 3 of the Ventilation Test Phase 1, Cases 1 through 5, performed at the North Las Vegas Atlas Facility. These data are used for model validation as described in Section 7.1.3.

Table 4-1. Ventilation Test Phase 1, Case 1, Outer Insulation and Air Temperatures Measured at Station 3

Time	Measured Outer Insulation Temperature at Station 3 (°C)				Measured Air Temperature at Station 3 (°C)			
	V3-RTD-03	V3-RTD-04	V3-RTD-05	V3-RTD-06	V3-HUM-T1	V3-RTD-01	V3-HUM-T2	V3-RTD-02
11/3/2000 14:03	29.14	28.78	28.42	28.08	25.73	27.34	25.48	27.36
11/3/2000 14:18	29.15	28.78	28.79	28.33	26.12	27.68	25.70	27.54
11/3/2000 14:49	29.17	28.32	28.05	27.72	27.48	28.40	26.18	28.36
11/3/2000 15:18	28.11	27.80	27.51	27.44	28.20	29.37	26.63	29.03
11/3/2000 15:48	27.39	27.30	27.03	26.97	28.35	29.46	26.68	29.23
11/3/2000 16:18	27.81	28.41	28.56	27.66	29.05	30.03	27.23	29.97
11/3/2000 16:48	27.75	28.43	28.14	27.75	29.35	30.28	27.48	30.14
11/3/2000 17:18	27.37	28.05	27.78	27.46	29.41	30.42	27.49	30.14
11/3/2000 17:49	27.30	27.75	27.54	27.28	29.34	30.40	27.37	30.16
11/3/2000 18:18	27.08	27.76	27.40	27.19	29.30	30.23	27.30	30.19
11/3/2000 18:49	27.07	27.51	27.24	27.26	29.28	30.50	27.27	29.91
11/3/2000 19:33	26.81	27.39	27.19	26.97	29.24	30.15	27.20	29.98
11/4/2000 7:03	27.16	25.68	24.44	25.23	28.63	29.04	26.16	28.77
11/4/2000 15:48	29.65	29.32	28.21	29.22	30.87	31.76	28.70	31.75
11/5/2000 6:33	28.22	26.60	24.73	25.61	29.25	29.22	26.62	29.11
11/5/2000 11:48	30.99	29.83	29.22	30.04	31.50	32.08	29.34	32.10
11/6/2000 8:03	27.23	26.45	24.80	25.61	29.00	28.93	26.25	28.83
11/6/2000 13:48	31.87	30.04	29.30	29.98	31.88	32.57	29.73	32.28
11/7/2000 6:48	26.41	25.14	23.74	24.27	28.12	27.97	25.24	28.03
11/7/2000 13:33	29.07	28.14	27.60	28.13	30.79	31.18	28.52	31.34
11/8/2000 6:48	27.05	24.84	22.95	23.80	27.86	27.65	25.03	27.47
11/8/2000 13:03	30.93	28.45	28.03	28.39	30.67	31.49	28.44	31.18
11/9/2000 6:18	27.09	25.76	23.95	24.78	28.22	28.08	25.54	28.09
11/9/2000 16:03	29.09	28.32	27.56	28.31	30.91	31.74	28.57	31.66
Nominal Measured Flow Rate (m^3/s)						**1.0**		
Nominal Measured Power (kW/m)						**0.36**		

DTN: SN0208F3409100.007

Table 4-2. Ventilation Test Phase 1, Case 2, Outer Insulation and Air Temperatures Measured at Station 3

Time	Measured Outer Insulation Temperature at Station 3 (°C)				Measured Air Temperature at Station 3 (°C)			
	V3-RTD-03	V3-RTD-04	V3-RTD-05	V3-RTD-06	V3-HUM-T1	V3-RTD-01	V3-HUM-T2	V3-RTD-02
11/20/2000 16:03	26.14	24.60	22.42	24.11	23.89	25.91	23.80	25.43
11/20/2000 16:18	26.98	24.40	22.55	24.39	24.21	26.29	24.27	25.99
11/20/2000 16:48	25.01	23.90	22.60	24.06	24.13	25.82	24.13	25.49
11/20/2000 17:19	24.08	23.77	22.58	22.71	23.86	25.08	23.73	24.80
11/20/2000 17:49	25.89	23.51	22.40	23.20	24.81	26.13	24.58	25.52
11/20/2000 18:18	25.97	24.20	22.63	23.36	24.96	25.98	24.68	25.70
11/20/2000 18:49	25.65	23.71	22.43	23.13	25.02	25.98	24.75	25.72
11/20/2000 19:19	25.81	23.31	22.27	23.27	24.91	26.13	24.62	25.74
11/20/2000 19:49	25.27	23.25	22.71	23.03	24.82	25.87	24.45	25.52
11/20/2000 20:19	25.07	23.65	22.52	22.87	24.66	25.76	24.34	25.33
11/21/2000 6:03	24.91	23.59	21.39	22.69	23.56	24.80	23.43	24.42
11/21/2000 14:03	29.57	27.78	24.80	28.23	28.54	29.74	28.20	29.30
11/22/2000 6:33	23.09	22.24	21.21	21.58	22.37	23.55	22.19	23.09
11/22/2000 13:49	29.19	27.41	26.00	27.57	27.78	29.17	27.66	29.02
11/23/2000 5:03	24.77	23.92	23.29	23.68	23.89	25.12	23.80	24.78
11/23/2000 14:48	30.62	29.66	27.00	29.87	29.74	31.38	29.62	30.73
11/24/2000 6:19	25.22	24.12	23.16	23.72	23.96	25.44	23.89	24.82
11/24/2000 14:18	30.47	29.53	27.35	29.69	29.63	30.98	29.58	30.58
11/25/2000 6:48	25.42	24.01	23.51	23.50	23.65	24.85	23.57	24.37
11/25/2000 14:03	30.32	29.22	27.79	29.43	29.41	30.61	29.31	30.40
11/26/2000 6:33	24.33	23.49	22.78	22.66	23.33	24.45	23.22	24.09
11/26/2000 13:33	29.78	28.85	27.48	29.01	29.12	30.67	29.04	30.32
11/27/2000 6:48	24.61	23.95	23.40	23.20	23.73	25.03	23.63	24.59
11/27/2000 11:33	28.96	27.22	26.22	27.17	26.84	28.81	26.85	28.19
Nominal Measured Flow Rate (m^3/s)						**2.0**		
Nominal Measured Power (kW/m)						**0.36**		

DTN: SN0208F3409100.007

Table 4-3. Ventilation Test Phase 1, Case 3, Outer Insulation and Air Temperatures Measured at Station 3

Time	Measured Outer Insulation Temperature at Station 3 (°C)				Measured Air Temperature at Station 3 (°C)			
	V3-RTD-03	V3-RTD-04	V3-RTD-05	V3-RTD-06	V3-HUM-T1	V3-RTD-01	V3-HUM-T2	V3-RTD-02
12/1/2000 15:03	20.39	20.82	20.61	20.41	19.29	21.10	19.22	20.84
12/1/2000 15:19	20.38	20.22	20.69	20.30	20.18	21.44	19.68	21.42
12/1/2000 15:48	20.00	19.98	20.46	20.31	22.10	22.77	20.99	23.04
12/1/2000 16:18	19.86	20.05	20.06	19.92	23.48	23.98	22.00	23.99
12/1/2000 16:48	19.51	19.10	19.54	19.30	24.34	24.89	22.64	24.81
12/1/2000 17:18	18.76	18.96	19.15	18.98	24.83	25.27	22.96	25.11
12/1/2000 17:49	20.49	21.30	21.45	20.60	25.15	25.46	23.21	25.26
12/1/2000 18:19	18.79	18.90	19.25	18.96	25.66	26.02	23.67	25.95
12/1/2000 18:48	21.13	21.81	22.32	21.38	25.85	26.18	23.81	26.07
12/1/2000 19:19	18.52	18.49	18.58	18.49	26.04	26.29	23.97	26.35
12/2/2000 7:03	22.42	22.90	21.78	22.05	27.56	27.75	24.46	27.45
12/2/2000 15:48	23.60	23.18	22.31	23.27	30.43	30.83	27.95	30.61
12/3/2000 7:18	19.62	18.37	17.99	18.81	28.69	28.36	25.10	28.39
12/3/2000 14:33	25.63	24.85	23.92	24.96	31.70	32.31	29.04	31.98
12/4/2000 7:19	21.23	20.53	20.08	21.08	29.18	28.74	25.50	28.78
12/4/2000 14:49	26.25	25.38	24.53	25.98	32.30	32.54	29.49	32.44
12/5/2000 7:18	22.20	21.96	21.48	22.18	29.58	29.14	26.03	29.32
12/5/2000 15:18	25.17	23.81	23.56	24.31	32.23	32.55	29.31	32.42
12/6/2000 6:34	23.07	22.58	20.64	21.83	29.71	28.97	25.85	29.10
12/6/2000 14:33	25.27	24.12	23.40	24.37	31.95	31.98	29.00	32.03
12/7/2000 7:18	24.60	24.00	23.32	24.28	30.56	29.95	27.05	30.04
12/7/2000 14:33	25.23	24.01	23.47	24.74	32.35	32.65	29.55	32.96
12/8/2000 7:03	22.08	21.63	20.88	21.62	30.05	29.39	26.33	29.55
12/8/2000 11:48	26.08	25.09	24.60	25.56	32.06	32.08	29.25	32.08
Nominal Measured Flow Rate (m^3/s)						**0.5**		
Nominal Measured Power (kW/m)						**0.36**		

DTN: SN0208F3409100.007

Table 4-4. Ventilation Test Phase 1, Case 4, Outer Insulation and Air Temperatures Measured at Station 3

Time	Measured Outer Insulation Temperature at Station 3 (°C)				Measured Air Temperature at Station 3 (°C)			
	V3-RTD-03	V3-RTD-04	V3-RTD-05	V3-RTD-06	V3-HUM-T1	V3-RTD-10	V3-HUM-T2	V3-RTD-02
10/9/2000 8:48	35.04	28.39	27.52	29.27	24.92	26.80	24.65	26.45
10/9/2000 9:19	26.45	26.78	26.39	26.33	26.03	27.32	25.27	27.08
10/9/2000 9:49	28.60	27.80	27.30	28.04	26.65	27.66	25.61	27.39
10/9/2000 10:18	27.72	26.88	26.91	27.54	26.98	28.25	25.81	27.84
10/9/2000 10:48	27.40	27.18	26.91	27.35	27.31	28.51	26.11	28.28
10/9/2000 11:19	28.14	27.33	27.28	27.52	27.63	29.12	26.39	28.50
10/9/2000 11:49	28.60	27.79	27.54	27.84	27.91	29.26	26.63	28.83
10/9/2000 12:18	28.34	27.88	27.57	28.33	28.16	29.48	26.84	29.54
10/9/2000 12:48	28.13	27.85	27.42	27.83	28.29	29.66	26.96	29.46
10/9/2000 13:33	28.50	27.85	27.64	28.36	28.43	29.82	27.13	29.48
10/10/2000 5:48	35.53	28.73	25.71	28.18	25.36	26.42	24.18	25.97
10/10/2000 14:19	27.09	26.92	26.69	26.97	27.68	29.04	26.64	28.63
10/11/2000 5:03	37.48	25.34	25.62	28.81	24.50	25.38	23.09	25.19
10/11/2000 12:48	27.93	27.23	26.83	27.40	27.53	28.61	26.53	28.36
10/12/2000 3:48	30.78	26.06	24.92	26.70	24.79	25.70	23.41	25.36
10/12/2000 15:33	34.28	28.56	27.93	29.94	27.39	28.41	26.35	28.33
10/13/2000 5:33	33.54	26.48	24.99	27.95	24.22	25.42	22.81	25.01
10/13/2000 13:33	36.86	28.41	27.91	30.40	27.79	29.13	26.78	28.85
10/14/2000 5:18	25.68	25.42	24.32	24.49	25.07	26.00	23.73	25.62
10/14/2000 14:33	29.05	28.84	27.80	28.86	28.34	29.43	27.34	29.13
10/15/2000 5:33	25.58	25.60	24.57	24.65	24.99	26.07	23.61	25.44
10/15/2000 12:33	28.39	26.87	27.26	27.34	28.12	29.44	27.08	29.21
10/16/2000 5:03	32.50	27.41	26.23	28.70	25.05	26.19	23.68	25.60
10/16/2000 8:03	29.04	27.63	27.26	27.66	27.02	28.26	25.99	27.68
Nominal Measured Flow Rate (m^3/s)						**1.0**		
Nominal Measured Power (kW/m)						**0.18**		

DTN: SN0208F3409100.007

Table 4-5. Ventilation Test Phase 1, Case 5, Outer Insulation and Air Temperatures Measured at Station 3

Time	Measured Outer Insulation Temperature at Station 3 (°C)				Measured Air Temperature at Station 3 (°C)			
	V3-RTD-03	V3-RTD-04	V3-RTD-05	V3-RTD-06	V3-HUM-T1	V3-RTD-10	V3-HUM-T2	V3-RTD-02
10/20/2000 8:33	28.89	27.33	27.20	27.44	24.92	26.54	24.45	26.25
10/20/2000 9:03	26.66	25.64	26.08	25.66	25.71	27.10	25.07	26.91
10/20/2000 9:33	28.10	27.41	27.04	27.64	26.80	28.13	26.10	27.85
10/20/2000 10:03	27.63	25.82	26.27	26.05	27.28	28.49	26.49	28.39
10/20/2000 11:03	27.43	26.63	26.50	26.05	27.91	29.28	27.00	29.24
10/20/2000 13:03	28.19	26.94	26.93	27.27	28.76	30.38	27.75	29.79
10/20/2000 20:33	27.77	27.81	27.15	28.25	29.45	30.63	28.30	30.64
10/20/2000 23:18	26.30	26.75	25.92	26.71	28.77	30.30	27.39	29.99
10/21/2000 5:33	26.29	26.58	25.29	26.52	28.67	29.63	27.13	29.59
10/21/2000 10:18	29.61	28.41	27.69	28.80	30.08	31.12	28.91	31.17
10/21/2000 15:48	29.08	28.95	28.12	28.81	30.51	31.49	29.31	31.49
10/22/2000 4:48	28.28	26.95	25.15	26.34	29.21	29.88	27.24	29.83
10/22/2000 12:33	27.61	27.27	26.08	26.85	29.36	30.30	27.59	30.01
10/22/2000 23:18	31.39	27.82	25.40	28.27	28.44	29.17	26.36	29.06
10/23/2000 3:33	32.31	27.53	26.10	28.69	28.47	28.97	26.59	29.08
10/23/2000 15:18	36.94	30.51	26.30	29.27	28.59	29.08	26.85	29.24
10/24/2000 5:18	26.47	25.21	23.93	24.97	27.92	28.59	26.01	28.49
10/24/2000 13:18	35.20	29.25	28.52	30.44	29.74	30.85	28.47	30.99
10/25/2000 6:19	30.79	28.14	25.58	28.70	28.33	28.98	26.40	29.04
10/25/2000 14:18	28.28	27.23	26.99	27.40	30.23	30.98	29.11	31.28
10/26/2000 6:48	35.53	29.25	27.59	30.26	28.87	29.40	27.10	29.61
10/26/2000 12:18	28.52	28.02	27.86	28.09	29.69	30.72	28.29	30.85
10/26/2000 18:48	28.99	28.63	27.97	28.40	30.47	31.44	29.08	31.54
10/27/2000 7:48	29.06	27.91	25.50	26.59	29.85	30.57	28.12	30.51
Nominal Measured Flow Rate (m^3/s)						**0.5**		
Nominal Measured Power (kW/m)						**0.18**		

DTN: SN0208F3409100.007

4.1.1.2 Thermophysical Properties of the Invert

Tables 4-6 through 4-9 list measured thermophysical properties of 4-10 crushed welded tuff and fine crushed tuff used as the invert ballast material. Tables 4-6 and 4-8 are for the 4-10 crushed tuff, and are used as inputs to the models and analyses described in Section 6 (see Section 5.5). Tables 4-7 and 4-9 are for the fine crushed tuff, and are used as inputs to the ANSYS modeling of the ventilation tests performed at the North Las Vegas Atlas Facility described in Section 7.1.3.

Table 4-6. Specific Heat, Thermal Conductivity, and Thermal Diffusivity of 4-10 Crushed Tuff

Sample Type	Sample Number	Specific Heat ($J/cm^3 \cdot °C$)	Thermal Conductivity ($W/m \cdot °C$)	Thermal Diffusivity (mm^2/s)	Temperature (°C)
4-10 crushed tuff	TK-CT-01	0.82	0.17	0.21	16.2
4-10 crushed tuff	TK-CT-02	0.84	0.14	0.16	15.8
4-10 crushed tuff	TK-CT-03	0.98	0.17	0.17	16.1
4-10 crushed tuff	TK-CT-04	0.98	0.17	0.17	16.4
4-10 crushed tuff	TK-CT-05	0.99	0.17	0.17	17.1
4-10 crushed tuff	TK-CT-06	0.92	0.16	0.18	17.5
4-10 crushed tuff	TK-CT-07	0.96	0.17	0.17	17.6
4-10 crushed tuff	TK-CT-07a	0.86	0.15	0.18	18.9
4-10 crushed tuff	TK-CT-08	0.88	0.16	0.18	18
4-10 crushed tuff	TK-CT-09	1.06	0.17	0.16	18.1
4-10 crushed tuff	TK-CT-10	0.94	0.17	0.18	18.5

DTN: GS000483351030.003

Table 4-7. Specific Heat, Thermal Conductivity, and Thermal Diffusivity of Fine Crushed Tuff

Sample Type	Sample Number	Specific Heat ($J/cm^3 \cdot °C$)	Thermal Conductivity ($W/m \cdot °C$)	Thermal Diffusivity (mm^2/s)	Temperature (°C)
fine crushed tuff	TK-FT-01	0.86	0.13	0.16	24.2
fine crushed tuff	TK-FT-02	0.79	0.13	0.16	24.5
fine crushed tuff	TK-FT-03	0.92	0.14	0.15	24.6
fine crushed tuff	TK-FT-04	0.92	0.14	0.15	24.7
fine crushed tuff	TK-FT-05	0.94	0.14	0.15	24.7
fine crushed tuff	TK-FT-06	0.96	0.14	0.15	24.8
fine crushed tuff	TK-FT-07	0.95	0.15	0.16	24.8
fine crushed tuff	TK-FT-07a	0.86	0.13	0.15	16.9
fine crushed tuff	TK-FT-08	0.98	0.15	0.15	24.9
fine crushed tuff	TK-FT-09	1.00	0.15	0.15	24.9
fine crushed tuff	TK-FT-10	0.93	0.14	0.15	24.9
fine crushed tuff	TK-FT-11	1.00	0.16	0.16	19.4
fine crushed tuff	TK-FT-12	0.99	0.17	0.17	19.5
fine crushed tuff	TK-FT-13	0.96	0.15	0.15	19.0
fine crushed tuff	TK-FT-14	1.03	0.16	0.15	19.1
fine crushed tuff	TK-FT-15	0.95	0.15	0.16	19.0
fine crushed tuff	TK-FT-16	0.97	0.17	0.17	19.2
fine crushed tuff	TK-FT-17	0.92	0.14	0.16	19.1
fine crushed tuff	TK-FT-18	1.00	0.16	0.16	19.1
fine crushed tuff	TK-FT-19	0.98	0.15	0.15	19.2
fine crushed tuff	TK-FT-20	0.92	0.15	0.16	19.0

DTN: GS000483351030.003

Table 4-8. Bulk Density of 4-10 Crushed Tuff

Sample Type	Sample Number	Bulk Density (g/cm^3)	Sample Type	Sample Number	Bulk Density (g/cm^3)
4-10 Crushed Tuff	UNCBD41A	1.3	4-10 Crushed Tuff	UNCBD53B	1.3
4-10 Crushed Tuff	UNCBD41B	1.2	4-10 Crushed Tuff	UNCBD54A	1.3
4-10 Crushed Tuff	UNCBD42A	1.3	4-10 Crushed Tuff	UNCBD54B	1.3
4-10 Crushed Tuff	UNCBD42B	1.3	4-10 Crushed Tuff	UNCBD55A	1.3
4-10 Crushed Tuff	UNCBD43A	1.3	4-10 Crushed Tuff	UNCBD55B	1.2
4-10 Crushed Tuff	UNCBD43B	1.2	4-10 Crushed Tuff	UNCBD56A	1.3
4-10 Crushed Tuff	UNCBD44A	1.3	4-10 Crushed Tuff	UNCBD56B	1.3
4-10 Crushed Tuff	UNCBD44B	1.2	4-10 Crushed Tuff	UNCBD57A	1.3
4-10 Crushed Tuff	UNCBD45A	1.3	4-10 Crushed Tuff	UNCBD57B	1.2
4-10 Crushed Tuff	UNCBD45B	1.2	4-10 Crushed Tuff	UNCBD58A	1.3
4-10 Crushed Tuff	UNCBD46A	1.2	4-10 Crushed Tuff	UNCBD58B	1.3
4-10 Crushed Tuff	UNCBD46B	1.2	4-10 Crushed Tuff	UNCBD59A	1.2
4-10 Crushed Tuff	UNCBD47A	1.3	4-10 Crushed Tuff	UNCBD59B	1.2
4-10 Crushed Tuff	UNCBD47B	1.3	4-10 Crushed Tuff	UNCBD60A	1.2
4-10 Crushed Tuff	UNCBD48A	1.3	4-10 Crushed Tuff	UNCBD60B	1.3
4-10 Crushed Tuff	UNCBD48B	1.3	4-10 Crushed Tuff	UNCBD61A	1.3
4-10 Crushed Tuff	UNCBD49A	1.3	4-10 Crushed Tuff	UNCBD61B	1.3
4-10 Crushed Tuff	UNCBD49B	1.2	4-10 Crushed Tuff	UNCBD62A	1.3
4-10 Crushed Tuff	UNCBD50A	1.2	4-10 Crushed Tuff	UNCBD62B	1.2
4-10 Crushed Tuff	UNCBD50B	1.2	4-10 Crushed Tuff	UNCBD63A	1.2
4-10 Crushed Tuff	UNCBD51A	1.3	4-10 Crushed Tuff	UNCBD63B	1.2
4-10 Crushed Tuff	UNCBD51B	1.3	4-10 Crushed Tuff	UNCBD64A	1.3
4-10 Crushed Tuff	UNCBD52A	1.3	4-10 Crushed Tuff	UNCBD64B	1.3
4-10 Crushed Tuff	UNCBD52B	1.3	4-10 Crushed Tuff	UNCBD65A	1.3
4-10 Crushed Tuff	UNCBD53A	1.3	4-10 Crushed Tuff	UNCBD65B	1.3

DTN: GS020183351030.001

Table 4-9. Bulk Density of Fine Crushed Tuff

Sample Type	Sample Number	Bulk Density (g/cm^3)	Sample Type	Sample Number	Bulk Density (g/cm^3)
Fine Crushed Tuff	UNCBD291A	1.2	Fine Crushed Tuff	UNCBD303B	1.1
Fine Crushed Tuff	UNCBD291B	1.2	Fine Crushed Tuff	UNCBD304A	1.1
Fine Crushed Tuff	UNCBD292A	1.2	Fine Crushed Tuff	UNCBD304B	1.2
Fine Crushed Tuff	UNCBD292B	1.2	Fine Crushed Tuff	UNCBD305A	1.2
Fine Crushed Tuff	UNCBD293A	1.2	Fine Crushed Tuff	UNCBD305B	1.2
Fine Crushed Tuff	UNCBD293B	1.2	Fine Crushed Tuff	UNCBD306A	1.2
Fine Crushed Tuff	UNCBD294A	1.2	Fine Crushed Tuff	UNCBD306B	1.2
Fine Crushed Tuff	UNCBD294B	1.2	Fine Crushed Tuff	UNCBD307A	1.2
Fine Crushed Tuff	UNCBD295A	1.2	Fine Crushed Tuff	UNCBD307B	1.2
Fine Crushed Tuff	UNCBD295B	1.2	Fine Crushed Tuff	UNCBD308A	1.2
Fine Crushed Tuff	UNCBD296A	1.1	Fine Crushed Tuff	UNCBD308B	1.2
Fine Crushed Tuff	UNCBD296B	1.2	Fine Crushed Tuff	UNCBD309A	1.2
Fine Crushed Tuff	UNCBD297A	1.1	Fine Crushed Tuff	UNCBD309B	1.2
Fine Crushed Tuff	UNCBD297B	1.2	Fine Crushed Tuff	UNCBD310A	1.2
Fine Crushed Tuff	UNCBD298A	1.2	Fine Crushed Tuff	UNCBD310B	1.2
Fine Crushed Tuff	UNCBD298B	1.2	Fine Crushed Tuff	UNCBD311A	1.1
Fine Crushed Tuff	UNCBD299A	1.2	Fine Crushed Tuff	UNCBD311B	1.2
Fine Crushed Tuff	UNCBD299B	1.2	Fine Crushed Tuff	UNCBD312A	1.1
Fine Crushed Tuff	UNCBD300A	1.1	Fine Crushed Tuff	UNCBD312B	1.2
Fine Crushed Tuff	UNCBD300B	1.2	Fine Crushed Tuff	UNCBD313A	1.2
Fine Crushed Tuff	UNCBD301A	1.2	Fine Crushed Tuff	UNCBD313B	1.1
Fine Crushed Tuff	UNCBD301B	1.1	Fine Crushed Tuff	UNCBD314A	1.2
Fine Crushed Tuff	UNCBD302A	1.2	Fine Crushed Tuff	UNCBD314B	1.1
Fine Crushed Tuff	UNCBD302B	1.2	Fine Crushed Tuff	UNCBD315A	1.1
Fine Crushed Tuff	UNCBD303A	1.2	Fine Crushed Tuff	UNCBD315B	1.2

DTN: GS020183351030.001

4.1.1.3 Relative Humidity

Relative humidity in the Enhanced Characterization of the Repository Block (ECRB) Cross-Drift was measured in the zones defined by the bulkheads. Table 4-10 summarizes the patterns of relative humidity measurements. Attachment XIII requires a single relative humidity to represent conditions in an open drift. That attachment uses 30% RH, based on the measurements taken before the first bulkhead.

Table 4-10. Patterns of Measured Relative Humidity in the ECRB Cross-Drift

Location	Patterns of Relative Humidity Measurements
Before the first bulkhead	Fluctuated between 10% and 40%, with a few instances where the humidity was greater than 60%
Between the first and second bulkhead	Remained close to about 95%
Between the second and third bulkhead	Remained close to about 95%
Behind the third bulkhead	About 90% before opening, about 80% after closing again

Source: BSC 2001a, p. 213

4.1.1.4 Laboratory Measured Saturation for Tptpll from Borehole Cores

Table 4-11 lists laboratory-measured values of saturation from borehole core data. DTN: MO0004QGFMPICK.000 was used to identify the depths for which the borehole core data corresponded to the Tptpll (lower lithophysal unit). These data are used in Attachment XIII, and the average of these measurements is referred to in Section 6.9.1.

Table 4-11. Laboratory Measured Saturation for Tptpll from Borehole Cores

USW SD-7 [a]		USW SD-9 [b]		USW NRG-6 [c]		USW NRG-7/7A [d]		USW UZ-7A [e]	
Depth (ft)	Sat.	Depth (ft)	Sat.	Depth (ft)	Sat.	Depth (m)	Sat.	Depth (m)	Sat.
809.2	0.862	847.2	0.852	816.6	0.24	269.1	0.8	184.2	0.606
819	0.904	849.6	0.775	817.9	0.71	271.9	0.84	185.3	0.702
824.7	0.911	853.4	0.843	820.8	0.8	272.8	0.71	186.3	0.669
835.4	0.874	859	0.974	823	0.87	274.1	0.61	188.6	0.636
836.8	0.698	865.3	0.907	826.1	0.63	276.7	0.67	189	0.715
842.5	0.891	879.6	1.02	829.2	0.78	280	0.57	190.7	0.733
847.6	0.862	888.8	0.774	831.7	0.98	285.7	0.71	191	0.635
848.4	0.775	897	0.898	835.4	0.54	287.5	0.64	197.1	0.73
856.9	0.794	899.5	0.854	838.6	0.71	288.3	0.61	198.3	0.76
857.7	0.845	905.8	0.886	841.7	0.39	290.2	0.62	198.9	0.84
862.3	0.863	921.9	0.794	844.8	0.89	291.1	0.63	203.6	0.705
864.9	0.778	924.2	0.717	851.9	0.75	292.1	0.56	205.1	0.818
867.4	0.942	936.1	0.728	854.9	0.83	293.9	0.66	205.4	0.839
872	0.72	938.9	0.812	857.8	0.12	295.7	0.6	206.6	0.779
874.4	0.772	944.6	0.787	861	0.08	296.4	0.57	207	0.803
875.5	0.835	948	0.796	862.7	0.28	297.2	0.56	208.1	0.85
878.8	0.844	954	0.865	865.8	0.64	298.2	0.7	210	0.846
884.2	0.821	958.1	0.776	867.7	0.7	300.3	0.69	210.7	0.844
885	0.879	962.6	0.791	871.5	0.83	301.1	0.78	211.7	0.876
887.6	0.888	968.7	0.837	873.8	0.64	304.8	0.6	212.8	0.749
891	0.843	971.9	0.716	877.6	0.58	306.7	0.97	213.2	0.776
894	0.864	975.5	0.91	879.7	0.77	313	0.46	213.7	0.744
897.3	0.904	981	0.793	886	0.86	314.1	0.55	214.8	0.784
899.5	0.924	984.7	0.742	890.7	0.66	314.9	0.5	215.7	0.678

Table 4-11. Laboratory Measured Saturation for Tptpll from Borehole Cores (Continued)

USW SD-7 [a]		USW SD-9 [b]		USW NRG-6 [c]		USW NRG-7/7A [d]		USW UZ-7A [e]	
Depth (ft)	Sat.	Depth (ft)	Sat.	Depth (ft)	Sat.	Depth (m)	Sat.	Depth (m)	Sat.
904.9	0.793	986.6	0.744	892.8	0.31	316.9	0.4	216.7	0.751
910.7	0.855	995.7	0.809	898.6	0.72	317.4	0.65	217.5	0.852
914.7	0.854	1003	0.672	901.6	0.75	318.5	0.56	218.2	0.719
916.2	0.902	1007.3	0.781	904.8	0.85	319.4	0.34	219.2	0.706
919.1	0.818	1012.3	0.731	910.7	0.69	322.1	0.72	220.2	0.756
920.4	0.831	1017.2	0.886	912.8	0.8	323.1	0.74	220.9	0.678
924.1	0.847	1023.8	0.89	917.1	0.78	324.9	0.57	221.7	0.814
928.4	0.903	1028.9	0.81	920.4	0.71	326.7	0.72	222.9	0.723
929.7	0.871	1033.1	0.903	928.8	0.8	328.5	0.66	224.4	0.779
932.8	0.798	1035.1	0.922	932	0.72	331.3	0.69	225.4	0.499
936.7	0.781	1038.8	0.95	936	0.67	332.2	0.73	227.7	0.664
940.7	0.903	1041	0.895	942.7	0.81	334.2	0.58	228.7	0.769
941.5	0.879	1044.2	0.874	949.3	0.49	334.9	0.53	230.1	0.762
946.4	0.825	1047.2	0.932	952.5	0.65	336.9	0.63	231.2	0.784
951.2	0.906	1050.2	0.871	955.4	0.75	337.8	0.68	234.2	0.579
954.5	0.847	1053.6	0.985	959	0.71	338.4	0.51	—	—
957	0.778	1055.8	0.909	962	0.77	340	0.52	—	—
961.4	0.762	1064.8	0.958	968.2	0.69	342.4	0.38	—	—
962.5	0.956	1068.1	0.798	970.8	0.65	344	0.79	—	—
966.9	0.839	1070.4	0.821	975.1	0.64	346	0.59	—	—
968.9	0.881	1076.7	0.92	977	0.82	348	0.53	—	—
971.4	0.905	1080.1	0.837	978.9	0.72	348.8	0.57	—	—
974.5	0.85	1086.4	0.918	985.1	0.77	353.2	0.48	—	—
978.1	0.918	1091.1	0.863	989	0.73	354.3	0.39	—	—
981	0.846	1095.4	0.84	991.6	0.75	355	0.52	—	—
983.8	0.831	1098.4	0.712	995.6	0.41	357	0.39	—	—
986.2	0.965	1101.3	0.757	1004.1	0.71	357.9	0.5	—	—
990.2	0.918	1104.1	0.596	1010.2	0.62	358.9	0.38	—	—
993.1	0.995	1106.4	0.761	1015.7	0.84	359.6	0.66	—	—
994.3	0.985	1110.3	0.729	1018.5	0.88	360.5	0.42	—	—
999	0.878	1113.5	0.706	1024.1	0.5	361.5	0.53	—	—
1005	0.901	1116	0.749	1033.8	0.41	362.6	0.53	—	—
1008.2	0.909	1119.2	0.755	1036	0.62	363.2	0.35	—	—
1013.3	0.955	1125.1	0.806	1040.1	0.84	366	0.76	—	—
1017.6	0.952	1128.6	0.877	1042.7	0.87	366.9	0.56	—	—
—	—	1133.6	0.799	1049	0.66	367.8	0.7	—	—
—	—	1139.6	0.84	1054.8	0.37	368.9	0.75	—	—
—	—	1142	0.903	1058.3	0.87	370.6	0.68	—	—
—	—	1146.1	0.863	1060.9	0.83	373.2	0.56	—	—
—	—	1149	0.865	1063.5	0.81	—	—	—	—
—	—	1152.7	0.855	1067	0.52	—	—	—	—

Table 4-11. Laboratory Measured Saturation for Tptpll from Borehole Cores (Continued)

USW SD-7 [a]		USW SD-9 [b]		USW NRG-6 [c]		USW NRG-7/7A [d]		USW UZ-7A [e]	
Depth (ft)	Sat.	Depth (ft)	Sat.	Depth (ft)	Sat.	Depth (m)	Sat.	Depth (m)	Sat.
—	—	1158.5	0.69	1069.8	0.82	—	—	—	—
—	—	1161.1	0.864	1076.1	0.68	—	—	—	—
—	—	1163.8	0.828	1079.1	0.72	—	—	—	—
—	—	1166.6	0.862	1081.9	0.75	—	—	—	—
—	—	1170.5	0.813	1084.2	0.77	—	—	—	—
—	—	1172.8	0.88	1087.1	0.8	—	—	—	—
—	—	1179	0.868	1090.3	0.86	—	—	—	—
—	—	—	—	1096.6	0.8	—	—	—	—

DTN: MO0004QGFMPICK.000

NOTES: [a] Contacts Tptpll at 803.3 to 1020 ft. Data from DTN: GS951108312231.009.
[b] Contacts Tptpll at 845.8 to 1182 ft. Data from DTN: GS950408312231.004.
[c] Contacts Tptpll at 810 ft. Data from DTN: GS000508312231.006.
[d] Contacts Tptpll at 877.6 to 1243 ft. Data from DTN: GS951108312231.010.
[e] Contacts Tptpll at 607 ft. Data from DTN: GS951108312231.011.

4.1.1.5 Water Potential Measurements Taken at the ECRB Station 15+00

Table 4-12 lists measurements of water potentials taken at the ECRB Station 15+00. These data are used in Attachment XIII.

Table 4-12. Water Potential Measurements Taken at the ECRB Station 15+00

Station (m)	Water Potential (m)
ST-1500-0.62	-259
ST-1500-1.12	-91
ST-1500-1.69	-10
ST-1500-2.12	-24
ST-1500-2.62	-37
ST-1500-3.12	-5
ST-1500-3.62	4
ST-1500-4.12	-12
ST-15004.62	-14
ST-1500-5.12	-8
ST-1500-5.62	-10

Source: DTN: LB0110ECRBH2OP.001 (C7-1500.xls, worksheet “wp-2000-plot”)

4.1.2 Parameters and Parameter Uncertainty

The following parameters and parameter uncertainties were used as inputs to develop the models and analyses described in Sections 6 and 7.

4.1.2.1 Thermophysical Properties of the Stratigraphic Layers

Table 4-13 through Table 4-17 list the thermophysical properties of the repository and non-repository stratigraphic units. Parameter distributions are only included for the repository stratigraphic units. These parameters are used as inputs to the models and analyses described in Section 6.

Table 4-13. Thermophysical Properties of the Repository Stratigraphic Units

	Dry Bulk Thermal Conductivity (W/m·K)		Wet Bulk Thermal Conductivity (W/m·K)		Dry Bulk Density (g/cc)		Matrix Porosity		Lithophysal Porosity	
Unit	Mean	Std. Dev.	Mean	Std. Dev.	Mean	Std. Dev.	Mean	Std. Dev.	Mean	Std. Dev.
Tptpul	1.1829	0.2440	1.7749	0.2474	1.8344	0.1496	0.1667	0.0412	0.1228	0.0613
Tptpmn	1.4189	0.2654	2.0741	0.2517	2.1483	0.0932	0.1287	0.0323	0.0254	0.0225
Tptpll	1.2784	0.2511	1.8895	0.2484	1.9793	0.1381	0.1486	0.0340	0.0883	0.0540
Tptpln	1.4900	0.2844	2.1303	0.2676	2.2114	0.0857	0.1058	0.0264	0.0302	0.0253
	Dry Matrix Thermal Conductivity (W/m·K)		Wet Matrix Thermal Conductivity (W/m·K)		Solid Thermal Conductivity (W/m·K)		Solid Connectivity			
Unit	Mean	Std. Dev.	Mean	Std. Dev.	Mean	Std. Dev.	Mean	Std. Dev.		
Tptpul	1.3453	0.2639	2.0201	0.2484	2.6011	0.3493	0.8517	0.1158		
Tptpmn	1.4553	0.2690	2.1276	0.2519	2.6033	0.3518	0.8476	0.1094		
Tptpll	1.3998	0.2640	2.0707	0.2455	2.6030	0.3413	0.8531	0.1130		
Tptpln	1.5356	0.2908	2.1958	0.2764	2.6017	0.3505	0.8492	0.1151		

DTN: SN0208T0503102.007

Source: BSC 2003b

Table 4-14. Specific Heat of the Repository Stratigraphic Units

	Average Rock Grain Specific Heat (J/g·K)	
Unit	Mean	Std. Dev.
Tptpul	0.93	0.16
Tptpmn	0.93	0.17
Tptpll	0.93	0.17
Tptpln	0.93	0.14

DTN: SN0303T0510902.002

NOTE: T = 25 to 325°C

Table 4-15. Emissivity of the Repository Stratigraphic Units

Unit	Emissivity	
	Minimum	Maximum
Tptpul	0.88	0.95
Tptpmn	0.88	0.95
Tptpll	0.88	0.95
Tptpln	0.88	0.95

Source: Incropera and DeWitt 1996, Table A.11 for Rocks

Table 4-16. Matrix Permeability and Van Genuchten Parameters of the Repository Stratigraphic Units

	Permeability (m^2)	Residual Saturation	α (1/Pa)	m
tsw34	1.77e-19	0.19	8.45e-6	0.317
tsw35	4.48e-18	0.12	1.08e-5	0.216
tsw36	2.00e-19	0.20	8.32e-6	0.442

DTN: LB0208UZDSCPMI.002 (Mean Infiltration Flux)

Table 4-17. Thermophysical Properties of the Non-Repository Stratigraphic Units

Unit	Dry Matrix Thermal Conductivity (W/m·K)		Wet Matrix Thermal Conductivity (W/m·K)		Dry Bulk Density (kg/m^3)		Matrix Porosity	
	Mean	Std. Dev.	Mean	Std. Dev.	Mean	Std. Dev.	Mean	Std. Dev.
Crystal-Rich Tiva/Post-Tiva	1.30	0.23	1.81	0.20	2190	177	0.12	0.05
Tpcp	1.30	0.23	1.81	0.20	2190	177	0.12	0.05
TpcLD	1.30	0.23	1.81	0.20	2190	177	0.12	0.05
Tpcpv3	0.69	0.23	0.80	0.25	2310	89	0.04	0.04
Tpcpv2	0.49	0.16	1.06	0.15	1460	337	0.39	0.13
Tpcpv1	0.49	0.16	1.06	0.15	1460	337	0.39	0.13
Tpbt4	0.49	0.16	1.06	0.15	1460	337	0.39	0.13
Yucca	0.49	0.16	1.06	0.15	1460	337	0.39	0.13
Tpbt3_dc	0.49	0.16	1.06	0.15	1460	337	0.39	0.13
Pah	0.49	0.16	1.06	0.15	1460	337	0.39	0.13
Tpbt2	0.49	0.16	1.06	0.15	1460	337	0.39	0.13
Tptrv3	0.49	0.16	1.06	0.15	1460	337	0.39	0.13
Tptrv2	0.49	0.16	1.06	0.15	1460	337	0.39	0.13
Tptrv1	0.69	0.23	0.80	0.25	2310	89	0.04	0.04
Tptrn	1.30	0.23	1.81	0.20	2190	177	0.12	0.05
Tptrl	1.30	0.23	1.81	0.20	2190	177	0.12	0.05
Tptf	1.30	0.23	1.81	0.20	2190	177	0.12	0.05
Tptpv3	0.69	0.23	0.80	0.25	2310	89	0.04	0.04
Tptpv2	0.49	0.16	1.06	0.15	1460	337	0.39	0.13
Tptpv1	0.49	0.16	1.06	0.15	1460	337	0.39	0.13
Tpbt1	0.49	0.16	1.06	0.15	1460	337	0.39	0.13
Calico	0.60	0.11	1.26	0.14	1670	157	0.33	0.05
Calicobt	0.60	0.11	1.26	0.14	1670	157	0.33	0.05
Prowuv	0.57	0.10	1.13	0.12	1790	117	0.30	0.04
Prowuc	0.57	0.10	1.13	0.12	1790	117	0.30	0.04
Prowmd	1.06	0.18	1.63	0.17	2070	139	0.21	0.06
Prowlc	0.57	0.10	1.13	0.12	1790	117	0.30	0.04
Prowlv	0.57	0.10	1.13	0.12	1790	117	0.30	0.04
Prowbt	0.57	0.10	1.13	0.12	1790	117	0.30	0.04
Bullfroguv	0.66	0.13	1.19	0.14	1880	167	0.23	0.06
Bullfroguc	0.66	0.13	1.19	0.14	1880	167	0.23	0.06
Bullfrogmd	1.30	0.24	1.81	0.20	2260	138	0.12	0.05
Bullfroglc	0.66	0.13	1.19	0.14	1880	167	0.23	0.06
Bullfroglv	0.66	0.13	1.19	0.14	1880	167	0.23	0.06
Bullfrogbt	0.66	0.13	1.19	0.14	1880	167	0.23	0.06
Tramuv	0.54	0.11	1.10	0.12	1760	195	0.33	0.06
Tramuc	0.54	0.11	1.10	0.12	1760	195	0.33	0.06
Trammd	1.06	0.18	1.63	0.17	2140	78	0.21	0.06
Tramlc	0.54	0.11	1.10	0.12	1760	195	0.33	0.06
Tramlv	0.54	0.11	1.10	0.12	1760	195	0.33	0.06
Trambt	0.54	0.11	1.10	0.12	1760	195	0.33	0.06

DTN: SN0303T0503102.008

Table 4-18. Specific Heat of the Non-Repository Stratigraphic Units

Unit	Average Rock Grain Specific Heat (J/g·K)	
	Mean	Std. Dev.
Tpc	0.93	0.16
Tpcpv23	0.95	0.14
pTn	0.96	0.29
Tptrv1	0.95	0.14
Tptrnf	0.93	0.18
Tptpv3	0.98	0.28
Tptpv2	0.98	0.22
Tptpv1-Tpbt1	1.08	0.47
Tac4	1.07	0.47
Tac3	1.07	0.42
Tac2	1.08	0.41
Tac1	1.08	0.40
Tacbt	1.02	0.27
Tcpuv	1.04	0.32
Tcpuc-Tcplc	0.93	0.17
Tcplv-Tcbuv	1.11	0.24
Tcbuc-Tcblc	0.93	0.15
Tcblv-Tctuv	1.05	0.26
Tctuc-Tctlc	0.94	0.16
Tctlv-Tctbt	0.94	0.16

DTN: SN0303T0510902.002

NOTE: T = 25 to 325°C

4.1.3 Other Inputs

The following other inputs (i.e., design information, other information, and physical constants) were used to develop the models and analyses described in Sections 6 and 7.

4.1.3.1 Ground Surface and Water Table Elevations and Temperatures

The ground surface and water table temperatures are calculated using the methodology described in Section 6.5.5. This methodology uses the information contained in Table 4-19. The location identified as R5C10, used in this report, is nearest to the UZ 2002 site scale grid column g_9 (see DTN: MO0303MWDSLTLC.000, file P2WR5C10.col) which corresponds to the UZ 2000 site scale grid column i71.

Table 4-19. Information Used to Calculate the Ground Surface and Water Table Temperatures

Grid/Mesh Column ID	Easting (m)	Northing (m)	Surface Elevation (m)	Surface Temperature (°C)	Water Table Elevation (m)	Water Table Temperature (°C)
g_9 [a]	170760	234920	N/A	N/A	N/A	N/A
Tpi71 [b]	170805.3	234886.6	1359.2	16.95	730.0	29.21
R5C10 [c]	170730.3	234912.7	1363.4	Calculated in Section 6.5.5	774.4	Calculated in Section 6.5.5

Sources: [a] DTN: LB03023DKMGRID.001 (file Grid_LA_3D.mesh)
[b] DTN: LB991201233129.001 (files MESH_rep.VF and INCON_thm_s32.dat)
[c] DTN: MO0303MWDSLTLC.000 (file P2WR5C10.col)

4.1.3.2 Waste Package Heat Decay

Table 4-20 shows the repository average lineal heat load as a function of time since waste emplacement. This design information is used as input to the models and analyses described in Section 6.

Table 4-20. Waste Package Heat Decay

Time Since Emplacement (years)	Lineal Heat Load (kW/m)	Time Since Emplacement (years)	Lineal Heat Load (kW/m)
0.000001	1.45E+00	26	8.525E-01
1	1.399E+00	27	8.382E-01
2	1.357E+00	28	8.245E-01
3	1.321E+00	29	8.114E-01
4	1.289E+00	30	7.992E-01
5	1.259E+00	31	7.858E-01
6	1.232E+00	32	7.730E-01
7	1.206E+00	33	7.610E-01
8	1.181E+00	34	7.493E-01
9	1.157E+00	35	7.381E-01
10	1.135E+00	36	7.262E-01
11	1.110E+00	37	7.150E-01
12	1.088E+00	38	7.042E-01
13	1.068E+00	39	6.938E-01
14	1.049E+00	40	6.838E-01
15	1.033E+00	41	6.733E-01
16	1.012E+00	42	6.632E-01
17	9.934E-01	43	6.535E-01
18	9.759E-01	44	6.441E-01
19	9.595E-01	45	6.351E-01
20	9.443E-01	46	6.258E-01
21	9.267E-01	47	6.169E-01
22	9.103E-01	48	6.083E-01
23	8.950E-01	49	6.000E-01
24	8.805E-01	50	5.920E-01
25	8.666E-01		

Source: BSC 2003c, Waste Package Decay Heat Generation

4.1.3.3 Kuehn and Goldstein Parameters for Natural Convection

Table 4-21 lists constants for large Rayleigh numbers in the Kuehn and Goldstein correlations for natural convection. These constants are used in the mixed convection correlation to calculate convection heat transfer coefficients. This information is used as input to the models and analyses described in Sections 6 and 7.

Table 4-21. Constants for Large Rayleigh Numbers in the Kuehn and Goldstein Correlations for Natural Convection

Term	Value
c_i	0.5
$\overline{C_i}$	0.12
c_o	1
$\overline{C_o}$	0.12
m	15

Source: Kuehn and Goldstein 1978, Eq. 1a and 1b

4.1.3.4 Thermophysical Properties of the Waste Package

Table 4-22 shows the thermophysical properties and dimensions of a 21-PWR waste package, its inner stainless steel shell, and its outer Alloy 22 shell. This design information is used as input to the models and analyses described in Section 6. Section 5.2 provides rationale for using a 21-PWR as a representative waste package.

Table 4-22. Thermophysical Properties of the Waste Package

	Reference Temperature (°C) [a]	Thermal Conductivity (W/m·K) [a]	Specific Heat (J/kg·K) [a]	Density (kg/m^3) [a]	Emissivity [a]	Thickness 21-PWR (mm) [b]	Nominal Diameter 21-PWR (mm) [b]
Waste Package Internal Cylinder (21-PWR)	N/A	1.5	378	3495	N/A	N/A	1644
Waste Package Inner Shell (316NG)	21.11	13.33	482.93	7980	N/A	50	
	37.78	13.67	488.19				
	65.56	14.19	499.38				
	93.33	14.54	500.68				
	121.11	15.06	511.31				
	148.89	15.58	521.64				
	176.67	15.92	522.43				
	204.44	16.44	528.75				
Waste Package Outer Shell (Alloy 22)	48, 52	10.1	414	8690	0.87	20	
	100	11.1	423				
	200	13.4	444				

Sources: [a] BSC 2002a; BSC 2001b, pp. 13 and 14
[b] BSC 2002a

4.1.3.5 In-Drift Geometry and Ventilation Parameters

Table 4-23 lists various in-drift geometric and preclosure ventilation parameters. This design information is used as input to the models and analyses described in Section 6.

Table 4-23. Emplacement Drift Geometries, Ventilation Flow Rate, Ventilation Duration

Parameter	Value	Source
Emplacement Drift Diameter (m)	5.5	BSC 2002b
Emplacement Drift Spacing (m)	81	BSC 2002b
Nominal Ventilation Airflow Rate Preclosure (m^3/s)	15	BSC 2002b
Ventilation Duration After Final Emplacement (years)	50	BSC 2002b
Height from Invert Top to Center of 21-PWR (mm)	1018	BSC 2003d
Invert Height (mm)	806	BSC 2003e

4.1.3.6 Thermophysical Properties of Air

Table 4-24 lists the thermophysical properties of air. This information is used as input to the models and analyses described in Section 6.

Table 4-24. Thermophysical Properties of Air

Reference Temperature (K)	Density (kg/m^3)	Specific Heat (kJ/kg·K)	Viscosity 10^7 ($N·s/m^2$)	Kinematic Viscosity 10^6 (m^2/s)	Thermal Conductivity 10^3 (W/m·K)	Thermal Diffusivity 10^6 (m^2/s)	Prandtl Number
250	1.3947	1.006	159.6	11.44	22.3	15.9	0.720
300	1.1614	1.007	184.6	15.89	26.3	22.5	0.707
350	0.995	1.009	208.2	20.92	30.0	29.9	0.700
400	0.8711	1.014	230.1	26.41	33.8	38.3	0.690

Source: Incropera and DeWitt 1996, Table A.4

4.1.3.7 Thermophysical Properties of Water

Table 4-25 lists the thermophysical properties of water. This information is used as input to the models and analyses described in Section 6.

Table 4-25. Thermophysical Properties of Water

Reference Temperature (K)	Specific Volume 10^3 (m^3/kg)	Heat of Vaporization (kJ/kg)	Specific Heat (kJ/kg·K)	Viscosity 10^6 ($N·s/m^2$)	Thermal Conductivity 10^3 (W/m·K)
273.15	1.000	2502	4.217	1750	569
300	1.003	2438	4.179	855	613
350	1.027	2317	4.195	365	668

Source: Incropera and DeWitt 1996, Table A.6

4.1.3.8 Kays and Leung Parameters for the Mixed Convection Coefficient Calculation

Table 4-26 lists Kays and Leung parameters used in the mixed convection correlation to calculate convection heat transfer coefficients. This information is used as input to the models and analyses described in Sections 6 and 7.

Table 4-26. Kays and Leung Parameters for the Mixed Convection Coefficient Calculations

	Annulus Radius Ratio (r^*)	Reynolds Number (Re)	Nusselt Number – Inner Surface Condition, Inner Surface Heated Alone (Nu_{ii})	Non-Dimensional Temperature – Inner Surface (θ_i)	Nusselt Number - Outer Surface Condition, Outer Surface Heated Alone (Nu_{oo})	Non-Dimensional Temperature – Outer Surface (θ_o)
Fluid with Prandtl Number = 0.700	0.2	1.00E+04	38.6	0.412	29.4	0.063
		3.00E+04	79.8	0.338	64.3	0.055
		1.00E+05	196	0.286	165	0.049
		3.00E+05	473	0.26	397	0.044
		1.00E+06	1270	0.235	1070	0.04
	0.5	1.00E+04	30.9	0.3	28.3	0.137
		3.00E+04	66	0.258	62	0.119
		1.00E+05	166	0.225	158	0.107
		3.00E+05	400	0.206	380	0.097
		1.00E+06	1080	0.185	1040	0.09

Source: Kays and Leung 1963, Table 1

4.1.3.9 Thermophysical Properties of the Simulated Waste Package

Table 4-27 lists thermophysical properties of the simulated waste package used in the ventilation tests performed at the North Las Vegas Atlas Facility. This information is used as input to the model validation exercises described in Section 7.

Table 4-27. Thermophysical Properties of the Simulated Waste Package

Property	Value	Source
Density (kg/m^3)	7840	Stroe 2001, p. 3 for Carbon Steel (averaged over 20 to 50°C)
Thermal Conductivity (W/m·K)	38.37	Stroe 2001, p. 3 for Carbon Steel (averaged over 20 to 50°C)
Specific Heat (J/kg·K)	410.98	Stroe 2001, p. 3 for Carbon Steel (averaged over 20 to 50°C)
Emissivity	0.8	Holman 1997, Table A-10 for Sheet Steel
Outside Diameter (in.)	16	CRWMS M&O 2000a

4.1.3.10 Physical Constants

Table 4-28 lists physical constants used as inputs to the model and analyses of Sections 6 and 7.

Table 4-28. Physical Constants

Property	Value	Source
Stefan-Boltzmann ($W/m^2 \cdot K^4$)	5.670×10^{-8}	Incropera and DeWitt 1996, Back cover
Gravity (m/s^2)	9.8	Incropera and DeWitt 1996, Back cover
Ideal Gas Law Constant (kJ/kmol·K)	8.315	Incropera and DeWitt 1996, Back cover
Prandtl Number Exponent (Dittus-Boelter Correlation)	0.4	Incropera and DeWitt 1996, Section 8.5
Molecular Weight of Water (g/mol)	18	Weast 1977
Molecular Weight of Air (g/mol)	29	Weast 1977

4.1.3.11 Thermophysical Properties of the Concrete Pipe

Table 4-29 lists thermophysical properties of the concrete pipe used in the ventilation tests performed at the North Las Vegas Atlas Facility. This information is used as input to the model validation exercises described in Section 7.

Table 4-29. Thermophysical Properties of the Concrete Pipe

Property	Value	Source
Density (kg/m^3)	2280	Stroe 2001, p. 3 for Concrete (averaged over 20 to 50°C)
Thermal Conductivity (W/m·K)	2.75	Stroe 2001, p. 3 for Concrete (averaged over 20 to 50°C)
Specific Heat (J/kg·K)	1016.16	Stroe 2001, p. 3 for Concrete (averaged over 20 to 50°C)
Emissivity	0.93	Incropera and DeWitt 1996, Table A.11 for Concrete
Inner Diameter (in.)	54	CRWMS M&O 2000a
Outside Diameter (in.)	65	CRWMS M&O 2000a

4.1.3.12 Thermophysical Properties of the Insulation

Table 4-30 lists thermophysical properties of the insulation used in the ventilation tests performed at the North Las Vegas Atlas Facility. This information is used as input to the model validation exercises described in Section 7.

Table 4-30. Thermophysical Properties of the Insulation

Property	Value	Source
Density (kg/m^3)	12	CertainTeed 1996 for Standard Fiber Glass Duct Wrap
Thermal Conductivity (W/m·K)	0.04	CertainTeed 1996 for Standard Fiber Glass Duct Wrap
Specific Heat (J/kg·K)	700	Holman 1997, Table A-3 for Insulation
Thickness (in.)	2	CRWMS M&O 2000a

4.1.3.13 Emissivity of the Invert Material

Table 4-31 lists the emissivity of the invert material. This information is used as input to the models and analyses described in Section 6 and the validation exercises described in Section 7.

Table 4-31. Emissivity of the Invert

Minimum	Maximum
0.88	0.95

Source: Incropera and DeWitt 1996, Table A.11 for Rocks

4.1.3.14 Correlation Between the GFM3.1 Lithostratigraphy and the UZ Model Layers

Table 4-32 shows the nomenclature correlation between the GFM3.1 lithostratigraphy and the UZ model layers. This is used to correlate the thermophysical properties listed in Section 4.1.2.1.

4.1.3.15 Ventilation Test Phase 1 and 2 Design Test Conditions, Average Flow Rates, and 24 Hour Averaged Temperatures

The Ventilation Test Phase 1 report, *Testing to Provide Data for Ventilation System Design: Phase 1* (BSC 2003f, Sections 2.2.4 and 3) presents 24-hour averages of measurements taken at the rate of four per hour. For the Phase 1 tests, the time period chosen was the last full day of data in cases where quasi steady-state conditions were achieved, or the last 24 hours of data collected in cases where recorded temperatures were still increasing with time. For the Phase 2 tests, the averaging period was chosen as the last 24-hour period of the test where the design test conditions were maintained.

A volume flow rate for each test within each phase was calculated using measured differential pressure, relative humidity, barometric pressure, and air temperatures at both the inlet (designated Station A) and the outlet (designated Station D) (BSC 2003f, Section 5.2). The 24-hour average flow rates for each of the forced ventilation tests were within 10% of the nominally desired values, as shown in Tables 4-33 and 4-34. No flow rate measurements were reported at Station D for Tests 15 or 16 of Phase 2.

Tables 4-33 and 4-34 also show the 24-hour average line load for each test, which is the total power input divided by the total heated length of the test train, 33.9 m (BSC 2003f, Section 2.2.2.2). The standard uncertainty in the 24-hour-average total load was 5.8 W (BSC 2003f, Section 3.3.2.4), which is equivalent to a standard uncertainty of 0.2 W/m in the average line load, much less than 1% of the measured average.

The test reports also tabulate average temperatures for 24-hour periods. Tables 4-35 through 4-37 present the calculated average temperatures at a point midway along the heated portion of the test train (Station 3). Values in the tables are reported by quadrant (top, right, bottom, and left) for sensors located on the external surface of the waste package, the internal and external surfaces of the concrete pipe, the external surface of the insulation, and within the annulus between the waste package and concrete pipe (ventilation air). The standard uncertainty for a 24-hour temperature average included a systematic component that varied with temperature (BSC 2003f, Table 3-17).

These data are used in Attachments IX, X, and XI to validate the correlation to calculate mixed convection heat transfer coefficients for the YMP EBS geometry. The mixed convection correlation is used throughout Section 6 and 7 to calculate convection heat transfer coefficients used in the ventilation models.

Table 4-32. Nomenclature Correlation Between GFM3.1 and UZ

GFM3.1 Lithostratigraphic	UZ Model Layer
Tiva_Rainier	tcw11
Tpcp	tcw12
TpcLD	
Tpcpv3	tcw13
Tpcpv2	
Tpcpv1	ptn21
Tpbt4	ptn22
Tpy (Yucca)	ptn23
	ptn24
Tpbt3	
Tpp (Pah)	ptn25
Tpbt2	ptn26
Tptrv3	
Tptrv2	
Tptrv1	tsw31
Tptrn	
	tsw32
Tptrl, Tptf	tsw33
Tptpul	
Tptpmn	tsw34
Tptpll	tsw35
Tptpln	tsw36
	tsw37
Tptpv3	tsw38
Tptpv2	tsw39
Tptpv1	ch1v, ch1z
Tpbt1	
Tac (Calico)	ch2v, ch2z
	ch3v, ch3z
	ch4v, ch4z
	ch5v, ch5z
Tacbt (Calicobt)	ch6
Tcpuv (Prowuv)	pp4
Tcpuc (Prowuc)	pp3
Tcpm (Prowmd)	pp2
Tcplc (Prowlc)	
Tcplv (Prowlv)	pp1
Tcpbt (Prowbt)	
Tcbuv (Bullfroguv)	
Tcbuc (Bullfroguc)	bf3
Tcbm (Bullfrogmd)	
Tcblc (Bullfroglc)	
Tcblv (Bullfroglv)	bf2
Tcbbt (Bullfrogbt)	
Tctuv (Tramuv)	
Tctuc (Tramuc)	tr3
Tctm (Trammd)	
Tctlc (Tramlc)	
Tctlv (Tramlv)	tr2
Tctbt (Trambt)	

Source: BSC 2001c, Table 10

Table 4-33. Averaged Flow Rates and Line Loads and Their Standard Uncertainties for EBS Ventilation Tests, Phase 1

Test No.	Nominal Flow Rate (m^3/s)	Station A, Flow Rate (m^3/s)	Station D, Flow Rate (m^3/s)	Flow Rate Uncertainty (m^3/sec)	Nominal Line Load (W/m)	Avg. Line Load (W/m)
1	1	0.997	1.001	0.014	180	182
2	0.5	0.50	0.495	0.03	180	179
3	1	0.998	1.016	0.014	360	359
4	2	1.990	1.990	0.008	360	362
5	0.5	0.519	0.525	0.03	360	362
6	3	3.048	3.052	0.02	360	364
NC1	—	—	—	—	120	120
NC2	—	—	—	—	240	242

Source: BSC 2003f, Tables 3-16 and 5-6

Table 4-34. Averaged Flow Rates and Line Loads and Their Standard Uncertainties for EBS Ventilation Tests, Phase 2

Test No.	Nominal Flow Rate (m^3/s)	Station A, Flow Rate (m^3/s)	Station D, Flow Rate (m^3/s)	Flow Rate Uncertainty (m^3/sec)	Nominal Line Load (W/m)	Avg. Line Load (W/m)
1	1	1.021	0.972	0.014	220	218
2	1	1.037	0.986	0.014	220	218
3	1	1.058	1.012	0.014	220	216
4	1	1.054	1.003	0.014	220	215
5	1	1.024	0.989	0.014	360	360
6	1	1.041	1.005	0.014	360	359
7	1	1.053	1.011	0.014	360	357
8	1	1.055	1.013	0.014	360	358
9	0.5	0.516	0.506	0.03	220	215
10	0.5	0.552	0.544	0.03	220	215
11	0.5	0.554	0.530	0.03	220	216
12	0.5	0.547	0.553	0.03	360	360
13	0.5	0.553	0.550	0.03	360	360
14	0.5	0.553	0.537	0.03	360	361
15	1	0.993	N/A	0.014	360	360
16	1	0.991	N/A	0.014	360	364

DTN: MO0306MWDVTPH2.000

Table 4-35. Averaged Temperature Values (C) at Station 3 for EBS Ventilation Tests, Phase 1

		Ventilating Air (°C)	WP Surface (°C)	Concrete Pipe Wall (°C)	Concrete/ Insulation Interface (°C)	Outside Insulation Surface (°C)
Test 1	top		47.4	30.5	30.7	30.3
	right	27.8	42.0	29.8	30.0	27.5
	bottom		39.1	28.4	28.2	26.7
	left	27.4	40.8	30.2	30.1	27.9
Test 2	top		51.6	33.6	33.1	28.8
	right	31.4	45.9	32.8	32.7	28.4
	bottom		42.9	30.5	30.1	27.1
	left	31.4	44.7	33.4	32.8	27.6
Test 3	top		63.4	33.8	33.5	27.8
	right	29.3	54.6	32.7	33.0	26.5
	bottom		50.3	30.6	30.0	25.1
	left	29.2	53.3	33.5	33.0	25.9
Test 4	top		57.4	29.9	30.0	27.0
	right	27.2	49.4	30.0	30.2	26.0
	bottom		45.3	28.8	28.3	25.2
	left	26.8	48.0	29.9	29.9	25.7
Test 5	top		65.6	34.6	33.7	24.5
	right	31.0	56.7	33.5	33.3	23.6
	bottom		52.0	29.2	28.4	22.6
	left	31.0	55.0	34.6	33.6	23.6
Test 6	top		48.0	23.4	23.5	21.2
	right	21.7	40.6	23.5	23.7	20.6
	bottom		36.8	23.3	23.0	20.0
	left	21.7	39.8	23.7	23.7	20.1
Test NC1	top		60.9	46.3	43.8	28.2
	right	48.7	56.9	45.7	43.6	28.3
	bottom		55.0	38.0	36.7	25.5
	left	48.4	56.3	45.5	43.3	27.4
Test NC2	top		93.2	69.4	64.4	33.0
	right	73.4	87.4	68.6	64.2	32.8
	bottom		84.9	56.1	51.6	29.0
	left	72.9	86.3	68.3	63.8	31.8

Source: BSC 2003f, Tables 5-7 through 5-14

NOTE: WP = waste package

Table 4-36. Averaged Temperature Values (C) at Station 3 for EBS Ventilation Tests, Phase 2, Tests 1 through 8

		Ventilating Air (°C)	WP Surface (°C)	Concrete Pipe Wall (°C)	Concrete/ Insulation Interface (°C)	Outside Insulation Surface (°C)
Test 1	top		50.5	30.8	30.8	28.5
	right	27.5	44.3	30.2	30.6	28.5
	bottom		41.1	29.4	30.7	28.0
	left	27.3	43.5	30.6	30.5	28.3
Test 2	top		59.3	38.8	37.9	30.0
	right	36.9	52.8	38.5	37.8	29.2
	bottom		49.9	35.3	35.8	28.4
	left	36.7	51.9	38.6	37.6	28.4
Test 3	top		68.4	48.4	47.1	36.6
	right	47.0	62.2	48.2	47.2	36.6
	bottom		59.6	44.2	44.7	35.1
	left	46.7	61.3	48.2	46.9	35.8
Test 4	top		67.9	48.0	46.6	35.9
	right	46.7	61.7	47.8	46.8	36.3
	bottom		59.1	43.8	44.2	34.4
	left	46.5	60.9	47.9	46.6	36.0
Test 5	top		64.1	34.4	34.4	31.1
	right	29.8	55.2	33.4	33.8	30.1
	bottom		50.8	31.8	33.0	28.7
	left	29.7	54.0	34.1	34.0	30.4
Test 6	top		73.6	43.8	43.4	37.2
	right	39.6	64.4	42.9	43.0	36.3
	bottom		60.4	39.8	40.9	34.4
	left	39.4	63.1	43.6	43.1	36.5
Test 7	top		81.4	51.8	50.3	37.8
	right	49.1	72.7	51.3	50.4	37.9
	bottom		69.0	46.4	47.0	35.4
	left	48.7	71.4	51.8	50.4	38.2
Test 8	top		81.4	51.6	50.1	37.2
	right	49.0	72.7	51.2	50.2	37.3
	bottom		69.0	46.4	46.9	34.8
	left	48.7	71.4	51.6	50.1	37.1

DTN: MO0306MWDVTPH2.000

Table 4-37. Averaged Temperature Values (C) at Station 3 for EBS Ventilation Tests, Phase 2, Tests 9 through 16

		Ventilating Air (°C)	WP Surface (°C)	Concrete Pipe Wall (°C)	Concrete/ Insulation Interface (°C)	Outside Insulation Surface (°C)
Test 9	top		55.2	35.3	35.3	33.0
	right	31.6	48.5	34.5	34.8	32.3
	bottom		45.1	33.1	34.8	31.0
	left	31.6	47.6	35.0	35.0	32.7
Test 10	top		63.5	43.0	42.4	36.2
	right	40.4	56.5	42.5	42.2	36.0
	bottom		53.5	39.5	40.9	34.2
	left	40.3	55.7	42.9	42.2	36.2
Test 11	top		71.7	51.0	49.7	39.6
	right	49.7	65.1	50.6	49.7	39.4
	bottom		62.3	46.1	47.1	36.9
	left	49.6	64.3	50.9	49.7	39.9
Test 12	top		71.2	41.0	40.9	35.6
	right	35.9	61.5	40.0	40.4	35.2
	bottom		56.9	38.0	39.6	33.8
	left	35.9	60.1	40.8	40.5	35.1
Test 13	top		78.0	47.3	46.3	34.8
	right	44.0	68.4	46.9	46.2	35.0
	bottom		64.4	42.3	43.1	33.1
	left	43.9	67.2	47.3	46.1	34.5
Test 14	top		86.1	55.6	53.7	38.4
	right	53.4	77.0	55.2	53.8	38.2
	bottom		73.2	48.3	48.9	35.1
	left	53.3	75.7	55.7	53.9	38.8
Test 15	top		68.6	38.4	37.8	29.4
	right	34.6	59.7	37.7	37.7	30.4
	bottom		55.4	35.0	36.4	28.8
	left	34.4	58.4	38.3	37.5	28.7
Test 16	top		68.6	37.9	37.2	27.9
	right	34.3	59.5	37.2	37.0	28.2
	bottom		55.2	34.8	36.1	27.4
	left	34.1	58.2	37.8	36.9	27.1

DTN: MO0306MWDVTPH2.000

4.2 CRITERIA

Technical Work Plan for: Engineered Barrier System Department Modeling and Testing FY03 Work Activities (BSC 2003a) identifies the following acceptance criteria (AC) for this model report based on the requirements mentioned in *Project Requirements Document* (Canori and Leitner 2003) and *Yucca Mountain Review Plan, Information Only* (NRC 2003).

AC1: System Description and Model Integration are Adequate
AC2: Data are Sufficient for Model Justification

AC1 is addressed in Sections 6.3, 6.4, and 6.10, while AC2 is addressed in Section 7. Note that the output of this report does not directly feed TSPA, but rather feeds downstream models and analyses which, in turn, feed TSPA. Other specific YMRP criteria are provided for these downstream models and analyses. However, two criteria apply from the Code of Federal Regulations specifying that this document account for uncertainties and variabilities in parameter values and provide the technical basis for parameter ranges, probability distributions, or bounding values in the model analysis (10 CFR 63.114b). Propagation of uncertainties, parameter ranges, and probability distributions for key input parameters are discussed in Section 6.11. The other criterion is that this document consider alternative conceptual models of processes that are consistent with available data and current scientific understanding, and evaluate the effects that alternative conceptual models have on the model analysis.

4.3 CODES AND STANDARDS

4.3.1 Codes

This report was prepared to comply with 10 CFR Part 63, the U.S. Nuclear Regulatory Commission rule on high-level radioactive waste. Subparts of this rule that are applicable to data include Subpart E, Section 114 (Requirements for Performance Assessment). The subpart applicable to models is also outlined in Subpart E Section 114. The subparts applicable to features, events, and processes (FEPs) are 10 CFR 63.114(d), (e), and (f). Other codes and standards used in this report are ANSI/NCSL Z540-2-1997, *American National Standard for Calibration — U.S. Guide to the Expression of Uncertainty in Measurement*, and ASME PTC 19.1-1998, *Test Uncertainty, Instruments and Apparatus*.

5. ASSUMPTIONS

5.1 REPRESENTATIVE LOCATION WITHIN THE REPOSITORY FOOTPRINT

Northing 234913 and Easting 170730 was chosen as a representative location within the repository footprint to perform the ventilation analyses. This assumption does not require confirmation. The rationale for choosing this location is that the repository lies within the tsw35 geologic unit in this area. In addition, this location is representative because it does not lie on an edge or corner of the repository footprint, and it experiences average infiltration rates. This is used in Section 6.5.1.

5.2 THERMAL PROPERITES OF A 21-PWR AS REPRESENTATIVE

The thermal properties of a 21-PWR were used as representative properties for all waste packages emplaced in the repository. This assumption does not require confirmation. The rationale for using these thermal properties is that the 21-PWR accounts for the majority of the repository inventory. This is used throughout Section 6.

5.3 INITIAL WATER SATURATION OF EACH OF THE STRATIGRAPHIC LAYERS

The initial water saturation of the stratigraphic layers is assumed to be approximately 90%. This assumption does not require confirmation. The rationale for this assumption is that measurements and hydrologic models demonstrate the range of saturation to be between 70 and 100%. This is used in Section 6.5.2 and Attachment II to account for saturation in obtaining effective thermophysical properties of the stratigraphic units. The sensitivity of the ventilation efficiency with respect to saturation is documented in Section 6.11.

5.4 LITHOPHYSAL POROSITY IS AIR FILLED

The lithophysal porosity is assumed to be 100% air-filled. This assumption does not require confirmation. The rationale for this assumption is that, based on unsaturated flow theory, the air entry pressure of the large void space is large enough to inhibit liquid flow through by pore water. This is used in Section 6.5.2 and Attachment II to account for air-filled lithophysal porosity in obtaining effective thermophysical properties of the stratigraphic units.

5.5 INVERT BALLAST MATERIAL

Repository/PA IED Emplacement Drift Committed Materials (BSC 2003e) describes the invert ballast material as crushed tuff. The nominal particle diameter of the crushed tuff is not specified. Therefore, the thermophysical properties of a 4-10 crushed tuff (for which these properties have been measured), will be used. This assumption does not require confirmation as the model is not sensitive to this parameter (Section 6.6.2). The rationale for this assumption is that difference in particle sizes will have little effect on the bulk thermophysical properties of the material. This is used in Section 6.5.3.

5.6 MIXED CONVECTION CORRELATION

The mixed convection correlation incorporates forced and natural convection correlations from experimental data. The correlations are for idealized configurations that are not the same as the EBS configuration. With one exception, the development of the correlation (documented in Attachment IX) recognizes that the idealizations are not true and considers their effects in an uncertainty analysis. The one exception applies to natural convection when the outer convective surface is hotter than the air. During the preclosure period the ventilating air removes heat. Because the drift wall is heated by thermal radiation from the waste package, the drift wall (outer convective surface) will be hotter than the air. The development of the mixed convection correlation assumes that the Kuehn-Goldstein correlation remains valid when the drift wall is hotter than the ventilation air. This assumption does not require confirmation. This is used in Attachment IX. The mixed convection correlation is used throughout Sections 6 and 7 to calculate convection heat transfer coefficients.

5.7 TEMPERATURE OF THE VENTILATION AIR AT THE INLET

The temperature of the ventilation air at the inlet to the drift is assumed to be equal to the temperature of the host rock at the start of preclosure. The sensitivity of the ventilation efficiency to the inlet air temperature is described in Section 6.11. This assumption does not require confirmation as long as the temperature of the inlet air lies within the bounds analyzed herein. Further analyses will be required if the inlet temperature of the ventilation air is outside the range of sensitivity described in Table 6-9 of Section 6.11. This assumption is used throughout Section 6.

6. MODEL DISCUSSION

A conceptual model and an alternative conceptual model for the preclosure heat transfer in and around a waste emplacement drift are developed, implemented, and documented in this section. Table 6-1 outlines the organization of this section. The primary output of the ventilation model is the ventilation efficiency, defined as the fraction of source heat removed by the ventilating air. The ventilation efficiency is expressed as both an instantaneous efficiency (time and distance from the drift inlet dependent), and an integrated efficiency (instantaneous efficiencies integrated over time and drift length).

Table 6-1. Outline of the Ventilation Model Documentation

Section	Content
6.1	Modeling and analysis objectives.
6.2	Lists and describes FEPs assigned to the Ventilation Model and a summary of their disposition.
6.3	Develops the conceptual model for preclosure heat transfer in and around a ventilated emplacement drift including the basis mathematical equations. The conceptual model includes thermal radiation, convection, and conduction heat transfer.
6.4	Describes the numerical implementations of the conceptual model using the ANSYS/Excel methodology and an analytical approach.
6.5	Lists additional inputs developed from the inputs of Section 4.
6.6	Presents and discusses the results of the numerical and analytical implementations of the conceptual model described in Section 6.4.
6.7	Develops the alternative conceptual model for preclosure heat transfer in and around a ventilated emplacement drift which includes the effects of moisture in the host rock.
6.8	Describes the implementations of the alternative conceptual model using analytical approaches.
6.9	Presents and discusses the results of the analytical approaches which implement the alternative conceptual model.
6.10	Discusses the applicability of the downstream use of the output of the ventilation model (i.e., ventilation efficiency) as a means of representing the preclosure heat transfer to initialize postclosure analyses.
6.11	Discusses the uncertainties associated with the ventilation modeling approaches and the design inputs and parameters, and quantifies the sensitivity of the model output (i.e., ventilation efficiency).

6.1 MODELING OBJECTIVES

The thermal energy removed by ventilation must be determined by analyzing, at the least, thermal radiation, thermal convection, and thermal conduction which occur simultaneously in the drift and the surrounding rock mass. The ventilation efficiency, expressed as the percentage of the total thermal energy removed by convection, is the primary output of the ventilation modeling. The ventilation efficiency is used as input in downstream models that do not explicitly simulate the preclosure period. Examples of these models include the MSTH, UZ, and Drift Degradation Models. The ventilation modeling and analysis objectives are to:

1. Develop a conceptual model for preclosure ventilation of an emplacement drift (Section 6.3).

2. Implement the ventilation conceptual model using developed software and methods, and the License Application design basis inputs and parameters to predict the preclosure ventilation efficiency (Section 6.4).

3. Verify the results of the numerical application of the ventilation conceptual model through comparative analyses (Section 6.6).

4. Develop an alternate conceptual model for preclosure ventilation which includes the impacts of water and water vapor mass transfer on the heat transfer (Section 6.7).

5. Implement the alternative conceptual model using analytical calculations to assess the impacts of moisture on the ventilation efficiency (Sections 6.8 and 6.9).

6. Demonstrate the applicability of the use of the ventilation efficiency as an abstraction method for downstream postclosure models to account for the preclosure heat removal (Section 6.10).

7. Demonstrate the sensitivity of the ventilation efficiency to discretization and uncertainties in key input parameters associated with the host rock and engineered components including thermal conductivity, matrix and lithophysal porosity, specific heat, emissivity, and convection heat transfer coefficient (Sections 6.6.1 and 6.11).

6.2 FEATURES, EVENTS, AND PROCESSES

The development of a comprehensive list of FEPs potentially relevant to postclosure performance of the potential Yucca Mountain repository is an ongoing, iterative process based on site-specific information, design, and regulations. The approach for developing an initial list of FEPs, in support of *Total System Performance Assessment for the Site Recommendation* (CRWMS M&O 2000b), was documented by Freeze et al. (2001). The initial FEP list contained 328 FEPs, of which 176 were included in TSPA-SR models (CRWMS M&O 2000b, Tables B-9 through B-17). To support TSPA-LA, the FEP list was re-evaluated in accordance with *The Enhanced Plan for Features, Events, and Processes (FEPs) at Yucca Mountain* (BSC 2002c, Section 3.2). Table 6-2 provides a listing of FEPs included in TSPA-LA models described and addressed in this document.

Table 6-2. Included FEPs Addressed by the Ventilation Model and Analysis Report

FEP	Name	Description	Section Where Disposition is Described	Summary of Disposition in TSPA-LA
1.1.02.02.0A	Preclosure Ventilation	The duration of preclosure ventilation acts together with waste package spacing (as per design) to control the extent of the boiling front.	Section 6.6	ANL-EBS-MD-000030 REV 03 calculates the preclosure thermal conditions in the host rock, and characterizes the preclosure host rock response in terms of a ventilation efficiency. T he ventilation efficiency is the fraction of total decay heat that is removed from the repository by the vent air. The ventilation efficiency is determined through simulation of temporally and spatially dependent heat transfer processes (thermal radiation, convection, and conduction) which occur simultaneously in the drift and the surrounding rock mass during the ventilating or preclosure period. The ventilation efficiency is a direct input to the MSTH Model, which in turn provides postclosure thermal conditions to the TSPA-LA. Because the uncertainty in the ventilation efficiency (which includes the effects of dry-out on the host rock thermal conductivity) can be propagated to downstream models, the effect of dry-out on the ventilation efficiency can be included in the MSTH Model. Therefore, the extent of the boiling front (or the zone of reduced water content) during the ventilation period (characterized by host rock temperatures) is accounted for in the TSPA-LA. Additional effects from the phase change of water and water vapor mass transport do not affect the ventilation efficiency.
2.1.08.03.0A	Repository Dry-Out Due to Waste Heat	Repository heat evaporates water from the UZ rocks near the drifts, as the temperature exceeds the vaporization temperature. This zone of reduced water content (reduced saturation) migrates outward during the heating phase and then migrates back to the containers as heat diffuses throughout the mountain and the radioactive heat sources decay. This FEP addresses the effects of dry-out within the repository drifts.	Sections 6.6 and 6.7	ANL-EBS-MD-000030 REV 03 calculates the preclosure thermal conditions in the host rock, and characterizes the preclosure host rock response in terms of a ventilation efficiency. T he ventilation efficiency is the fraction of total decay heat that is removed from the repository by the vent air. The ventilation efficiency is determined through simulation of temporally and spatially dependent heat transfer processes (thermal radiation, convection, and conduction) which occur simultaneously in the drift and the surrounding rock mass during the ventilating or preclosure period. The ventilation efficiency is a direct input to the MSTH Model, which in turn provides postclosure thermal-hydrologic conditions to the TSPA-LA. Dry-out during the preclosure period causes the thermal conductivity of the rock to decrease, which in turn causes the ventilation efficiency to increase. The latent heat contribution caused by evaporation during the preclosure period is insignificant.

6.3 CONCEPTUAL MODEL FOR IN-DRIFT VENTILATION

When air is directed into an emplacement drift, thermal energy released from the waste packages is transferred to the in-drift and host rock surroundings. The heat transfer processes are time and axial position (i.e., the distance down the length of the drift from the airflow entrance point) dependent.

6.3.1 Heat Transfer Processes

The heat transfer processes for ventilation of an emplacement drift is shown in Figure 6-1. Figure 6-1 also includes other heat and mass transfer processes that will be outlined later in Section 6.7 where the alternative conceptual model for ventilation is presented.

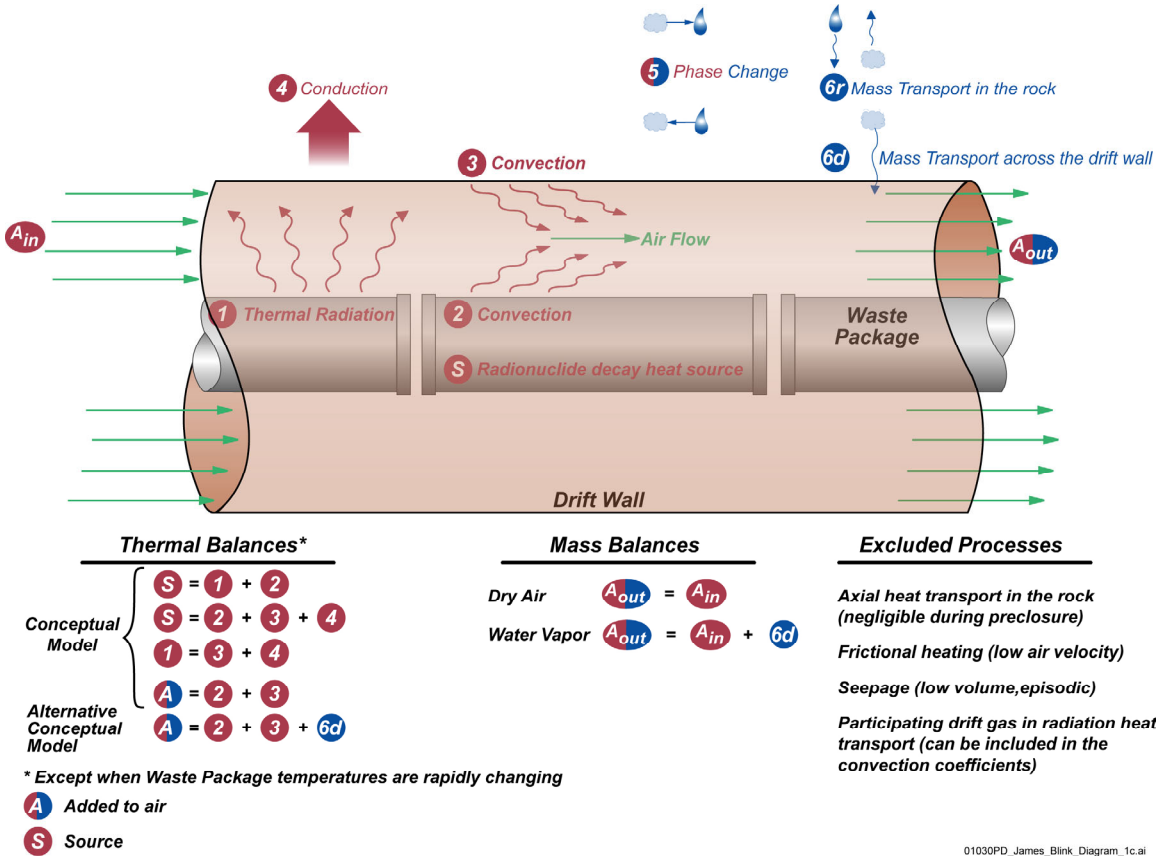

Figure 6-1. Conceptual Model for Heat and Mass Transfer Within and Around an Emplacement Drift

The heat transfer processes depicted in Figure 6-1 include:

1. Thermal radiation heat transfer from the surface of the waste package to the drift wall. The rate at which the heat is transferred can be calculated using the Stefan-Boltzmann Law for gray surface radiation exchange, at any time during the preclosure period, using the waste package surface and drift wall temperatures. This calculation also requires knowledge of the geometry and emissivities of the waste package and drift wall surfaces.

2. Convection heat transfer from the surface of the waste package to the airflow due to the temperature differences between the surface and the moving air. The heat flow rate can be calculated using Newton's Law of Cooling at any time during the preclosure period, using the bulk temperature of the airflow and the temperature of the waste package surface. This calculation also requires knowledge of the convective heat transfer coefficients that implicitly describe the effects of the airflow, the drift geometry, and the surface properties on the heat transfer rates.

3. Convection heat transfer from the drift wall surface directly to the airflow due to the temperature differences between the wall surface and the moving air, similar to process 2. The sum of the two convective heat transfer rates determines the rate of energy addition to the moving air, and can be used to calculate the axial rate of air temperature increase. This calculation also requires knowledge of the convective heat transfer coefficients that implicitly describe the effects of the airflow, the drift geometry, and surface properties on the heat transfer rates. Axially along the drift, the convection heat transfer (processes 2 and 3) can be combined with the air mass flow rate and its specific heat to calculate the axial change of air temperature.

4. Conduction heat transfer within the rock mass due to changes in drift wall temperature. The heat flow rate into the rock can be determined using Fourier's Law of Conduction, at any time during the preclosure period, using the temperature gradient in the rock mass. This calculation requires knowledge of the thermal conductivity, saturation, density, and heat capacity of the rock (which vary spatially).

The heat transfer for the processes described above can be related by considering the overall conservation of thermal energy except during the early transient response when the waste package temperature is rapidly changing. The following summarizes the coupled components of the thermal energy conservation during quasi-steady-state conditions when energy storage is relatively constant:

- The sum of the radiative heat transfer rate from the waste package to the drift wall (process 1 from above), and the convective heat transfer rate from the waste package into the airflow (process 2), must equal the total rate of heat released from the waste package.

- The sum of the convective heat transfer rates from the waste package and drift wall into the airflow (processes 2 and 3), and the conductive heat transfer rate into the rock (process 4), must equal the total rate of heat released from the waste package.

- The sum of the convective heat transfer rates from the drift wall into the airflow (process 3), and the conductive heat transfer rate into the rock (process 4), must equal the rate of radiant heat released from the waste.

Five additional processes have not been explicitly included in the conceptual model. The first includes the mass transport of water and water vapor and the coupled latent and sensible heat transfer associated with the phase change and movement of water. However, these latent heat effects and near-field host rock mass transport processes can be approximated using boiling point

temperature dependent values for the thermal conductivity and specific heat of the rock. This can account for vaporization of pore water and dryout in an approximate sense, but cannot accurately track changes of saturation and evolution of properties. In most cases, the temperatures needed to change these properties are not reached during the preclosure period. These processes are presented in greater detail in Section 6.7.

The second process excluded from the conceptual model is the axial transport of heat and mass within the rock domain. This process has negligible influence on the ventilation efficiency during the 50-year preclosure period due to the small thermal diffusivity of rock ($\sim 1 \times 10^{-7}$ m^2/s) and the large (hundreds of meters) scale of the repository footprint. The axial heat transport process, especially about the end of the drift, is captured in the MSTH Model.

The third process not included in the ventilation conceptual model is the frictional heating of the air and engineered components due to the moving air. This process is negligible when compared to the waste package heat source due to the low air flow velocities.

The fourth process not included in the ventilation conceptual model is episodic flow of liquid water into the drift air (due to heterogeneities in the host rock and episodic infiltration). The total heat added to the airflow by vaporizing such seeps is small compared to the heat from radionuclide decay. It should be noted here that the alternative conceptual model does account for vaporization of liquid water within the host rock and movement of the vapor into the drift, but that process adds only the sensible heat due to the temperature difference between the entering water vapor and the airflow.

Finally, the fifth process not included in the ventilation conceptual model is the participation of the drift gas in the radiation process. Water vapor is an effective absorber of infrared radiation; however, the effect of its absorption and re-radiation of thermal energy is negligible due to low in-drift relative humidity during the ventilation period.

6.3.2 Heat Transfer Equations for the Ventilation Model

The following three equations represent energy balances for processes 1, 2, and 3 as outlined above in Section 6.3.1 and Figure 6-1:

$$Q_s = \pi L \cdot \left[d_s h_{rad} (T_s^4 - T_w^4) + d_s h_s (T_s - T_{air-bulk}) \right] \quad \text{Eq. 6-1}$$

$$Q_w = \pi L \cdot \left[d_s h_{rad} (T_s^4 - T_w^4) - d_w h_w (T_w - T_{air-bulk}) \right] \quad \text{Eq. 6-2}$$

$$(\dot{m} C_p)_{air} (T_{out} - T_{in}) = \pi L \cdot \left[d_s h_s (T_s - T_{air-bulk}) + d_w h_w (T_s - T_{air-bulk}) \right] \quad \text{Eq. 6-3}$$

where

Q_s = heat generated by the waste package (W)
Q_w = heat conducted into the rock (W)
T_s = waste package surface temperature (K)
T_w = drift wall temperature (K)
$T_{air\text{-}bulk} = (T_{air\text{-}in} + T_{air\text{-}out})/2$
T_{in} = ventilation air temperature at the drift segment inlet (K)

T_{out} = ventilation air temperature at the drift segment outlet (K)
h_s = waste package surface convection heat transfer coefficient ($W/m^2 \cdot K$)
h_w = drift wall convection heat transfer coefficient ($W/m^2 \cdot K$)
h_{rad} = radiation heat transfer coefficient ($W/m^2 \cdot K^4$)
L = drift segment length (m)
d_s = waste package diameter (m)
d_w = drift diameter (m)
$\dot{m}$ = ventilation mass flow rate (kg/s)
C_p = specific heat of air (J/kg·K)

6.3.3 Mixed Convection Heat Transfer Coefficient Correlation

Energy from the waste package is transferred to the ventilating air by a combination of forced and natural convection, or mixed convection. Morgan developed a general approach for calculating the average heat transferred from horizontal cylinders in mixed convection for various flow regimes and various flow directions (Gebhart et al. 1988, Section 10.4.1). While this approach can be used for the YMP geometry, the specific correlations cannot (they are for external flow). The approach is simplistic:

- Calculate an effective Reynolds number for mixed convection.
- Use the mixed convection Reynolds number to calculate a mixed convection Nusselt number.
- Use the mixed convection Nusselt number to calculate a mixed convection heat transfer coefficient. The drift wall and waste package surfaces are considered independently, thus coefficients for each wall are derived.

Calculating the Reynolds number for forced convection is completed using the definition for Reynolds number for flow in a circular tube (Incropera and DeWitt 1996, p. 369, Equation 8.1).

Calculating the Reynolds number for natural convection is not as straightforward. It involves first using literature-provided correlations to calculate a Nusselt number for pure natural convection, and then using this value with the chosen forced convection correlation to determine a Reynolds number that would result in the same heat transfer. The Kuehn-Goldstein (1978) correlation is generally accepted as the best available model for natural convection, and was chosen for the mixed convection model. The correlation defines Nusselt numbers for the inner and outer cylinders as a function of the Rayleigh number and constants derived from experimental data. The Kays-Leung (1963) model for forced convection in a circular annulus was chosen as the forced convection correlation. In this model the Nusselt number is defined as a function of the heat fluxes and temperatures of the surfaces, and influence coefficients. The influence coefficients are semi-empirical in nature and were determined in conjunction with experimental data. The radii of the cylinders, Reynolds number, and the fluids' Prandtl number influence the values.

The two Reynolds numbers are then combined to give a "mixed" Reynolds number (using Morgan's approach) as the square root of the sum of the squares of the Reynolds number for

forced convection and an equivalent Reynolds number for natural convection. Once a "mixed" Reynolds number is calculated, it can be used in conjunction with the chosen forced convection model (Kays and Leung 1963) to determine the heat transfer coefficients from the inner (waste package) and outer (drift wall) surfaces.

Attachment IX of this report provides a detailed review of the mixed convection correlation, including the development of the method, a review of the sensitivity of the method to each of its parameters, the estimated uncertainty in the heat transfer coefficients predicted by the method, and a comparison of the method results to experimental data from the ventilation tests. Based on these analyses, the mixed convection correlation is valid for the flow conditions attributed to the design parameters presented in Section 4, including a ventilation air flow rate between 10 and 30 m^3/s. Outside this range of flow rates, the applicability of the correlation would have to be investigated.

6.3.4 Radiation Heat Transfer Coefficient

The radiation heat transfer coefficient is calculated from an analytical solution for concentric cylinders (Incropera and DeWitt 1996, p. 811, Table 13-3):

$$h_{rad} \equiv \frac{\sigma A_s}{\frac{1}{e_s} + \left(\frac{1 - e_w}{e_w}\right) \cdot \frac{d_s}{d_w}} \qquad \text{Eq. 6-4}$$

where

σ = Stefan-Boltzmann constant ($W/m^2 \cdot K^4$)
e_s = surface emissivity of source
e_w = surface emissivity of drift wall

6.3.5 Ventilation Efficiency

The instantaneous ventilation efficiency is both a function of time and distance from the entrance and is defined by:

$$\eta(t, x) \equiv \frac{Q_{air}(t, x)}{Q_s(t)} \qquad \text{Eq. 6-5}$$

where

$\eta(t,x)$ = instantaneous ventilation efficiency (dimensionless)
Q_{air} = heat convected to the air from the waste package and drift wall surfaces (W/m)
Q_s = heat generated by the waste package (W/m)
t = time since ventilation began
x = distance from the drift entrance (m)

The integrated ventilation efficiency is defined by:

$$\eta_{integrated} \equiv \frac{\int_0^a \int_0^b Q_{air}(t,x) \cdot dx \cdot dt}{x \cdot \int_0^b Q_s(t) \cdot dt} \quad \text{Eq. 6-6}$$

where

$\eta_{integrated}$ = integrated ventilation efficiency (dimensionless)
a = limit of integration in terms of the total drift length
b = limit of integration in terms of the total ventilation duration

6.4 NUMERICAL APPLICATION OF THE CONCEPTUAL MODEL

Two numerical applications and one analytical application of the conceptual model for in-drift ventilation heat transfer are performed. The two numerical applications use the ANSYS software code, and the analytical uses a spreadsheet. The results of each application are compared later in Section 6.6. The first ANSYS based application, named ANSYS-LA-Coarse, divides the drift into segments of 1, 10, 100, 200, 300, 400, 500, 600, 700, and 800 meters. The second ANSYS based application, named ANSYS-LA-Fine, divides the drift into 24 equal segments of 25 meters, for a total of 600 meters. The spreadsheet application, named Analytical-LA-Coarse, is similar to the ANSYS-Coarse model, and was developed to benchmark the analytical approach against ANSYS.

6.4.1 ANSYS Methodology

The ANSYS methodology implemented to calculate the various dependent variables in the ventilation model is based on the following four energy balances: The waste package is the power source in the drift and transfers heat (actually power, i.e., energy per unit time) to the flowing air by forced convection and to the drift wall by radiant heat transfer. The energy balance based on these two heat transfer mechanisms is written in Equation 6-1. The drift wall, as a cylindrical surface, receives energy by radiant heat transfer from the waste package, transfers energy to the flowing air by forced convection, and transfers energy into the rock by conduction. The energy balance based on these three heat transfer mechanisms is written in Equation 6-2. The flowing air stream receives energy from the two convection surfaces (i.e., the waste package surface and the drift wall, and the resulting temperature change is written in the energy balance in Equation 6-3). The energy balance that describes the temperature of the drift wall, and in the rock, is written as a two-dimensional transient heat conduction equation for a cylinder in a medium bounded vertically by the location of the mountain surface, the water table, and two vertical insulated boundaries located (usually) equal distant horizontally (to the left and right). There is no heat transfer in the rock along the axis of the drift. Thus, at this point in this methodology description there are three explicit energy balance equations and one implicit (the transient energy balance).

Implementation of the ANSYS methodology proceeds by dividing the total drift length into a number of equal lengths, or segments. Within each segment the energy balances for the waste-

package surface, drift wall surface, and rock mass, are solved with the restriction that the inlet air temperature is held (fixed) constant at its inlet value for the duration of a time step. For the first segment that receives (fresh) air this temperature is usually fixed for the entire ventilation duration. Information supplied to ANSYS includes the heat transfer coefficients for the waste package and drift wall surfaces, the dimensions of the waste package and drift wall, the waste package power as a function of time, and the inlet air temperatures in the form of a lookup table, and the thermophysical properties of the surrounding rock layers. The transient solution is then calculated for each time step up to some specified ventilation duration. Then, in order to calculate the exiting air temperature from the segment, the energy that was transferred to the fixed air temperature for each time step is used to calculate this exiting air temperature based on the total flow (in the time step) and heat capacity of air. This exiting air temperature for this segment for this time step then becomes the inlet air temperature to the next segment. This air exit-temperature calculation is performed external to ANSYS in a spreadsheet.

The waste-package power is specified as a linear power density, for example, kilowatts per meter. This specified linear power density is applied to the entire segment as if the waste package surface occupied the entire segment. Thus, the waste package surface(s) is larger than what will occur in reality, and only approximates reality when the waste-package spacing is very small (i.e., 0.1 meter).

By fixing the air temperature at the inlet value for the duration of the time step, an assertion is made that the (air) temperature within a segment is everywhere the same (i.e., the air is well-mixed). The concept of a well mixed segment, sometimes referred to as a volume element, is invoked in the engineering design of plug-flow, or “pipe” reactors, and thus this concept is not new. It can be shown that a series of well-mixed volume elements approximates a plug flow reactor with the restriction that the total volume of the well-mixed volume elements equals that of the plug flow reactor (Levenspiel 1972, p. 139). This concept of a well-mixed volume element means that the air temperature is not a function of location in a segment, even though it is intuitive that the air temperature increases as a function of increasing position within the segment. However, when invoking the concept of a well-mixed volume element, there is no difference in the temperature (or anything else) at the beginning of the segment relative to that at the end of the segment. The question that then arises is: How many segments must be specified in order to obtain results that are considered to be descriptive of the tubular flow situation? The number of series segments must be determined by comparing results when the number of segments is increased (through a range) and it is observed that the results do not change; this is sometimes called a “discretization” study.

6.4.2 Analytical Approach

The ventilation calculation technique described in this section is based on the same heat-transfer physics used in the previous ANSYS methodology description in Section 6.4.1. The only change relative to the ANSYS methodology here is in the calculation techniques used to solve the heat transfer equations. This technique is based on two technical approaches to problem solving; the use of a steady-state approximation, and the principle of superposition to calculate the temperature response of the drift wall due to an arbitrary heat flux. By implementing these two techniques, it is not necessary to perform a stand-alone spreadsheet calculation for the air

temperature from segment to segment, and there is no requirement to solve the energy equation for the drift wall (rock mass) for every segment.

The use of the steady-state approximation, sometimes referred to as a quasi-steady-state approximation, allows the energy balance equations to be written with no time derivatives, only algebraic equations which can then be solved by any number of methods. The solution method used here is to algebraically solve the resulting equations, where there are four equations and four unknowns. The energy balance equations derived as a result of using the steady-state approximation apply for the duration of a time step. The progress of the calculation through time is exactly like that of integrating a function using Euler's method for numerical integration, summing a "stair-step" approximation. Each step represents a steady state for a particular time interval.

Application of the superposition technique is based on the repeated use of a single temperature response of the drift wall due to a short-duration constant flux. This short-duration constant flux is referred to as a "pulse." By repeatedly applying a series of short-duration scaled constant fluxes to the drift wall, the resulting temperature due to an arbitrary flux can be calculated. Thus the arbitrary flux is approximated like "stair steps." Part of the ventilation calculation then involves calculating the temperature response of the drift wall due to a single short-duration constant flux, and demonstrating that the short duration, which is the time step, is sufficient to allow the drift-wall temperature to be calculated by superposition for the time-varying fluxes of interest. This temperature response must be calculated independently of the ventilation calculation itself, but is calculated only once for a given set of thermophysical rock properties. The use of a time-series of a constant flux (pulses) to calculate the temperature of the drift wall as a function of time is presented in Section 6.4.2.2.

6.4.2.1 Derivation of the Energy Balance Equations that Describe an Algebraic Solution for Ventilation Calculations

This section describes the derivation of the energy balance equations of the analytical ventilation heat-transfer process. This derivation uses a common engineering concept described earlier, well mixed volume elements. In a well mixed volume element the variables of interest, such as temperature, are everywhere the same. The concept of a well mixed volume element appears under different names in the engineering literature such as backmix reactor, or continuous-stirred-tank-reactor (Levenspiel 1972, p. 139). Using this concept, the drift is divided into a number of well-mixed volume elements that are in series, and the output of air from one is the input to the next (as is done in the ANSYS methodology).

The energy balance equations for the algebraic ventilation calculation derivation that follows uses a linearized radiant heat transfer coefficient, the concept of which is not new (Perry et al. 1984, p. 10-13). The use of a linearized radiant heat transfer coefficient introduces a trial-and-error calculation itself, but has been found to converge very quickly using a successive approximation solution. This linearization does away with the nonlinear nature of radiant heat transfer. The details on the use of the linearized radiant heat transfer coefficient are presented in Section 6.4.2.3.

The objective of this derivation is to obtain algebraic expressions for the four dependent variables of interest, these are the air temperature, T (no subscript), drift-wall temperature, T_w, the power-source

(waste-package) surface temperature, T_s, and the total energy per unit time conducted into the drift wall (into the rock), Q_{wall} (which when divided by the drift-wall area yields an energy flux). Consider a well-mixed volume element of a tunnel, or tube, with a heated source inside, air moving through this tunnel, at steady state. A volume element is defined by the "air" volume in a specified length of tunnel. The net energy per time transported by air through the element is written as:

$$(T - T_{in})\dot{m} C_p = Q_{air} \quad \text{Eq. 6-7}$$

where $\dot{m}$ (m "dot") is the air mass flow rate, C_p is the heat capacity of air at constant pressure, T_{in} is the inlet air temperature, and Q_{air} is the net energy/time transported by the air. The air in the volume element is considered well mixed (i.e., a continuous stirred tank reactor or backmix reactor) thus T is the same everywhere in the volume element.

The energy per time transferred from the heated source to the air by convection is written as:

$$q_{sa} = h_s A_s (T_s - T) \quad \text{Eq. 6-8}$$

where h_s is the appropriate heat transfer coefficient, A_s is the area of the source in the well-mixed volume element, and T_s is the temperature of the source (surface). The energy per time transferred from the tunnel wall to the air by convection is written as:

$$q_{wa} = h_w A_w (T_w - T) \quad \text{Eq. 6-9}$$

where h_w is the appropriate heat transfer coefficient, A_w is the tunnel-wall area in the well-mixed volume element, and T_w is the tunnel-wall temperature.

Energy per time transferred to the air occurs only from the wall and source, so using Equations 6-8 and 6-9, rewrite Equation 6-7 as:

$$(T - T_{in})\dot{m} C_p = h_s A_s (T_s - T) + h_w A_w (T_w - T) \quad \text{Eq. 6-10}$$

Now consider the heated source. All of the energy per time is lost instantaneously; this implies zero heat capacitance for the source. The energy per time balance for the source is written as:

$$p_s = h_s A_s (T_s - T) + h_{rs} A_s (T_s - T_w) \quad \text{Eq. 6-11}$$

where p_s is the source power in the well-mixed volume element, the second term on the right is the energy per time transferred to the wall by radiant heat transfer, and h_{rs} is a linearized radiant heat transfer coefficient discussed in Section 6.4.2.3.

The energy per time balance at the wall is written on a coordinate frame where energy per time transferred to the wall (surface) is positive, thus:

$$h_{rs} A_s (T_s - T_w) - h_w A_w (T_w - T) - Q_{wall} = 0 \quad \text{Eq. 6-12}$$

where the first term is the radiant energy per time transferred to the wall for $T_s > T_w$, and is thus positive; the second term is the convective energy per time transferred from the wall to the air for

$T_w > T$, and is thus negative; and Q_{wall} is the energy per time transferred by conduction into (from) the wall (medium) in the well-mixed volume element, and is thus negative. Q_{wall} itself can be either negative or positive.

Consider now the approximations that can be made for short time intervals in the well-mixed volume element. Fix the wall flux, Q_{wall}/A_w, and the source energy per time, p_s, for a yet to be determined time interval (time step). In order to progress with respect to time, approximate the power source and wall flux as a series of constant fluxes (not the same). Section 6.4.2.2 describes the details of how a series of constant fluxes (also known as finite-width pulses) can be used to predict the drift-wall temperature. With Q_{wall} and p_s fixed for a short time interval, Equations 6-11 and 6-12 can be used to eliminate T_s and T_w from Equation 6-10.

Rearrange Equation 6-11 as:

$$A_s(h_s + h_{rs})T_s - A_s h_{rs} T_w = p_s + A_s h_s T \qquad \text{Eq. 6-13}$$

And rearrange Equation 6-12 as:

$$A_s h_{rs} T_s - (A_s h_{rs} + A_w h_w)T_w = Q_{wall} - A_w h_w T \qquad \text{Eq. 6-14}$$

Rewrite Equations 6-13 and 6-14 in matrix notation as:

$$\begin{bmatrix} A_s(h_s + h_{rs}) & -A_s h_{rs} \\ A_s h_{rs} & -(A_s h_{rs} + A_w h_w) \end{bmatrix} \begin{bmatrix} T_s \\ T_w \end{bmatrix} = \begin{bmatrix} p_s + A_s h_s T \\ Q_{wall} - A_w h_w T \end{bmatrix} \qquad \text{Eq. 6-15}$$

Write the determinant of the 2×2 matrix as:

$$D \equiv -A_s(h_s + h_{rs})(A_s h_{rs} + A_w h_w) + A_s^2 h_{rs}^2 \qquad \text{Eq. 6-16}$$

Expand D to obtain:

$$D = -A_s^2 h_s h_{rs} - A_s A_w h_s h_w - A_s^2 h_{rs}^2 - A_s A_w h_{rs} h_w + A_s^2 h_{rs}^2 \qquad \text{Eq. 6-17}$$

Cancel the squared terms to obtain:

$$D = -\left(A_s^2 h_s h_{rs} + A_s A_w h_s h_w + A_s A_w h_{rs} h_w\right) \qquad \text{Eq. 6-18}$$

And finally obtain:

$$D = -\left[A_s^2 h_s h_{rs} + A_s A_w h_w (h_s + h_{rs})\right] \qquad \text{Eq. 6-19}$$

Now solve for T_s using Cramer's rule. Do this by replacing column 1 in the 2×2 matrix with the right side of matrix Equation 6-15, the forcing vector, and obtain (multiply by D to obtain DT_s):

$$D\,T_s = \begin{bmatrix} p_s + A_s h_s T & -A_s h_{rs} \\ Q_{wall} - A_w h_w T & -(A_s h_{rs} + A_w h_w) \end{bmatrix} \quad \text{Eq. 6-20}$$

Expand the 2×2 determinant to obtain:

$$D\,T_s = -(p_s + A_s h_s T)(A_s h_{rs} + A_w h_w) + A_s h_{rs}(Q_{wall} - A_w h_w T) \quad \text{Eq. 6-21}$$

Collect the coefficient of T, and a constant:

$$D\,T_s = (-A_s h_s (A_s h_{rs} + A_w h_w) - A_s h_{rs} A_w h_w)T + A_s h_{rs} Q_{wall} - p_s (A_s h_{rs} + A_w h_w) \quad \text{Eq. 6-22}$$

Rearrange the coefficient of T to obtain:

$$D\,T_s = -(A_s^2 h_s h_{rs} + A_s A_w h_w (h_s + h_{rs}))T + A_s h_{rs} Q_{wall} - p_s (A_s h_{rs} + A_w h_w) \quad \text{Eq. 6-23}$$

Note that the coefficient of T above is D as given by Equation 6-19, so dividing by D to obtain T_s yields:

$$T_s = T + \frac{-Q_{wall} A_s h_{rs} + p_s (A_s h_{rs} + A_w h_w)}{A_s^2 h_s h_{rs} + A_s A_w h_w (h_s + h_{rs})} \quad \text{Eq. 6-24}$$

Solve for T_w in the same manner from Equation 6-15 by replacing column 2 with the forcing vector to obtain:

$$D\,T_w = \begin{bmatrix} A_s (h_s + h_{rs}) & p_s + A_s h_s T \\ A_s h_{rs} & Q_{wall} - A_w h_w T \end{bmatrix} \quad \text{Eq. 6-25}$$

Expand the determinant to obtain:

$$D\,T_w = A_s (h_s + h_{rs})(Q_{wall} - A_w h_w T) - (p_s + A_s h_s T) A_s h_{rs} \quad \text{Eq. 6-26}$$

Collect coefficient of T, and a constant:

$$D\,T_w = -(A_s^2 h_s h_{rs} + A_s A_w h_w (h_s + h_{rs}))T + Q_{wall} A_s (h_s + h_{rs}) - A_s h_{rs} p_s \quad \text{Eq. 6-27}$$

So that the result for T_w after dividing by D, Equation 6-19, becomes:

$$T_w = T + \frac{-Q_{wall} A_s (h_s + h_{rs}) + A_s h_{rs} p_s}{A_s^2 h_s h_{rs} + A_s A_w h_w (h_s + h_{rs})} \quad \text{Eq. 6-28}$$

Write T_s from Equation 6-24, and T_w from Equation 6-28, as:

$$T_s = T + B_s \quad \text{Eq. 6-29}$$

$$T_w = T + B_w \quad \text{Eq. 6-30}$$

And the coefficients B_w and B_s are defined (use the ≡ sign) from Equations 6-24 and 6-28 as:

$$B_w \equiv \frac{-Q_{wall} A_s (h_s + h_{rs}) + A_s h_{rs} p_s}{A_s^2 h_s h_{rs} + A_s A_w h_w (h_s + h_{rs})} \quad \text{Eq. 6-31}$$

$$B_s \equiv \frac{-Q_{wall} A_s h_{rs} + p_s (A_s h_{rs} + A_w h_w)}{A_s^2 h_s h_{rs} + A_s A_w h_w (h_s + h_{rs})} \quad \text{Eq. 6-32}$$

Use Equation 6-29 for T_s and Equation 6-30 for T_w to rewrite Equation 6-10 for T as:

$$(T - T_{in}) \dot{m} C_p = h_s A_s (T + B_s - T) + h_w A_w (T + B_w - T) \quad \text{Eq. 6-33}$$

The expression for T becomes:

$$T = T_{in} + \frac{h_s A_s B_s + h_w A_w B_w}{\dot{m} C_p} \quad \text{Eq. 6-34}$$

Consider a simplification of Equation 6-34, by rewriting this equation as:

$$(T - T_{in}) \dot{m} C_p = h_s A_s B_s + h_w A_w B_w \quad \text{Eq. 6-35}$$

and substitute B_w and B_s from Equation 6-31 and Equation 6-32 to obtain:

$$(T - T_{in}) \dot{m} C_p = \frac{h_s A_s (-Q_{wall} A_s h_{rs} + p_s (A_s h_{rs} + A_w h_w))}{A_s^2 h_s h_{rs} + A_s A_w h_w (h_s + h_{rs})} + \frac{h_w A_w (-Q_{wall} A_s (h_s + h_{rs}) + A_s h_{rs} p_s)}{A_s^2 h_s h_{rs} + A_s A_w h_w (h_s + h_{rs})} \quad \text{Eq. 6-36}$$

Regroup Q_{wall} and p_s, work on the numerator(s) above to obtain:

$$-Q_{wall} A_s^2 h_s h_{rs} + p_s h_s A_s (A_s h_{rs} + A_w h_w) - Q_{wall} A_s A_w h_w (h_s + h_{rs}) + p_s A_s A_w h_w h_{rs} =$$

$$-Q_{wall} (A_s^2 h_s h_{rs} + A_s A_w h_w (h_s + h_{rs})) + p_s (A_s^2 h_s h_{rs} + A_s A_w h_s h_w + A_s A_w h_w h_{rs}) =$$

$$-Q_{wall} (A_s^2 h_s h_{rs} + A_s A_w h_w (h_s + h_{rs})) + p_s (A_s^2 h_s h_{rs} + A_s A_w h_w (h_s + h_{rs})) \quad \text{Eq. 6-37}$$

The coefficients of Q_{wall} and p_s cancel with the denominator(s) in Equation 6-36, so the net result is:

$$(T - T_{in}) \dot{m} C_p = -Q_{wall} + p_s \quad \text{Eq. 6-38}$$

This result can be obtained by writing an energy balance on just the air in the well-mixed volume element. To see this, consider the control envelope to be the air in the volume element, so $T - T_{in} = \Delta T$, and multiplication by $\dot{m} C_p$ yields the net rate of energy transported through the volume element carried by the air. Since p_s is the energy per time added by the source, and $+Q_{wall}$ is the energy per time transferred by conduction into the wall (see the text following Equation 6-12 for the sign convection), $-Q_{wall} + p_s$ is the net energy per time removed from the volume element by the air (moving through). This rather simple energy balance is recovered from the preceding equations.

At this point an equation is required that relates T_w and Q_{wall}, and this is obtained from use of the superposition principle as described in Section 6.4.2.2. This equation is (and is also Equation 6-48):

$$\sum_{2 \to N} + \frac{Pt_1 Q_{wall}}{A_w P_b} = T_w \qquad \text{Eq. 6-39}$$

The summation symbol denotes the pulse contributions to the temperature T_w from all previous wall fluxes, N denotes the number of time steps, and for the situation where the time step is one year, N denotes the total time. The summation runs from 2 to N, not 1 to N, because the current wall flux is not (yet) known (it is Q_{wall}/A_w). The current wall flux is multiplied by Pt_1 which is the pulse temperature response at an age of 1 year due to the application of a constant flux of a known strength (for example, 1.0 W/m^2). In other words, in the stand-alone term above the contribution to the wall temperature is being calculated at the end of 1 year due to the flux Q_{wall}/A_w being applied for 1 year. But all the other wall fluxes are known and do not change, they are "history," and their contribution to T_w diminishes with respect to time because with each time step they get "older." The contribution of all of the older fluxes to the temperature T_w are taken into account in the summation. The factor P_b is a scale factor that takes into account any units conversion necessary between the wall flux, Q_{wall}/A_w, and the pulse flux basis. For example, suppose that the applied constant flux is 1.0 W/m^2 and the units of Q_{wall}/A_w are W/m^2, then the scale factor is unity. However, if English units for Q_{wall}/A_w are used, such as $Btu/(hr \cdot ft^2)$, then P_b would be 0.3171 (see List of Conversions), which is the conversion of 1.0 W/m^2 to $Btu/(hr\ ft^2)$.

Now write Equation 6-38 as:

$$T = \frac{-Q_{wall} + p_s}{\dot{m} C_p} + T_{in} \qquad \text{Eq. 6-40}$$

And substitute this expression for T in Equation 6-30 to obtain:

$$T_w = \frac{-Q_{wall} + p_s}{\dot{m} C_p} + T_{in} + B_w \qquad \text{Eq. 6-41}$$

There are now two equations for T_w, Equations 6-39 and 6-41. Equate T_w from each of these equations to obtain one equation with one unknown, and that unknown is Q_{wall}. Proceeding:

$$\sum_{2 \to N} + \frac{Pt_1 Q_{wall}}{A_w P_b} = \frac{-Q_{wall} + p_s}{\dot{m} C_p} + T_{in} + \frac{-Q_{wall} A_s (h_s + h_{rs}) + A_s h_{rs} p_s}{A_s^2 h_s h_{rs} + A_s A_w h_w (h_s + h_{rs})} \qquad \text{Eq. 6-42}$$

The numerator on the right is -D in Equation 6-19, so condense notation one more time keeping –D:

$$\sum_{2\to N} + \frac{Pt_1 Q_{wall}}{A_w P_b} = \frac{-Q_{wall} + p_s}{\dot{m} C_p} + T_{in} + \frac{-Q_{wall} A_s (h_s + h_{rs}) + A_s h_{rs} p_s}{(-D)} \qquad \text{Eq. 6-43}$$

Now solve for Q_{wall}.

$$Q_{wall}\left[\frac{Pt_1}{A_w P_b} + \frac{1}{\dot{m} C_p} + \frac{A_s (h_s + h_{rs})}{(-D)}\right] = -\sum_{2\to N} + \frac{p_s}{\dot{m} C_p} + T_{in} + \frac{A_s h_{rs} p_s}{(-D)} \qquad \text{Eq. 6-44}$$

Or:

$$Q_{wall} = \frac{-\sum_{2\to N} + \frac{p_s}{\dot{m} C_p} + T_{in} + \frac{A_s h_{rs} p_s}{(-D)}}{\frac{Pt_1}{A_w P_b} + \frac{1}{\dot{m} C_p} + \frac{A_s (h_s + h_{rs})}{(-D)}} \qquad \text{Eq. 6-45}$$

The net result is an equation for Q_{wall} in terms of the knowns of the calculation.

The implementation of the calculation proceeds from Q_{wall} above. The calculated value of Q_{wall} is then used to calculate B_w from Equation 6-31, and B_s from Equation 6-32. Then T_s follows immediately from Equation 6-29, and T_w follows from Equation 6-30. T, which is the temperature of the air, follows immediately from Equation 6-38. Thus, the four variables of interest, T, T_w, T_s, and Q_{wall}, are determined.

The use of a linearized radiant heat transfer coefficient introduces a trial-and-error calculation which is implemented as follows. An initial guess of the radiant heat transfer coefficient, h_{rs}, is used to start the calculation. A reasonable value can be obtained by examining the information given in the engineering literature (Perry et al. 1984, p. 10-13). Using the initial guess, the calculation proceeds as described above and values for T_s and T_w are obtained. These just-calculated values are now used to calculate h_{rs}, as described in Section 6.4.2.3, and the entire calculation repeated. This "successive approximation" is repeated until the temperatures T_s and T_w change very little from one trial to the next, say 0.1 degrees. The radiant heat transfer coefficient does not vary excessively for the parameters of the problem, again seen by examining the engineering literature. In other words, h_{rs} varies by about a factor of 2 over the range of parameters of interest, and as a result the convergence is easily obtained.

The calculation progresses with respect to time by solving for the variables of interest at a time step using the equations noted above, and then stepping to the next time interval. The summation in Equation 6-39 then increases by 1 (which is N), and the calculation repeated out to the specified ventilation duration.

6.4.2.2 Description of the Use of a Constant-Flux Temperature Response to Calculate the Temperature Due to an Arbitrary Flux

Consider an arbitrary energy flux applied to a solid. The temperature response of this solid can be calculated by summing the temperature responses from individual constant fluxes applied over short time intervals in such a manner that the constant fluxes approximate the arbitrary flux. The temperature response being referred to here is the temperature at the surface of the drift wall. The temperature response can be calculated in this way due to the use of the superposition principle for the heat conduction equation (Nagle and Saff 1994, p. 166). In order to illustrate this calculation technique and establish an indexing system, the following description is presented.

Suppose that the temperature response S due to a single unit flux pulse f is tabulated at every $n \cdot \Delta t$ for n = 1,2,3,...., refer to Figure 6-2, specifically to the upper plot of the temperature S versus time. In the first time interval, Δt, the unit flux pulse is "on," and from here on refer to the unit flux pulse as the "pulse." After Δt the pulse is "off," and the boundary condition where the flux was applied is flux = 0. The temperature response S decreases with respect to time because the energy delivered to the solid is being conducted, or diffused, into the solid (rock mass), and as such the temperature decreases.

Now suppose an arbitrary flux is available in functional or tabulated form. Refer to the middle plot in Figure 6-2 of an arbitrary flux f as a function of time.

In order to calculate the temperature T illustrated in Figure 6-2 due to the arbitrary flux applied up to time = $7 \cdot \Delta t$ (the 7 is arbitrary, for illustration only), the temperature contribution from each of the applied single pulses within each Δt is scaled by the flux at the time the flux was applied, and the temperature contributions summed. In order to illustrate this, consider the contribution to the temperature T due to the pulse applied in the first Δt between t_0 and t_1. The temperature response will "age," or "decay," to the value indicated at S_7. But the S-versus-time plot is based on a unit flux (or whatever flux one chooses). Therefore S_7 must be scaled by the value of the arbitrary flux applied in the first Δt, so the contribution to the temperature T at t_7 due to this flux is $S_7 \cdot f_1$, and this is illustrated in the plot of T versus time with a "line" connecting S_7 and f_1. This "line" means multiply these two values. Instead of using f_1 as indicated, a midpoint or average value of the flux in this time interval can be used.

Likewise, consider the contribution to the temperature T due to the flux applied between t_6 and t_7. This temperature response is S_1 because it is only one Δt from its origin in time. This value of S_1 is scaled by the flux used between the times indicated. Thus the contribution to the temperature T at t_7 due to this flux is $S_1 \cdot f_7$, and this is added to the sum of contributions, and also illustrated in the plot of T versus time with a "line" connecting S_1 and t_7.

In general, suppose the time index of interest is N, and the time is $t = N \cdot \Delta t$, then T_N is written as:

$$T_N = \sum_{n=1}^{N} S_n f_{N-n+1} \qquad \text{Eq. 6-46}$$

To illustrate the indexing in this summation, consider N = 7, let n = 1, then N - n + 1 = 7, and the product is $S_1 \cdot f_7$. Now let n = 7, then N - n + 1 = 1, and the product is $S_7 \cdot f_1$.

A table of how the indices run for N = 7 can be found in Table 6-3.

Table 6-3. Example of the Indexing for the Pulse Response Method

n	N - n +1	$S_n \cdot f_{N-n+1}$
1	7	$S_1 \cdot f_7$
2	6	$S_2 \cdot f_6$
3	5	$S_3 \cdot f_5$
4	4	$S_4 \cdot f_4$
5	3	$S_5 \cdot f_3$
6	2	$S_6 \cdot f_2$
7	1	$S_7 \cdot f_1$

The temperature T_N is then the sum of $S_n f_{N-n+1}$ in the last column. This computation scheme is intended to calculate the temperature on the time "nodes" as indicated.

Now suppose that the flux f in the last time interval, Δt between t_6 and t_7, is an unknown. All the other fluxes are "history" because they have already occurred, and hence are known. Thus the above summation can be written as a sum of what occurred (known), and what is going to occur (unknown) in the current time step as:

$$T_N = \sum_{n=2}^{N} S_n f_{N-n+1} + S_1 f_N \qquad \text{Eq. 6-47}$$

In the illustration using N = 7 the indices of the last term above are $S_1 f_7$ which illustrates, referring to Figure 6-2, that the flux in the indicated time interval (the last one) is being scaled by S_1. This form of the summation equation for the temperature is used in the main text as Equation 6-39, and rewritten with the following notation:

$$\sum_{2 \to N} + \frac{Pt_1 Q_{wall}}{A_w P_b} = T_w \qquad \text{Eq. 6-48}$$

In this form of the summation equation, Pt_1 corresponds to S_1, Q_{wall}/A_w corresponds to f_N, and P_b is a scale factor (inserted for future convenience). Q_{wall} in the main text is the total energy per time delivered to the total drift wall in the segment, thus dividing by the total drift wall area in the segment, A_w, yields the indicated flux Q_{wall}/A_w.

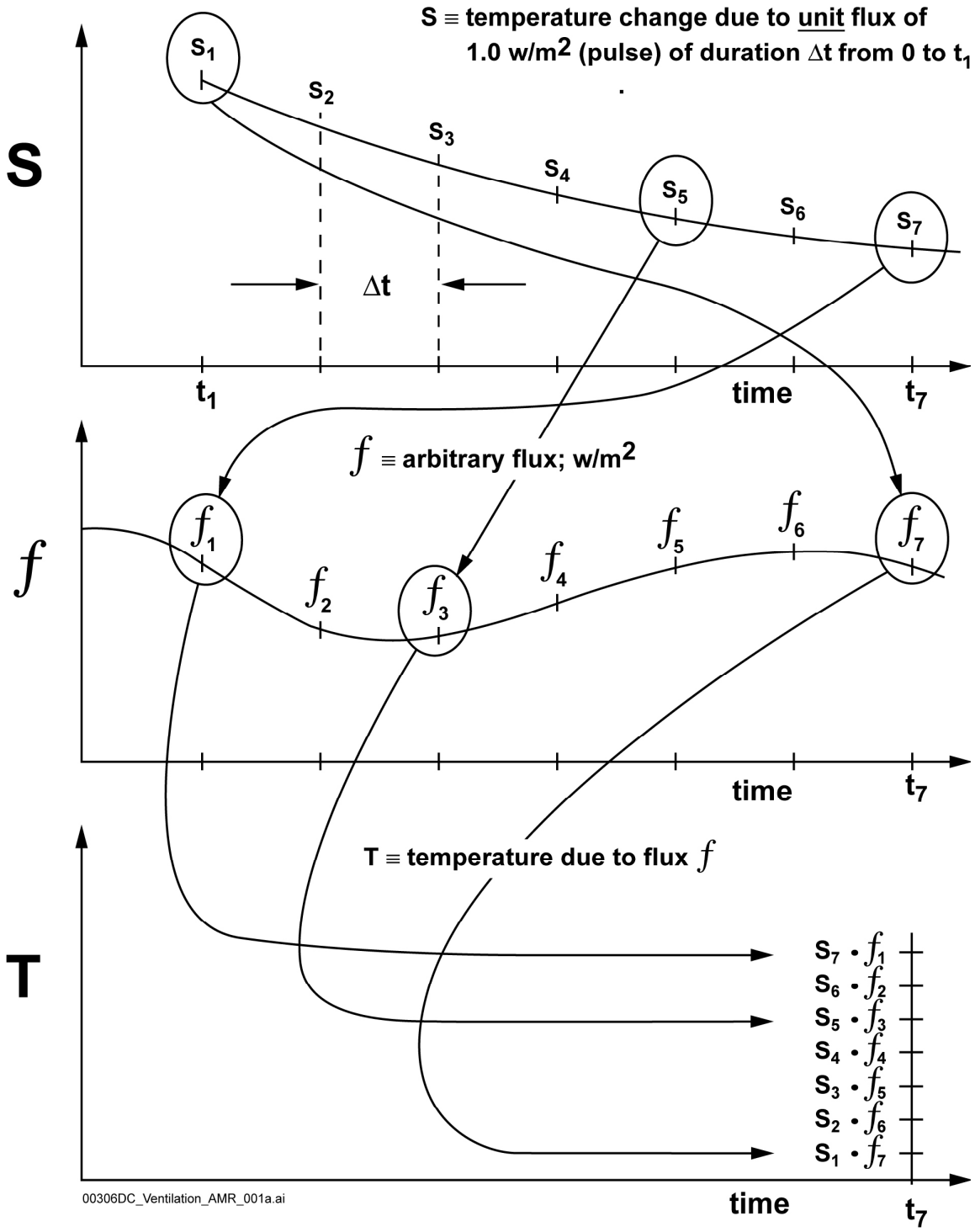

Figure 6-2. Illustration of How to Calculate a Temperature T Due to an Arbitrary Flux f Using the Repeated Application of the Temperature Response S Due to a Unit Flux Pulse Applied Initially Between Time = 0 and t_1. This Calculation Methodology is Based on the Superposition Principle and Thus Adds the Temperature Contributions from Each Scaled Flux, S·f, to Obtain the Temperature T at the Indicated Time Diagram of the Pulse Response by the Superposition Method

6.4.2.3 Linearized Radiant Heat Transfer Coefficient

The linearization of radiant energy transfer is discussed in numerous texts (Carslaw and Jaeger 1959, p. 21; Perry et al. 1984, p. 10-13, use the terminology "radiation film coefficient;" Kern 1950, p. 77, describes a fictitious film coefficient to represent the rate at which radiation passes from one surface of a radiator). In order to derive a linearized radiant heat transfer coefficient for a heated tunnel, consider the transport of heat by radiation in an annulus as given by Bird et al. (1960, p. 453, problem $14.G_2$):

$$Q_{12} = \frac{\sigma(T_1^4 - T_2^4)}{\left[\frac{1}{A_1 e_1} + \frac{1}{A_2}\left(\frac{1}{e_2} - 1\right)\right]} \; [\equiv] \; \frac{\text{energy}}{\text{time} \cdot \text{length}} \qquad \text{Eq. 6-49}$$

Q_{12} is the net radiant energy interchange between surface 1 and 2, T_1 and T_2 are the respective surface absolute temperatures, e_1 and e_2 are the respective emissivities, σ is the Stephan Boltzmann constant, and A_1 is the surface area of the inner cylinder per unit length (see Example 14.5-2 by Bird et al. [1960, p. 448] for a similar problem where "unit length" is used), and the [≡] symbol means "has units of." Therefore, change the subscripts from 1 ⇒ s (the source which is the inner cylinder), and from 2 ⇒ w (the wall which is the outer cylinder). So the energy per time (heat) transferred becomes:

$$Q_{sw} = \frac{\sigma(T_s^4 - T_w^4)}{\left[\frac{1}{A_s e_s} + \frac{1}{A_w}\left(\frac{1}{e_w} - 1\right)\right]} \; [\equiv] \; \frac{\text{energy}}{\text{time} \cdot \text{length}} \qquad \text{Eq. 6-50}$$

The energy (heat) transferred for a length Δx (i.e., the length of the well-mixed volume element) is:

$$Q_{sw}\,\Delta x = \frac{\sigma(T_s^4 - T_w^4)\,\Delta x}{\left[\frac{1}{A_s e_s} + \frac{1}{A_w}\left(\frac{1}{e_w} - 1\right)\right]} \; [\equiv] \; \frac{energy}{time} \qquad \text{Eq. 6-51}$$

At this point it is necessary to recognize that the areas here, A_s and A_w, as written above in Equation 6-51 are not the same areas that appear in Equation 6-10. The areas in Equation 6-51 are more appropriately "specific" areas (i.e., area per unit length). Those areas in Equation 6-10 are areas in the well-mixed volume element. Therefore, change the notation in Equation 6-51 to denote "specific" areas, to do this define the specific area for A_s as A_{us} where the subscript "us" denotes per unit length. Likewise for A_w use A_{uw}. Equation 6-51 now appears as:

$$Q_{sw}\,\Delta x = \frac{\sigma(T_s^4 - T_w^4)\,\Delta x}{\left[\frac{1}{A_{us} e_s} + \frac{1}{A_{uw}}\left(\frac{1}{e_w} - 1\right)\right]} \; [\equiv] \; \frac{energy}{time} \qquad \text{Eq. 6-52}$$

Note that $Q_{sw}\Delta x$ is the total energy per time transferred from the source in the well-mixed volume element. Now define (use the ≡ symbol for "define") a linearized radiant transfer coefficient based on the power source area A_s in the well-mixed volume element (see Equation 6-11) as:

$$h_{rs} A_s (T_s - T_w) = h_{rs} (\pi D_s \Delta x)(T_s - T_w) \equiv Q_{sw} \Delta x \qquad \text{Eq. 6-53}$$

So using Equation 6-52 for Q_{SW}:

$$h_{rs} \pi D_s (T_s - T_w) \equiv \frac{\sigma (T_s^4 - T_w^4)}{\left[\frac{1}{A_{us} e_s} + \frac{1}{A_{uw}} \left(\frac{1}{e_w} - 1 \right) \right]} \qquad \text{Eq. 6-54}$$

So that by definition:

$$h_{rs} \equiv \frac{\sigma (T_s^4 - T_w^4)/(T_s - T_w)}{\pi D_s \left[\frac{1}{A_{us} e_s} + \frac{1}{A_{uw}} \left(\frac{1}{e_w} - 1 \right) \right]} [\equiv] \frac{energy}{time \cdot area \cdot temperature} \qquad \text{Eq. 6-55}$$

Carrying out the indicated division yields:

$$h_{rs} \equiv \frac{\sigma (T_s^3 + T_s^2 T_w + T_s T_w^2 + T_w^3)}{\pi D_s \left[\frac{1}{A_{us} e_s} + \frac{1}{A_{uw}} \left(\frac{1}{e_w} - 1 \right) \right]} \qquad \text{Eq. 6-56}$$

And hence when using such a linearization a trial-and-error calculation is introduced because T_s and T_w must be specified.

Therefore, the linearized radiant-heat transfer coefficient defined in Equation 6-55, h_{rs}, is the coefficient that multiplies the source area in the well-mixed volume element, but note that the areas appearing in Equation 6-56 are specific areas.

6.4.2.4 Thermal Pulse Calculation

In order to implement the ventilation calculation using the analytical approach described in Section 6.4.2, it is necessary to have a temperature response of the drift wall due to the application of a pulse of energy put into the drift wall. This temperature pulse response was introduced in Equation 6-39 in the derivation of the analytical equations, and its use further described in Section 6.4.2.2. The sections that follow here describe how to calculate this temperature response analytically using results from the open literature. This analytical temperature pulse response is based on using two analytical temperature solutions; these are the temperature in the infinite region bounded internally by a cylinder for a constant heat flux (Carslaw and Jaeger 1959, p. 338), and the temperature in the semi-infinite solid for a constant heat flux (Carslaw and Jaeger 1959, p. 75). The first analytical solution, that for the region bounded internally by a cylinder, is used to describe the drift-wall temperature for the early times

of the pulse response, and the second analytical solution, that for the semi-infinite solid, is used for the drift-wall temperature for the later, or long-term, times of the pulse response. The reason the temperature response from the semi-infinite solid can be used for later times is that a pulse of energy put into the drift wall spreads out to the adiabatic boundary at midpillar at later times, and then transports vertically as in a slab. A pulse response for each of these time frames is obtained from these constant-flux solutions by shifting the analytical result by one year (for a one-year pulse) and subtracting from the unshifted solution. This shift-and-subtract operation to yield the pulse is based on the superposition principle as described by Nagle and Saff (1994, p. 166). The entire temperature pulse response is then generated by taking the maximum of these two pulses out to the maximum time of interest.

6.4.2.4.1 The Infinite Region Bounded Internally by a Cylinder

The temperature in the infinite region bounded internally by a cylinder is (Carslaw and Jaeger 1959, p. 338, Equation 17):

$$v = -\frac{2Q}{\pi K}\int_0^\infty (1 - e^{-\kappa u^2 t})\frac{J_o(ur)\,Y_1(ua) - Y_o(ur)\,J_1(ua)}{u^2\,[J_1^2(ua) + Y_1^2(ua)]}\,du \qquad \text{Eq. 6-57}$$

where v is the temperature, Q is a constant flux, a is the cylinder radius, J_o, J_1, Y_o, and Y_1 are Bessel functions as used by Carslaw and Jaeger (1959), and the other symbols are previously described. This equation can be put into a dimensionless form that is convenient because it is then necessary to perform the calculation indicated only once for any value of drift radius, a, thermal conductivity, K, and thermal diffusivity, κ. To put the above equation in dimensionless form, proceed by defining the dimensionless variable ξ as:

$$\xi \equiv ua \qquad \text{Eq. 6-58}$$

which differentiating with respect to u yields:

$$d\xi = a\,du \qquad \text{Eq. 6-59}$$

Substituting the above two results into Equation 6-57 yields:

$$v = -\frac{2Q}{\pi K}\int_0^\infty (1 - e^{-\kappa(\xi/a)^2 t})\frac{J_o\left(\xi\frac{r}{a}\right)Y_1(\xi) - Y_o\left(\xi\frac{r}{a}\right)J_1(\xi)}{\frac{\xi^2}{a^2}\,[J_1^2(\xi) + Y_1^2(\xi)]}\frac{d\xi}{a} \qquad \text{Eq. 6-60}$$

Now define a dimensionless time τ as:

$$\tau \equiv \frac{\kappa t}{a^2} \qquad \text{Eq. 6-61}$$

And evaluate the temperature at the cylinder surface (i.e., drift wall) by setting r = a and obtain a dimensionless temperature written as:

$$\theta \equiv \frac{K\, v(r=a)}{Q\, a} = -\frac{2}{\pi}\int_0^{\infty}(1 - e^{-\xi^2\tau})\frac{J_o(\xi)Y_1(\xi) - Y_o(\xi)J_1(\xi)}{\xi^2[J_1^2(\xi) + Y_1^2(\xi)]}d\xi \qquad \text{Eq. 6-62}$$

This equation is used to generate the temperatures of interest at specific times as follows. Suppose that the dimensionless temperatures have been generated as a function of dimensionless time, τ, for $\Delta\tau$ = 1, 2, … up to some maximum τ_{max}. Now suppose that the temperature is required at times of every year, Δt = 1; use Equation 6-61 to write:

$$\tau_n = \left(\frac{\kappa}{a^2}\right)(n\,\Delta t), \quad for\ n = 1,2,3... \qquad \text{Eq. 6-63}$$

To further illustrate, suppose that κ = 26 m^2/year and a = 2.75 meters (for a 5.5-meter diameter drift), so that the above becomes:

$$\tau_n \approx 3.43(n\,\Delta t), \quad for\ n = 1,2,3... \qquad \text{Eq. 6-64}$$

To generate the temperature v at the desired times of one-year increments, the *a priori* calculated dimensionless temperature and dimensionless time at discrete values of τ can be interpolated accordingly from those at τ_n in Equation 6-63.

6.4.2.4.2 The Semi-Infinite Slab

The temperature in the semi-infinite slab is (Carslaw and Jaeger 1959, p. 75, Equation 7):

$$v(t) = \frac{2\cdot F_0}{K}\cdot\left[\left(\frac{\kappa\cdot t}{\pi}\right)^{\frac{1}{2}}\cdot e^{\frac{-x^2}{4\cdot\kappa\cdot t}} - \frac{x}{2}\cdot erfc\left(\frac{x}{2\sqrt{\kappa\cdot t}}\right)\right] \qquad \text{Eq. 6-65}$$

where v is the temperature, F_0 is a constant flux (equal to one-half the linear power at the drift wall, applied over the area determined by the drift spacing), erfc(z) is the complementary error function, and the other symbols are previously described. The temperature at the face, or x = 0, is:

$$v(t) = \frac{2\cdot F_0}{K}\cdot\sqrt{\frac{\kappa\cdot t}{\pi}} \qquad \text{Eq. 6-66}$$

To generate the temperature response due to a one-year pulse, again shift the solution by one year and subtract from the unshifted solution:

$$v(t) = 2\cdot\frac{F_0}{K}\cdot\left(\sqrt{\frac{\kappa\cdot t}{\pi}} - \sqrt{\frac{\kappa\cdot(t-1)}{\pi}}\right) \qquad \text{Eq. 6-67}$$

for $t \geq 1$.

For geometries modeled here, F_0 is 1 W/m applied at the drift wall.

6.5 DEVELOPED INPUTS, BOUNDARY CONDITIONS, AND MESHES

This section summarizes the inputs developed from Section 4.1.1, which are used in the ANSYS and analytical models.

6.5.1 Thickness of Each of the Stratigraphic Layers

The rme6 v1.2 and YMESH v1.54 software routines (Sections 3.2 and 3.3) were used for scoping prior to their qualification to generate preliminary product output in the form of stratigraphic layer thickness at a specified northing and easting coordinate pair (DTN: MO0303MWDSLTLC.000). This preliminary product output was used in the ANSYS based ventilation models. Qualified versions of rme6 v1.2 and YMESH v1.54 were later used to generate the another set of stratigraphic layer thickness at the same northing and easting coordinate pair (DTN: MO0306MWDSLTLC.000). The two sets of stratigraphic layer thickness are compared in Table 6-4. There was no change between the product output from the preliminary and the qualified versions of rme6 v1.2 and YMESH v1.54, justifying the use of the preliminary output for use in the ANSYS based ventilation models.

Table 6-4. Thickness of the Stratigraphic Layers from Both the Unqualified and Qualified Versions of rme6 v1.2 and YMESH v1.54

	Unqualified versions of rme6 v.12 and YMESH v1.54 [a]	Qualified versions of rme6 v.12 and YMESH v1.54 [b]
Northing	234912.719	234912.719
Easting	170730.297	170730.297
Stratigraphic Unit	**Thickness (m)**	**Thickness (m)**
tcw12	20.2	20.2
tcw13	4.0	4.0
ptn21	7.2	7.2
ptn22	5.6	5.6
ptn23	2.0	2.0
ptn24	12.5	12.5
ptn25	36.5	36.5
ptn26	11.3	11.3
tsw31	2.0	2.0
tsw32	45.6	45.6
tsw33	85.3	85.3
tsw34	33.0	33.0
tsw35	104.7	104.7
tsw36	25.8	25.8
tsw37	12.9	12.9
tsw38	21.9	21.9
tsw9z	6.6	6.6
ch1z	15.0	15.0
ch2z	20.3	20.3
ch3z	20.3	20.3
ch4z	20.3	20.3
ch5z	20.3	20.3
ch6z	17.6	17.6
pp4	19.7	19.7
pp3	14.3	14.3
pp2	4.1	4.1

NOTES: [a] DTN: MO0303MWDSLTLC.000
[b] DTN: MO0306MWDSLTLC.000

6.5.2 Effective Thermophysical Properties of the Stratigraphic Layers

Table 6-5 lists the effective thermophysical properties of the stratigraphic units which take into account the effects of 90% water saturation of the matrix porosity (Section 5.3) and 100% air saturation of the lithophysal porosity (Section 5.4) on the thermal conductivity, density, and specific heat. These properties were obtained using Table 4-13, Table 4-14, Table 4-17, and Table 4-18. The calculation of these properties is documented in Attachments I and II. These properties were used in the ANSYS-based models.

Table 6-5. Effective Thermophysical Properties of the Stratigraphic Units Used in the ANSYS Models

Unit	Effective Thermal Conductivity (W/m·K)	Effective Specific Heat (J/kg·K)	Effective Density (kg/m^3)
tcw12	1.76	930	2673
tcw13	0.89	950	2721
ptn21	1.00	960	2973
ptn22	1.00	960	2973
ptn23	1.00	960	2973
ptn24	1.00	960	2973
ptn25	1.00	960	2973
ptn26	1.00	960	2973
tsw31	1.27	940	2561
tsw32	1.76	930	2673
tsw33	1.74	930	2578
tsw34	2.01	930	2665
tsw35	1.83	930	2563
tsw36	2.07	930	2635
tsw37	2.07	930	2635
tsw38	0.79	980	2449
tsw9z	1.00	980	2942
ch1z	1.00	1080	2805
ch2z	1.19	1070	2844
ch3z	1.19	1070	2844
ch4z	1.19	1080	2833
ch5z	1.19	1080	2833
ch6z	1.19	1020	2902
pp4	1.07	1040	2878
pp3	1.07	930	3007
pp2	1.32	930	2962

Source: Attachments I and II

6.5.3 Average Thermophysical Properties of the Invert

Table 6-6 lists the average thermophysical properties of the invert ballast material taken from Tables 4-6 and 4-8.

Table 6-6. Average Thermophysical Properties of the Invert

Specific Heat		Thermal Conductivity		Thermal Diffusivity	Bulk Density	
$(J/cm^3 \cdot °C)^1$	$(J/kg \cdot K)^2$	$(W/m \cdot °C)^3$	$(W/m \cdot K)^4$	$(mm^2/s)^5$	$(g/cm^3)^6$	$(kg/m^3)^7$
0.93	1177.38	0.16	0.16	0.18	1.266	1266

NOTES: [1] Average of Table 4-6 for Specific Heat
[2] Convert [1] from $J/cm^3 \cdot °C$ to $J/kg \cdot K$ using the Bulk Density [6]
[3] Average of Table 4-6 for Thermal Conductivity
[4] Convert [3] from °C to K
[5] Average of Table 4-6 for Thermal Diffusivity
[6] Average of Table 4-8 for Bulk Density
[7] Convert [6] from g/cm^3 to kg/m^3

6.5.4 In-Drift Cross Sectional Area Available for Flow

The in-drift cross sectional area available for air flow is calculated in Attachment XVI and is 19.5 m^2. This calculation takes into account the cross sectional area of the drift, minus the cross sectional area of the waste package and the cross sectional area of the invert.

6.5.5 Temperature and Flux Boundary Conditions at the Ground Surface, Water Table, and Mid-Pillar

The temperature at the ground surface is calculated from the following equation (BSC 2001d, p. 66):

$$T_s = T_{s-ref} - \lambda\left(Z_s - Z_{s-ref}\right) \qquad \text{Eq. 6-68}$$

where

T_s = ground surface temperature (°C)
$T_{s\text{-}ref}$ = surface temperature at the reference elevation Z_{ref} (°C)
λ = dry adiabatic atmospheric lapse rate = 0.01°C/m
Z_s = ground surface elevation (m)
$Z_{s\text{-}ref}$ = surface elevation for which the temperature $T_{s\text{-}ref}$ is known (m)

T_s is calculated using the information provided in Table 4-19:

$T_{s\text{-}ref}$ = 16.95°C
λ = 0.01°C/m
$Z_{s\text{-}ref}$ = 1359.2 m
Z_s = 1363.4 m
T_s = 16.91°C = 16.9°C

The water table temperature is calculated by linear interpolation using the following equation:

$$T_w = \frac{\left(Z_w - Z_{w-ref}\right)\left(T_w - T_{w-ref}\right)}{Z_w - Z_{w-ref}} + T_{w-ref} \qquad \text{Eq. 6-69}$$

where

T_w = water table surface temperature (°C)
$T_{w\text{-}ref}$ = water table surface temperature at the reference elevation $Z_{w\text{-}ref}$ (°C)
Z_w = water table surface elevation (m)
$Z_{w\text{-}ref}$ = water table surface elevation for which the temperature $T_{w\text{-}ref}$ is known (m)

T_w is calculated using the information provided in Table 4-19:

$T_{w\text{-}ref}$ = 29.21°C
$Z_{w\text{-}ref}$ = 730.0 m
Z_w = 774.4 m
T_w = 28.35°C = 28.4°C

The flux boundary condition at the mid-pillar is adiabatic.

6.5.6 Temperature of the Ventilation Air at the Drift Inlet

The temperature of the ventilation air at the drift inlet is assumed to be equal to the temperature of the host rock at the repository horizon (Section 5.7). The temperature of the host rock at the repository horizon prior to preclosure was calculated by ANSYS using the boundary conditions described in Section 6.5.5 and the thermophysical properties of the rock layers described in Section 6.5.2. The temperature was calculated to be 22.82°C (DTN: MO0306MWDASLCV.001).

6.6 RESULTS OF THE NUMERICAL APPLICATION OF THE CONCEPTUAL MODEL

The results for the ANSYS-LA-Coarse, ANSYS-LA-Fine, and Analytical-LA-Coarse models are presented in terms of temporally and spatially varying temperatures. In addition, ventilation efficiencies are presented for the ANSYS-LA-Coarse and Analytical-LA-Coarse models. A comparison between the ANSYS-LA-Coarse and ANSYS-LA-Fine models quantifies the impact of the axial discretization along the drift length and serves as a model verification exercise. A comparison between the ANSYS-LA-Coarse and Analytical-LA-Coarse models benchmarks the analytical approach in preparation for further use in the implementation of the alternative conceptual model and the uncertainty/sensitivity analysis (Sections 6.9.2 and 6.11).

6.6.1 The Effects of Axial Discretization

The general trends of waste package, drift wall, and drift air temperatures as functions of time and drift length for the ANSYS-based models are shown in Figures 6-3 and 6-4 for a 600 meter drift length case. The waste package and drift wall temperatures are perimeter-averaged results, while the in-drift air temperatures are bulk averaged. The temperatures for the waste package, drift wall, and drift air for the ANSYS-LA-Coarse and ANSYS-LA-Fine models are within 0.4°C for all distances from the drift entrance and times since emplacement. The following general observations with respect to waste package, drift wall, and drift air temperatures for the ANSYS-based models can be made:

- With respect to time, temperatures peak at one year into the ventilation period and afterwards decline in an exponential fashion similar to the waste package heat energy input decay curve.

- With respect to location along the length of the drift, temperatures increase linearly, with the maximum temperatures occurring at the end of the drift.

- The ANSYS methodology is insensitive to the number and length of sub-divisions in the axial direction.

6.6.2 Temperature and Ventilation Efficiency Comparisons for the ANSYS-LA-Coarse and Analytical-LA-Coarse Models

The same general trends of temperature variation with time and distance from the drift entrance, as noted in Section 6.6.1 for the ANSYS numerical models, is observed for the Analytical-LA-Coarse. Figure 6-5 shows the ANSYS-LA-Coarse and Analytical-LA-Coarse temperatures as a function of time for locations 100 m, 600 m, and 800 m from the drift entrance. Figure 6-6 shows temperatures as function of axial distance from the drift entrance for ventilation durations of 5 and 50 years. The temperatures for the waste package, drift wall, and drift air for the two models are within 5°C for all distances from the drift entrance and times since emplacement, with the Analytical-LA-Coarse temperatures being consistently higher than the corresponding ANSYS temperatures.

The instantaneous ventilation efficiency is calculated using Equation 6-5. Figure 6-7 shows the ANSYS-LA-Coarse and Analytical-LA-Coarse instantaneous ventilation efficiencies as a function of time for locations 100 m, 600 m, and 800 m from the drift entrance. Figure 6-8 shows ventilation efficiencies as function of axial distance from the drift entrance for ventilation durations of 5 and 50 years. The ventilation efficiencies for the two models are within 4% for all distances from the drift entrance and times since emplacement. The overall or integrated ventilation efficiency is calculated using Equation 6-6. Table 6-7 shows the integrated efficiency over 600 and 800 meters of drift length, and 50 years of ventilation for the two models. Use of the ventilation efficiency is discussed in Section 6.10.

It should be noted that the ANSYS-based model simulates an eccentrically located waste package and an invert, while the analytical model simulates a concentrically located waste package and no invert. Based on the reasonable comparisons of temperature and efficiency, the ventilation model is not sensitive to the eccentricity of the waste package, nor the presence of the invert (including its thermophysical properties).

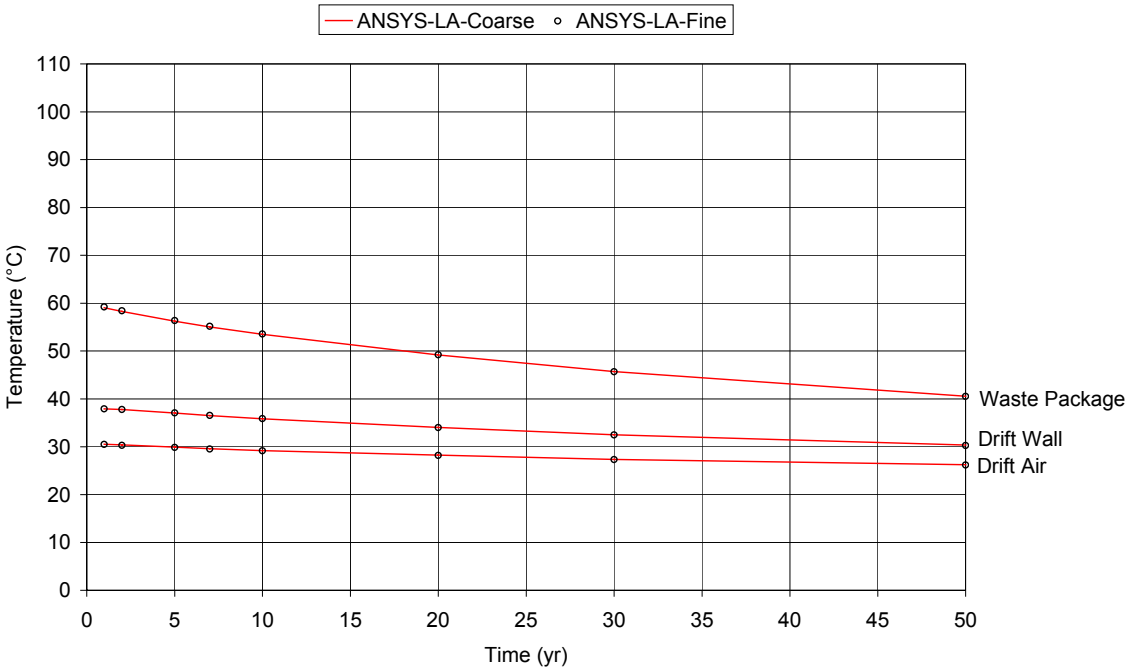

(a) 100 meters

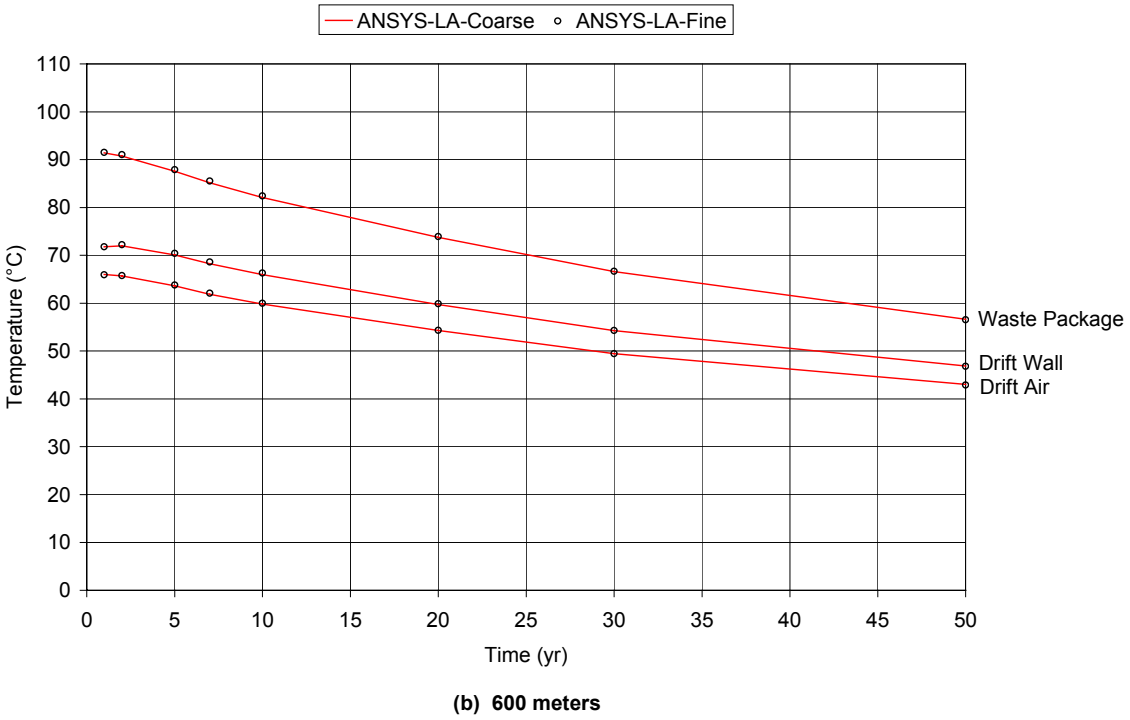

(b) 600 meters

DTN: MO0306MWDASLCV.001
MO0306MWDALAFV.000

Figure 6-3. Waste Package, Drift Wall, and Drift Air Temperatures as Function of Time for (a) 100 meters and (b) 600 meters from the Drift Entrance for the ANSYS-LA-Coarse and ANSYS-LA-Fine Models

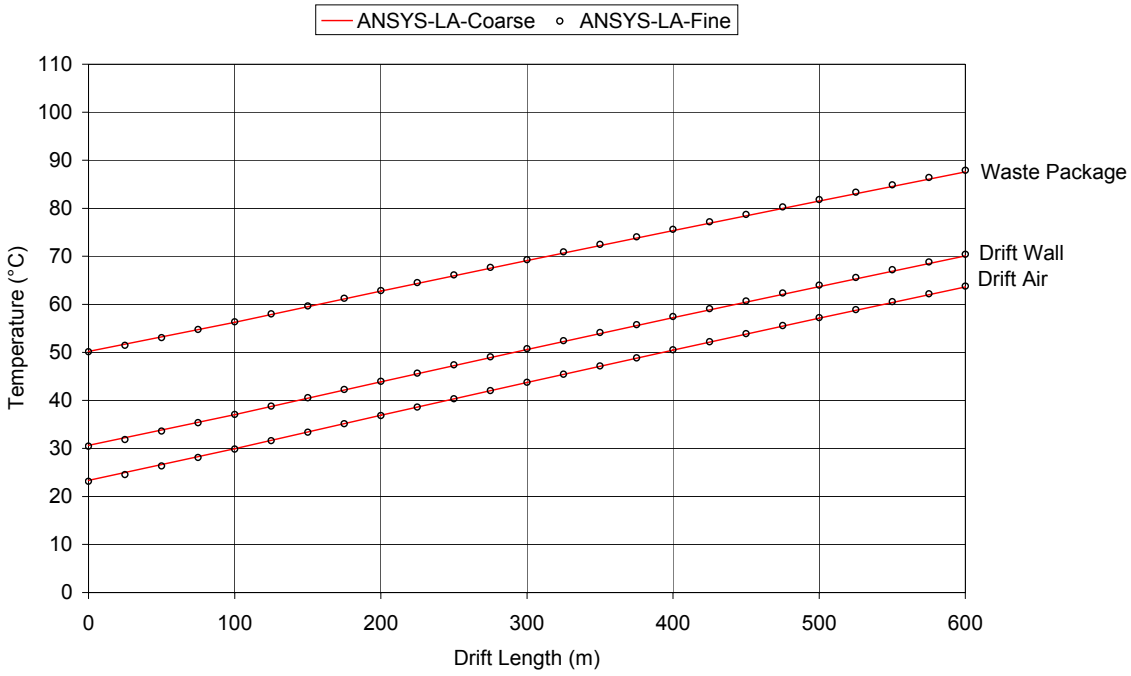

(a) 5 years

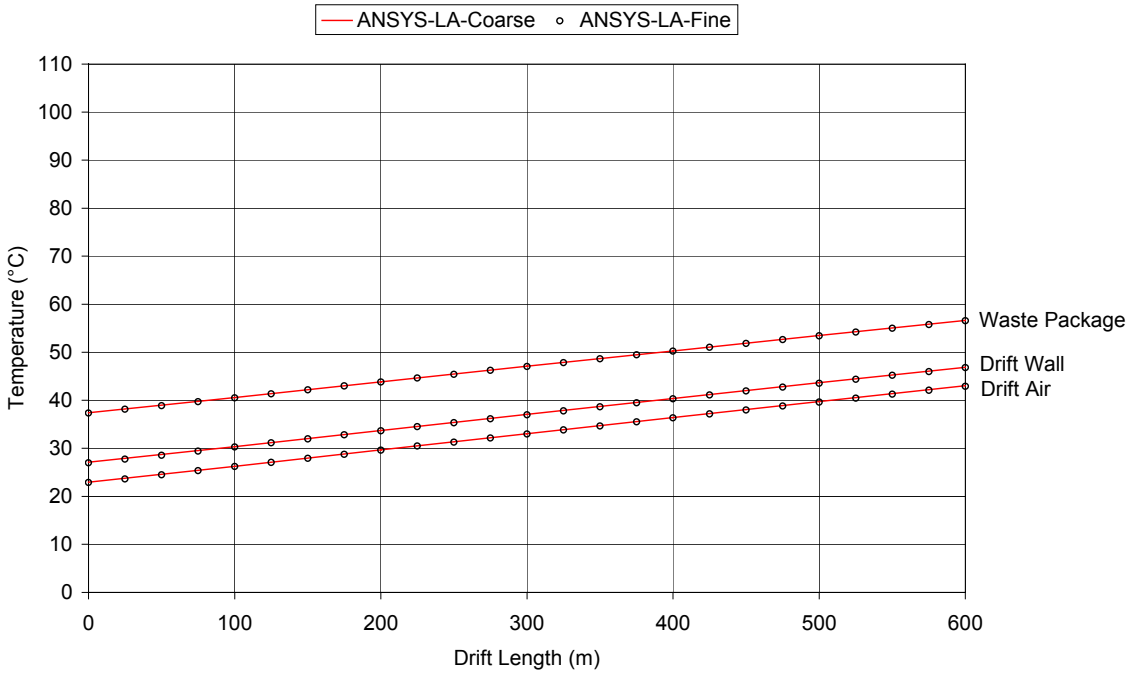

(b) 50 years

DTN: MO0306MWDASLCV.001
MO0306MWDALAFV.000

Figure 6-4. Waste Package, Drift Wall, and Drift Air Temperatures as Function of Drift Length for (a) 5 Years and (b) 50 Years from the Time of Waste Emplacement for the ANSYS-LA-Coarse and ANSYS-LA-Fine Models

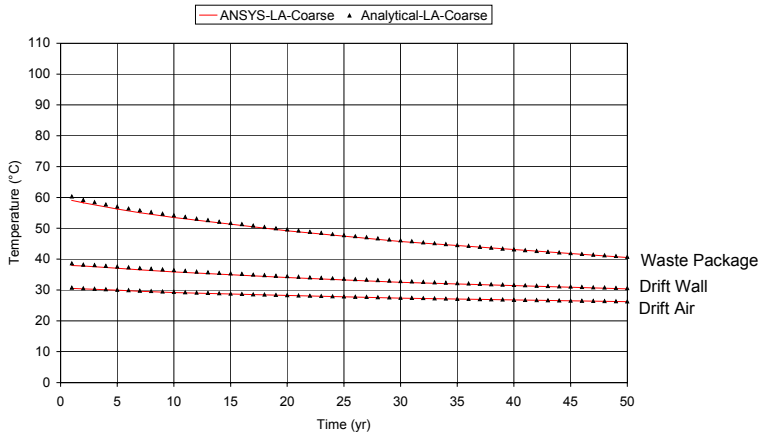

(a) 100 meters

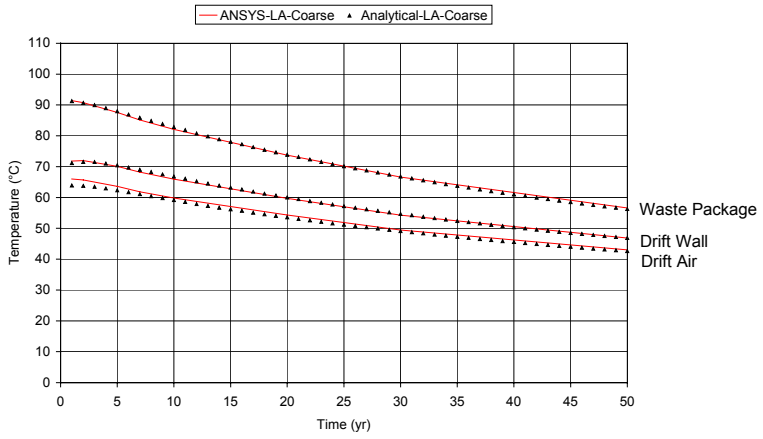

(b) 600 meters

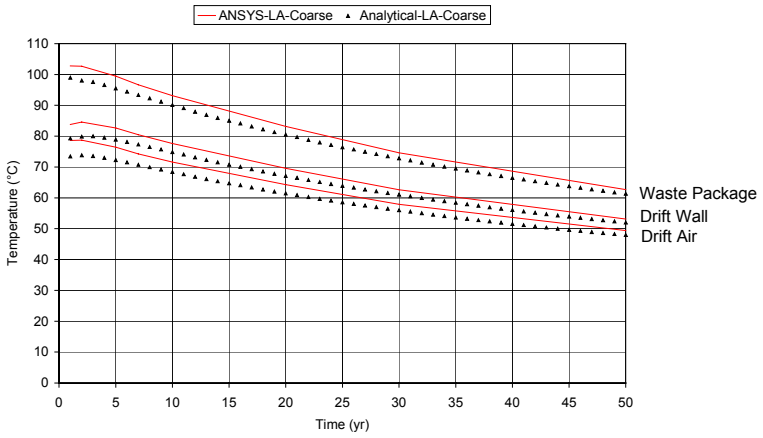

(c) 800 meters

DTN: MO0306MWDASLCV.001
MO0307MWDAC8MV.000

Figure 6-5. Waste Package, Drift Wall, and Drift Air Temperatures as Function of Time for (a) 100 meters, (b) 600 meters, and (c) 800 meters from the Drift Entrance for the ANSYS-LA-Coarse and Analytical-LA-Coarse Models

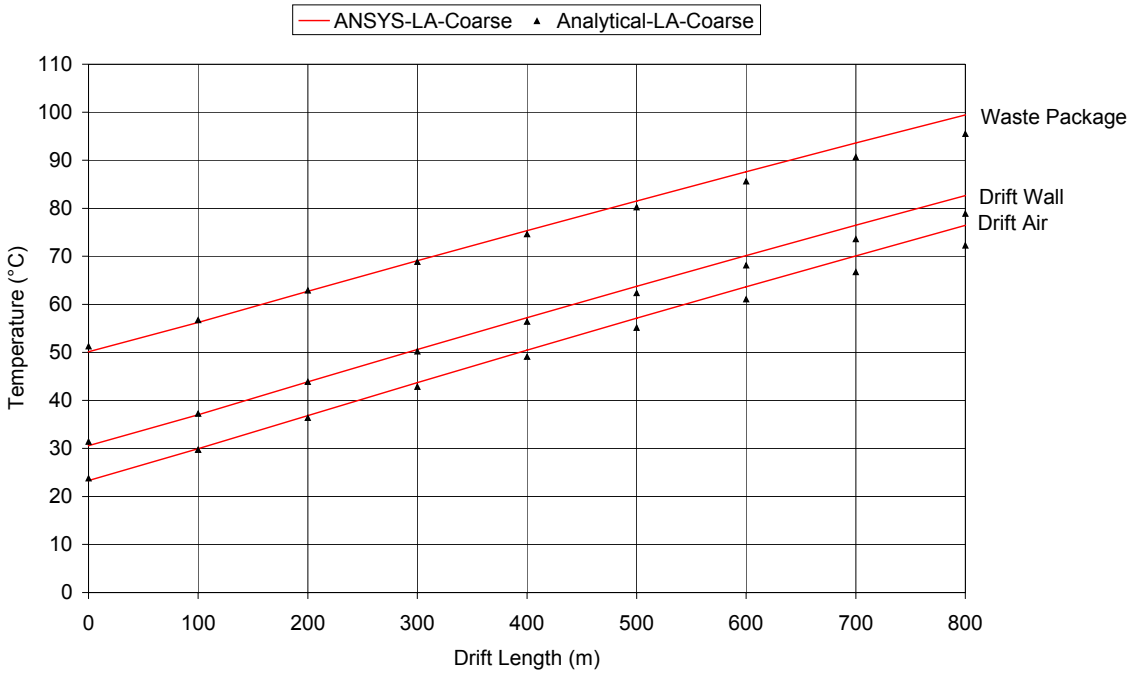

(a) 5 years

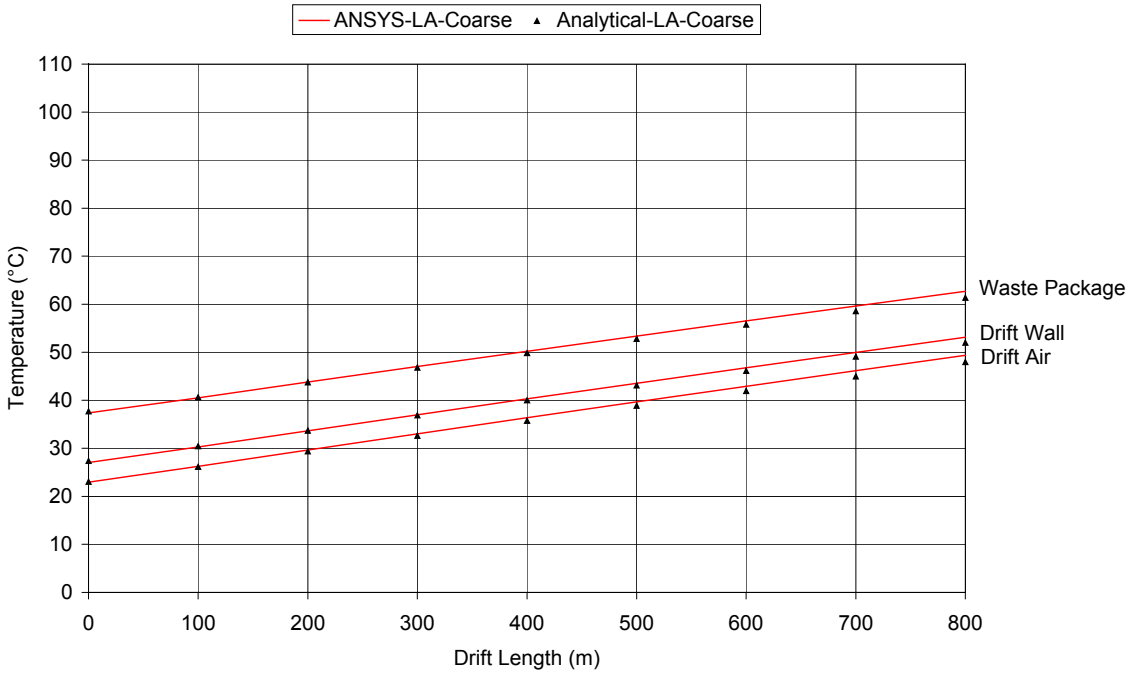

(b) 50 years

DTN: MO0306MWDASLCV.001
MO0307MWDAC8MV.000

Figure 6-6. Waste Package, Drift Wall, and Drift Air Temperatures as Function of Drift Length for (a) 5 Years and (b) 50 Years from the Time of Waste Emplacement for the ANSYS-LA-Coarse and Analytical-LA-Coarse Models

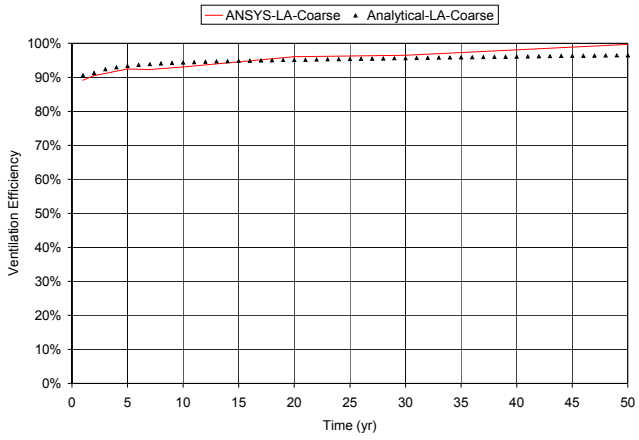

(a) 100 meters

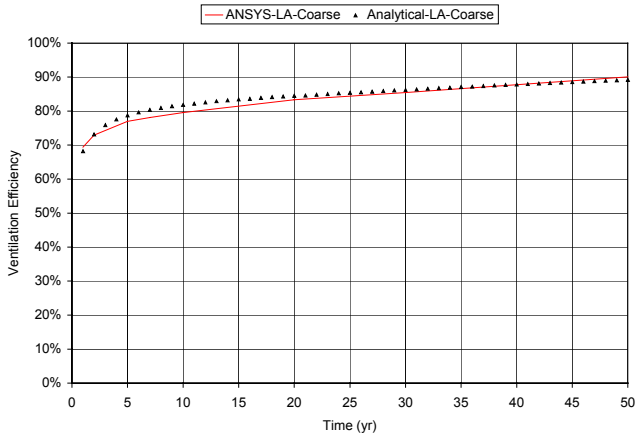

(b) 600 meters

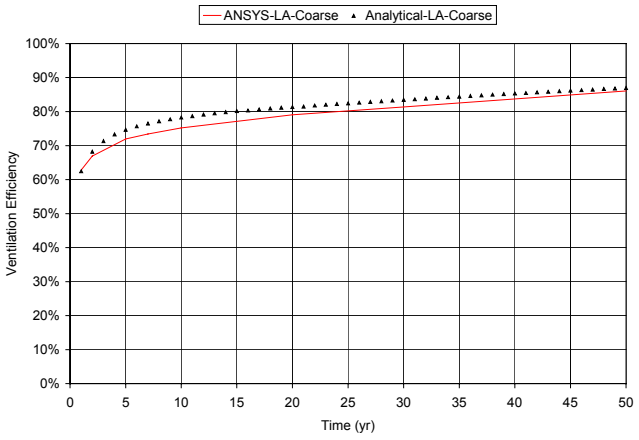

(c) 800 meters

DTN: MO0306MWDASLCV.001
MO0307MWDAC8MV.000

Figure 6-7. Ventilation Efficiency as Function of Time for (a) 100 meters, (b) 600 meters, and (c) 800 meters from the Drift Entrance for the ANSYS-LA-Coarse and Analytical-LA-Coarse Models

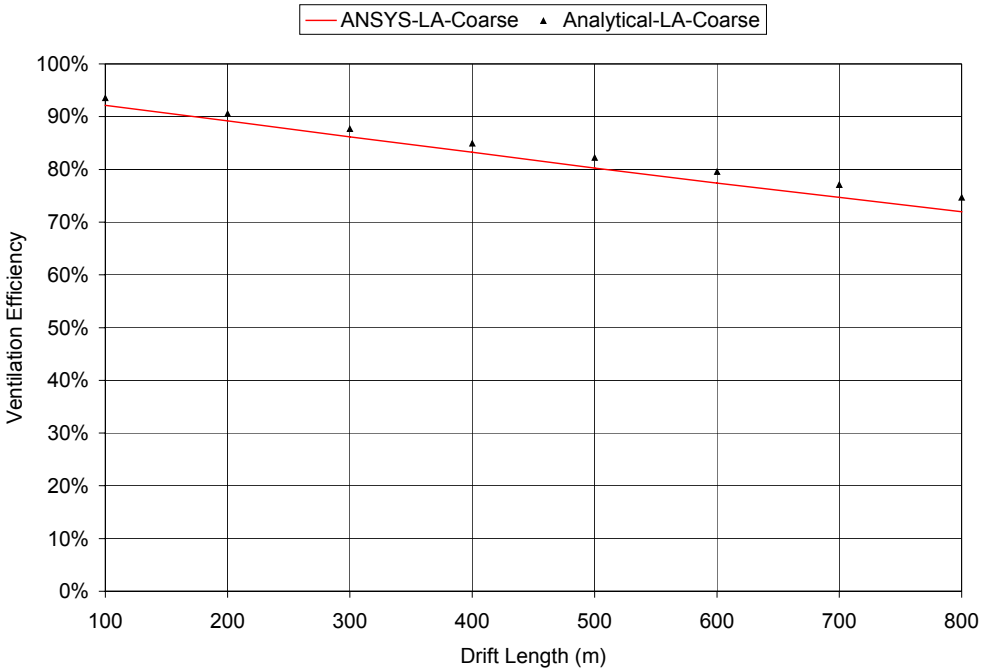

(a) 5 years

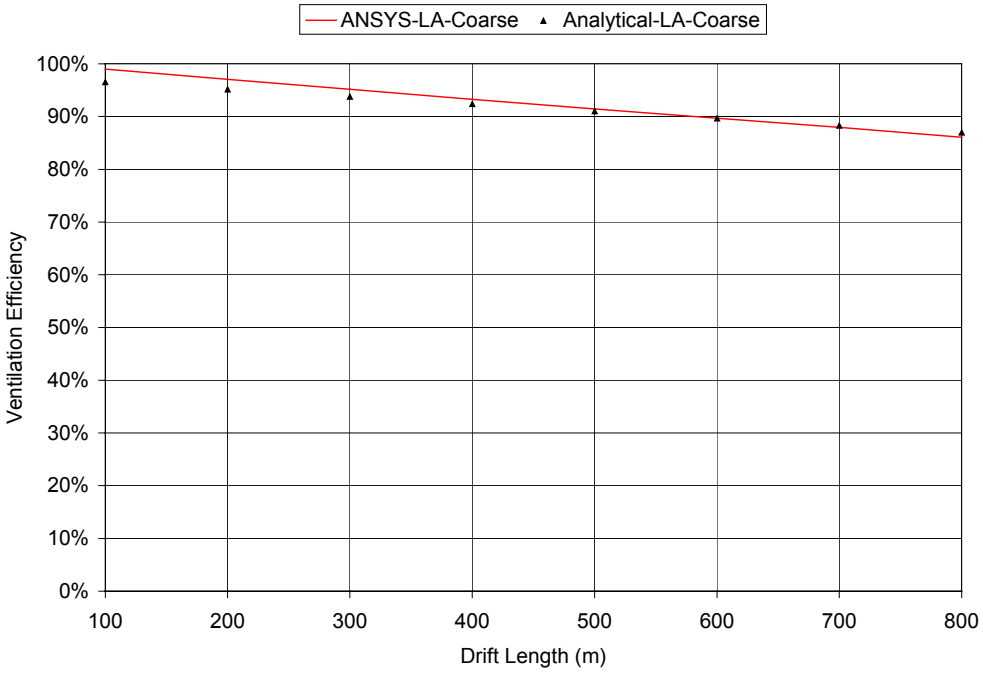

(b) 50 years

DTN: MO0306MWDASLCV.001
MO0307MWDAC8MV.000

Figure 6-8. Ventilation Efficiency as Function of Drift Length for (a) 5 years and (b) 50 Years from the Time of Waste Emplacement for the ANSYS-LA-Coarse and Analytical-LA-Coarse Models

Table 6-7. Integrated Ventilation Efficiency for a 600-meter and 800-meter Drift and 50 Years of Ventilation

Model	Integrated Ventilation Efficiency (Eq. 6-6)
600-meter Drift, 50 years of Ventilation	
ANSYS-LA-Coarse [a]	88.3%
Analytical-LA-Coarse [b]	88.0%
800-meter Drift, 50 years of Ventilation	
ANSYS-LA-Coarse [a]	85.8%
Analytical-LA-Coarse [b]	86.0%

NOTES [a] DTN: MO0306MWDLACVD.000
[b] DTN: MO0307MWDAC8VD.000

6.7 ALTERNATIVE CONCEPTUAL MODEL FOR IN-DRIFT VENTILATION

The alternative conceptual model for in-drift ventilation includes the addition of water and water vapor mass transport in the host rock, across the drift wall, and into the ventilation airstream. Water and water vapor mass transport is directly coupled to the heat transfer processes described in the conceptual model for in-drift ventilation. The impacts of the mass transport, in terms of latent heat transfer, temperature, heat removal rates, and near-field host rock dryout are evaluated using analytical approaches.

6.7.1 Alternative Conceptual Model Heat and Mass Transfer Processes

The coupled heat and mass transfer processes for the alternative conceptual model for in-drift ventilation are the same as those for the conceptual model described in Section 6.3.1 and Figure 6-1 with the addition of two other processes:

1. Water phase change (evaporation and condensation) occurs within the host rock as the temperature and vapor pressure change which causes the host rock saturation to decline, thus lowering the thermal conductivity of the rock.

2. Water (liquid and vapor phases) mass transfer occurs within the host rock and the in-drift air. Water vapor may move within the host rock via diffusion to cooler regions where it condenses, as described in process 5. It also may enter the in-drift airflow at the drift wall, causing a change in relative humidity, and can potentially condense in cooler regions of the ventilation system, such as the exhaust main drift and exhaust shafts.

The heat transfer rates for processes 5 and 6 can be related to processes 1 through 4 by again considering the overall conservation of thermal energy except during the early transient response when the waste package temperature is rapidly changing. The following is an addition to the thermal energy conservation described in Section 6.3.1:

- The sum of the convective heat transfer rates from the waste package and the drift wall into the airflow (processes 2 and 3), and the heat of the water vapor transported back across the drift wall (process 6) equal the total heat added to the ventilation air.

Additionally, the mass transfer rates for processes 1 through 6 can be related by considering the overall conservation of mass during the ventilation period. The following summarizes the coupled components of the mass balance:

- The sum of the mass of the ventilation air into the drift and the water vapor that moves across the drift wall from the surrounding host rock, equals the mass of the air exiting the drift.

Vapor diffusion or enhanced vapor diffusion have the potential of locally increasing the heat flux rate for saturations that are intermediate to full matrix-fracture saturation, and in the dry condition in which water vapor is absent. Vapor diffusion is defined as the movement of water vapor under Fick's Law. Enhanced vapor diffusion is the movement of water vapor to areas where water is retained, condensed and then evaporated.

The alternative conceptual model considers how the ventilation efficiency changes when water phase change and mass transfer occurs across the drift wall and within the host rock. Consider the situation where water in the rock evaporates, and the water vapor moves down the thermal gradient and condenses. When this occurs, the apparent thermal conductivity of the rock decreases in the region of evaporation, and increases in the region of condensation. When the thermal conductivity of the rock increases, more energy would be transferred to the rock, thus decreasing the ventilation efficiency. Conversely, when the thermal conductivity of the rock decreases, the in-drift environment becomes more insulated, and the ventilation efficiency increases.

When water in the rock evaporates, the water vapor may also move back up the thermal gradient through the rock and exit into the ventilation air stream. When this occurs, the latent heat (energy) of the phase change must be supplied by the source, and this latent heat (energy) must be put into the rock. The exiting of the water vapor from the rock into the air involves no energetics. More energy must be put into the rock to attain the same temperature when there is no evaporation. In this situation, again, the ventilation efficiency must decrease because more energy is put into the rock.

6.8 IMPLEMENTATION OF THE ALTERNATIVE CONCEPTUAL MODEL

To assess the impact on the ventilation efficiency to the alternative conceptual model processes, the following analyses were performed:

- An analytical calculation which bounds the latent heat contribution to the in-drift ventilation air stream (Attachment XIII).

- Ventilation analyses using the analytical spreadsheet calculation (named Analytical-LA-Wet-vs-Dry-kth, Attachment VIII) for host rock at different levels of saturation (and therefore different values of thermal conductivity).

- An analysis of experimental data for vapor diffusion and enhanced vapor diffusion.

6.9 RESULTS OF THE APPLICATION OF THE ALTERNATIVE CONCEPTUAL MODEL

The results of the analytical calculation to bound the latent heat contribution to the in-drift ventilation air stream, the Analytical-LA-Wet-vs-Dry-kth model, and the analysis of experimental data to quantify the effects of vapor diffusion and enhanced vapor diffusion follow.

6.9.1 Moisture Effects on the In-Drift Ventilation Air Stream

An analytical calculation was performed which bounds the latent heat contribution to the in-drift ventilation air stream over a 600 m drift length and 50-year ventilation period in terms of the matrix hydrologic properties. Analytical equations for steady state unsaturated flow in porous media to a specified moisture potential boundary condition at the drift wall were developed with the help of Jury et al. (1991, pp. 51, 60, 113, 151, Section 3.4) and Fetter (1993, pp. 172, 181, 182). Using 30% relative humidity in the drift, the moisture potential at the drift wall was calculated to be 1.985×10^6 cm (Attachment XIII-6). The moisture potential in the surrounding host rock at some distance from the drift wall is calculated using two different sets of measured data: the first being the mean of the measurements from borehole core of matrix saturation in the Tptpll (tsw35) geologic unit (Table 4-11) and the second being measurements of water potential taken from the ECRB Cross-Drift in the Tptpll (tsw35) geologic unit (Table 4-12).

The average saturation from the borehole core measurements (Table 4-11) is 74%, which translates to a water potential of 2908 cm (Attachment XIII-7). Using these potentials, a radius of influence of 6 m, and the hydrologic properties of Tptpll (tsw35) from Table 4-16, the steady state liquid flux toward the drift (which evaporates) is calculated to be 0.061 mm/year (Attachment XIII-8).

The measured water potential at 5.62 m from the drift wall is 1000 cm (Table 4-12). Using this data, the potential calculated at the drift wall based on a relative humidity conditions, and the hydrologic properties of Tptpll (tsw35) from Table 4-16, the steady state liquid flux toward the drift (which evaporates) is calculated to be 0.278 mm/year (Attachment XIII-8).

If all the moisture which fluxes to the drift wall over the entire length of the emplacement drift is evaporated at some constant temperature, the total latent heat contribution to the in-drift air over the 50-year preclosure period can be calculated. The latent heat contribution is then divided by the total heat output by the waste packages over the same 50-year period and 600 meter long drift. The results are presented in Table 6-8.

Table 6-8. Latent Heat Contribution Expressed as a Percentage of the Total Waste Package Heat Over 50 Years and 600 Meters of Drift

Model	Latent Heat Contribution
Analytical model with a moisture flux = 0.061 mm/year [1]	0.01%
Analytical model with a moisture flux = 0.278 mm/year [2]	0.04%

NOTES: [1] Attachment XIII-8, flux based on the mean saturation from Table 4-11
[2] Attachment XIII-8, flux based on measured water potential from a borehole in the ECRB Cross-Drift (Table 4-12)

The analytical calculation indicates that:

- The contribution of heat by vaporization of moisture is rate limited by the hydrogeologic properties of the host rock.
- The contribution of heat by vaporization of moisture is a small percentage of the total heat input.

For a comparative calculation which bounds the latent heat contribution, we take a present day percolation flux and apply it at the drift wall. For northing 234912.7 and easting 170730.3, the closest UZ grid mesh column ID is g_9 (Table 4-19). The percolation flux (present day climate, upper case) reported for UZ grid mesh column ID g_9 at the base of the ptn unit is 15.70959 mm/year (DTN: LB0302PTNTSW9I.001, file preq_uz_ptn.q). If this percolation flux is flow focused through matrix and fracture network over the width of two drift diameters, and arrives at the drift wall where it is evaporated, the latent heat contribution can be calculated. Using the thermophysical properties of water at 350 K (Table 4-25), the total latent heat contribution over the 50-year ventilation period and 600 meters of drift is calculated as follows:

$$\left(\frac{15.70959\text{mm}}{\text{yr}}\right)\cdot\left(\frac{0.001\text{m}}{1\text{mm}}\right)\cdot\left(\frac{2\cdot 5.5\text{m}\cdot 600\text{m}}{1}\right)\cdot\left(\frac{50\text{yr}}{1}\right)\cdot\left(\frac{973.7\text{kg}}{\text{m}^3}\right)\cdot\left(\frac{2317\text{kJ}}{\text{kg}}\right)\cdot\left(\frac{1000\text{J}}{1\text{kJ}}\right)=1.170\cdot 10^{13}\,\text{J}$$

The total waste package heat input over the 50-year ventilation period and 600 meter long drift is $8.605\cdot 10^{14}$ J (DTN: MO0307MWDAC8MV.000, worksheet "Ventilation Efficiency"). The latent heat contribution expressed as a percentage of the total waste package heat input is:

$$\frac{1.170\cdot 10^{13}\,\text{J}}{8.605\cdot 10^{14}\,\text{J}}=1.4\%$$

This calculations supports the conclusion reached earlier, that the contribution of heat by vaporization of moisture is a small percentage of the total heat input.

Therefore, neglecting latent heat in the calculation of ventilation efficiencies does not introduce significant error, even if the liquid flux to the drift wall were much larger than the value used here. The reason is that heat transferred to the host rock that is used to vaporize water during the ventilation period, would be carried back to the drift as latent heat of the water vapor and would subsequently be removed by the ventilation air.

The reduction in relative humidity to the in-drift ventilation air for a 600 meter long drift is calculated using the methodology outlined in Attachment XXVII of ANSYS Calculations in Support of Natural Ventilation Parametric Study for SR (BSC 2001e) and Mine Ventilation and Air Conditions (Hartman et. al. 1982, pages 596-597). Using the percolation flux of 15.7 mm/yr and the thermophysical properties of water at 350 K (Table 4-25), the mass flux of water which arrives at the drift wall is:

$$\left(\frac{15.70959mm}{yr}\right)\cdot\left(\frac{0.001m}{1mm}\right)\cdot\left(\frac{1yr}{31556926s}\right)\cdot\left(\frac{2\cdot 5.5m\cdot 600m}{1}\right)\cdot\left(\frac{973.7kg}{m^3}\right)\cdot\left(\frac{1grain}{6.5\times 10^{-5}kg}\right)=49.371\,\frac{grains_{water}}{s}$$

The mass flux of the ventilation air at 22.8°C from Section 6.5.6 (or approximately 300 K) is:

$$\left(\frac{15 m^3}{s}\right)\cdot\left(\frac{1.1614 kg}{m^3}\right)\cdot\left(\frac{2.2046 lb}{1 kg}\right) = 38.406 \frac{lb_{air}}{s}$$

The distribution of mass flux of water to the mass flux of ventilation air (percolation component) is:

$$\left(\frac{49.371 \frac{grains_{water}}{s}}{38.406 \frac{lb_{air}}{s}}\right) = 1.285 \frac{grains_{water}}{lb_{air}}$$

The relative humidity of the inlet air is taken to be 20.31%, which has a moisture content of 28.210 $grains_{water}/lb_{air}$ (BSC 2003g, Table 3 for P1 Early Emplacement Drift, Intake Main). The new moisture content of the ventilation air is then the sum of the percolation and relative humidity components:

$$28.210 \frac{grains_{water}}{lb_{air}} + 1.285 \frac{grains_{water}}{lb_{air}} = 29.495 \frac{grains_{water}}{lb_{air}}$$

Converting $29.495 grains_{water}/lb_{air}$ to lb_{water}/lb_{air}:

$$\left(\frac{29.495 grains_{water}}{1 lb_{air}}\right)\cdot\left(\frac{6.479891\times10^{-5} kg}{1 grain}\right)\cdot\left(\frac{2.2046 lb}{1 kg}\right) = 0.00421 \frac{lb_{water}}{lb_{air}}$$

The average barometric pressure is 26.3322 inHg (BSC 2003g, Table 3 for P1 Early Emplacement Drift, Intake Main). The partial pressure can be calculated by (Hartman et al. 1982, Eq. 21-5 rearranging to solve for pv):

$$\frac{0.00421 \frac{lb_{water}}{lb_{air}} \cdot 26.3322 inHg}{0.622 + 0.00421 \frac{lb_{water}}{lb_{air}}} = 0.177 inHg$$

The air temperature at the outlet of the 600 meter long drift after 50 years of ventilation is approximately 42°C from the results of the Analytical-LA-Coarse ventilation model (Table 8-6). The saturated vapor pressure at 42°C (107.6°F) is (Hartman et al. 1982, Eq. 21-1):

$$0.18079 e^{\frac{(17.27\cdot 107.6°F)-552.64}{107.6°F+395.14}} = 2.427 inHg$$

The relative humidity at the outlet of the 600 meter long drift is (Hartman et al. 1982, Eq. 21-4):

$$\frac{0.177 inHg}{2.427 inHg}\cdot 100\% = 7.3\%$$

Therefore, while the ventilation air stream picks up moisture through evaporation of the near field host rock pore water at a rate of approximately 16 mm/yr, the relative humidity over 600

meters of drift and 50 years of ventilation decreases from approximately 20% to 7% due to the increase in air temperature.

6.9.2 Ventilation Analysis for Host Rock at Varying Degrees of Saturation

An analytical spreadsheet ventilation analysis, Analytical-LA-Wet-vs-Dry-kth, assessed the impact of varying degrees of host rock saturation on the waste package, drift wall, and in-drift air temperatures and the ventilation efficiency for a 600 meter long drift. These analyses used the thermophysical properties of the tws35 unit for the repository horizon and matrix water saturation ranging from 0% to 100%. Figure 6-9 shows the impact of a "wet" versus "dry" thermal conductivity on the temperatures of the waste package, drift wall, and in-drift air. The temperatures for the two cases are within 4°C for all distances from the drift entrance and times since emplacement, with the "dry" case being consistently hotter. Figure 6-10 plots the integrated ventilation efficiency as a function of matrix saturation and host rock thermal conductivity. The integrated ventilation efficiency changes from approximately 87.3% to 90.4% when the matrix saturation goes from wet to dry.

6.9.3 Evaluation of Vapor Diffusion and Enhanced Vapor Diffusion on the Host Rock Thermal Conductivity and Thus Ventilation Efficiency

In addition to the conduction of heat under a temperature gradient, it is possible to have vapor phase diffusion (Jury et al. 1991, p. 211) within the rock mass. In addition, enhanced vapor phase diffusion may occur (Jury et al. 1991, p. 212). These related phenomena are not included in the ventilation analysis presented above nor in the ANSYS calculations. Vapor diffusion and/or enhanced vapor diffusion (due to evaporation and condensation in the pores) tend to increase the aggregate thermal conductivity from that for stagnant fluid components.

The following discussion presents information regarding vapor diffusion and enhanced vapor diffusion by Jury et al. (1991, pp. 211 to 213). Experimental results obtained by Moyne et al. (1990) are then discussed to illustrate vapor and enhanced vapor diffusion effects. Experimental results obtained from laboratory measurements on core samples and the results from the large scale Drift Scale Test are then presented.

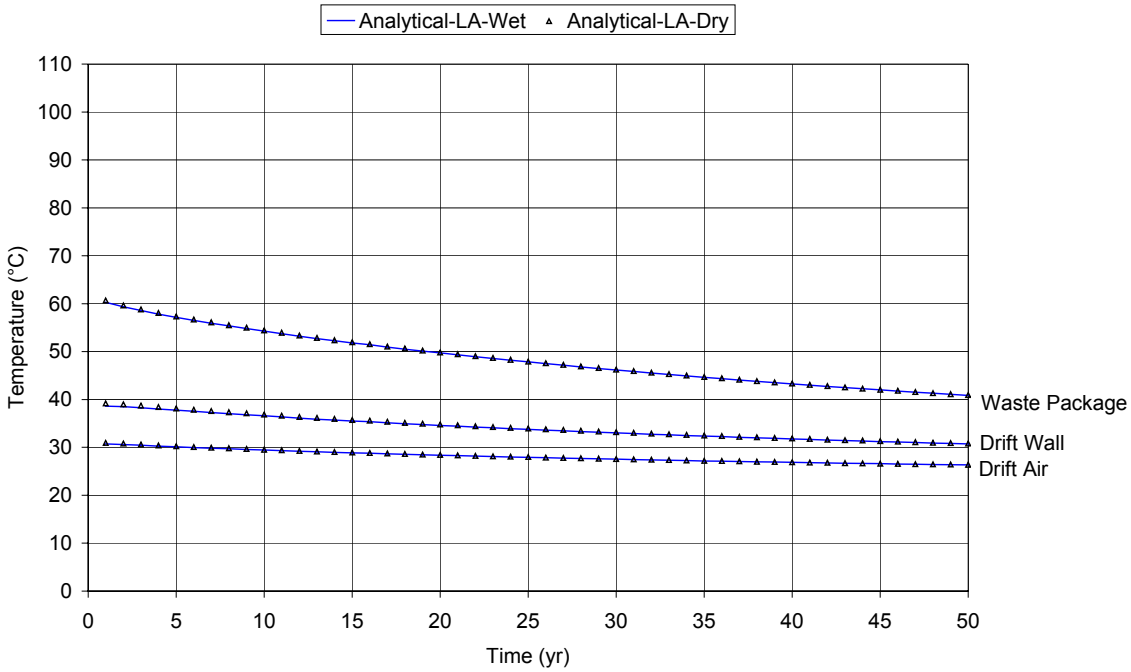

(a) 100 meters

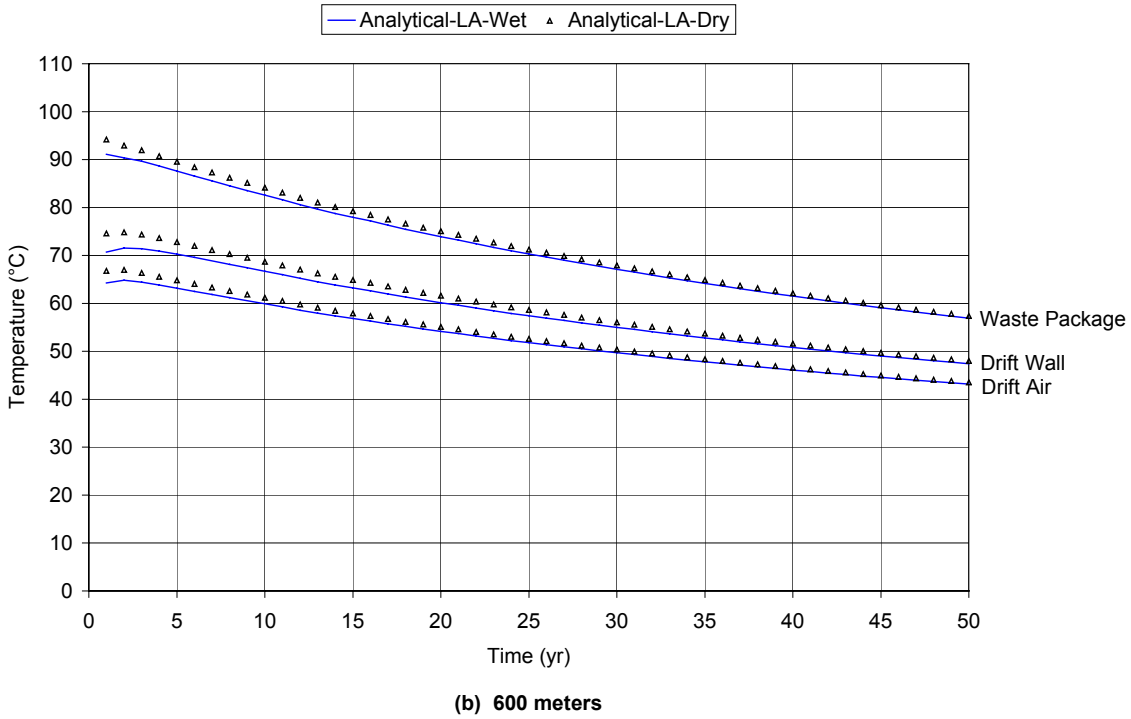

(b) 600 meters

DTN: MO0306MWDRTCCV.000

Figure 6-9. Waste Package, Drift Wall, and Drift Air Temperatures as Function of Time for (a) 100 meters and (b) 600 meters from the Drift Entrance for the Analytical-LA-Wet-vs-Dry-kth Ventilation Model (Attachment VIII)

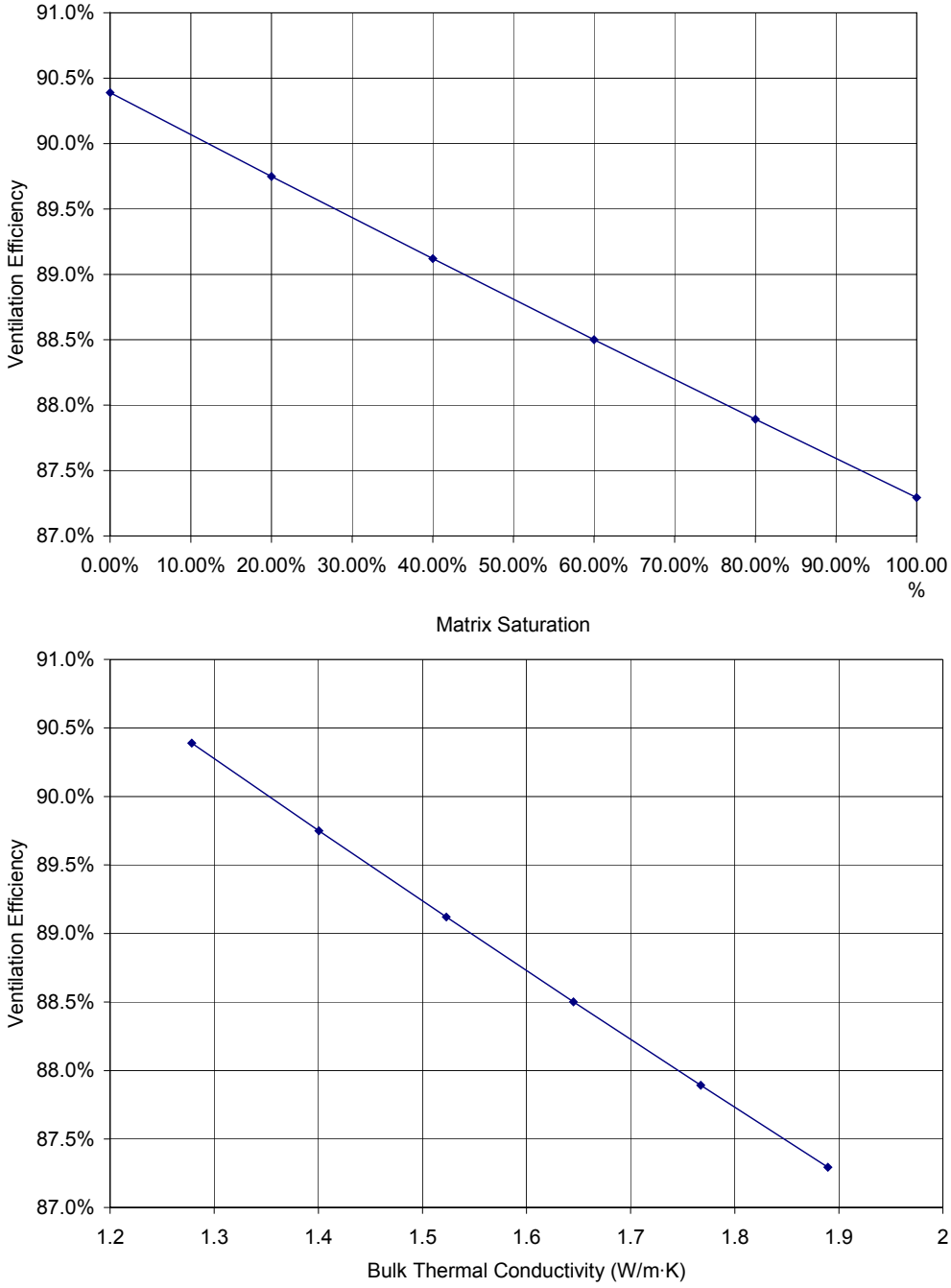

DTN: MO0306MWDRTCCV.000

Figure 6-10. Ventilation Efficiency as Function of Matrix Saturation and Bulk Thermal Conductivity Calculated Using the Analytical-LA-Wet-vs-Dry-kth Ventilation Model (Attachment VIII)

6.9.3.1 Vapor Diffusion by Jury et al. (1991)

Jury et al. (1991) provides a general discussion of vapor diffusion. Laboratory tests have shown that when temperature gradients were placed across soil samples, the measured vapor fluxes were 10 times larger than that predicted by Fick's Law. It was found that two mechanisms could increase the potential for vapor diffusion. The first mechanism is that water vapor that is fluxing towards moisture that is retained in the pore space may condense on one side and evaporate on the other side (Jury et al. 1991, p. 212, Figure 6.7).

The second enhancement mechanism relates to the thermal gradients across the liquid phase contained within the pore space. The thermal conductivity of the solid phase is several times larger than the thermal conductivity of water. Since the thermal gradients within the pore space are more likely to be influenced by liquid water, the effective thermal gradients for a uniform heat flux would be higher. Theoretical considerations suggest that the thermal gradients might be a factor of two to three higher.

6.9.3.2 Vapor Diffusion by Moyne et al. (1990)

Moyne et al. (1990) presented experimental measurements of these phenomena for various materials as a function of a term that he defined as the humidity ratio. These included lightweight porous concrete, glass spheres, and compacted clay. For intermediate saturations, their analysis and experimental data showed the potential for increased thermal conductivity due to enhanced vapor phase diffusion with increasing saturation for the lightweight concrete but not for compacted clay. The humidity ratio is defined as the ratio of the mass of water to the mass of solids, and is therefore proportional to the saturation and porosity, and inversely proportional to the specific gravity of the solids.

Moyne et al. (1990) provides an alternate method for evaluating the combined effects of tortuosity, and enhanced vapor diffusion. Figure 6-11 presents a series of gas tortuosity factors as a function of air content for comparison. Moyne et al. (1990) deduced the experimental resistance factor to gaseous diffusion from the experimental results. It should be noted that while Moyne et al. (1990) refers to a high resistance factor, a high factor is associated with increased aggregate thermal conductivity, and a low resistance to heat flow. Also, it should be noted that while other tortuosity relationships such as the Millington-Quirk relationship show an increased value when approaching a high air content, the resistance factor as deduced from Moyne et al. (1990) shows a reduction to zero at high air content. The reason for the reduction is that the experimental resistance factor also accounts for the occurrence of water vapor within the pore space while the other relationships show the relation of resistance to mass transport. At a high air content, the pore space dries out, and the Moyne et al. (1990) resistance factor goes to zero.

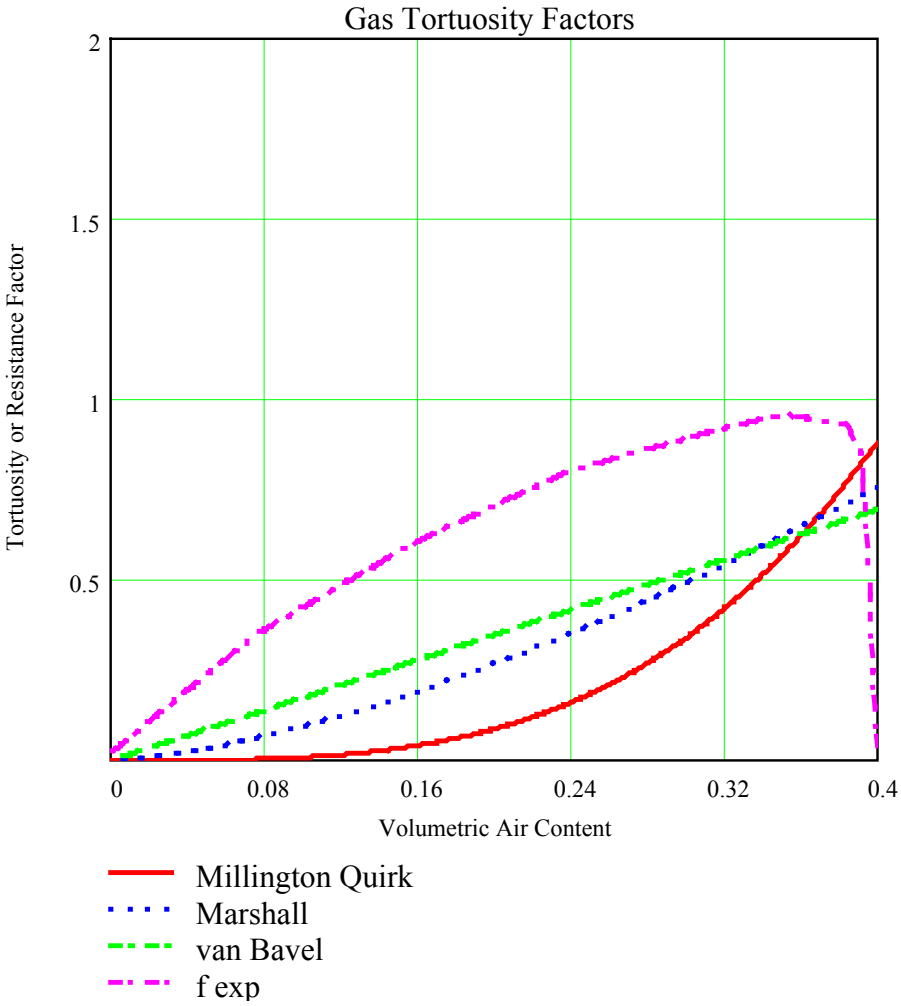

Source: Jury et al. 1991; Moyne et al. 1990

Figure 6-11. Comparison of the Experimental Resistance Factor with Other Factors

Figure 6-12 and Figure 6-13 present the experimental resistance factor and the apparent thermal conductivity for glass beads. The results show that as humidity ratio increases reflecting a decrease in air content, there is a decrease in the experimental resistance factor. This is in contrast to the factored tortuosity relationships presented above. Apparently, the experimental resistance factor for glass spheres at high air content reflects the absence of water vapor condensation/evaporation that results in a high resistance factor.

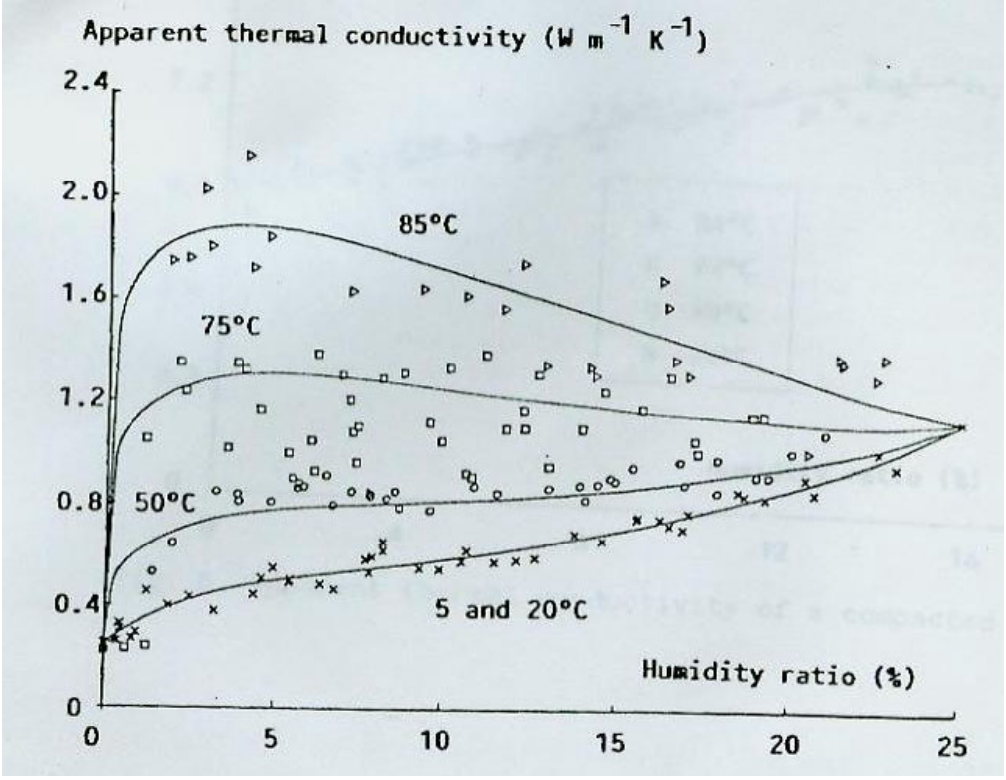

Source: Moyne et al. 1990

Figure 6-12. Apparent Thermal Conductivity for Glass Spheres

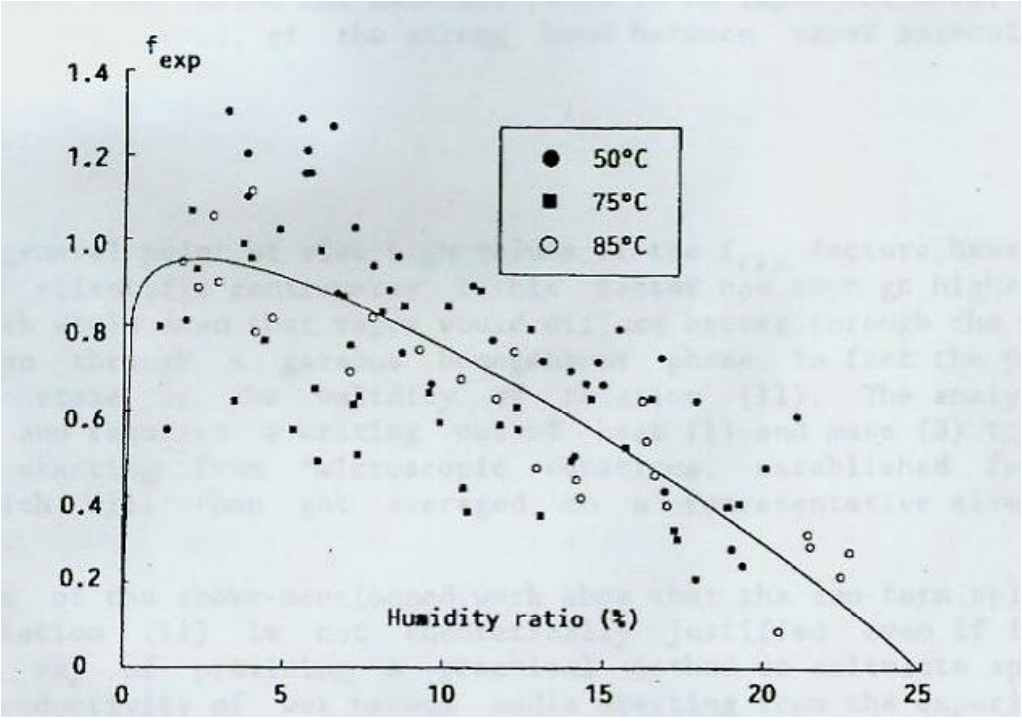

Source: Moyne et al. 1990

Figure 6-13. Experimental Resistance Factor for Glass Spheres

The aggregate thermal conductivity for the glass spheres is a function of both the humidity ratio and temperature. The results show that at the extreme of complete saturation, the voids are filled with water, and are unavailable for the diffusion of vapor. The apparent thermal conductivity equals the aggregate thermal conductivity in which the voids are saturated with water and the mineral solids. At the other extreme the porous media is devoid of water. The apparent thermal conductivity equals the aggregate thermal conductivity in which the voids are filled with air and the mineral solids. At low humidity ratios (0 to 10) and at higher temperature, the experimental results show that very high apparent thermal conductivities can occur. For the glass spheres, the measured results show apparent thermal conductivity of 2 W/m·K, which is 66% higher than the saturated thermal conductivity.

Figure 6-14 presents the apparent thermal conductivity for compacted clay. Moyne et al. (1990) describes this material as "a very highly compacted clay (calcite smectite) compacted over 2000 bars." It would be expected that this material would be highly consolidated, and the nature of the clay while exhibiting porosity might not exhibit an interconnected porosity. The experimental results show a sharp contrast to the results presented for glass spheres. The results do not show any evidence of vapor diffusion or enhanced vapor diffusion.

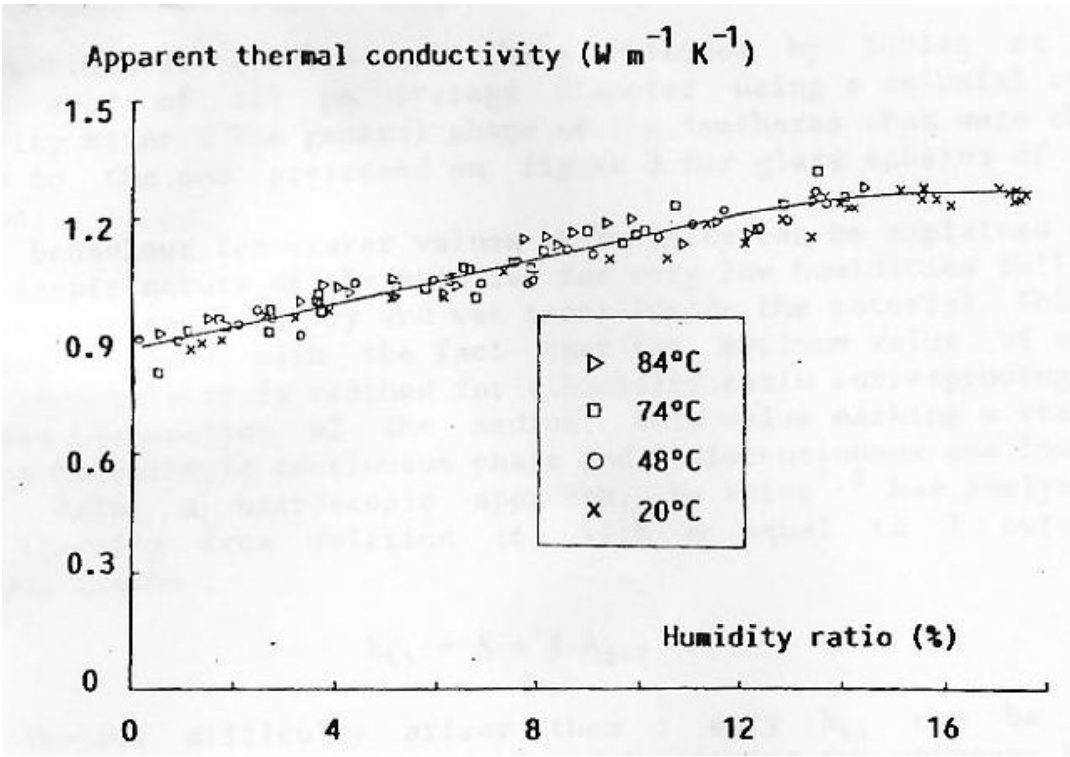

Source: Moyne et al. 1990

Figure 6-14. Experimental Resistance Factor for Glass Spheres

Moyne et al. (1990, p. 116) attributes the clay's weak thermal conductivity dependence on temperature to the strong bond between vapor molecules and the solid. However, it is also true that if the material had tortuous paths for the movement of water vapor that the effect of this resistance would reduce vapor movement and the apparent increase in aggregate thermal conductivity. It would be expected that a material exhibiting a high interconnected porosity such as glass spheres would be subject to vapor diffusion effects while a material such as a highly

compacted clay with a smaller or more poorly interconnected porosity would show no aggregate increase in thermal conductivity due to enhanced vapor diffusion.

Moyne et al. (1990, Figure 6) also present resistance factors for a lightweight concrete, and a C/SiC composite material as a function of the humidity ratio. These results show high factors for low humidity ratios. The maximum factor for light concrete (f_{exp}=0.90) is similar to the maximum ratio for glass beads. However, the maximum value is higher for C/SiC composite (f_{exp}=0.90).

6.9.3.3 Measured Results for the Tptpmn Unit

The following presents a discussion of the relationship of apparent thermal conductivity to saturation on core measurements from the large-scale Drift Scale Test.

Sandia National Laboratories conducted a laboratory investigation in which thermal conductivity as a function of saturation state for welded and nonwelded tuff specimens. Rock core samples were recovered from the repository site to determine the relationship between thermal conductivity and saturation state for both welded and nonwelded tuffs. Welded tuff from the Tptpmn unit was taken from Alcove 5 of the Exploratory Studies Facility. All thermal conductivity tests were conducted at 30°C and at intermediate moisture conditions.

The results of the laboratory investigations below a saturation of 90 percent are presented in Figure 6-19. The measured values are compared to the measurements for enhanced vapor diffusion from Moyne et al. (1990).

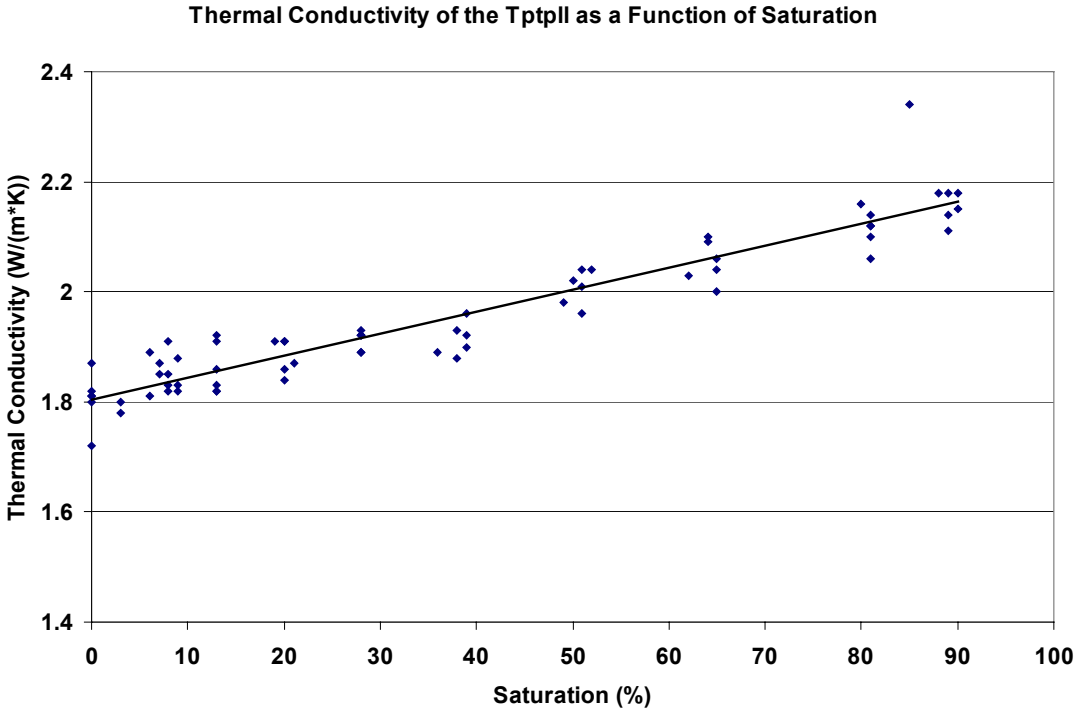

DTN: SNL22100196001.006

Figure 6-15. Rock Matrix Thermal Conductivity as a Function of Saturation

The measured results at a temperature of 30°C on the densely welded tuff recovered from core samples taken from the large scale Drift Scale Test are in general agreement and show a similar trend with the measured results for a highly compacted clay from Moyne et al. 1990. It should be emphasized that at a low temperature of 30°C, the vapor pressure of water is not very high, and the general theory presented by Moyne et al. (1990) would not predict a very large increase in aggregate thermal conductivity. Nevertheless, there is no indication of vapor diffusion or enhanced vapor diffusion when the potential uncertainty of the results is considered.

Wildenschild and Roberts (1999) performed an investigation of thermally driven water vapor diffusion in the middle nonlithophysal zone of the Topopah Spring Tuff (Tptpmn) using a transient-state thermal conductivity measurement. Thermal conductivity was measured for a single sample of welded tuff indirectly as a function of total pore pressure, temperature and water content. Enhancement of vapor diffusion in welded tuff was not observed at any of the combinations of saturation, temperature and imposed pressures. At a temperature of approximately 50°C, the aggregate rock matrix thermal conductivity increased modestly with the degree of saturation from about 1.1 W/m·K at a saturation of 0.1 to about 1.3 W/m·K at a saturation of 0.78 (Wildenschild and Roberts 1999, Figure 5). From a saturation of 0.1 to a saturation of 0.35, the thermal conductivity was approximately constant. The results showed a stronger dependence on temperature than on saturation. The guarded heat flow results are corroborative with the experimental results for a single sample of welded tuff presented by Wildenschild and Roberts (1999). Wildenschild and Roberts (1999) show that the aggregate thermal conductivity over the saturation range of from 0 percent to 78 percent was 18 percent. This increase compares well with increase of about 16 percent in Figure 6-15 over this same saturation range.

In conclusion, if the temperature range during the preclosure period is considered as being about 50°C, the results of various experimental studies on welded tuff do not show evidence of enhanced vapor diffusion that increase the aggregate thermal conductivity, and result in a reduction of ventilation efficiency.

6.10 APPLICABILITY OF THE VENTILATION EFFICIENCY AS AN ABSTRACTION METHOD

The ventilation efficiency can be expressed as a single value by integrating over both the duration of the preclosure period and the length of the drift (Equation 6-6). It may also be applied as a function of time and drift length (Equation 6-5). Downstream models that do not explicitly model the ventilation period may implement ventilation efficiency as an abstraction in one of two ways during their preclosure runs to initialize their postclosure runs.

The first way is to introduce the heat flux adjusted by the ventilation efficiency directly to the drift wall. Typically, a downstream model that uses the ventilation efficiency in this manner does not model the in-drift components. In this case, the only heat transfer mechanism being simulated is the conduction from the drift wall out to the host rock. Because the solution of the heat conduction equation is linear in nature with constant temperature heat sinks at the upper and lower boundaries of the domain, a unique solution for the temperature of the drift wall exists. Therefore, this method will result in both the same heat flux at the drift wall and the same drift

wall temperature history as that predicted by the ventilation model from which the ventilation efficiency was derived.

The second way the ventilation efficiency may be used involves downstream models that include the in-drift components in their domains. These models typically reduce the waste package heat generation rate by the ventilation efficiency and apply this new heat flux directly to the waste package rather than the drift wall. This type of application relies on both radiation and conduction heat transfer to deliver the right amount of heat to the drift wall, and replicate the drift wall temperature history as predicted by the upstream ventilation model. This approach is less straightforward than the first and requires further discussion as to its feasibility.

6.10.1 Theoretical Use of the Ventilation Efficiency at the Waste Package

Consider the case where the preclosure waste package heat output reduced by the ventilation efficiency (calculated by an upstream ventilation model) is used as a substitute for the preclosure convection to represent the preclosure heat removal by ventilation. An energy balance for the ventilation model is:

$$Q_s = Q_{conv-s} + Q_{rad} \quad \text{Eq. 6-70}$$

where

$$Q_{conv-s} = A \cdot (T_s - T) \quad \text{Eq. 6-71}$$

$$Q_{rad} = C \cdot (T_s^4 - T_w^4) \quad \text{Eq. 6-72}$$

The fraction of heat removed by the ventilation (i.e., by convection) is:

$$\eta = \frac{Q_{conv-s} + Q_{conv-w}}{Q_s} \quad \text{Eq. 6-73}$$

where

$$Q_{conv-w} = B \cdot (T_w - T) \quad \text{Eq. 6-74}$$

The constants *A*, *B*, and *C* are defined as:

$$A = d_s \cdot h_s \quad \text{Eq. 6-75}$$

$$B = d_w \cdot h_w \quad \text{Eq. 6-76}$$

$$C = d_s \cdot h_{rad} \quad \text{Eq. 6-77}$$

Substituting Equations 6-71 and 6-72 into Equation 6-70 yields:

$$Q_s = A \cdot (T_s - T) + C(T_s^4 - T_w^4) \quad \text{Eq. 6-78}$$

Substituting Equations 6-71, 6-74, and 6-78 into Equation 6-73 yields:

$$\eta = \left[\frac{\left[A \cdot \left(T_s - T \right) + B \cdot \left(T_w - T \right) \right]}{\left[A \cdot \left(T_s - T \right) + C \cdot \left(T_s^4 - T_w^4 \right) \right]} \right] \quad \text{Eq. 6-79}$$

For the downstream model, the waste package heat output is multiplied by the ventilation efficiency to account for the heat removed during the preclosure ventilation period. Equation 6-80 represents the fraction of heat delivered to the drift wall:

$$Q_w' \equiv Q_s \cdot \left(1 - \eta \right) \quad \text{Eq. 6-80}$$

Substituting Equations 6-78 and 6-79 into Equation 6-80 yields:

$$Q_w' = \left[A \cdot \left(T_s - T \right) + C \cdot \left(T_s^4 - T_w^4 \right) \right] \cdot \left[1 - \frac{\left[A \cdot \left(T_s - T \right) + B \cdot \left(T_w - T \right) \right]}{\left[A \cdot \left(T_s - T \right) + C \cdot \left(T_s^4 - T_w^4 \right) \right]} \right] \quad \text{Eq. 6-81}$$

An energy balance for the downstream model considered in this case (i.e., where the ventilation efficiency is used as substitute for the heat transfer via convection) is:

$$Q_w' = Q_{rad}' \quad \text{Eq. 6-82}$$

where

$$Q_{rad}' = C \cdot \left(T_s'^4 - T_w'^4 \right) \quad \text{Eq. 6-83}$$

where

T_s' = waste package temperature of the downstream model (K)

T_w' = drift wall temperature of the downstream model (K)

Substituting Equations 6-81 and 6-83 into Equation 6-82 and simplifying yields:

$$\left(T_s'^4 - T_w'^4 \right) = \left(T_s^4 - T_w^4 \right) - \frac{B}{C} \cdot \left(T_w - T \right) \quad \text{Eq. 6-84}$$

If $T_s' = T_s$ and $T_w' = T_w$ are to be true, then the term $\frac{B}{C} \cdot \left(T_w - T \right)$ must be zero. For this to be true either the coefficient B must be zero, and/or the terms T_w and T must be equal. The implication for either of these conditions is that there is no convective heat transfer between the drift wall and the drift air, which of course is not true. Therefore, a downstream application in which the ventilation efficiency is used as a substitute for the convective heat transfer to simulate the preclosure heat removal by ventilation cannot accurately represent both the preclosure waste package and drift wall temperatures as calculated by the ventilation model.

However, if the use of the ventilation efficiency in the downstream model is to simply initialize the drift wall temperature such that $T_w' = T_w$, then T_s' can be numerically forced to be:

$$T_s' = \sqrt[4]{\left(T_s^4 - T_w^4\right) - \frac{B}{C}\cdot\left(T_w - T\right) + T_w'^4} \qquad \text{Eq. 6-85}$$

6.10.2 Numerical Example Using the Ventilation Efficiency as an Abstraction Method

Two numerical examples that apply the theoretical use of the ventilation efficiency as described in Section 6.10.1 are presented below in Sections 6.10.2.3 and 6.10.2.4. Beforehand, total energy balances are presented using the results of the ANSYS-LA-Coarse model and Equation 6-5 for calculating the instantaneous heat removal efficiency as a function of time and drift length, and Equation 6-6 for calculating an integrated heat removal efficiency.

6.10.2.1 Using Equation 6-5 to Calculate the Heat Removal Efficiency as a Function of Time and Drift Length

Using the results of the ANSYS-LA-Coarse model and Equation 6-5 to calculate the heat removal efficiency as a function of both time and drift length, the total energy delivered to the host rock over the 50-year preclosure period and a 600 meter long drift becomes:

$$Energy_{rock-total} = \int_0^{600m}\int_0^{50yr} Q_s(t)\cdot\left(1-\eta(t,x)\right)\cdot dt\cdot dx \qquad \text{Eq. 6-86}$$

where

$Energy_{rock\text{-}total}$ = total energy to the host rock (J)
$Q_s(t)$ = waste package lineal heat decay as a function of time (W/m)
$\eta(t,x)$ = instantaneous ventilation heat removal efficiency at some time, t, and some distance from the drift entrance, x, (dimensionless)

Using the heat decay from Table 4-20, and the heat removal efficiencies calculated as a function of time and drift length for the ANSYS-LA-Coarse model (DTN: MO0306MWDASLCV.001), the total energy delivered to the host rock over 50 years and 600 meters is $1.01\cdot10^{14}$ J (DTN: MO0306MWDASLCV.001).

6.10.2.2 Using Equation 6-6 to Calculate an Integrated Ventilation Heat Removal Efficiency

Finally, using the results of the ANSYS-LA-Coarse model and Equation 6-6 to calculate an integrated ventilation heat removal efficiency, the total energy to the system over the 50-year preclosure period and 600 meter long drift becomes:

$$Energy_{total} = 600m\cdot\int_0^{50yr} Q_s(t)\cdot\left(1-\eta_{integrated}\right)\cdot dt \qquad \text{Eq. 6-87}$$

where

$\eta_{integrated}$ = integrated ventilation heat removal efficiency given by Eq. 6-6 (dimensionless)

Using the heat decay from Table 4-20 and the integrated ventilation efficiency of 88.3% reported in Table 6-7 for the ANSYS-LA-Coarse model, the total energy to the system over 50 years and 600 meters is $1.01 \cdot 10^{14}$ J (DTN: MO0306MWDASLCV.001). This result balances with the energy calculated in Section 6.10.2.1.

6.10.2.3 Numerical Example of Using the Ventilation Efficiency as Function of Time and Drift Length

A numerical example of the theoretical use of the ventilation efficiency as described above in Section 6.10.1 is presented below. The example uses the ventilation efficiency as function of time and drift length, as calculated by the ANSYS-Coarse-LA ventilation model, to reduce the waste package heat generation rate in a radiation and conduction only based ANSYS model, called ANSYS-LA-Coarse-Instantaneous-Efficiency. The results are depicted in Figure 6-16.

This example illustrates the conclusion reached in Section 6.10.1 that it is numerically impossible to use the ventilation efficiency as substitute for the heat removed by convection and predict the same waste package and drift wall temperatures as those from which the ventilation efficiency came. This example also illustrates the numerical difficulty in solving the non-linear radiation heat transfer. Because the radiation involves the difference in temperatures to the fourth power, a unique solution depends upon the energy balance between the other heat transfer mechanisms. However, the constant temperatures imposed at the ground surface and the water table are far enough away from the repository horizon that they act as semi-infinite boundaries, leaving the numerical solution somewhat unbounded. The results of this example clearly illustrates this, as the temperatures of the waste package and drift wall for the model that used the ventilation efficiency are different than the original temperatures.

6.10.2.4 Numerical Example of Using T'_{wp} as Function of Time and Drift Length Calculated From Equation 6-85

This example uses Equation 6-85 to constrain the waste package temperature over time and drift length. The derivation of Equation 6-85 takes into account the reduction of the waste package power by the ventilation efficiency from Equation 6-80; however, in this case a temperature boundary condition is assigned to the waste package surface rather than inputting the adjusted heat flux. The energy radiated to the drift wall is the same as in the example presented in Section 6.10.2.3. However, for this application, a numerical solver is able to calculate the right temperature history of the drift wall as shown in Figure 6-17. This model is called ANSYS-LA-Coarse-Instantaneous-Twp-Efficiency.

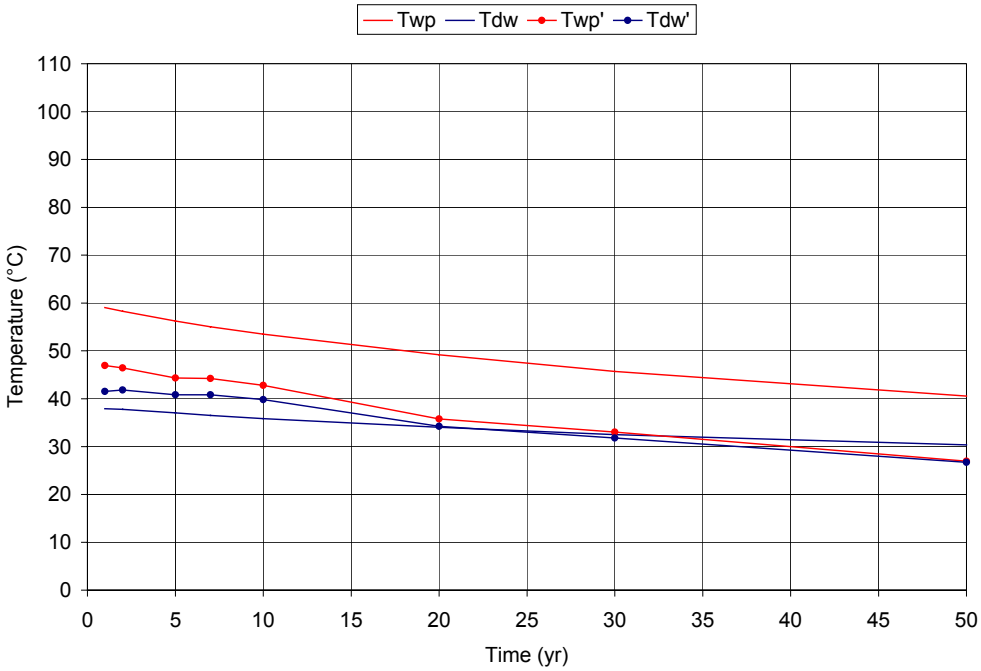

(a) 100 meters

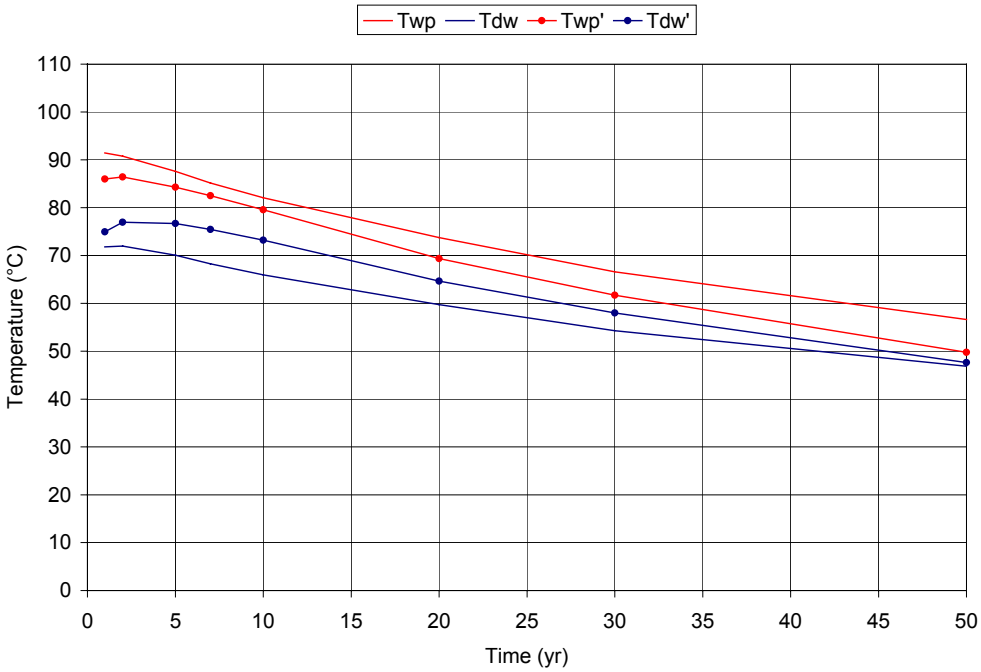

(b) 600 meters

DTN: MO0306MWDCIEAP.000

Figure 6-16. Application of the Ventilation Efficiency as a Function of Time and Drift Length to Reduce the Waste Package Heat Decay, Adjusted Heat Load Applied at the Waste Package Surface with Temperature Results Shown for 100 m and 600 m from the Drift Entrance

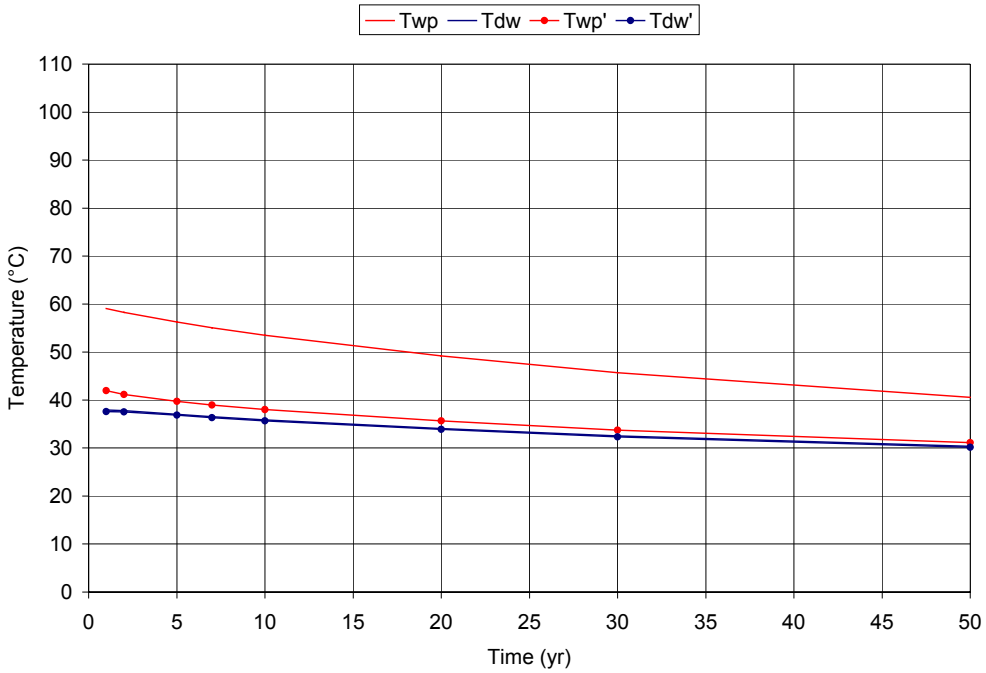

(a) 100 meters

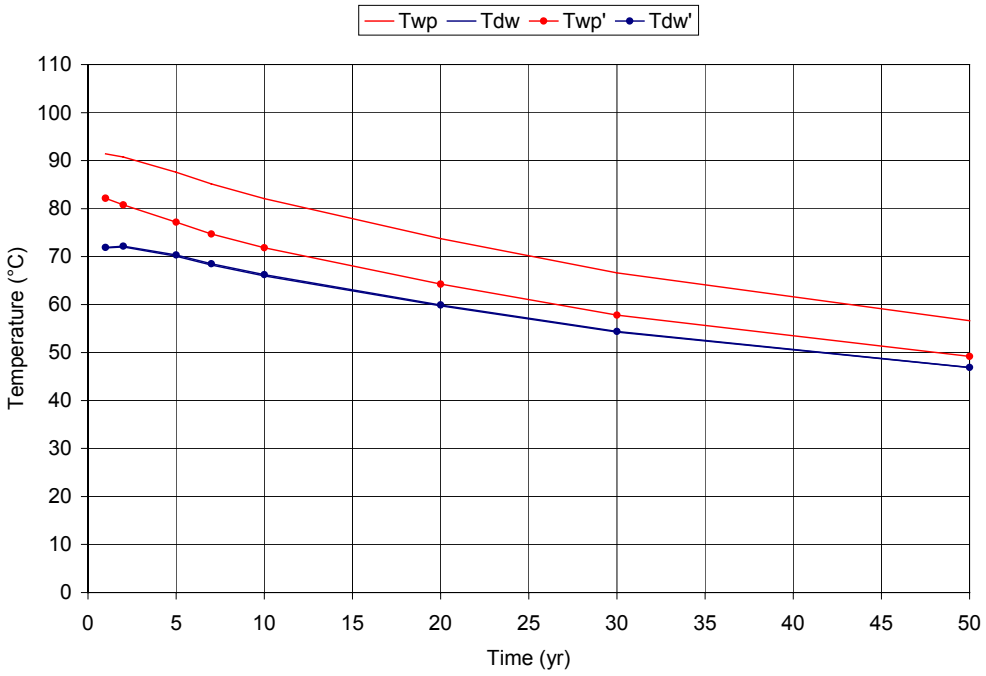

(b) 600 meters

DTN: MO0306MWDCIETA.000

Figure 6-17. Application of the Ventilation Efficiency as a Function of Time and Drift Length to Reduce the Waste Package Heat Decay, Adjusted Waste Package Temperature Calculated from Eq. 6-85 and Applied at the Waste Package Surface with Temperature Results Shown for 100 m and 600 m from the Drift Entrance

6.11 SENSITIVITY OF THE VENTILATION EFFICIENCY TO UNCERTAINTIES IN KEY INPUTS AND DESIGN PARAMETERS

The sensitivity of the ventilation efficiency to uncertainties in key inputs and design parameters was investigated using the Delta Method, also referred to as the "generation of system moments" or "statistical error propagation." The Delta Method involves calculating the mean system performance, in this case the integrated ventilation efficiency, and its standard deviation using the means and variances of the component variables which make up the system. Equations 6-88 and 6-89 describe the Delta Method mathematically (Hahn and Shapiro 1967, pp. 228 to 231). Equation 6-90 describes the standard deviation based on the variance (Hahn and Shapiro 1967, pp. 228 to 231).

$$E(z) = h[E(x_1), E(x_2), ..., E(x_n)] + \frac{1}{2}\sum_{i=1}^{n} \frac{\partial^2 \overline{h}}{\partial x_i^2} Var(x_i) \qquad \text{Eq. 6-88}$$

$$Var(z) = \sum_{i=1}^{n} \left(\frac{\partial h}{\partial x_i} \right)^2 Var(x_i) \qquad \text{Eq. 6-89}$$

$$Var(x_i) = [\sigma(x_i)]^2 \qquad \text{Eq. 6-90}$$

where

$E(z)$ = mean system performance
$E(x_{1, 2, ..., n})$ = mean of the xth component variable
h = function that describes the system performance based on the components variable (set of equations from Section 6.4.2 describing the ventilation model)
$Var(x_{1, 2, ...n})$ = variance of the xth component variable
$Var(z)$ = variance of the system performance
$\sigma(x_i)$ = standard deviation of the xth component variable

When the system performance is a linear function of the component variables, the second and higher order partial derivatives are zero. In other words, the second term of Equation 6-88 goes to zero and the mean system performance can be calculated using only the means of the component variables.

In terms of the ventilation model, *E(z)* represents the mean integrated ventilation efficiency where $h[E(x_1), E(x_2),\ldots, E(x_n)]$ represents the equations of Section 6.4.2 used to perform the algebraic ventilation calculation, and $E(x_1, _2, \ldots, _n)$ represents the mean values of the inputs and design parameters. $Var(x_1, _2, \ldots, _n)$ then represents the variances of the inputs and design parameters. $h[E(x_1), E(x_2),\ldots, E(x_n)]$ is evaluated using the analytical method. The variance or standard deviation of the integrated efficiency is calculated using Equation 6-89 which propagates the uncertainties in select inputs and design parameters (expressed by variances or standard deviations).

Table 6-9 shows the key inputs and design parameters selected for the Delta Method, along with their respective standard deviations. Where available, standard deviations were assigned from

DTNs. Where unknown, standard deviations using normal distributions were determined based on engineering judgement. Rationale for determining these standard deviations is documented in Table 6-9. Attachment IV documents that the integrated ventilation efficiency is generally a linear function of each of the selected inputs and design parameters contained in Table 6-9, and hence the mean integrated ventilation efficiency can be calculated by ignoring the second term of Equation 6-88.

Table 6-9. Inputs and Design Parameters, and Their Respective Standard Deviations, Selected for the Delta Method to Assess the Sensitivity of the Integrated Ventilation Efficiency

Input/Design Parameter	Mean Value	Source	Standard Deviation	Rationale for Determining Standard Deviation
Dry Bulk Thermal Conductivity (W/m·K)	1.2784	Table 4-13 for Tptpll (tsw35)	0.2511	Table 4-13 for Tptpll (tsw35)
Wet Bulk Thermal Conductivity (W/m·K)	1.8895	Table 4-13 for Tptpll (tsw35)	0.2484	Table 4-13 for Tptpll (tsw35)
Grain Density (kg/m^3)	2593	Attachment II for tsw35 (column K)	138	Table 4-13 for Tptpll (tsw35) dry bulk density
Solids Specific Heat (J/kg·K)	930	Table 4-14 for Tptpll (tsw35)	170	Table 4-14 for Tptpll (tsw35)
Matrix Porosity	14.86%	Table 4-13 for Tptpll (tsw35)	3.4%	Table 4-13 for Tptpll (tsw35)
Matrix Saturation	90.5%	Section 5.3	10%	Saturation cannot exceed 100%
Lithophysal Porosity	8.83%	Table 4-13 for Tptpll (tsw35)	5.4%	Table 4-13 for Tptpll (tsw35)
Drift Diameter (m)	5.5	Table 4-23	0.5	Engineering judgement
Waste Package Diameter (m)	1.644	Table 4-22	0.5	Cover range of waste packages from 24-BWR to DHLW
Inlet Air Temperature (°C)	22.82	Section 6.5.6	5	Engineering judgement
Air Flow Rate (m^3/s)	15	Table 4-23	2	Engineering judgement
Drift Wall Emissivity	0.9	Table 4-15 for Tptpll	0.1	Emissivity cannot exceed 1.0
Waste Package Emissivity	0.87	Table 4-22	0.13	Emissivity cannot exceed 1.0
Inner Convection Heat Transfer Coefficient ($W/m^2 \cdot K$)	4.23	DTN: MO0307MWDAC8MV.000 (Analytical) (average of hs for all time steps and CSTRs in worksheet *CSTR Analysis*)	0.63	25% of the Mean (Attachment IX)
Outer Convection Heat Transfer Coefficient ($W/m^2 \cdot K$)	3.87	DTN: MO0307MWDAC8MV.000 (Analytical) (average of hw for all time steps and CSTRs in worksheet *CSTR Analysis*)	0.58	15% of the Mean (Attachment IX)

Using the mean values for the inputs and design parameters listed in Table 6-9, the mean integrated ventilation efficiency is 88.0% for a 600 meter long drift, and 86% for an 800 meter long drift. By employing the Delta Method to propagate the standard deviations of the inputs and design parameters listed in Table 6-9 through the analysis, the standard deviation (normally distributed) of the integrated ventilation efficiency about the mean of 88.0% is 2.6% for the 600 meter long drift, and 2.7% about the mean of 86% for the 800 meter long drift. Expressed in

terms of the normal distribution, the integrated ventilation efficiency for the 600 meter long drift will be between approximately 85% and 91%, 68% of the time; between 83% and 93%, 96% of the time; and between 80% and 96%, 99% of the time (Hahn and Shapiro 1967). The documentation of this analysis is in Attachment VII.

Table 6-10 summarizes the first step of the Delta Method, which is to calculate the mean system performance (ventilation efficiency) using the means of the system components (input/design parameters) from Equation 6-88. Then, independently and one at a time, each system component mean is replaced by its mean plus/minus a standard deviation, and a new system performance is calculated using Equation 6-88. The standard deviation of the ventilation efficiency is calculated using the 5th and 7th columns of Table 6-10 and Equations 6-89 and 6-90.

Table 6-10. Using the Delta Method to Determine the Sensitivity of the Ventilation Efficiency Due to Uncertainties in Key Inputs and Design Parameters for a 600-meter Long Drift

Input/Design Parameter	Mean	Efficiency (Eq. 6-88)	Mean + Standard Deviation	Efficiency (Eq. 6-88, substituting the mean of the x^{th} component variable for the mean + standard deviation)	Mean - Standard Deviation	Efficiency (Eq. 6-88, substituting the mean of the x^{th} component variable for the mean - standard deviation)
Dry Bulk Thermal Conductivity (W/m·K)	1.2784	88.0%	1.5295	87.88%	1.0273	88.06%
Wet Bulk Thermal Conductivity (W/m·K)	1.8895		2.1379	87.12%	1.6411	88.87%
Grain Density (kg/m^3)	2593		2731	87.88%	2455	88.06%
Solids Specific Heat (J/kg·K)	930		1100	87.68%	760	88.31%
Matrix Porosity	14.86%		18.26	87.93%	11.46	88.01%
Matrix Saturation	90.5%		100	87.70%	81.084	88.24%
Lithophysal Porosity	8.83%		14.23	88.10%	3.43	87.85%
Drift Diameter (m)	5.5		6	87.86%	5	88.07%
Waste Package Diameter (m)	1.644		2.144	88.11%	1.144	87.80%
Inlet Air Temperature (°C)	22.82		27.82	85.82%	17.82	90.12%
Air Flow Rate (m^3/s)	15		17	88.81%	13	86.89%
Drift Wall Emissivity	0.9		1	87.94%	0.8	88.00%
Waste Package Emissivity	0.87		1	87.85%	0.74	88.12%
Inner Convection Heat Transfer Coefficient (W/m^2·K)	4.23		4.86	88.17%	0.6333	87.74%
Outer Convection Heat Transfer Coefficient (W/m^2·K)	3.87		4.45	88.24%	0.5799	87.63%

NOTES [a] DTN: MO0306MWDLACVD.000

In addition, the influence of each of the standard deviations of the inputs and design parameters on the mean integrated ventilation efficiency was determined. Their individual influence on the

standard deviation of the integrated efficiency was also determined. These influences are plotted against each other in Figure 6-18. All values of influence for the respective axes of the plot were normalized by dividing by the largest corresponding value. The purpose of Figure 6-18 is to give a qualitative assessment of which inputs and design parameters are most significant (and those that are not significant) in the ventilation model. The significance is determined by the variable's influence, relative to other variables, on both the mean integrated ventilation efficiency and its standard deviation. Figure 6-18 shows that the most significant variables in the ventilation model are the inlet air temperature, the air flow rate, the host rock thermal conductivity (as a function of matrix saturation and specific heat), and the convection heat transfer coefficients.

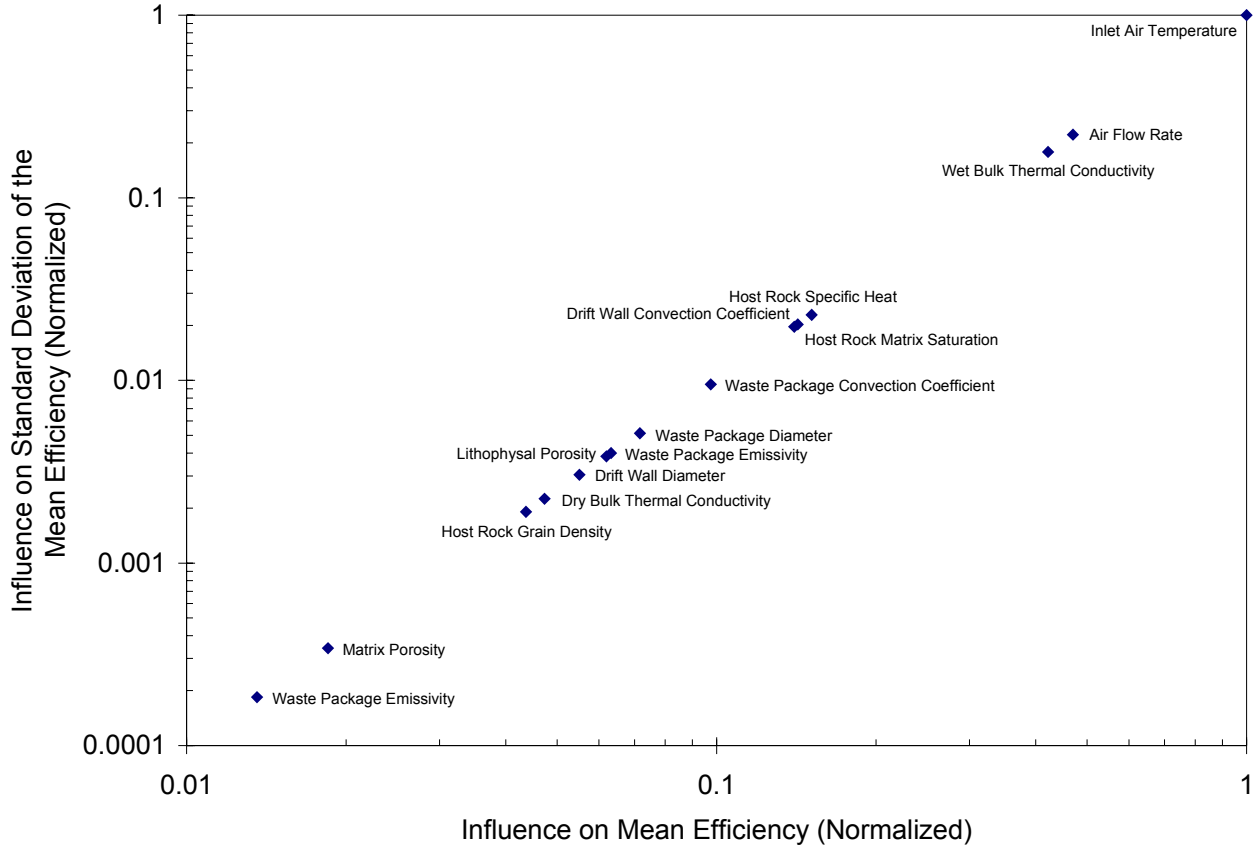

DTN: MO0306MWDLACVD.000

Figure 6-18. Qualitative Plot Showing the Influence of Ventilation Model Inputs and Design Parameters on the Mean Integrated Ventilation Efficiency and Its Standard Deviation

7. VALIDATION

This section presents the results of model validation exercises. *Technical Work Plan for: Engineered Barrier System Department Modeling and Testing FY03 Work Activities* (BSC 2003a) determined the level of validation to be low for the Ventilation Model based on the following:

1. It is not extrapolated over large distances, spaces, or time frames.

2. It has nominal uncertainties in pertinent input parameters such as surface emissivities, convection heat and mass transfer coefficients, and rock mass thermal conductivity.

3. It is not used to demonstrate compliance or licensing positions.

4. Its output will not have significant impacts on TSPA dose calculations results.

The approach for validating the conceptual model for preclosure ventilation involves an inspection of the processes 1 through 4, as outlined in Section 6.3.1 in terms of their applicability to adequately simulate the heat transfer in and around a ventilated emplacement drift. These processes and the methods to validate them are outlined in Table 7-1.

Table 7-1. Validation Methods

Conceptual Model Process	Validation Method	Pertinent Input Parameter	Criteria used to Determine Validation	Section
Thermal radiation heat transfer between the surfaces of the waste package and the drift wall using the Stefan-Boltzmann Law	Corroboration with published literature	Surface Emissivity	Engineering Judgement	7.1.1
Convection heat transfer to the ventilation airstream off the waste package and drift wall surfaces by use of convection heat transfer coefficients	Corroboration of post-test analyses with acquired testing results from the quarter-scale ventilation tests conducted at the Atlas Facility	Heat Transfer Coefficient	Match the model results to the test data within ±5°C using a reasonable range of heat transfer coefficients	7.1.2
Conduction dominated heat transfer within the rock mass surrounding the emplacement drift using Fourier's Law	Corroboration with published results from the Drift Scale Test	Rock Thermal Conductivity	Engineering Judgement	7.1.4

If these processes can be validated for a range of pertinent input parameters (i.e., surface emissivity, convection coefficient, and host rock thermal conductivity), then any numerical application of the conceptual model that uses the input parameters appropriately need only satisfy the conservation of energy and mass to be of use.

7.1 VALIDATION OF THE HEAT TRANSFER PROCESSES OF THE VENTILATION CONCEPTUAL MODEL

The following sections provide the validation exercises for the heat transfer processes outlined above in Table 7-1.

7.1.1 Validation of the Radiation Heat Transfer Model

The use of the Stefan-Boltzmann Law to calculate the radiative heat transfer between two surfaces is an accepted approach within the scientific and engineering community. The valid use

of the Stefan-Boltzmann Law to calculate the radiative heat transfer between the surface of an eccentrically located waste package and the drift wall requires the following:

1. An assumption that the in-drift air does not participate in the radiation heat transfer by absorbing significant amounts of energy that would have been otherwise transferred to the drift wall.

2. Appropriate values for the emissivities of the waste package and drift wall surfaces.

7.1.1.1 Thermal Radiation to a Participating Gas

For enclosures such as an emplacement drift, a medium such as air that separates the radiating surfaces is said to be nonparticipating if it neither absorbs nor scatters the thermal radiation, and it emits no radiation itself. Incropera and DeWitt (1996, Section 13.5) state that:

> The foregoing conditions and the related equations [summarized in Section 6.3.4 of this report] may often be used to obtain reliable first estimates and, in most cases, highly accurate results for radiation heat transfer in an enclosure…For *nonpolar* gases, such as O_2 or N_2, such neglect [of participating gaseous radiation] is justified, since the gases do not emit radiation and are essentially transparent to the incident thermal radiation. However, the same may not be said for polar molecules, such as CO_2, H_2O (vapor), NH_3, and hydrocarbon gases, which emit and absorb over a wide temperature range (italics added).

The design of the preclosure ventilation system draws air from the outside environment to the intake shafts and then to the emplacement drifts. The initial composition of the ventilation airstream will resemble that of the outside air, or approximately 78% N_2 and 22% O_2 with some small fraction of water vapor. The composition of the ventilation airstream may change as it proceeds through the emplacement drift and acquires additional water vapor and CO_2 from the host rock. However, the range of relative humidities observed in the Exploratory Studies Facility, 10 to 40% (Section 4.1.1.3), shows that the ventilation airstream does not acquire enough water vapor to make any significant impact on the thermal radiation heat transfer.

7.1.1.2 Validation Criteria Met for the Radiation Heat Transfer Model

Engineering judgement dictates the use of the Stefan-Boltzmann Law to model radiation heat transfer within waste emplacement drifts. This is corroborated by its use in the engineering community outside of the Yucca Mountain Project. Further bounding calculations, and where available analysis of exhaust air from the Exploratory Studies Facility, may be needed to further validate the argument that the in-drift air does not offer any significant participation in the radiation heat transfer between the waste package and drift wall during the ventilation period. However, for the level of confidence required for the Ventilation Model, this validation criteria is met.

7.1.2 Validation of the Convection Heat Transfer Model

The validation of the convection heat transfer model used in the Ventilation Conceptual Model hinges upon the appropriate use of convective heat transfer coefficients. Phases 1 and 2 of the

one-quarter scale ventilation tests performed at the North Las Vegas Atlas Facility during 2001 and 2002 provide valuable data for determining a range of valid convection heat transfer coefficients. A detailed description of the ventilation tests is provided in the Phase 1 report (BSC 2003f).

The ventilation test train was constructed by connecting segments of concrete pipes. Twenty-five simulated waste packages were fabricated from steel pipe. A steel structure designed to simulate current waste package support was used to support the simulated waste packages. Crushed tuff from the Yucca Mountain muck pile was used as the invert ballast material. Electric heaters within the waste packages simulated the decay heat (BSC 2003f, Section 2.2.2). The test configuration is described in the test report (BSC 2003f, Sections 2.2.2.1 and 2.2.2.2). The test setup was nominally ¼ scale of the repository.

The tests were conducted in two phases. The primary difference between phases 1 and 2 is that the ventilation air in Phase 2 was conditioned to better control its inlet temperature and relative humidity. The Phase 1 test brought in ambient air from outside the test train that exhibited diurnal temperature changes of around 4°C. The same ventilation air flow rates and linear heat loads were used for both phases. Considering these aspects, that the ANSYS methodology for simulating ventilation does not account for the relative humidity of the in-drift air, and that the results of Section 6.9 show that the moisture has no significant impact on the ventilation, the Phase 1 test data are sufficient to provide the level of validation required for the ANSYS model. Therefore, the use of the ventilation test data for post-test ANSYS modeling and validation for this revision of the Ventilation Model Report is confined to the Phase 1 cases. It is not anticipated that post-test modeling of the Phase 2 ventilation test cases will provide any higher level of confidence in the validation process. Table 7-2 lists the Phase 1 ventilation tests and cases for which ANSYS post-test modeling was performed.

Table 7-2. Ventilation Phase 1 Test Matrix

Case No.	Nominal Flow (m^3/s)	Nominal Power (kW/m)
1	1	0.36
2	2	0.36
3	0.5	0.36
4	1	0.18
5	0.5	0.18

Source: BSC 2003f, Table 3-1

7.1.3 Post-Test ANSYS Model

Figure 7-1 shows the saddle-like temperature trends for the waste package of Case 4 of Ventilation Test Phase 1. The same trend is observed in all the other cases. The temperature peaks that occur around Station 3 are due to heat losses at the inlet and outlet of the test train. However, the ANSYS methodology outlined in Section 6.4.1 is not capable of modeling the profile of axial temperature exhibited by the test data. An underlying assumption of the ANSYS methodology is that temperatures of the in-drift components, drift wall, and ventilation air are always increasing as the calculation proceeds down the length of the drift. This limitation forced

the development of a two-dimensional ANSYS-based ventilation model. In other words, only a two-dimensional cross-section at Station 3 was modeled using ANSYS, rather than the ANSYS/Excel methodology described in Section 6.4.1 for a pseudo-three-dimensional analysis from Station 1 to Station 5.

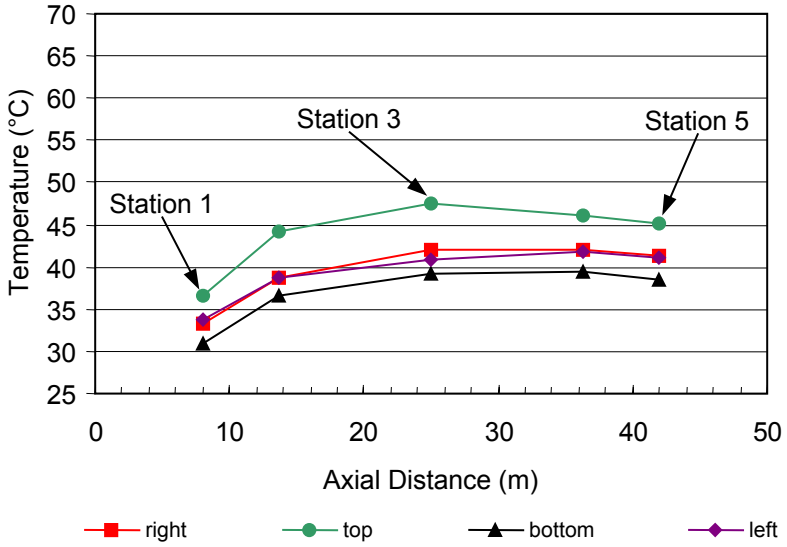

Source: BSC 2003f, Figure 7-5

Figure 7-1. Ventilation Phase 1, Case 4 Waste Package Temperatures versus Axial Distance Down the Test Train for Data Recorded 10/15/00

7.1.3.1 Mesh

Figure 7-2 shows a detailed drawing through a cross-section of the test train. It also includes the relative locations of the instrumentation. Figure 7-3 shows the discretization of the test domain or the computational mesh used for the ANSYS post-test modeling. The pallet that supports the simulated waste package is not continuous in the test configuration. Rather, it supports only the ends of the package. The contribution of heat transfer via conduction from the package through the pallet, and into the invert is considered to be negligible in comparison to the amount of heat transferred by radiation. For this reason, the pallet was not modeled.

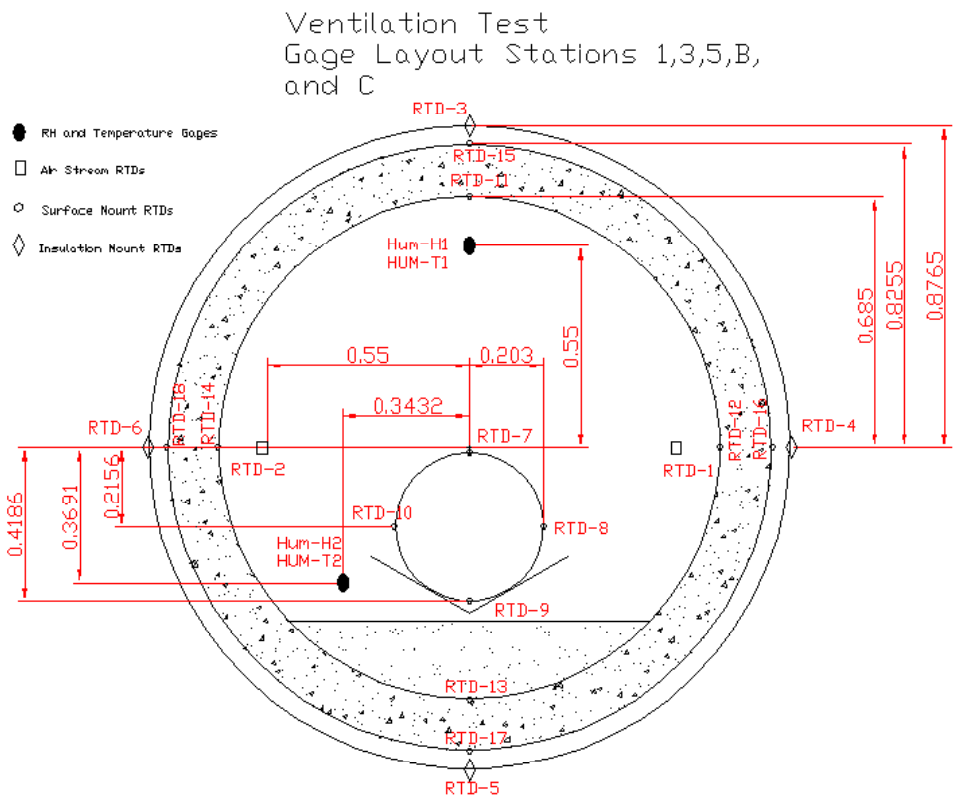

Source: CRWMS M&O 2000a

NOTE: All dimensions are in meters.

Figure 7-2. Cross-Sectional View of the Ventilation Test Train

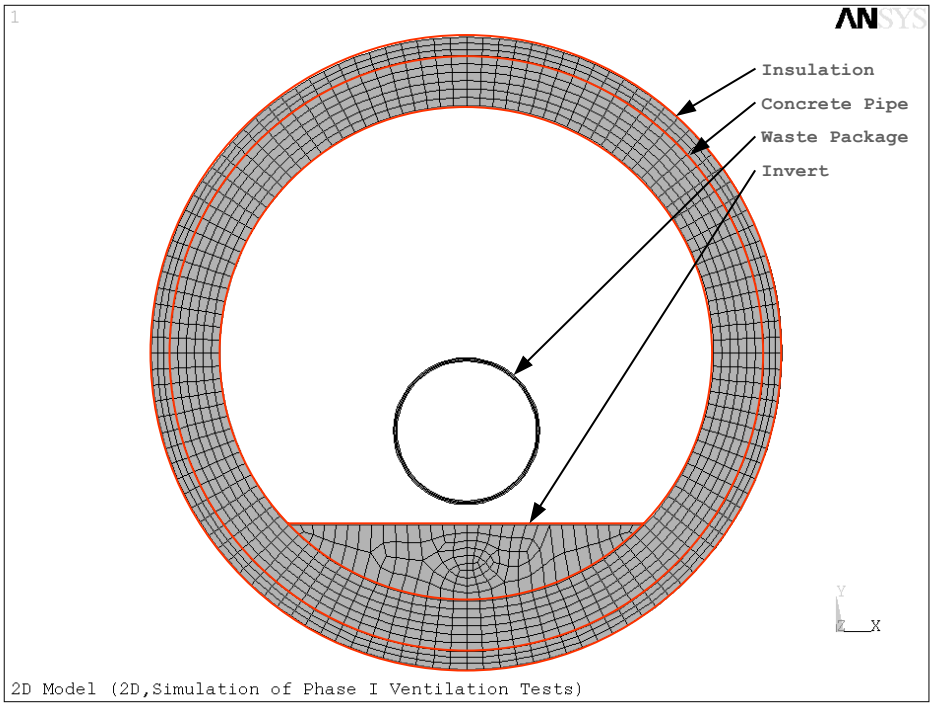

Figure 7-3. ANSYS Mesh

7.1.3.2 Developed Inputs

Table 7-3 lists the average thermophysical properties of the invert ballast material taken from Tables 4-7 and 4-9.

Table 7-3. Average Thermophysical Properties of the Invert

Specific Heat		Thermal Conductivity		Thermal Diffusivity	Bulk Density	
$(J/cm^3 \cdot °C)^1$	$(J/kg \cdot K)^2$	$(W/m \cdot °C)^3$	$(W/m \cdot K)^4$	$(mm^2/s)^5$	$(g/cm^3)^6$	$(kg/m^3)^7$
0.94	1112.37	0.15	0.15	0.16	1.178	1178

NOTES
[1] Average of Table 4-7 for Specific Heat
[2] Convert [1] from $J/cm^3 \cdot °C$ to $J/kg \cdot K$ using the Bulk Density [6]
[3] Average of Table 4-7 for Thermal Conductivity
[4] Convert [3] from °C to K
[5] Average of Table 4-7 for Thermal Diffusivity
[6] Average of Table 4-7 for Bulk Density
[7] Convert [6] from g/cm^3 to kg/m^3

7.1.3.3 Boundary Conditions

The recorded temperatures on the outer insulation at Station 3 of the test train were used as the outer boundary conditions for the ANSYS post-test models. Each test case had a different set of recorded temperatures over its life span. Due the difficulty in maintaining constant ambient conditions in the high-bay of the facility, a data fit for each case was performed on the outer insulation temperature histories to aid in the implementation of this boundary condition. Figure 7-4 shows the outer insulation temperature histories and the data fits for the cases modeled.

The ANSYS methodology requires that an inlet ventilation air stream temperature be specified. Therefore, the temperatures of the ventilation air stream recorded at Station 3 were used as input to the ANSYS post-test models. Each test case had a different set of air stream temperature histories. Again, a data fit for each case was performed on the recorded temperature data to simplify its implementation into the models. Figure 7-5 shows the ventilation air stream temperature histories and the data fits for the cases modeled.

The simulated waste packages were hollow rolled steel tubes, with heater rods suspended concentrically inside. Due to the nature of the experimental set-up, natural convection cells developed within the placid annulus of the waste packages. This caused a non-uniform heat flux, and hence temperature distribution, around the circumference of the waste package. No temperature measurements were recorded inside the waste package (i.e., the annulus air or the rod-heater). Rather than model the complexity of the natural convection inside of the waste package, the ANSYS model supplied a heat flux at the waste package wall. The heat flux was partitioned around the waste package circumference using the recorded steady-state temperature distributions as a basis. Table 7-4 summarizes the distributions for the test cases listed in Table 7-2. The validity of this partitioning methodology is confirmed by the consistency of the calculated distributions from case to case.

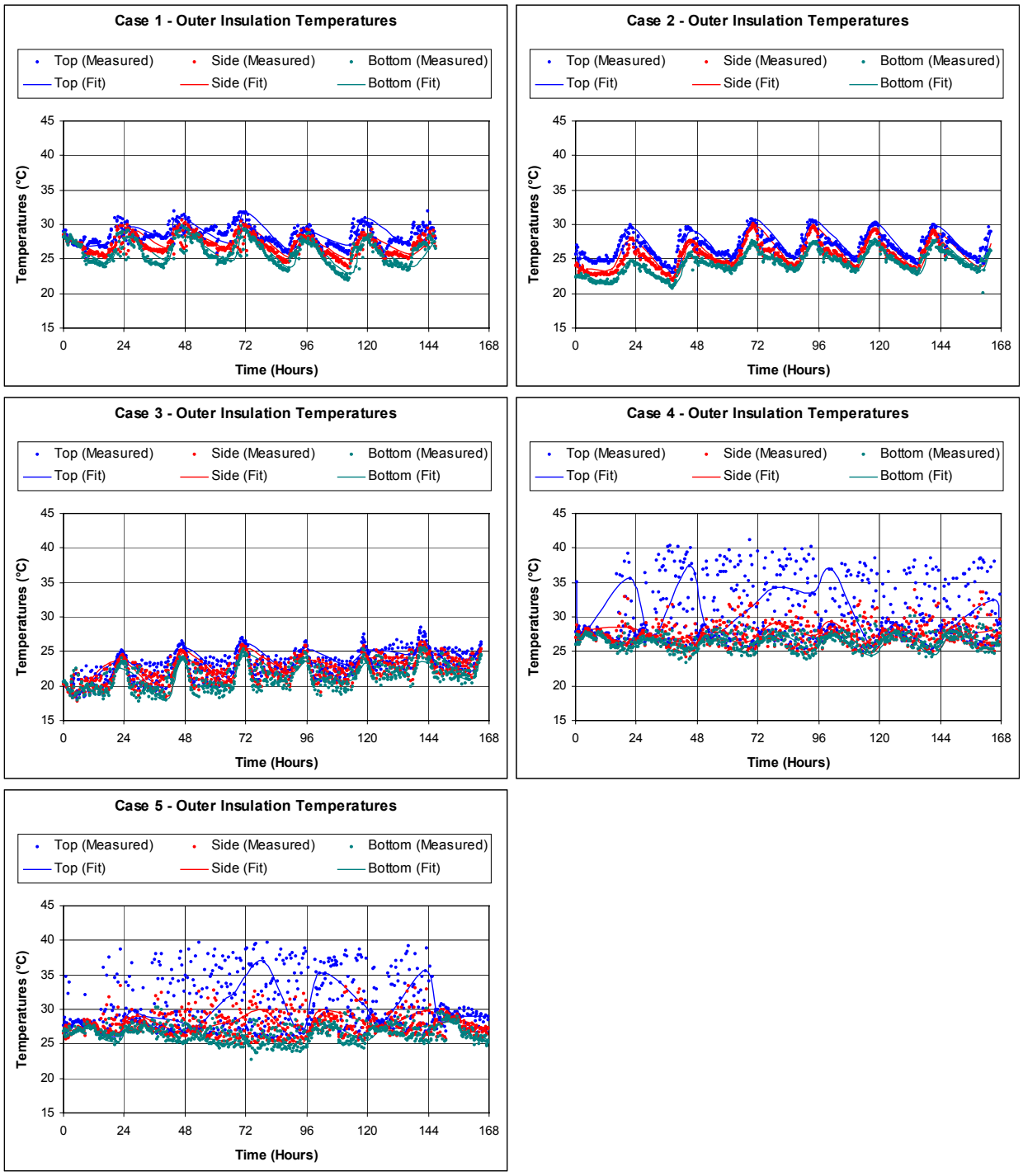

Source: DTN: MO0209MWDANS30.017 vti-a-data.xls (case 4), vti-b-data.xls (case 5), vti-c-data.xls (case 1), vti-d-data.xls (case 2), vti-e-data.xls (case 3) and worksheets “Measured Air and Insu Temp” of vti-aa.xls (case 4), vti-ba.xls (case 5), vti-ca.xls (case 1), vti-da.xls (case 2), vti-ea.xls (case 3)

Figure 7-4. Outer Insulation Boundary Temperatures for the ANSYS Post-Test Ventilation Model

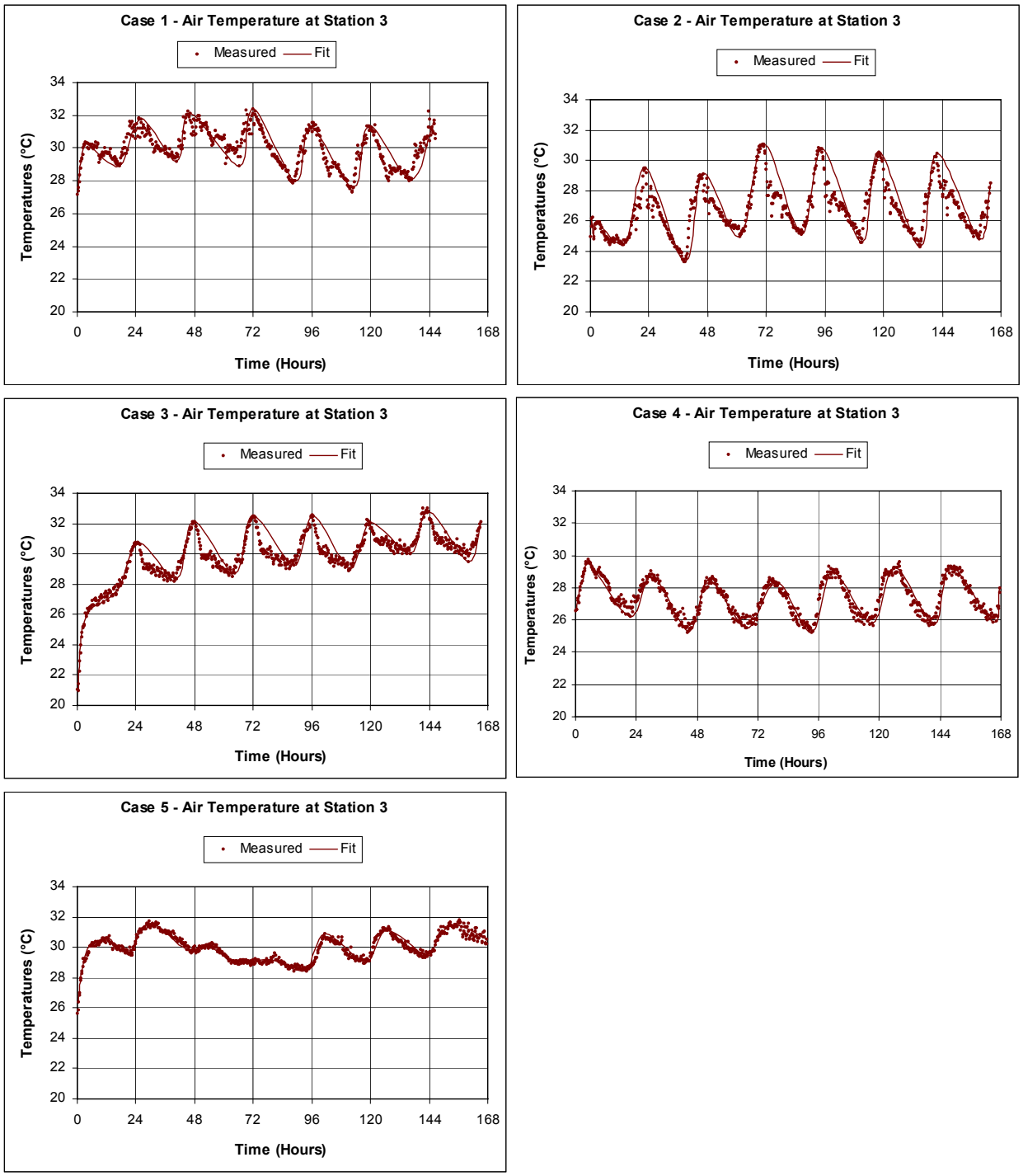

Source: DTN: MO0209MWDANS30.017 vti-a-data.xls (case 4), vti-b-data.xls (case 5), vti-c-data.xls (case 1), vti-d-data.xls (case 2), vti-e-data.xls (case 5) and worksheets “Measured Air and Insu Temp” of vti-aa.xls (case 4), vti-ba.xls (case 5), vti-ca.xls (case 1), vti-da.xls (case 2), vti-ea.xls (case 5)

Figure 7-5. Measured Air Temperature Histories at Station 3 Used as the Inlet Air for the ANSYS Post-Test Ventilation Model

Table 7-4. Distribution of Total Power to the Top, Sides, and Bottom Quarters of the Waste Package Based on Temperature Measurements

Case No.	Nominal Power (kW/m)	WP Top Quarter (%)	WP Side Quarters (%)	WP Bottom Quarter (%)
1	0.36	32%	24%	20%
2	0.36	32%	24%	20%
3	0.36	31%	24%	21%
4	0.18	32%	24%	20%
5	0.18	32%	24%	20%

Source: DTN: MO0209MWDANS30.017; worksheets "Heat Removal" of vti-aa.xls (case 4), vti-ba.xls (case 5), vti-ca.xls (case 1), vti-da.xls (case 2), vti-ea.xls (case 3)

7.1.3.4 Correlating the Model Results to the Test Data Using Heat Transfer Coefficients

Having determined appropriate distributions of power around the circumference of the waste package, ANSYS models were run iteratively using different values for the heat transfer coefficients until the model results matched the test data.

7.1.3.5 Results

Table 7-5 shows the heat transfer coefficient values which resulted in close agreement to the measured temperature data. The temperature results from the ANSYS models are compared to the recorded test data in Figures 7-6 through 7-10. Table 7-6 compares the fitted average heat transfer coefficient for each test case from Table 7-5 to heat transfer coefficients calculated using the Mixed Convection Correlation and the Dittus-Boelter correlation for fully developed turbulent flow inside a smooth circular tube (Incropera and DeWitt 1996, Section 8.5).

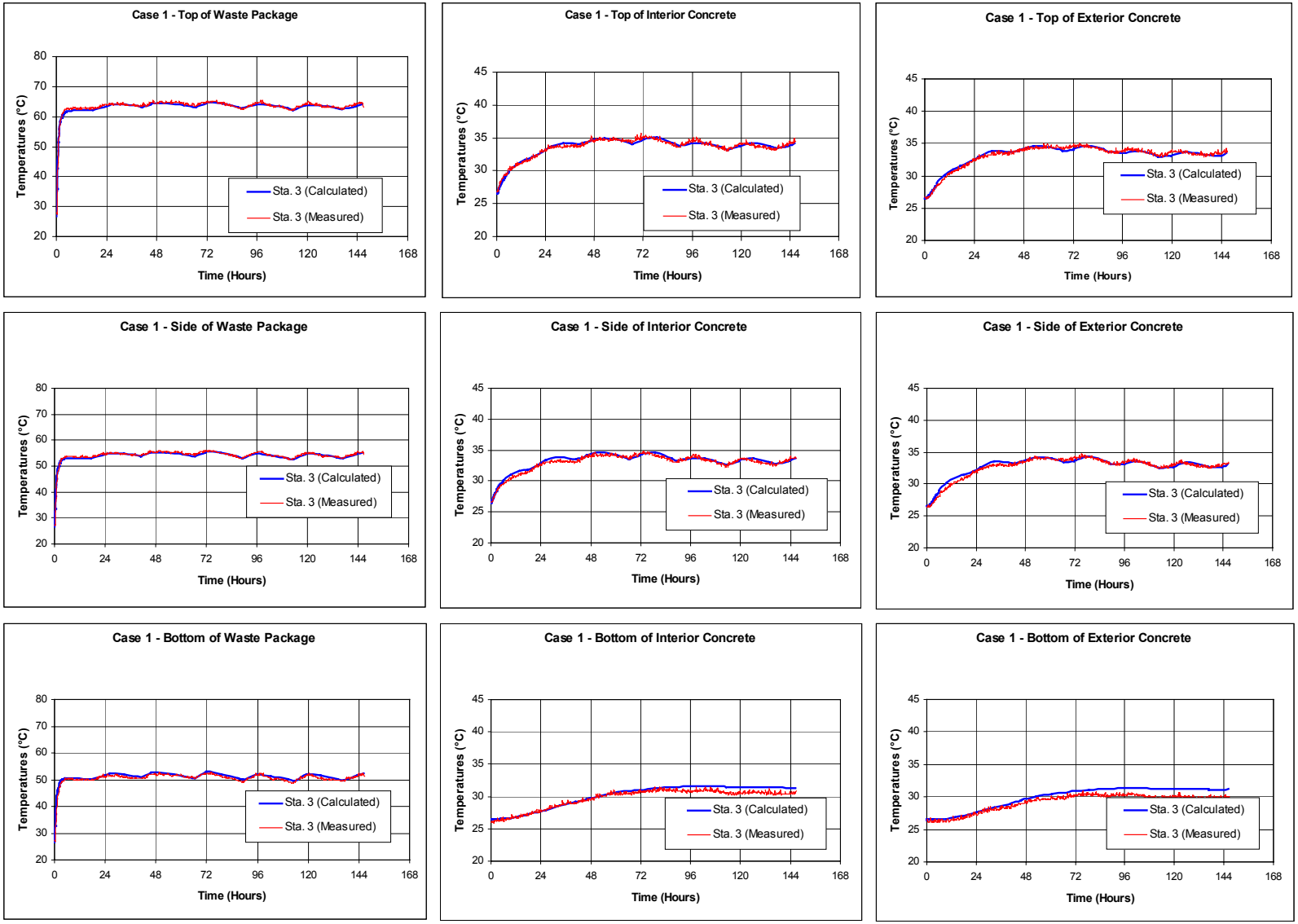

Source: DTN: MO0209MWDANS30.017, vit-c-data.xls and worksheet "ANSYS Results" of vti-ca.xls

Figure 7-6. ANSYS Post-Test Ventilation Model versus Measured Results for Ventilation Test Phase 1, Case 1

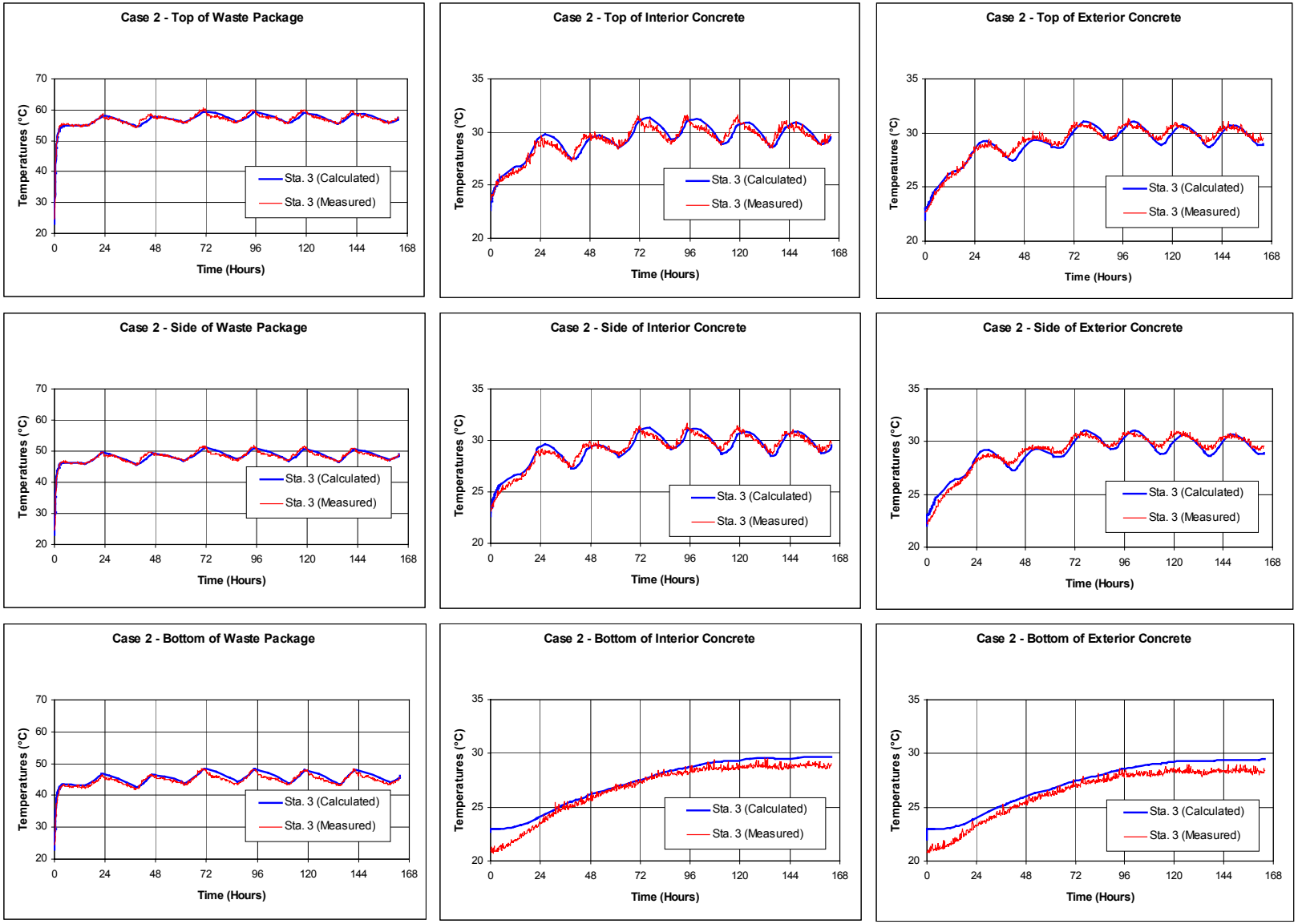

Source: DTN: MO0209MWDANS30.017, vit-d-data.xls and worksheet "ANSYS Results" of vti-da.xls

Figure 7-7. ANSYS Post-Test Ventilation Model versus Measured Results for Ventilation Test Phase 1, Case 2

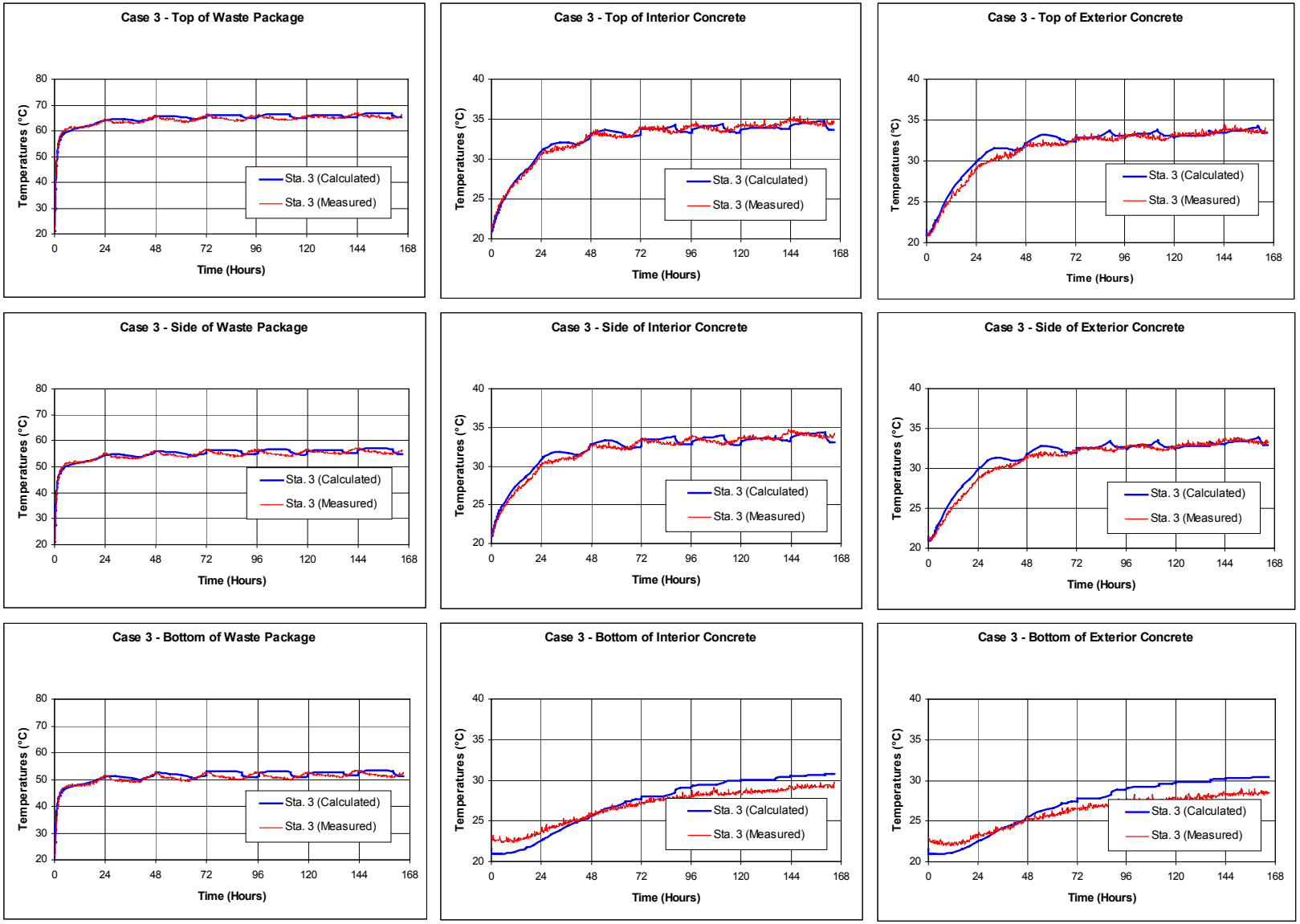

Source: DTN: MO0209MWDANS30.017, vit-e-data.xls and worksheet "ANSYS Results" of vti-ea.xls

Figure 7-8. ANSYS Post-Test Ventilation Model versus Measured Results for Ventilation Test Phase 1, Case 3

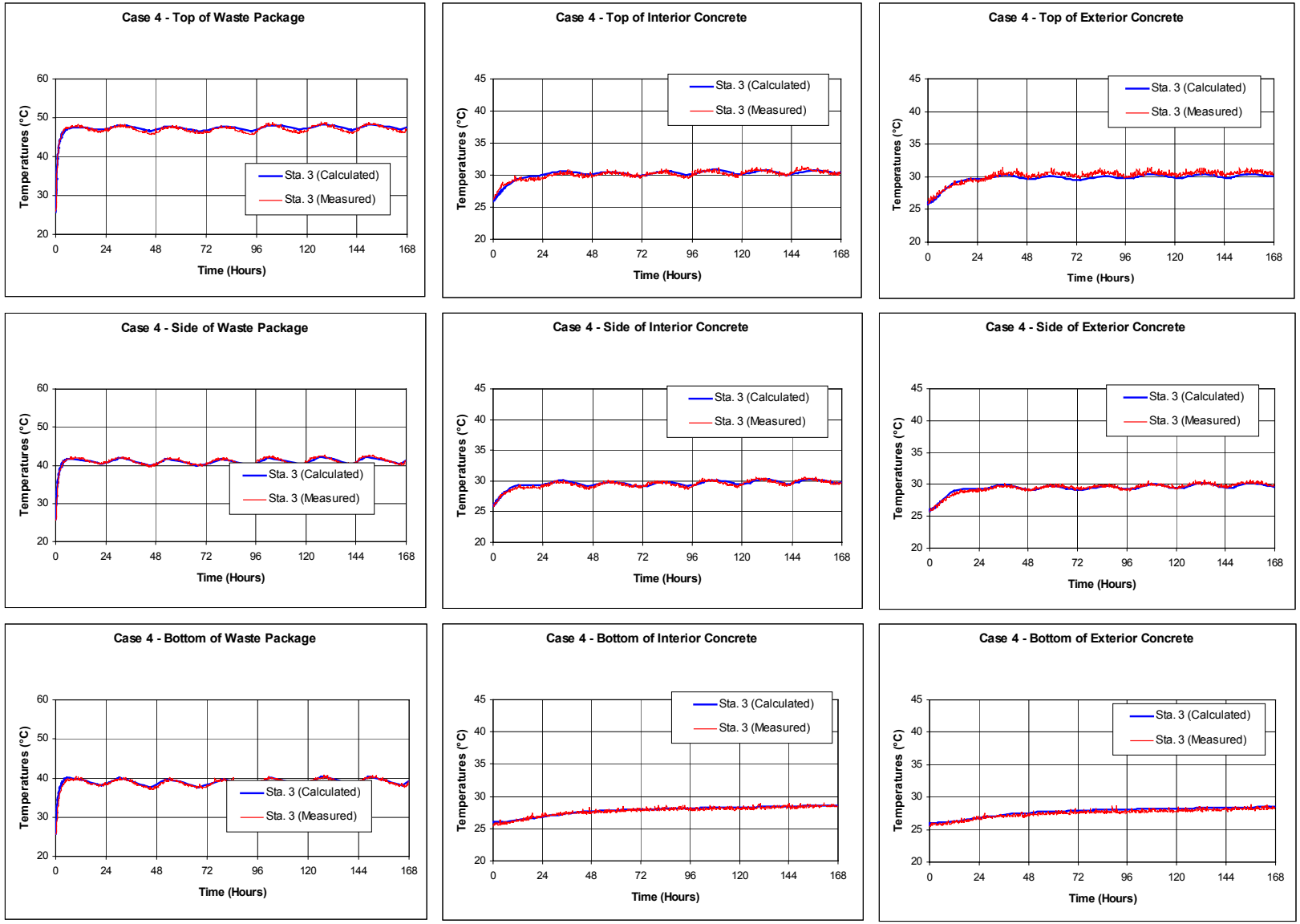

Source: DTN: MO0209MWDANS30.017, vit-a-data.xls and worksheet "ANSYS Results" of vti-aa.xls

Figure 7-9. ANSYS Post-Test Ventilation Model versus Measured Results for Ventilation Test Phase 1, Case 4

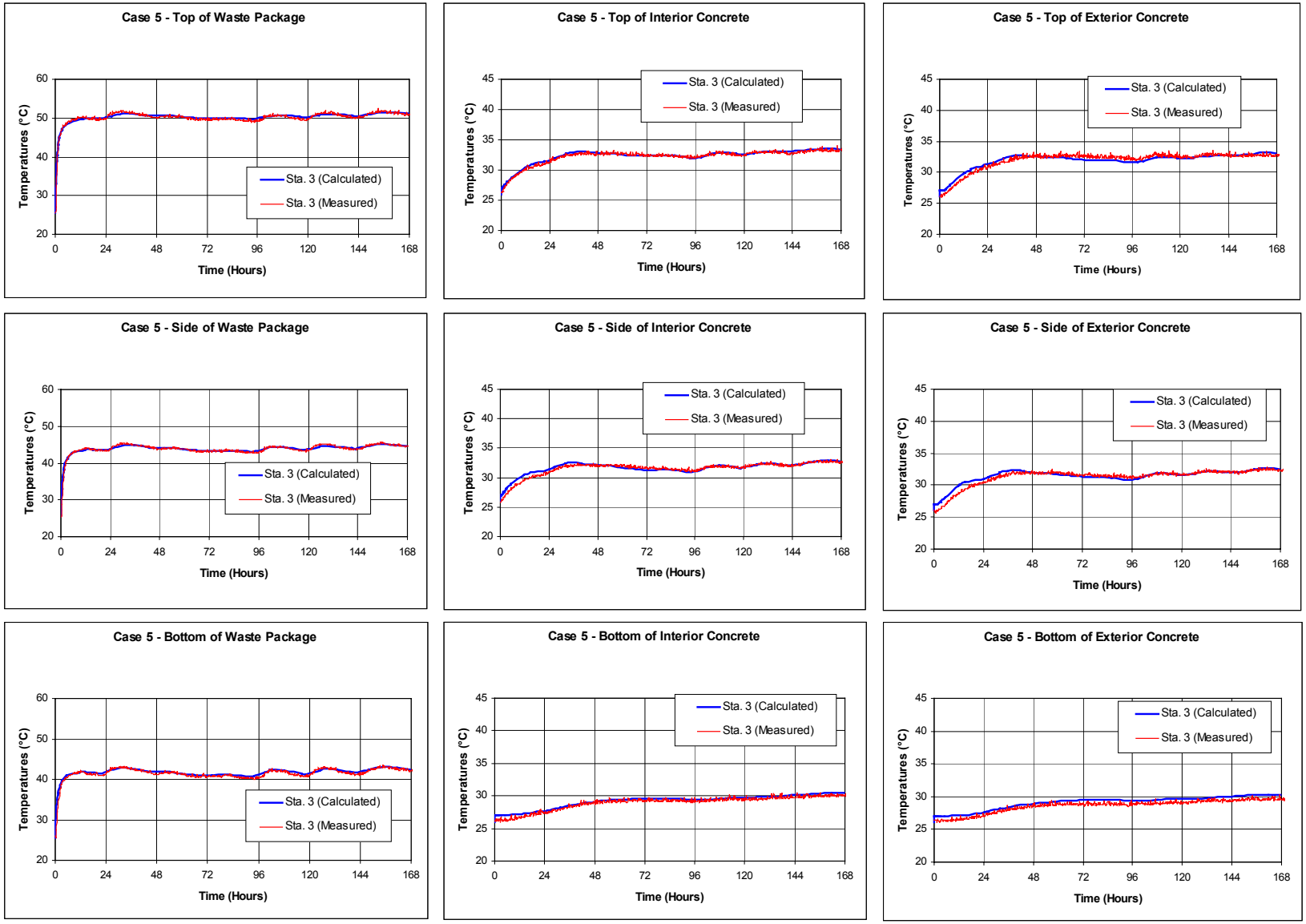

Source: DTN: MO0209MWDANS30.017, vit-b-data.xls and worksheet "ANSYS Results" of vti-ba.xls

Figure 7-10. ANSYS Post-Test Ventilation Model versus Measured Results for Ventilation Test Phase 1, Case 5

Table 7-5. Developed Heat Transfer Coefficients from the ANSYS Post-Test Modeling of Phase 1 of the Ventilation Test

		Heat Transfer Coefficient ($W/m^2 \cdot K$)				
Case No.	WP Top Quarter	WP Side Quarters	WP Bottom Quarter	Upper Concrete	Lower Concrete	Invert
1	2.0	8.0	8.0	7.0	11.0	6.0
2	3.5	9.5	10.5	13.0	15.0	2.0
3	1.0	7.5	8.5	9.5	16	5.0
4	0.5	7.5	7.0	5.0	9.0	9.0
5	0.0	7.0	7.0	5.0	15.0	9.0

Source: DTN: MO0209MWDANS30.017, worksheets "Heat Removal" of vti-aa.xls (case 4), vti-ba.xls (case 5), vti-ca.xls (case 1), vti-da.xls (case 2), vti-ea.xls (case 3)

Table 7-6. Comparison of Heat Transfer Coefficients Using Data-Fitting to the Mixed Convection and Dittus-Boelter Correlations

		Heat Transfer Coefficient ($W/m^2 \cdot K$)				
Case No.	Flow Rate (m^3/s)	ANSYS WP [a]	Mixed Convection Correlation – Inner Surface (i.e., waste package surface)	ANSYS Concrete and Invert [a]	Mixed Convection Correlation – Outer Surface (i.e., inner concrete surface and invert surface)	Dittus-Boelter [b]
1	1	6.0	4.8 [c]	8.0	8.0 [h]	3.3
2	2	7.8	6.5 [d]	10.0	11.2 [i]	5.7
3	0.5	5.7	4.5 [e]	10.2	8.7 [j]	1.9
4	1	5	4.3 [f]	7.7	7.9 [k]	3.3
5	0.5	4.7	3.6 [g]	9.7	8.5 [l]	1.9

Source: [a] Average from Table 7-5
[b] Value from Table XVII-1
[c] Value from Table IX-26, Test 3
[d] Value from Table IX-26, Test 4
[e] Value from Table IX-26, Test 5
[f] Value from Table IX-26, Test 1
[g] Value from Table IX-26, Test 2
[h] Value from Table IX-29, Test 3
[i] Value from Table IX-29, Test 4
[j] Value from Table IX-29, Test 5
[k] Value from Table IX-29, Test 1
[l] Value from Table IX-29, Test 2

The average of the heat transfer coefficients range from approximately two to five times larger than heat transfer coefficients calculated using the Dittus-Boelter correlation. Two reasons would tend to account for the differences. First, the Dittus-Boelter equation is a forced convection correlation. Analyses of the ventilation test data indicate a mixed (i.e., natural and forced) convection regime inside the concrete pipe annulus. Second, the Dittus-Boelter correlation for calculating a forced convection heat transfer coefficient was developed for hollow tube geometries. The correlation can be extended to a cylinder within a tube (i.e., waste package inside a drift) by using the hydraulic diameter instead of the geometric diameter. However, a cylinder within a tube, eccentrically located, is a different geometry which would tend to invalidate the Dittus-Boelter correlation within the range of air flow velocities being considered

for preclosure. Add an invert, and the geometry of the problem lies even farther beyond the range of the Dittus-Boelter correlation. The values presented in Table 7-6 for the ANSYS fitted heat transfer coefficients argue that both natural and forced convection are important heat removal mechanisms for the experimental set-up of the Ventilation Test. Although scaling the quarter scale test results to a full scale drift is beyond the scope of this model report, it stands to reason that a convection coefficient correlation which considers both natural and forced convection is more appropriate for use than the Dittus-Boelter equation (for the current drift design, heat load range, and ventilation flow rate).

Table 7-7 summarizes the ventilation heat removal rates for the 5 cases as modeled by ANSYS.

Table 7-7. Heat Removal Ratios for the ANSYS Post-Test Ventilation Models

Case No.	Ventilation Efficiency
1	78%
2	93%
3	81%
4	87%
5	83%

Source: DTN: MO0209MWDANS30.017, worksheets "Heat Removal" of vti-aa.xls (case 4), vti-ba.xls (case 5), vti-ca.xls (case 1), vti-da.xls (case 2), vti-ea.xls (case 3)

7.1.3.6 Validation Criteria Met for the Convection Heat Transfer Model

The ANSYS numerical model matched the Phase I Ventilation Test results within the validation criteria of ±5°C using a reasonable range of heat transfer coefficients. The range of heat transfer coefficients required to match the test results indicates a mixed convection regime inside the test train. The Dittus-Boelter correlation for calculating forced convection heat transfer coefficients is therefore, at best, only a conservative approach. The impact of using such a correlation is a lower or more conservative rate of heat removal by ventilation. A more realistic correlation is one that accounts for both natural and forced convection to remove heat from the drift, such as the mixed convection correlation used in these analyses. Therefore, the validation criteria for the convection heat transfer model is considered to be met with respect to the level of confidence required in the model.

7.1.4 Validation of the Host Rock Conduction Heat Transfer Model

Conduction heat transfer dominates other heat transfer mechanisms (i.e., convection in fractures and lithophysae, and latent heat) in the host rock. This is supported by data and modeling of the Drift Scale Test (Sass et al. 1988, Birkholzer and Tsang 2000). For the level of confidence required for the Ventilation Model, the assertion that conduction dominates the heat transfer in the host rock does not compromise the validity of the conceptual model.

8. CONCLUSIONS

This model and analysis report develops, validates, and implements a conceptual model for heat transfer in and around a ventilated emplacement drift. This conceptual model includes thermal radiation between the waste package and the drift wall, convection from the waste package and drift wall surfaces into the flowing air, and conduction in the surrounding host rock. These heat transfer processes are coupled and vary both temporally and spatially, so numerical and analytical methods are used to implement the mathematical equations which describe the conceptual model. These numerical and analytical methods predict the transient response of the system, at the drift scale, in terms of spatially varying temperatures and ventilation efficiencies. The ventilation efficiency describes the effectiveness of the ventilation process in removing radionuclide decay heat from the drift environment.

An alternative conceptual model is also developed which evaluates the influence of water and water vapor mass transport on the ventilation efficiency. These effects are described using analytical methods which bound the contribution of latent heat to the system, quantify the effects of varying degrees of host rock saturation (and hence host rock thermal conductivity) on the ventilation efficiency, and evaluate the effects of vapor and enhanced vapor diffusion on the host rock thermal conductivity.

8.1 SUMMARY OF RESULTS

As described by the conceptual model and its mathematical implementations, ventilation is found to be an effective way to remove heat produced by the decay of radionuclides in the in-drift environment, and to mitigate the peak waste package and drift wall temperatures that would otherwise occur. Given the License Application design parameters and inputs listed in Section 4 (including a ventilation flow rate of 15 m^3/s, an inlet air temperature of 23°C, and a preclosure period of 50 years, the integrated ventilation efficiency is 88% for a 600 meter long drift and 86% for an 800 meter long drift. Revision 01 ICN 01 (BSC 2002d), and Revision 02 (BSC 2002e) of this report cited integrated ventilation efficiencies of 87.6% and 84% for a 600 meter long drift. The differences between these values, and those reported in the revisions are small. Temperatures of the waste package, drift wall, and drift air do not exceed 105, 85, or 80°C respectively. The most influential parameters on the effectiveness of the ventilation to remove heat from the drift are the temperature of the inlet ventilation air and the ventilation flow rate.

The effects of water and water vapor mass transport under sub-boiling conditions, described by the alternative conceptual model, on the ventilation efficiency and the waste package, drift wall, and drift air temperatures are minor. The latent heat contribution associated with the evaporation of host rock matrix water near the drift wall is limited by the hydrologic properties of the rock, and is determined to be less than 1% of the total waste package energy provided to the in-drift and host rock environment. The change in temperatures associated with varying the host rock matrix saturation (and hence the bulk thermal conductivity) from completely dry to completely wet is found to be less than 5°C at any given time and distance from the drift entrance. The integrated ventilation efficiency for a 600 meter long drift ranges from about 90% for completely dry conditions, to about 87% for completely wet conditions. Finally, there was no evidence of enhancement to the host rock thermal conductivity due to vapor and enhanced vapor diffusion.

8.2 MODEL OUTPUTS

The DTNs produced by this report are given in Table 8-1.

Table 8-1. DTNs Produced by the Ventilation Model and Analysis Report

DTN	Description
MO0303MWDSLTLC.000	Preliminary Stratigraphic Layer Thickness (Section 6.5.1)
MO0306MWDSLTLC.000	Stratigraphic Layer Thickness (Section 6.5.1)
MO0306MWDASLCV.001	Input/Output and Analysis of the ANSYS-LA-Coarse Ventilation Model (Section 6.6.1 and 6.6.2)
MO0306MWDALAFV.000	Input/Output and Analysis of the ANSYS-LA-Fine Ventilation Model (Section 6.6.2)
MO0306MWDCIEAP.000	ANSYS-LA-Coarse-Instantaneous-Efficiency Application (Section 6.10.2.3)
MO0306MWDCIETA.000	ANSYS-LA-Coarse-Instantaneous-Twp-Efficiency Application (Section 6.10.2.4)
MO0307MWDAC8MV.000	Analytical-LA-Coarse Ventilation Model (Section 6.6.1)
MO0306MWDRTCCV.000	Analytical-LA-Coarse-Wet-vs-Dry-kth Ventilation Model (Section 6.9.2)
MO0306MWDLACVD.000	Analytical-LA-Coarse-Delta-Method Ventilation Model (Section 6.11)
MO0307MWDAC8VD.000	Analytical-LA-Coarse-Delta-Method_800m Ventilation Model (Section 6.11)
MO0209MWDANS30.017	Input/Output and Analysis of ANSYS Post Test Modeling of the Ventilation Test Phase I for Model Validation (Section 7.1.3)
MO0306MWDVTPH2.000	Ventilation Test Phase II Data Analysis (Attachment XI)
MO0306MWDMXCNV.000	Analyses to Support the Mixed Convection Correlation (Attachment X)

8.2.1 Summary of Model Outputs

Given the design parameters and inputs listed in Section 4, the primary outputs of the Ventilation Model are:

- Ventilation efficiencies as a function of time and location from the inlet of the drift, whose trend is to increase with time, but decrease with distance from the drift inlet (Table 8-2, from the Analytical-LA-Coarse results. Note that the results of the ANSYS-LA-Coarse model may also be used).
- Integrated ventilation efficiencies and standard deviations for 600 and 800 meter long drifts (Table 8-3, from the Analytical-LA-Coarse-Delta-Method results. Note that the results of the ANSYS-LA-Coarse model may also be used, however these results are not reported with uncertainty expressed as a standard deviation).
- Waste package, drift wall, and in-drift air preclosure temperatures as function of time and location from the inlet of the drift, whose trend is to decrease with time, but increase with distance from the drift inlet (Tables 8-4 through 8-6, from the Analytical-LA-Coarse results. Note that the results of the ANSYS-LA-Coarse model may also be used).

Table 8-2. Ventilation Efficiency as a Function of Time and Distance from the Drift Inlet

Time (years)	Ventilation Efficiency							
	100-m	200-m	300-m	400-m	500-m	600-m	700-m	800-m
1	90.8%	86.1%	81.3%	76.7%	73.0%	69.3%	65.8%	62.5%
2	91.5%	87.7%	84.2%	80.7%	77.4%	74.2%	71.1%	68.2%
3	92.5%	89.1%	85.9%	82.8%	79.7%	76.8%	74.0%	71.3%
4	93.1%	90.0%	87.0%	84.0%	81.2%	78.4%	75.8%	73.3%
5	93.5%	90.5%	87.7%	84.9%	82.2%	79.6%	77.1%	74.6%
6	93.8%	91.0%	88.2%	85.5%	82.9%	80.4%	78.0%	75.7%
7	94.0%	91.3%	88.6%	86.1%	83.5%	81.1%	78.8%	76.5%
8	94.2%	91.5%	89.0%	86.5%	84.0%	81.7%	79.4%	77.2%
9	94.3%	91.8%	89.3%	86.8%	84.5%	82.1%	79.9%	77.8%
10	94.5%	92.0%	89.5%	87.1%	84.8%	82.5%	80.4%	78.3%
11	94.6%	92.1%	89.7%	87.4%	85.1%	82.9%	80.7%	78.6%
12	94.7%	92.3%	90.0%	87.7%	85.4%	83.3%	81.2%	79.1%
13	94.8%	92.4%	90.1%	87.9%	85.7%	83.6%	81.5%	79.5%
14	94.9%	92.6%	90.3%	88.1%	86.0%	83.8%	81.8%	79.8%
15	94.9%	92.7%	90.5%	88.3%	86.2%	84.1%	82.1%	80.1%
16	95.0%	92.7%	90.5%	88.4%	86.3%	84.2%	82.2%	80.3%
17	95.1%	92.9%	90.7%	88.6%	86.5%	84.5%	82.5%	80.6%
18	95.1%	92.9%	90.8%	88.8%	86.7%	84.7%	82.8%	80.9%
19	95.2%	93.0%	90.9%	88.9%	86.9%	84.9%	83.0%	81.1%
20	95.2%	93.1%	91.0%	89.0%	87.0%	85.1%	83.2%	81.4%
21	95.2%	93.2%	91.1%	89.1%	87.1%	85.2%	83.3%	81.5%
22	95.3%	93.3%	91.2%	89.3%	87.3%	85.4%	83.6%	81.8%
23	95.4%	93.4%	91.4%	89.4%	87.5%	85.6%	83.8%	82.0%
24	95.4%	93.4%	91.5%	89.5%	87.7%	85.8%	84.0%	82.2%
25	95.5%	93.5%	91.6%	89.7%	87.8%	86.0%	84.2%	82.4%
26	95.5%	93.6%	91.7%	89.8%	87.9%	86.1%	84.4%	82.6%
27	95.6%	93.6%	91.8%	89.9%	88.1%	86.3%	84.5%	82.8%
28	95.6%	93.7%	91.9%	90.0%	88.2%	86.5%	84.7%	83.1%
29	95.7%	93.8%	92.0%	90.2%	88.4%	86.6%	84.9%	83.3%
30	95.7%	93.9%	92.1%	90.3%	88.5%	86.8%	85.1%	83.5%
31	95.8%	93.9%	92.1%	90.4%	88.6%	86.9%	85.3%	83.6%
32	95.8%	94.0%	92.3%	90.5%	88.8%	87.1%	85.5%	83.8%
33	95.9%	94.1%	92.4%	90.6%	88.9%	87.3%	85.7%	84.1%
34	95.9%	94.2%	92.4%	90.8%	89.1%	87.4%	85.8%	84.2%
35	96.0%	94.2%	92.5%	90.9%	89.2%	87.6%	86.0%	84.4%
36	96.0%	94.3%	92.6%	91.0%	89.3%	87.7%	86.1%	84.6%
37	96.0%	94.4%	92.7%	91.1%	89.5%	87.9%	86.3%	84.8%
38	96.1%	94.4%	92.8%	91.2%	89.6%	88.0%	86.5%	85.0%
39	96.1%	94.5%	92.9%	91.3%	89.7%	88.2%	86.6%	85.1%
40	96.2%	94.6%	93.0%	91.4%	89.8%	88.3%	86.8%	85.3%
41	96.2%	94.6%	93.0%	91.5%	89.9%	88.4%	86.9%	85.5%

Table 8-2. Ventilation Efficiency as a Function of Time and Distance from the Drift Inlet (Continued)

Time (years)	Ventilation Efficiency							
	100-m	200-m	300-m	400-m	500-m	600-m	700-m	800-m
42	96.2%	94.7%	93.1%	91.6%	90.1%	88.6%	87.1%	85.7%
43	96.3%	94.7%	93.2%	91.7%	90.2%	88.7%	87.3%	85.8%
44	96.3%	94.8%	93.3%	91.8%	90.3%	88.9%	87.4%	86.0%
45	96.4%	94.9%	93.4%	91.9%	90.4%	89.0%	87.6%	86.2%
46	96.4%	94.9%	93.4%	92.0%	90.5%	89.1%	87.7%	86.3%
47	96.4%	95.0%	93.5%	92.1%	90.7%	89.2%	87.9%	86.5%
48	96.5%	95.0%	93.6%	92.2%	90.8%	89.4%	88.0%	86.6%
49	96.5%	95.1%	93.7%	92.3%	90.9%	89.5%	88.1%	86.8%
50	96.6%	95.1%	93.7%	92.4%	91.0%	89.6%	88.3%	86.9%

DTN: MO0307MWDAC8MV.000

NOTE: Linear interpolation between two times and/or drift locations is approximate.

Table 8-3. Integrated Ventilation Efficiency Over 50 Years of Preclosure, and 600 and 800 meters of Drift

Length of Drift (meters)	Length of Ventilation (years)	Mean	Standard Deviation
600[a]	50	88.0%	2.6%
800[b]	50	86.0%	2.7%

NOTES: [a] DTN: MO0306MWDLACVD.000
[b] DTN: MO0307MWDAC8VD.000

Table 8-4. Waste Package Temperatures as a Function of Time and Distance from the Drift Inlet

Time (years)	Temperature (°C)							
	100 m	200 m	300 m	400 m	500 m	600 m	700 m	800 m
1	59.98	66.56	73.25	78.68	84.95	89.84	94.50	98.95
2	58.82	65.24	71.32	77.24	82.82	88.27	93.24	98.02
3	58.09	64.45	70.59	76.48	82.16	87.62	92.66	97.54
4	57.36	63.63	69.68	75.53	81.17	86.62	91.67	96.57
5	56.70	62.87	68.84	74.61	80.20	85.60	90.63	95.51
6	56.08	62.15	68.03	73.72	79.24	84.59	89.58	94.43
7	55.49	61.45	67.24	72.85	78.30	83.59	88.53	93.34
8	54.93	60.79	66.48	72.01	77.38	82.60	87.49	92.25
9	54.39	60.15	65.76	71.20	76.50	81.65	86.47	91.18
10	53.87	59.53	65.05	70.41	75.62	80.70	85.47	90.12
11	53.37	58.94	64.36	69.64	74.78	79.79	84.49	89.08
12	52.81	58.27	63.60	68.78	73.84	78.76	83.39	87.92
13	52.31	57.68	62.91	68.01	72.98	77.83	82.40	86.86
14	51.86	57.14	62.29	67.31	72.21	76.98	81.49	85.89
15	51.44	56.64	61.71	66.66	71.48	76.20	80.64	84.99
16	51.06	56.18	61.18	66.06	70.82	75.47	79.86	84.15
17	50.58	55.61	60.53	65.32	70.01	74.58	78.91	83.14

Table 8-4. Waste Package Temperatures as a Function of Time and Distance from the Drift Inlet (Continued)

Time (years)	Temperature (°C)							
	100 m	200 m	300 m	400 m	500 m	600 m	700 m	800 m
18	50.15	55.10	59.93	64.65	69.26	73.76	78.02	82.19
19	49.74	54.61	59.36	64.01	68.55	72.99	77.19	81.31
20	49.36	54.16	58.84	63.42	67.89	72.27	76.41	80.47
21	49.01	53.73	58.35	62.86	67.27	71.59	75.68	79.69
22	48.59	53.23	57.77	62.21	66.56	70.81	74.84	78.79
23	48.21	52.78	57.24	61.62	65.89	70.08	74.05	77.95
24	47.85	52.34	56.74	61.05	65.27	69.39	73.31	77.16
25	47.51	51.93	56.27	60.52	64.67	68.74	72.61	76.41
26	47.18	51.54	55.82	60.00	64.10	68.12	71.94	75.69
27	46.84	51.14	55.35	59.48	63.52	67.48	71.25	74.95
28	46.49	50.73	54.88	58.95	62.93	66.84	70.56	74.20
29	46.17	50.34	54.43	58.43	62.36	66.21	69.88	73.49
30	45.85	49.96	53.99	57.95	61.82	65.62	69.24	72.80
31	45.56	49.61	53.59	57.49	61.31	65.06	68.64	72.15
32	45.23	49.22	53.14	56.98	60.75	64.45	67.98	71.44
33	44.92	48.85	52.71	56.50	60.21	63.86	67.34	70.76
34	44.63	48.50	52.31	56.04	59.71	63.31	66.74	70.12
35	44.34	48.17	51.92	55.60	59.22	62.77	66.16	69.50
36	44.07	47.84	51.54	55.17	58.74	62.24	65.60	68.89
37	43.78	47.49	51.14	54.72	58.24	61.69	65.00	68.26
38	43.50	47.16	50.76	54.29	57.76	61.17	64.44	67.65
39	43.23	46.84	50.39	53.87	57.30	60.67	63.89	67.07
40	42.98	46.54	50.04	53.47	56.86	60.18	63.37	66.50
41	42.73	46.24	49.69	53.09	56.43	59.71	62.86	65.95
42	42.46	45.93	49.33	52.68	55.98	59.21	62.32	65.38
43	42.21	45.63	48.99	52.29	55.54	58.74	61.81	64.83
44	41.97	45.34	48.65	51.91	55.12	58.28	61.31	64.29
45	41.73	45.06	48.33	51.55	54.72	57.83	60.83	63.78
46	41.51	44.79	48.02	51.20	54.33	57.40	60.37	63.28
47	41.27	44.51	47.70	50.83	53.92	56.96	59.89	62.77
48	41.05	44.24	47.39	50.48	53.53	56.54	59.43	62.28
49	40.83	43.98	47.09	50.15	53.16	56.12	58.98	61.80
50	40.62	43.73	46.80	49.82	52.79	55.72	58.55	61.33

DTN: MO0307MWDAC8MV.000

Table 8-5. Drift Wall Temperatures as a Function of Time and Distance from the Drift Inlet

Time (years)	Temperature (°C)							
	100 m	200 m	300 m	400 m	500 m	600 m	700 m	800 m
1	38.29	45.14	52.06	58.64	64.01	69.36	74.45	79.29
2	37.85	44.68	51.22	57.56	63.47	69.25	74.65	79.84
3	37.69	44.49	51.04	57.34	63.39	69.21	74.69	79.98
4	37.47	44.17	50.65	56.89	62.91	68.72	74.21	79.52
5	37.23	43.83	50.21	56.38	62.34	68.11	73.57	78.86
6	37.00	43.48	49.77	55.85	61.74	67.45	72.86	78.10
7	36.76	43.14	49.32	55.31	61.12	66.76	72.11	77.31
8	36.53	42.80	48.88	54.78	60.50	66.07	71.35	76.49
9	36.31	42.47	48.45	54.25	59.89	65.38	70.59	75.67
10	36.09	42.14	48.02	53.73	59.28	64.69	69.83	74.84
11	35.88	41.82	47.60	53.22	58.69	64.01	69.09	74.03
12	35.64	41.47	47.13	52.65	58.02	63.25	68.25	73.11
13	35.43	41.15	46.71	52.13	57.41	62.56	67.47	72.27
14	35.24	40.86	46.33	51.66	56.86	61.92	66.77	71.49
15	35.06	40.59	45.97	51.22	56.34	61.33	66.11	70.77
16	34.90	40.34	45.64	50.81	55.86	60.78	65.50	70.10
17	34.69	40.03	45.24	50.32	55.28	60.12	64.76	69.29
18	34.50	39.75	44.86	49.86	54.74	59.50	64.07	68.53
19	34.33	39.48	44.51	49.43	54.23	58.92	63.42	67.81
20	34.17	39.24	44.19	49.02	53.75	58.37	62.81	67.14
21	34.01	39.00	43.88	48.65	53.31	57.86	62.23	66.51
22	33.83	38.73	43.53	48.21	52.80	57.28	61.58	65.79
23	33.67	38.49	43.20	47.81	52.32	56.73	60.97	65.12
24	33.51	38.25	42.89	47.43	51.87	56.22	60.40	64.49
25	33.37	38.03	42.60	47.07	51.45	55.73	59.85	63.89
26	33.22	37.82	42.32	46.73	51.04	55.27	59.33	63.31
27	33.08	37.60	42.04	46.38	50.63	54.79	58.80	62.73
28	32.93	37.38	41.75	46.02	50.21	54.31	58.26	62.14
29	32.79	37.17	41.47	45.68	49.81	53.85	57.75	61.57
30	32.66	36.97	41.21	45.35	49.42	53.41	57.25	61.02
31	32.53	36.78	40.96	45.05	49.06	52.99	56.78	60.51
32	32.39	36.58	40.68	44.71	48.66	52.54	56.28	59.95
33	32.26	36.38	40.42	44.39	48.29	52.10	55.79	59.41
34	32.13	36.19	40.18	44.09	47.93	51.69	55.33	58.90
35	32.01	36.01	39.94	43.80	47.58	51.29	54.88	58.41
36	31.89	35.84	39.71	43.51	47.24	50.91	54.45	57.93
37	31.77	35.65	39.47	43.21	46.89	50.50	54.00	57.43
38	31.65	35.48	39.24	42.93	46.56	50.12	53.57	56.95
39	31.54	35.31	39.01	42.65	46.23	49.75	53.15	56.49
40	31.43	35.14	38.80	42.39	45.92	49.39	52.75	56.05
41	31.32	34.99	38.59	42.13	45.62	49.04	52.36	55.62
42	31.21	34.82	38.37	41.87	45.30	48.68	51.95	55.17
43	31.10	34.66	38.17	41.61	45.00	48.33	51.56	54.74
44	31.00	34.51	37.96	41.36	44.70	47.99	51.18	54.32
45	30.90	34.36	37.77	41.12	44.42	47.67	50.82	53.92
46	30.80	34.22	37.58	40.89	44.15	47.35	50.46	53.53
47	30.70	34.07	37.39	40.65	43.87	47.03	50.10	53.13
48	30.61	33.93	37.20	40.43	43.60	46.72	49.75	52.74
49	30.51	33.79	37.02	40.20	43.34	46.42	49.42	52.37
50	30.42	33.66	36.85	39.99	43.08	46.13	49.09	52.00

DTN: MO0307MWDAC8MV.000

Table 8-6. Drift Air Temperatures as a Function of Time and Distance from the Drift Inlet

Time (years)	Temperature (°C)							
	100 m	200 m	300 m	400 m	500 m	600 m	700 m	800 m
1	30.35	37.51	44.28	50.69	56.81	62.63	68.17	73.44
2	30.13	37.15	43.90	50.38	56.61	62.58	68.32	73.83
3	29.99	36.90	43.58	50.01	56.22	62.20	67.98	73.56
4	29.84	36.63	43.20	49.56	55.70	61.64	67.39	72.96
5	29.70	36.36	42.82	49.08	55.15	61.02	66.72	72.25
6	29.56	36.10	42.45	48.61	54.59	60.39	66.02	71.49
7	29.43	35.85	42.09	48.15	54.04	59.75	65.31	70.72
8	29.30	35.60	41.73	47.69	53.49	59.12	64.61	69.94
9	29.18	35.37	41.39	47.25	52.96	58.51	63.92	69.18
10	29.06	35.13	41.05	46.82	52.43	57.90	63.23	68.42
11	28.94	34.91	40.73	46.40	51.92	57.31	62.55	67.67
12	28.82	34.67	40.37	45.93	51.36	56.65	61.80	66.84
13	28.70	34.44	40.04	45.51	50.84	56.04	61.12	66.07
14	28.60	34.24	39.75	45.12	50.37	55.49	60.49	65.37
15	28.50	34.05	39.47	44.76	49.93	54.98	59.90	64.72
16	28.41	33.88	39.22	44.43	49.53	54.50	59.36	64.11
17	28.31	33.67	38.91	44.04	49.04	53.93	58.71	63.39
18	28.21	33.48	38.63	43.67	48.59	53.40	58.10	62.70
19	28.12	33.30	38.36	43.32	48.16	52.90	57.53	62.06
20	28.03	33.13	38.12	42.99	47.76	52.43	57.00	61.46
21	27.95	32.97	37.88	42.69	47.39	51.99	56.49	60.90
22	27.86	32.79	37.62	42.34	46.97	51.49	55.92	60.26
23	27.77	32.62	37.37	42.02	46.57	51.02	55.38	59.65
24	27.69	32.46	37.13	41.71	46.19	50.58	54.88	59.09
25	27.61	32.31	36.91	41.42	45.84	50.16	54.40	58.55
26	27.54	32.17	36.70	41.15	45.50	49.76	53.94	58.04
27	27.47	32.02	36.49	40.86	45.15	49.36	53.48	57.51
28	27.39	31.87	36.27	40.58	44.80	48.94	53.00	56.98
29	27.32	31.73	36.06	40.30	44.47	48.55	52.55	56.47
30	27.25	31.60	35.86	40.04	44.14	48.17	52.11	55.98
31	27.18	31.47	35.67	39.79	43.84	47.81	51.70	55.52
32	27.11	31.33	35.47	39.53	43.51	47.42	51.26	55.03
33	27.05	31.20	35.27	39.27	43.20	47.05	50.83	54.55
34	26.98	31.07	35.08	39.03	42.90	46.70	50.43	54.09
35	26.92	30.95	34.90	38.79	42.61	46.35	50.04	53.65
36	26.86	30.83	34.73	38.56	42.33	46.02	49.66	53.22
37	26.80	30.71	34.55	38.32	42.03	45.68	49.26	52.78
38	26.74	30.59	34.37	38.10	41.75	45.35	48.88	52.35
39	26.68	30.48	34.21	37.88	41.48	45.03	48.51	51.94
40	26.62	30.37	34.05	37.67	41.22	44.72	48.16	51.54
41	26.57	30.26	33.89	37.46	40.97	44.43	47.82	51.16
42	26.52	30.15	33.73	37.25	40.71	44.12	47.47	50.76
43	26.46	30.05	33.57	37.04	40.46	43.82	47.12	50.37
44	26.41	29.94	33.42	36.84	40.21	43.53	46.79	50.00
45	26.36	29.84	33.28	36.65	39.98	43.25	46.47	49.64
46	26.31	29.75	33.14	36.47	39.75	42.98	46.16	49.29
47	26.26	29.65	32.99	36.28	39.52	42.71	45.85	48.94
48	26.21	29.56	32.85	36.10	39.29	42.44	45.54	48.59
49	26.17	29.47	32.72	35.92	39.08	42.18	45.25	48.26
50	26.12	29.38	32.59	35.75	38.87	41.94	44.96	47.94

DTN: MO0307MWDAC8MV.000

8.2.2 Recommendations for Downstream Use of the Model Outputs

Use of the Ventilation Model outputs, specifically the ventilation efficiency, is recommended for downstream thermal models that do not explicitly model the preclosure period. Either the ANSYS-LA-Coarse or the Analytical-LA-Coarse results may be used. The ventilation efficiency can be used to reduce the thermal energy produced by the waste package during the preclosure period as a means of initializing postclosure conditions in the host rock. If the intent of the initialization of the downstream postclosure thermal model is to only account for the correct amount of heat energy supplied to the host rock during the preclosure period, then the use of the ventilation efficiency in this manner (either as a function of time and distance from the drift inlet, or the integrated efficiency) is appropriate. However, if the intent of the initialization of the downstream postclosure thermal model is to account for the correct amount of heat energy supplied to the host rock during the preclosure period and the correct drift wall temperature at the start of postclosure, then the use of the integrated ventilation efficiency as described above by itself is inadequate. For this case, the downstream model should use the ventilation efficiency as a function of time and distance from the drift inlet (not the integrated efficiency) to reduce the thermal energy produced by the waste package during the preclosure period, and Equation 6-85 with the Ventilation Model output temperatures for the waste package, drift wall, and in-drift air, and the convection and radiation heat transfer coefficients, to constrain the waste package temperature during the postclosure initialization run.

8.2.3 Output Uncertainty

Uncertainty in the model output, specifically the integrated ventilation efficiency, is characterized using the mean and standard deviation listed in Table 8-3. Key input data and parameter uncertainties are also characterized using the means and standard deviations identified in Table 6-9. Input data and parameter uncertainties were propagated through the ventilation analysis using the Delta Method (see Section 6.11). The most influential design inputs and parameters on the uncertainty of the model output are the temperature of the inlet ventilation air, the ventilation flow rate, bulk thermal conductivity and specific heat of the host rock, and the convection heat transfer coefficients.

The uncertainties associated with the model and methods of analyses are characterized by comparing the results of the implementations of the conceptual model to the results of the implementations of the alternative conceptual model, and by comparing the results of the actual methods themselves to each other (i.e., comparing the ANSYS results to the analytical results). Two examples demonstrate these points. First, the uncertainty associated with including, or not including, water and water vapor mass transport in the ventilation analysis is shown to be minimal when comparing the results of both models. Second, there is some uncertainty associated with linearizing the radiation heat transfer in the analytical method. When comparing the temperature results of the analytical method to the results of the ANSYS method which explicitly treats the fourth order radiation heat transfer equation, there is little difference and hence no impact. These same arguments may be made for other sources of model and methods uncertainty such as: substituting the thermal pulse methodology in the analytical method for the transient conduction heat transfer analysis performed by ANSYS; the insensitivity of the length of well mixed volume elements in which the coupled heat transfer occurs, as addressed in the

discretization study; or using finite element numerical iteration techniques in the ANSYS method compared to exact solutions obtained by the analytical approach.

The uncertainty in the output of the Ventilation Model is propagated through downstream models that use this output by taking the standard deviation of the integrated ventilation efficiency about the mean, and comparing the sensitivity of the downstream results to the results obtained by the mean.

9. INPUTS AND REFERENCES

9.1 DOCUMENTS CITED

Bird, R.B.; Stewart, W.E.; and Lightfoot, E.N. 1960. *Transport Phenomena*. New York, New York: John Wiley & Sons. TIC: 208957.

Birkholzer, J.T. and Tsang, Y.W. 2000. "Modeling the Thermal-Hydrologic Processes in a Large-Scale Underground Heater Test in Partially Saturated Fractured Tuff." Water Resources Research, 36, (6), 1431-1447. Washington, D.C.: American Geophysical Union. TIC: 248278.

BSC (Bechtel SAIC Company, LLC) 2001a. *In Situ Field Testing of Processes*. ANL-NBS-HS-000005 REV 01. Las Vegas, Nevada: Bechtel SAIC Company. ACC: MOL.20020108.0351.

BSC 2001b. *Repository Multiple Waste Package Thermal Calculation*. CAL-WIS-TH-000010 REV 00. Las Vegas, Nevada: Bechtel SAIC Company. ACC: MOL.20010814.0330.

BSC 2001c. *Development of Numerical Grids for UZ Flow and Transport Modeling*. ANL-NBS-HS-000015 REV 00 ICN 01. Las Vegas, Nevada: Bechtel SAIC Company. ACC: MOL.20020211.0002.

BSC 2001d. *UZ Flow Models and Submodels*. MDL-NBS-HS-000006 REV 00 ICN 01. Las Vegas, Nevada: Bechtel SAIC Company. ACC: MOL.20020417.0382.

BSC 2001e. *ANSYS Calculations in Support of Natural Ventilation Parametric Study for SR*. CAL-SVS-HV-000003 REV 00 ICN 01. Las Vegas, Nevada: Bechtel SAIC Company. ACC: MOL.20010613.0250.

BSC 2002a. *Repository Design Project, Repository/PA IED Typical Waste Package Components Assembly*. 800-IED-EBS0-00100-000-00A. Las Vegas, Nevada: Bechtel SAIC Company. ACC: MOL.20021015.0310.

BSC 2002b. *Repository Design Project, Repository/PA IED Emplacement Drift Configuration*. 800-IED-EBS0-00200-000-00A. Las Vegas, Nevada: Bechtel SAIC Company. ACC: MOL.20021031.0104.

BSC 2002c. *The Enhanced Plan for Features, Events, and Processes (FEPs) at Yucca Mountain*. TDR-WIS-PA-000005 REV 00. Las Vegas, Nevada: Bechtel SAIC Company. ACC: MOL.20020417.0385.

BSC 2002d. *Ventilation Model*. ANL-EBS-MD-000030 REV 01 ICN 01. Las Vegas, Nevada: Bechtel SAIC Company. ACC: MOL.20021106.0055.

BSC 2002e. *Ventilation Model Report*. ANL-EBS-MD-000030 REV 02. Las Vegas, Nevada: Bechtel SAIC Company. ACC: MOL.20030102.0140.

BSC 2003a. *Technical Work Plan for: Engineered Barrier System Department Modeling and Testing FY03 Work Activities*. TWP-MGR-MD-000015 REV 03. Las Vegas, Nevada: Bechtel SAIC Company. ACC: DOC.20030225.0001.

BSC 2003b. *Repository Design Project, Repository/PA IED Geotechnical and Thermal Parameters*. 800-IED-MGR0-00100-000-00B. Las Vegas, Nevada: Bechtel SAIC Company. ACC: ENG.20030303.0005.

BSC 2003c. *Repository Design, Repository/PA IED Subsurface Facilities*. 800-IED-EBS0-00403-000-00B. Las Vegas, Nevada: Bechtel SAIC Company. ACC: MOL.20030109.0147.

BSC 2003d. *Repository Design Project, Repository/PA IED Emplacement Drift Configuration 1 of 2*. 800-IED-EBS0-00201-000-00A. Las Vegas, Nevada: Bechtel SAIC Company. ACC: ENG.20030630.0002.

BSC 2003e. *Repository Design Project, Repository/PA IED Emplacement Drift Committed Materials*. 800-IED-EBS0-00301-000-00A. Las Vegas, Nevada: Bechtel SAIC Company. ACC: ENG.20030311.0022.

BSC 2003f. *Testing to Provide Data for Ventilation System Design: Phase 1*. TDR-EBS-MD-000021 REV 00. Las Vegas, Nevada: Bechtel SAIC Company. ACC: DOC.20030711.0001.

BSC 2003g. *Repository Design Project, Repository/PA IED Emplacement Drift Configuration (2)*. 800-IED-EBS0-00202-000-00A. Las Vegas, Nevada: Bechtel SAIC Company. ACC: ENG.20030630.0003.

Canori, G.F. and Leitner, M.M. 2003. *Project Requirements Document*. TER-MGR-MD-000001 REV 01. Las Vegas, Nevada: Bechtel SAIC Company. ACC: DOC.20030404.0003.

Carslaw, H.S. and Jaeger, J.C. 1959. *Conduction of Heat in Solids*. 2nd Edition. Oxford, Great Britain: Oxford University Press. TIC: 206085.

CertainTeed. 1996. Submittal Sheet, Standard Fiber Glass Duct Wrap. Valley Forge, Pennsylvania: CertainTeed Corporation. TIC: 249257.

Cho, Y.I.; Ganic, E.N.; Hartnett, J.P.; and Rohsenow, W.M. 1998. "Basic Concepts of Heat Transfer." Chapter 1 of Handbook of Heat Transfer. 3rd Edition. Rohsenow, W.M.; Hartnett, J.P.; and Cho, Y.I., eds. New York, New York: McGraw-Hill. TIC: 253612.

Conte, S.D. and de Boor, C. 1972. *Elementary Numerical Analysis, An Algorithmic Approach*. 2nd Edition. New York, New York: McGraw-Hill. TIC: 224146.

CRWMS M&O (Civilian Radioactive Waste Management System Management and Operating Contractor) 2000a. *Conceptual Arrangement Simulated Emplacement Ventilation Test*. Las Vegas, Nevada: CRWMS M&O. ACC: MOL.20001219.0107.

CRWMS M&O 2000b. *Total System Performance Assessment for the Site Recommendation*. TDR-WIS-PA-000001 REV 00 ICN 01. Las Vegas, Nevada: CRWMS M&O. ACC: MOL.20001220.0045.

Ebadian, M.A. and Dong, Z.F. 1998. "Forced Convection, Internal Flow in Ducts." Chapter 5 of Handbook of Heat Transfer. 3rd Edition. Rohsenow, W.M.; Hartnett, J.P.; and Cho, Y.I.; eds. New York, New York: McGraw-Hill. TIC: 253612.

Fetter, C.W. 1993. *Contaminant Hydrogeology*. Upper Saddle River, New Jersey: Prentice Hall. TIC: 240691.

Freeze, G.A.; Brodsky, N.S.; and Swift, P.N. 2001. *The Development of Information Catalogued in REV00 of the YMP FEP Database*. TDR-WIS-MD-000003 REV 00 ICN 01. Las Vegas, Nevada: Bechtel SAIC Company. ACC: MOL.20010301.0237.

Gebhart, B.; Jaluria, Y.; Mahajan, R.L.; and Sammakia, B. 1988. *Buoyancy-Induced Flows and Transport*. Textbook Edition. New York, New York: Hemisphere Publishing Corporation. TIC: 102802.

Hahn, G.J. and Shapiro, S.S. 1967. *Statistical Models in Engineering*. New York, New York: John Wiley & Sons. TIC: 247729.

Hartman, H.L. 1982. *Mine Ventilation and Air Conditioning*. Mutmansky, J.M. and Wang, Y.J., eds. 2nd Edition. New York, New York: John Wiley & Sons. TIC: 210152.

Holman, J.P. 1997. *Heat Transfer*. 8th Edition. New York, New York: McGraw-Hill. TIC: 239954.

Incropera, F.P. and DeWitt, D.P. 1985. *Fundamentals of Heat and Mass Transfer*. 2nd Edition. New York, New York: John Wiley & Sons. TIC: 208420.

Incropera, F.P. and DeWitt, D.P. 1996. *Fundamentals of Heat and Mass Transfer*. 4th Edition. New York, New York: John Wiley & Sons. TIC: 243950.

Jury, W.A.; Gardner, W.R.; and Gardner, W.H. 1991. *Soil Physics*. 5th Edition. New York, New York: John Wiley & Sons. TIC: 241000.

Kays, W.M. and Leung, E.Y. 1963. "Heat Transfer in Annular Passages—Hydrodynamically Developed Turbulent Flow with Arbitrarily Prescribed Heat Flux." *International Journal of Heat and Mass Transfer*, *6*, (7), 537-557. New York, New York: Pergamon. TIC: 253626.

Kays, W.M. and Perkins, H.C. 1973. "Forced Convection, Internal Flow in Ducts." Section 7 of *Handbook of Heat Transfer*. Rohsenow, W.M. and Hartnett, J.P., eds. New York, New York: McGraw-Hill. TIC: 253611.

Kern, D.Q. 1950. *Process Heat Transfer*. New York, New York: McGraw-Hill. TIC: 248066.

Kuehn, T.H. and Goldstein, R.J. 1976. "Correlating Equations for Natural Convection Heat Transfer Between Horizontal Circular Cylinders." *International Journal of Heat and Mass Transfer*, *19*, (10), 1127-1134. New York, New York: Pergamon Press. TIC: 238411.

Kuehn, T.H. and Goldstein, R.J. 1978. "An Experimental Study of Natural Convection Heat Transfer in Concentric and Eccentric Horizontal Cylindrical Annuli." *Journal of Heat Transfer*, *100*, ([4]), 635-640. New York, New York: American Society of Mechanical Engineers. TIC: 244433.

Levenspiel, O. 1972. *Chemical Reaction Engineering*. 2nd Edition. New York, New York: John Wiley & Sons. TIC: 224877.

Morgan, V.T. 1975. "The Overall Convective Heat Transfer from Smooth Circular Cylinders." *Advances in Heat Transfer*. Volume 11. Irvine, T.F., Jr. and Hartnett, J.P., eds. 199-264. New York, New York: Academic Press. TIC: 254306.

Moyne, C.; Batsale, J.C.; Degiovanni, A.; and Maillet, D. 1990. "Thermal Conductivity of Wet Porous Media: Theoretical Analysis and Experimental Measurements." *Thermal Conductivity 21, Proceedings of the Twenty-First International Thermal Conductivity Conference, October 15-18, 1989, Lexington, Kentucky*. Cremers, C.J. and Fine, H.A., eds. Pages 109-120. New York, New York: Plenum Press. TIC: 249322.

Nagle, R.K. and Saff, E.B. 1994. *Fundamentals of Differential Equations and Boundary Value Problems*. Reading, Massachusetts: Addison-Wesley Publishing. TIC: 238891.

NRC (U.S. Nuclear Regulatory Commission) 2003. *Yucca Mountain Review Plan, Information Only*. NUREG-1804, Draft Final Revision 2. Washington, D.C.: U.S. Nuclear Regulatory Commission, Office of Nuclear Material Safety and Safeguards. TIC: 254002.

Perry, R.H.; Green, D.W.; and Maloney, J.O., eds. 1984. *Perry's Chemical Engineers' Handbook*. 6th Edition. New York, New York: McGraw-Hill. TIC: 246473.

Raithby, G.D. and Hollands, K.G.T. 1998. "Natural Convection." Chapter 4 of *Handbook of Heat Transfer*. 3rd Edition. Rohsenow, W.M.; Hartnett, J.P.; and Cho, Y.I.; eds. New York, New York: McGraw-Hill. TIC: 253612.

Reamer, C.W. and Williams, D.R. 2001a. Summary Highlights of NRC/DOE Technical Exchange and Management Meeting on Repository Design and Thermal-Mechanical Effects. Meeting held February 6-8, 2001, Las Vegas, Nevada. Washington, D.C.: U.S. Nuclear Regulatory Commission. ACC: MOL.20010307.0511 through MOL.20010307.0521.

Reamer, C.W. and Williams, D.R. 2001b. Summary Highlights of NRC/DOE Technical Exchange and Management Meeting on Thermal Effects on Flow. Meeting held January 8-9, 2001, Pleasanton, California. Washington, D.C.: U.S. Nuclear Regulatory Commission. ACC: MOL.20010202.0095 through MOL.20010202.0108.

Reynolds, W.C.; Lundberg, R.E.; and McCuen, P.A. 1963. "Heat Transfer in Annular Passages. General Formulation of the Problem for Arbitrarily Prescribed Wall Temperatures or Heat Fluxes." *International Journal of Heat and Mass Transfer*, *6*, (6), 483-493. New York, New York: Pergamon Press. TIC: 253625.

Sass, J.H.; Lachenbruch, A.H.; Dudley, W.W., Jr.; Priest, S.S.; and Munroe, R.J. 1988. *Temperature, Thermal Conductivity, and Heat Flow Near Yucca Mountain, Nevada: Some Tectonic and Hydrologic Implications*. Open-File Report 87-649. Denver, Colorado: U.S. Geological Survey. TIC: 203195.

Stroe, D.E. 2001. "PO#: A18763CM0A, Transmittal of Test Results." Letter from D.E. Stroe (Anter Laboratories) to M. Knudsen (CRWMS M&O), January 31, 2001, PR20939-51554c, with attachment. ACC: MOL.20010220.0057.

Sutherland, W.A. and Kays, W.M. 1964. "Heat Transfer in an Annulus with Variable Circumferential Heat Flux." *International Journal of Heat and Mass Transfer*, *7*, (11), 1187-1194. New York, New York: Pergamon. TIC: 253693.

Weast, R.C., ed. 1977. *CRC Handbook of Chemistry and Physics*. 58th Edition. Cleveland, Ohio: CRC Press. TIC: 242376.

Wildenschild, D. and Roberts, J.J. 1999. *Experimental Tests of Enhancement of Vapor Diffusion in Topopah Spring Tuff*. UCRL-JC-134850. Livermore, California: Lawrence Livermore National Laboratory. TIC: 246923.

9.2 CODES, STANDARDS, REGULATIONS, AND PROCEDURES

10 CFR 63. Energy: Disposal of High-Level Radioactive Wastes in a Geologic Repository at Yucca Mountain, Nevada. Readily available.

ANSI/NCSL Z540-2-1997. *American National Standard for Calibration — U.S. Guide to the Expression of Uncertainty in Measurement*. Boulder, Colorado: NCSL International. TIC: 251472.

AP-2.14Q, Rev. 2, ICN 2. *Review of Technical Products and Data*. Washington, D.C.: U.S. Department of Energy, Office of Civilian Radioactive Waste Management. ACC: DOC.20030206.0001.

AP-2.27Q, Rev. 1. *Planning for Science Activities.* Washington, D.C.: U.S. Department of Energy, Office of Civilian Radioactive Waste Management. ACC: DOC.20030611.0004.

AP-3.15Q, Rev. 4, ICN 2. *Managing Technical Product Inputs*. Washington, D.C.: U.S. Department of Energy, Office of Civilian Radioactive Waste Management. ACC: DOC.20030627.0002.

AP-SI.1Q, Rev. 5. *Software Management*. Washington, D.C.: U.S. Department of Energy, Office of Civilian Radioactive Waste Management. ACC: MOL.20030422.0012.

AP-SIII.10Q, Rev. 1, ICN 2. *Models*. Washington, D.C.: U.S. Department of Energy, Office of Civilian Radioactive Waste Management. ACC: DOC.20030627.0003.

AP-SV.1Q, Rev. 0, ICN 3. *Control of the Electronic Management of Information*. Washington, D.C.: U.S. Department of Energy, Office of Civilian Radioactive Waste Management. ACC: MOL.20020917.0133.

ASME PTC 19.1-1998. *Test Uncertainty, Instruments and Apparatus*. New York, New York: American Society of Mechanical Engineers. TIC: 249327.

9.3 SOURCE DATA, LISTED BY DATA TRACKING NUMBER

GS000483351030.003. Thermal Properties Measured 12/01/99 to 12/02/99 Using the Thermolink Soil Multimeter and Thermal Properties Sensor on Selected Potential Candidate Backfill Materials Used in the Engineered Barrier System. Submittal date: 11/09/2000.

GS000508312231.006. Physical Properties and Water Content from Borehole USW NRG-6, 3/19/94 to 3/27/95. Submittal date: 05/23/00.

GS020183351030.001. Uncompacted Bulk Density for Analyses Performed 02/02/00 to 05/23/00 on Potential Backfill Materials Used in the Engineered Barrier System. Submittal date: 01/22/2002.

GS950408312231.004. Physical Properties and Water Potentials of Core from Borehole USW SD-9. Submittal date: 03/01/1995.

GS951108312231.009. Physical Properties, Water Content, and Water Potential for Borehole USW SD-7. Submittal date: 09/26/1995.

GS951108312231.010. Physical Properties and Water Content for Borehole USW NRG-7/7A. Submittal date: 09/26/1995.

GS951108312231.011. Physical Properties, Water Content, and Water Potential for Borehole USW UZ-7A. Submittal date: 09/26/1995.

LB0110ECRBH2OP.001. Water Potential Data from Three Locations in the ECRB. Submittal date: 11/12/2001.

LB0208UZDSCPMI.002. Drift-Scale Calibrated Property Sets: Mean Infiltration Data Summary. Submittal date: 08/26/2002.

LB03023DKMGRID.001. UZ 3-D Site Scale Model Grids. Submittal date: 02/26/2003.

LB0302PTNTSW9I.001. PTN/TSW Interface Percolation Flux Maps for 9 Infiltration Scenarios. Submittal date: 02/28/2003.

LB991201233129.001. The Mountain-Scale Thermal-Hydrologic Model Simulations for AMR U0105, "Mountain-Scale Coupled Processes (TH) Models." Submittal date: 03/11/2000.

MO0004QGFMPICK.000. Lithostratigraphic Contacts from MO9811MWDGFM03.000 to be Qualified Under the Data Qualification Plan, TDP-NBS-GS-000001. Submittal date: 04/04/2000.

SN0208F3409100.007. Preclosure Ventilation Test: 1/4 Scale, Including Data from Cases 1 through 6 (with Results from 10/05/2000 through 12/22/2000), Final Data Revised August 2002. Submittal date: 08/27/2002.

SN0208F3409100.009. Preclosure Ventilation Test: 1/4 Scale, Phase 2, Including Data from Tests 1 through 16 (with Results from 4/25/01 to 10/01/2001), Final Data Revised August 2002. Submittal date: 08/27/2002.

SN0208T0503102.007. Thermal Conductivity of the Potential Repository Horizon Rev 3. Submittal date: 08/26/2002.

SN0303T0503102.008. Revised Thermal Conductivity of the Non-Repository Layers of Yucca Mountain. Submittal date: 03/19/2003.

SN0303T0510902.002. Revised Heat Capacity of Yucca Mountain Stratigraphic Units. Submittal date: 03/28/2003.

SNL22100196001.006. Laboratory Measurements of Thermal Conductivity as a Function of Saturation State for Welded and Nonwelded Tuff Specimens. Submittal date: 06/08/1998.

9.4 SOFTWARE CODES

Software Code: ANSYS. V5.6.2. IRIX 6.5. 10145-5.6.2-00.

Software Code: ANSYS. V5.6.2. HP-UX 11.00. 10364-5.6.2-01.

Software Code: rme6. v1.2. SUN. 10617-1.2-00.

Software Code: YMESH. v1.54. SUN. 10172-1.54-00.

9.5 OUTPUT DATA, LISTED BY DATA TRACKING NUMBER

MO0209MWDANS30.017. Revised ANSYS Calculations in Support of Ventilation Model Validation Based on Measurements from Phase I Ventilation Tests. Sun, Y. Las Vegas, Nevada.

MO0303MWDSLTLC.000. Sratigraphic Layer Thickness for LDTH Chimney P2WR5C10. Chipman, V. Las Vegas, Nevada.

MO0306MWDALAFV.000. ANSYS-LA-Fine Ventilation. Chipman, V. Las Vegas, Nevada.

MO0306MWDASLCV.001. ANSYS-LA-Coarse Ventilation. Chipman, V. Las Vegas, Nevada.

MO0306MWDCIEAP.000. ANSYS-LA-Coarse-Instantaneous-Efficiency-Application Run. Chipman, V. Las Vegas, Nevada.

MO0306MWDCIETA.000. ANSYS-LA-Coarse-Instantaneous-Efficiency-Twp-Application Run. Chipman, V. Las Vegas, Nevada.

MO0306MWDLACVD.000. Analytical-LA-Coarse Ventilation with the Delta Method Analysis. Chipman, V. Las Vegas, Nevada.

MO0306MWDMXCNV.000. Calculations in Support of the Mixed Convection Correlation Used in the Ventilation Model and Analysis Report Rev. 03. Chipman, V. Las Vegas, Nevada.

MO0306MWDRTCCV.000. Effect of Varying the Host Rock Thermal Condcutivity (Based on Saturation Level) on the Analytical-LA-Coarse Ventilation. Chipman, V. Las Vegas, Nevada.

MO0306MWDSLTLC.000. Sratigraphic Layer Thickness for LDTH Chimney P2WR5C10. Chipman, V. Las Vegas, Nevada.

MO0306MWDVTPH2.000. Ventilation Test Phase II Data Processing in Support of the Ventilation Model and Analysis Report Rev. 03. Chipman, V. Las Vegas, Nevada.

MO0307MWDAC8MV.000. Analytical-LA-Coarse-800m Ventilation. Chipman, V. Las Vegas, Nevada.

MO0307MWDAC8VD.000. Analytical-LA-Coarse-800m Ventilation with the Delta Method Analysis. Chipman, V. Las Vegas, Nevada.

10. ATTACHMENTS

Attachment I	Using the GFM and Mineralogic Hydrostatigraphic Units to Assign Thermophysical Properties to the UZ Units
Attachment II	Calculating Effective Thermophysical Properties for the Ansys-based models
Attachment III	Documentation of the Dimensionless Pulse Response Calculation
Attachment IV	Documentation of the ANSYS-LA-Coarse Ventilation Model (Inputs and Outputs)
Attachment V	Documentation of the ANSYS-LA-Fine Ventilation Model (Inputs and Outputs)
Attachment VI	Documentation of the Analytical-LA-Coarse Ventilation Model (Spreadsheet Methods)

Attachment VII	Documentation of Delta Method Using the Analytical Ventilation Model (Spreadsheet Methods)
Attachment VIII	Documentation of the Effect of Water Saturation on the Integrated Ventilation Efficiency Using the Analytical Ventilation Model (Spreadsheet Methods)
Attachment IX	Documentation of the Mixed Convection Correlation
Attachment X	Validation Calculations in Support of the Mixed Convection Correlation (Attachment IX)
Attachment XI	Analysis of the Ventilation Test Phase II Data in Support of the Calculations Performed in Attachment X
Attachment XII	Documentation of the Ventilation Phase I Post-Test ANSYS Analyses for Model Validation (Inputs and Outputs)
Attachment XIII	Analytical Solution Using MathCAD for the Contribution of Latent Heat to the In-Drift Air of a Ventilated Emplacement Drift Using a Solution for Steady State Unsaturated Flow to Moisture Potential Boundary at the Drift Wall
Attachment XIV	Documentation of the ANSYS-LA-Coarse-Instantaneous-Efficiency-Application (Inputs and Outputs)
Attachment XV	Documentation of the ANSYS-LA-Coarse-Instantaneous-Efficiency-Twp-Application (Inputs and Outputs)
Attachment XVI	Calculation for Estimating the In-Drift Cross Sectional Area Available for Air Flow
Attachment XVII	Calculation of Dittus-Boelter Heat Transfer Coefficients for the Ventilation Test Phase I Cases 1 through 5

ATTACHMENT I

USING THE GFM AND MINERALOGIC HYDROSTATIGRAPHIC UNITS TO ASSIGN THERMOPHYSICAL PROPERTIES TO THE UZ UNITS

INTENTIONALLY LEFT BLANK

DTN: SN0303T0503102.008 and SN0208T0503102.007					
GFM 3.1 Unit	Dry Bulk Thermal Conductivity (W/m·K)	Wet Bulk Thermal Conductivity (W/m·K)	Matrix Porosity	Lithophysal Porosity	Dry Bulk Density (kg/m^3)
Tpcp	1.3000	1.8100	0.1190	0.0000	2190
TpcLD	1.3000	1.8100	0.1190	0.0000	2190
Tpcpv3	0.6880	0.7960	0.0360	0.0000	2310
Tpcpv2	0.4900	1.0600	0.3850	0.0000	1460
Tpcpv1	0.4900	1.0600	0.3850	0.0000	1460
Tpbt4	0.4900	1.0600	0.3850	0.0000	1460
Tpy	0.4900	1.0600	0.3850	0.0000	1460
Tpbt3	0.4900	1.0600	0.3850	0.0000	1460
Tpp	0.4900	1.0600	0.3850	0.0000	1460
Tpb2	0.4900	1.0600	0.3850	0.0000	1460
Tptrv3	0.4900	1.0600	0.3850	0.0000	1460
Tptrv2	0.4900	1.0600	0.3850	0.0000	1460
Tptrv1	0.6880	0.7960	0.0360	0.0000	2310
Tptrn	1.3000	1.8100	0.1190	0.0000	2190
Tptrl, Tptf	1.3000	1.8100	0.1190	0.0000	2190
Tptpul RHHtop	1.1829	1.7749	0.1667	0.1228	1834
Tptpmn	1.4189	2.0741	0.1287	0.0254	2148
Tptpll	1.2784	1.8895	0.1486	0.0883	1979
Tptpln	1.4900	2.1303	0.1058	0.0302	2211
Tptpv3	0.6880	0.7960	0.0360	0.0000	2310
Tptpv2	0.4900	1.0600	0.3850	0.0000	1460
Tptpv1	0.4900	1.0600	0.3850	0.0000	1460
Tpbt1	0.4900	1.0600	0.3850	0.0000	1460
Tac	0.5950	1.2600	0.3330	0.0000	1670
Tacbt	0.5950	1.2600	0.3330	0.0000	1670
Tcpuv	0.5690	1.1300	0.3000	0.0000	1790
Tcpuc	0.5690	1.1300	0.3000	0.0000	1790
Tcpmd	1.0600	1.6300	0.2090	0.0000	2070
Tcplc	0.5690	1.1300	0.3000	0.0000	1790

DTN: SN0303T0510902.002	
Mineralogic Unit	Specific Heat (J/g·K)
Tpc	0.930
Tpcpv23	0.950
pTn	0.960
Tptrv1	0.950
Tptrnf	0.930
Tptpul	0.930
Tptpmn	0.930
Tptpll	0.930
Tptpln	0.930
Tptpv3	0.980
Tptpv2	0.980
Tptpv1-Tpbt1	1.080
Tac4	1.070
Tac3	1.070
Tac2	1.080
Tac1	1.080
Tacbt	1.020
Tcpuv	1.040
Tcpuc-Tcplc	0.930

UZ UNIT	Dry Bulk Thermal Conductivity (W/m·K)	Wet Bulk Thermal Conductivity (W/m·K)	Matrix Porosity	Lithophysal Porosity	Dry Bulk Density (kg/m^3)	Specific Heat (J/g·K)
tcw12	1.300	1.810	0.119	0.000	2190	0.930
tcw13	0.589	0.928	0.211	0.000	1885	0.950
ptn21	0.490	1.060	0.385	0.000	1460	0.960
ptn22	0.490	1.060	0.385	0.000	1460	0.960
ptn23	0.490	1.060	0.385	0.000	1460	0.960
ptn24	0.490	1.060	0.385	0.000	1460	0.960
ptn25	0.490	1.060	0.385	0.000	1460	0.960
ptn26	0.490	1.060	0.385	0.000	1460	0.960
tsw31	0.994	1.303	0.078	0.000	2250	0.940
tsw32	1.300	1.810	0.119	0.000	2190	0.930
tsw33	1.241	1.792	0.143	0.061	2012	0.930
tsw34	1.419	2.074	0.129	0.025	2148	0.930
tsw35	1.278	1.890	0.149	0.088	1979	0.930
tsw36	1.490	2.130	0.106	0.030	2211	0.930
tsw37	1.490	2.130	0.106	0.030	2211	0.930
tsw38	0.688	0.796	0.036	0.000	2310	0.980
tsw39	0.490	1.060	0.385	0.000	1460	0.980
ch1	0.490	1.060	0.385	0.000	1460	1.080
ch2	0.595	1.260	0.333	0.000	1670	1.070
ch3	0.595	1.260	0.333	0.000	1670	1.070
ch4	0.595	1.260	0.333	0.000	1670	1.080
ch5	0.595	1.260	0.333	0.000	1670	1.080
ch6	0.595	1.260	0.333	0.000	1670	1.020
pp4	0.569	1.130	0.300	0.000	1790	1.040
pp3	0.569	1.130	0.300	0.000	1790	0.930
pp2	0.815	1.380	0.255	0.000	1930	0.930

DTN: SN0303T0503102.008 and SN0208T0503102.007					
GFM 3.1 Unit	Dry Bulk Thermal Conductivity (W/m·K)	Wet Bulk Thermal Conductivity (W/m·K)	Matrix Porosity	Lithophysal Porosity	Dry Bulk Density (kg/m^3)
Tpcp	1.3	1.81	0.119	0	2190
TpcLD	1.3	1.81	0.119	0	2190
Tpcpv3	0.688	0.796	0.036	0	2310
Tpcpv2	0.49	1.06	0.385	0	1460
Tpcpv1	0.49	1.06	0.385	0	1460
Tpbt4	0.49	1.06	0.385	0	1460
Tpy	0.49	1.06	0.385	0	1460
Tpbt3	0.49	1.06	0.385	0	1460
Tpp	0.49	1.06	0.385	0	1460
Tpb2	0.49	1.06	0.385	0	1460
Tptrv3	0.49	1.06	0.385	0	1460
Tptrv2	0.49	1.06	0.385	0	1460
Tptrv1	0.688	0.796	0.036	0	2310
Tptrn	1.3	1.81	0.119	0	2190
Tptrl, Tptf	1.3	1.81	0.119	0	2190
Tptpul RHHtop	1.1829	1.7749	0.1667	0.1228	1834
Tptpmn	1.4189	2.0741	0.1287	0.0254	2148
Tptpll	1.2784	1.8895	0.1486	0.0883	1979
Tptpln	1.49	2.1303	0.1058	0.0302	2211
Tptpv3	0.688	0.796	0.036	0	2310
Tptpv2	0.49	1.06	0.385	0	1460
Tptpv1	0.49	1.06	0.385	0	1460
Tpbt1	0.49	1.06	0.385	0	1460
Tac	0.595	1.26	0.333	0	1670
Tacbt	0.595	1.26	0.333	0	1670
Tcpuv	0.569	1.13	0.3	0	1790
Tcpuc	0.569	1.13	0.3	0	1790
Tcpmd	1.06	1.63	0.209	0	2070
Tcplc	0.569	1.13	0.3	0	1790

DTN: SN0303T0510902.002	
Mineralogic Unit	Specific Heat (J/g·K)
Tpc	0.93
Tpcpv23	0.95
pTn	0.96
Tptrv1	0.95
Tptrnf	0.93
Tptpul	0.93
Tptpmn	0.93
Tptpll	0.93
Tptpln	0.93
Tptpv3	0.98
Tptpv2	0.98
Tptpv1-Tpbt1	1.08
Tac4	1.07
Tac3	1.07
Tac2	1.08
Tac1	1.08
Tacbt	1.02
Tcpuv	1.04
Tcpuc-Tcplc	0.93

UZ UNIT	Dry Bulk Thermal Conductivity (W/m·K)	Wet Bulk Thermal Conductivity (W/m·K)	Matrix Porosity	Lithophysal Porosity	Dry Bulk Density (kg/m^3)	Specific Heat (J/g·K)
tcw12	=AVERAGE(D5:D6)	=AVERAGE(E5:E6)	=AVERAGE(F5:F6)	=AVERAGE(G5:G6)	=AVERAGE(H5:H6)	=D37
tcw13	=AVERAGE(D7:D8)	=AVERAGE(E7:E8)	=AVERAGE(F7:F8)	=AVERAGE(G7:G8)	=AVERAGE(H7:H8)	=D38
ptn21	=D9	=E9	=F9	=G9	=H9	=D39
ptn22	=AVERAGE(D10:D11)	=AVERAGE(E10:E11)	=AVERAGE(F10:F11)	=AVERAGE(G10:G11)	=AVERAGE(H10:H11)	=D39
ptn23	=D11	=E11	=F11	=G11	=H11	=D39
ptn24	=AVERAGE(D11:D12)	=AVERAGE(E11:E12)	=AVERAGE(F11:F12)	=AVERAGE(G11:G12)	=AVERAGE(H11:H12)	=D39
ptn25	=D13	=E13	=F13	=G13	=H13	=D39
ptn26	=AVERAGE(D14:D16)	=AVERAGE(E14:E16)	=AVERAGE(F14:F16)	=AVERAGE(G14:G16)	=AVERAGE(H14:H16)	=D39
tsw31	=AVERAGE(D17:D18)	=AVERAGE(E17:E18)	=AVERAGE(F17:F18)	=AVERAGE(G17:G18)	=AVERAGE(H17:H18)	=AVERAGE(D40:D41)
tsw32	=D18	=E18	=F18	=G18	=H18	=D41
tsw33	=AVERAGE(D19:D20)	=AVERAGE(E19:E20)	=AVERAGE(F19:F20)	=AVERAGE(G19:G20)	=AVERAGE(H19:H20)	=AVERAGE(D41:D42)
tsw34	=D21	=E21	=F21	=G21	=H21	=D43
tsw35	=D22	=E22	=F22	=G22	=H22	=D44
tsw36	=D23	=E23	=F23	=G23	=H23	=D45
tsw37	=D23	=E23	=F23	=G23	=H23	=D45
tsw38	=D24	=E24	=F24	=G24	=H24	=D46
tsw39	=D25	=E25	=F25	=G25	=H25	=D47
ch1	=AVERAGE(D26:D27)	=AVERAGE(E26:E27)	=AVERAGE(F26:F27)	=AVERAGE(G26:G27)	=AVERAGE(H26:H27)	=D48
ch2	=D28	=E28	=F28	=G28	=H28	=D49
ch3	=D28	=E28	=F28	=G28	=H28	=D50
ch4	=D28	=E28	=F28	=G28	=H28	=D51
ch5	=D28	=E28	=F28	=G28	=H28	=D52
ch6	=D29	=E29	=F29	=G29	=H29	=D53
pp4	=D30	=E30	=F30	=G30	=H30	=D54
pp3	=D31	=E31	=F31	=G31	=H31	=D55
pp2	=AVERAGE(D32:D33)	=AVERAGE(E32:E33)	=AVERAGE(F32:F33)	=AVERAGE(G32:G33)	=AVERAGE(H32:H33)	=D55

ATTACHMENT II

CALCULATING EFFECTIVE THERMOPHYSICAL PROPERTIES FOR THE ANSYS-BASED MODELS

INTENTIONALLY LEFT BLANK

For geologic media that is comprised of air, water, and rock, the heat capacity per unit volume of the composite material is the sum of the heat capacities of the constituents weighted by volume fractions. Jury expresses this capacity as (Jury et al. 1991, p. 179):

$$C_{soil} = \chi_a \cdot C_a + \chi_w \cdot C_{vw} + \sum_{j=1}^{N} \chi_{sj} \cdot C_{sj} \quad \text{(Eq. II-1)}$$

where

χ_a = volume fraction of the air
χ_w = volume fraction of the water
χ_{sj} = volume fraction of jth component of the solids
C_a = volumetric heat capacity of the air
C_{vw} = volumetric heat capacity of the water
C_{sj} = volumetric heat capacity of the jth component of the solids

More specifically for the geologic units at Yucca Mountain, Equation II-1 can be written:

$$C_{rock} = \chi_{am} \cdot C_a + \chi_{al} \cdot C_a + \chi_w \cdot C_{vw} + \chi_s \cdot C_s \quad \text{(Eq. II-2)}$$

where

χ_{am} = volume fraction of the air in the matrix
χ_{al} = volume fraction of the air in the lithophysae
χ_w = volume fraction of the water in the matrix and
χ_s = volume fraction of the solids

The various volume fractions can be written as:

$$\chi_{al} = \frac{V_{al}}{V_s + V_{wm} + V_{am} + V_{al}} \quad \text{(Eq. II-3)}$$

$$\chi_{am} = \frac{V_{am}}{V_s + V_{wm} + V_{am} + V_{al}} \quad \text{(Eq. II-4)}$$

$$\chi_w = \frac{V_w}{V_s + V_{wm} + V_{am} + V_{al}} \quad \text{(Eq. II-5)}$$

$$\chi_s = \frac{V_s}{V_s + V_{wm} + V_{am} + V_{al}} \quad \text{(Eq. II-6)}$$

By substituting these equations into Equation II-2 and using the identity that the product of the density and the specific heat of a material is the volumetric heat capacity (Incropera and DeWitt 1996, Section 2.2.2) we obtain:

$$(V_s + V_{wm} + V_{am} + V_{al}) \cdot C_{rock} = V_{am} \cdot C_a + V_{al} \cdot C_a + V_w \cdot C_{vw} + V_s \cdot \rho_g \cdot C_p \quad \text{(Eq. II-7)}$$

where

V_{al} = volume of the air in the lithophysae
V_{am} = volume of the air in the matrix
V_{wm} = volume of the water in the matrix
V_s = volume of the solids (which equals 1)

Now consider the definitions for the matrix porosity and the lithophysal porosity. The matrix porosity is defined as the ratio of the volume of the matrix to the total volume:

$$\phi_m = \frac{V_m}{V_s + V_m} \quad \text{(Eq. II-8)}$$

where $V_m = V_{am} + V_{wm}$.

Solving for the matrix volume in terms of the matrix porosity:

$$V_m = \frac{\phi_m}{1 - \phi_m} \cdot V_s \quad \text{(Eq. II-9)}$$

The lithophysal porosity is defined as the ratio of the volume of the lithophysae to the total volume:

$$\phi_l = \frac{V_{al}}{V_s + V_m + V_{al}} \quad \text{(Eq. II-10)}$$

Solving for the volume of lithophysae:

$$V_{al} = \phi_l \cdot (V_s + V_m + V_{al}) \quad \text{(Eq. II-11)}$$

Substituting Equation II-9 into Equation II-11 yields:

$$V_{al} = \frac{\phi_l}{1 - \phi_l} \cdot (1 + \frac{\phi_m}{1 - \phi_m}) \cdot V_s \quad \text{(Eq. II-12)}$$

The saturation (S) is used to estimate the volume occupied by water:

$$V_w = S \cdot \frac{\phi_m}{1 - \phi_m} \cdot V_s \quad \text{(Eq. II-13)}$$

Substituting Equation II-12 into Equation II-7, and neglecting the heat capacity of the air ($C_a << C_{vw}$) (Jury et al. 1991, p. 180), the following equation is obtained:

$$\left(V_s + \frac{\phi_m V_s}{1 - \phi_m} + \frac{\phi_l}{1 - \phi_l} \cdot \left(1 + \frac{\phi_m}{1 - \phi_m} \right) \cdot V_s \right) \cdot C_{rock} = S \cdot \frac{\phi_m}{1 - \phi_m} C_{vw} V_s + \rho_g \cdot C_p V_s \quad \text{(Eq. II-14)}$$

Solving for C_{rock} and canceling out the volume of the solids, V_s, the volumetric heat capacity is expressed as:

$$C_{rock} = \frac{S \cdot \frac{\phi_m}{1-\phi_m} C_{vw} + \rho_g \cdot C_p}{\left(1 + \frac{\phi_m}{1-\phi_m} + \frac{\phi_l}{1-\phi_l} \cdot \left(1 + \frac{\phi_m}{1-\phi_m}\right)\right)} \qquad \text{(Eq. II-15)}$$

This methodology is implemented in the following spreadsheet to calculate effective thermophysical properties for the ANSYS models.

	C	D	E	F	G	H	I	J	K	L	M
3	Assumed Saturation =		91%								
4	Density of Water =		997	kg/m3 at	300	K					
5	Specifici Heat of Water =		4179	J/kg·K at	300	K					
7	UZ UNIT	Dry Bulk Thermal Conductivity (W/m·K)	Wet Bulk Thermal Conductivity (W/m·K)	ANSYS Thermal Conductivity (W/m·K)	Matrix Porosity	Lithophysal Porosity	ANSYS Specific Heat (J/kg·K)	Dry Bulk Density (kg/m^3)	Rock Grain Density (kg/m^3)	Volumetric Heat Capacity (J/m^3·K)	ANSYS Density (kg/m^3)
8	tcw12	1.30	1.81	1.76	0.12	0.00	930	2190	2486	2485615	2673
9	tcw13	0.59	0.93	0.90	0.21	0.00	950	1885	2388	2584840	2721
10	ptn21	0.49	1.06	1.01	0.39	0.00	960	1460	2374	2853974	2973
11	ptn22	0.49	1.06	1.01	0.39	0.00	960	1460	2374	2853974	2973
12	ptn23	0.49	1.06	1.01	0.39	0.00	960	1460	2374	2853974	2973
13	ptn24	0.49	1.06	1.01	0.39	0.00	960	1460	2374	2853974	2973
14	ptn25	0.49	1.06	1.01	0.39	0.00	960	1460	2374	2853974	2973
15	ptn26	0.49	1.06	1.01	0.39	0.00	960	1460	2374	2853974	2973
16	tsw31	0.99	1.30	1.27	0.08	0.00	940	2250	2439	2407361	2561
17	tsw32	1.30	1.81	1.76	0.12	0.00	930	2190	2486	2485615	2673
18	tsw33	1.24	1.79	1.74	0.14	0.06	930	2012	2528	2397584	2578
19	tsw34	1.42	2.07	2.01	0.13	0.03	930	2148	2539	2478536	2665
20	tsw35	1.28	1.89	1.83	0.15	0.09	930	1979	2593	2383196	2563
21	tsw36	1.49	2.13	2.07	0.11	0.03	930	2211	2559	2450901	2635
22	tsw37	1.49	2.13	2.07	0.11	0.03	930	2211	2559	2450901	2635
23	tsw38	0.69	0.80	0.79	0.04	0.00	980	2310	2396	2399606	2449
24	tsw39	0.49	1.06	1.01	0.39	0.00	980	1460	2374	2883174	2942
25	ch1	0.49	1.06	1.01	0.39	0.00	1080	1460	2374	3029174	2805
26	ch2	0.60	1.26	1.20	0.33	0.00	1070	1670	2504	3043109	2844
27	ch3	0.60	1.26	1.20	0.33	0.00	1070	1670	2504	3043109	2844
28	ch4	0.60	1.26	1.20	0.33	0.00	1080	1670	2504	3059809	2833
29	ch5	0.60	1.26	1.20	0.33	0.00	1080	1670	2504	3059809	2833
30	ch6	0.60	1.26	1.20	0.33	0.00	1020	1670	2504	2959609	2902
31	pp4	0.57	1.13	1.08	0.30	0.00	1040	1790	2557	2993320	2878
32	pp3	0.57	1.13	1.08	0.30	0.00	930	1790	2557	2796420	3007
33	pp2	0.81	1.38	1.33	0.25	0.00	930	1930	2589	2754976	2962

	L	M	N	O	P
2					
3					
4					
5					
6					
7	Dry Bulk Density (kg/m^3)	Rock Grain Density (kg/m^3)	Volumetric Heat Capacity (J/m^3·K)	ANSYS Density (kg/m^3)	
8	2190	=L8*(1+((G8+H8)/(1-(G8+H8))))	=(E3*(G8/(1-G8))*E4*E5+M8*I8)/((1+(G8/(1-G8)))*(1+(H8/(1-H8))))	=N8/I8	
9	1885	=L9*(1+((G9+H9)/(1-(G9+H9))))	=(E3*(G9/(1-G9))*E4*E5+M9*I9)/((1+(G9/(1-G9)))*(1+(H9/(1-H9))))	=N9/I9	
10	1460	=L10*(1+((G10+H10)/(1-(G10+H10))))	=(E3*(G10/(1-G10))*E4*E5+M10*I10)/((1+(G10/(1-G10)))*(1+(H10/(1-H10))))	=N10/I10	
11	1460	=L11*(1+((G11+H11)/(1-(G11+H11))))	=(E3*(G11/(1-G11))*E4*E5+M11*I11)/((1+(G11/(1-G11)))*(1+(H11/(1-H11))))	=N11/I11	
12	1460	=L12*(1+((G12+H12)/(1-(G12+H12))))	=(E3*(G12/(1-G12))*E4*E5+M12*I12)/((1+(G12/(1-G12)))*(1+(H12/(1-H12))))	=N12/I12	
13	1460	=L13*(1+((G13+H13)/(1-(G13+H13))))	=(E3*(G13/(1-G13))*E4*E5+M13*I13)/((1+(G13/(1-G13)))*(1+(H13/(1-H13))))	=N13/I13	
14	1460	=L14*(1+((G14+H14)/(1-(G14+H14))))	=(E3*(G14/(1-G14))*E4*E5+M14*I14)/((1+(G14/(1-G14)))*(1+(H14/(1-H14))))	=N14/I14	
15	1460	=L15*(1+((G15+H15)/(1-(G15+H15))))	=(E3*(G15/(1-G15))*E4*E5+M15*I15)/((1+(G15/(1-G15)))*(1+(H15/(1-H15))))	=N15/I15	
16	2250	=L16*(1+((G16+H16)/(1-(G16+H16))))	=(E3*(G16/(1-G16))*E4*E5+M16*I16)/((1+(G16/(1-G16)))*(1+(H16/(1-H16))))	=N16/I16	
17	2190	=L17*(1+((G17+H17)/(1-(G17+H17))))	=(E3*(G17/(1-G17))*E4*E5+M17*I17)/((1+(G17/(1-G17)))*(1+(H17/(1-H17))))	=N17/I17	
18	2012	=L18*(1+((G18+H18)/(1-(G18+H18))))	=(E3*(G18/(1-G18))*E4*E5+M18*I18)/((1+(G18/(1-G18)))*(1+(H18/(1-H18))))	=N18/I18	
19	2148	=L19*(1+((G19+H19)/(1-(G19+H19))))	=(E3*(G19/(1-G19))*E4*E5+M19*I19)/((1+(G19/(1-G19)))*(1+(H19/(1-H19))))	=N19/I19	
20	1979	=L20*(1+((G20+H20)/(1-(G20+H20))))	=(E3*(G20/(1-G20))*E4*E5+M20*I20)/((1+(G20/(1-G20)))*(1+(H20/(1-H20))))	=N20/I20	
21	2211	=L21*(1+((G21+H21)/(1-(G21+H21))))	=(E3*(G21/(1-G21))*E4*E5+M21*I21)/((1+(G21/(1-G21)))*(1+(H21/(1-H21))))	=N21/I21	
22	2211	=L22*(1+((G22+H22)/(1-(G22+H22))))	=(E3*(G22/(1-G22))*E4*E5+M22*I22)/((1+(G22/(1-G22)))*(1+(H22/(1-H22))))	=N22/I22	
23	2310	=L23*(1+((G23+H23)/(1-(G23+H23))))	=(E3*(G23/(1-G23))*E4*E5+M23*I23)/((1+(G23/(1-G23)))*(1+(H23/(1-H23))))	=N23/I23	
24	1460	=L24*(1+((G24+H24)/(1-(G24+H24))))	=(E3*(G24/(1-G24))*E4*E5+M24*I24)/((1+(G24/(1-G24)))*(1+(H24/(1-H24))))	=N24/I24	
25	1460	=L25*(1+((G25+H25)/(1-(G25+H25))))	=(E3*(G25/(1-G25))*E4*E5+M25*I25)/((1+(G25/(1-G25)))*(1+(H25/(1-H25))))	=N25/I25	
26	1670	=L26*(1+((G26+H26)/(1-(G26+H26))))	=(E3*(G26/(1-G26))*E4*E5+M26*I26)/((1+(G26/(1-G26)))*(1+(H26/(1-H26))))	=N26/I26	
27	1670	=L27*(1+((G27+H27)/(1-(G27+H27))))	=(E3*(G27/(1-G27))*E4*E5+M27*I27)/((1+(G27/(1-G27)))*(1+(H27/(1-H27))))	=N27/I27	
28	1670	=L28*(1+((G28+H28)/(1-(G28+H28))))	=(E3*(G28/(1-G28))*E4*E5+M28*I28)/((1+(G28/(1-G28)))*(1+(H28/(1-H28))))	=N28/I28	
29	1670	=L29*(1+((G29+H29)/(1-(G29+H29))))	=(E3*(G29/(1-G29))*E4*E5+M29*I29)/((1+(G29/(1-G29)))*(1+(H29/(1-H29))))	=N29/I29	
30	1670	=L30*(1+((G30+H30)/(1-(G30+H30))))	=(E3*(G30/(1-G30))*E4*E5+M30*I30)/((1+(G30/(1-G30)))*(1+(H30/(1-H30))))	=N30/I30	
31	1790	=L31*(1+((G31+H31)/(1-(G31+H31))))	=(E3*(G31/(1-G31))*E4*E5+M31*I31)/((1+(G31/(1-G31)))*(1+(H31/(1-H31))))	=N31/I31	
32	1790	=L32*(1+((G32+H32)/(1-(G32+H32))))	=(E3*(G32/(1-G32))*E4*E5+M32*I32)/((1+(G32/(1-G32)))*(1+(H32/(1-H32))))	=N32/I32	
33	1930	=L33*(1+((G33+H33)/(1-(G33+H33))))	=(E3*(G33/(1-G33))*E4*E5+M33*I33)/((1+(G33/(1-G33)))*(1+(H33/(1-H33))))	=N33/I33	
34					

	B	C	D	E	F	G	H	I	J
2									
3		Assumed Saturation =		0.90542					
4		Density of Water =		997	kg/m3 at	300	K		
5		Specifici Heat of Water =		4179	J/kg·K at	300	K		
6									
7		**UZ UNIT**	**Dry Bulk Thermal Conductivity (W/m·K)**	**Wet Bulk Thermal Conductivity (W/m·K)**	**ANSYS Thermal Conductivity (W/m·K)**	**Matrix Porosity**	**Lithophysal Porosity**	**ANSYS Specific Heat (J/kg·K)**	
8		tcw12	1.3	1.81	=D8+((E8-D8)/100)*E3*100	0.119	0	='GFM to UZ Raw Data'!I58*1000	
9		tcw13	0.589	0.928	=D9+((E9-D9)/100)*E3*100	0.2105	0	='GFM to UZ Raw Data'!I59*1000	
10		ptn21	0.49	1.06	=D10+((E10-D10)/100)*E3*100	0.385	0	='GFM to UZ Raw Data'!I60*1000	
11		ptn22	0.49	1.06	=D11+((E11-D11)/100)*E3*100	0.385	0	='GFM to UZ Raw Data'!I61*1000	
12		ptn23	0.49	1.06	=D12+((E12-D12)/100)*E3*100	0.385	0	='GFM to UZ Raw Data'!I62*1000	
13		ptn24	0.49	1.06	=D13+((E13-D13)/100)*E3*100	0.385	0	='GFM to UZ Raw Data'!I63*1000	
14		ptn25	0.49	1.06	=D14+((E14-D14)/100)*E3*100	0.385	0	='GFM to UZ Raw Data'!I64*1000	
15		ptn26	0.49	1.06	=D15+((E15-D15)/100)*E3*100	0.385	0	='GFM to UZ Raw Data'!I65*1000	
16		tsw31	0.994	1.303	=D16+((E16-D16)/100)*E3*100	0.0775	0	='GFM to UZ Raw Data'!I66*1000	
17		tsw32	1.3	1.81	=D17+((E17-D17)/100)*E3*100	0.119	0	='GFM to UZ Raw Data'!I67*1000	
18		tsw33	1.24145	1.79245	=D18+((E18-D18)/100)*E3*100	0.14285	0.0614	='GFM to UZ Raw Data'!I68*1000	
19		tsw34	1.4189	2.0741	=D19+((E19-D19)/100)*E3*100	0.1287	0.0254	='GFM to UZ Raw Data'!I69*1000	
20		tsw35	1.2784	1.8895	=D20+((E20-D20)/100)*E3*100	0.1486	0.0883	='GFM to UZ Raw Data'!I70*1000	
21		tsw36	1.49	2.1303	=D21+((E21-D21)/100)*E3*100	0.1058	0.0302	='GFM to UZ Raw Data'!I71*1000	
22		tsw37	1.49	2.1303	=D22+((E22-D22)/100)*E3*100	0.1058	0.0302	='GFM to UZ Raw Data'!I72*1000	
23		tsw38	0.688	0.796	=D23+((E23-D23)/100)*E3*100	0.036	0	='GFM to UZ Raw Data'!I73*1000	
24		tsw39	0.49	1.06	=D24+((E24-D24)/100)*E3*100	0.385	0	='GFM to UZ Raw Data'!I74*1000	
25		ch1	0.49	1.06	=D25+((E25-D25)/100)*E3*100	0.385	0	='GFM to UZ Raw Data'!I75*1000	
26		ch2	0.595	1.26	=D26+((E26-D26)/100)*E3*100	0.333	0	='GFM to UZ Raw Data'!I76*1000	
27		ch3	0.595	1.26	=D27+((E27-D27)/100)*E3*100	0.333	0	='GFM to UZ Raw Data'!I77*1000	
28		ch4	0.595	1.26	=D28+((E28-D28)/100)*E3*100	0.333	0	='GFM to UZ Raw Data'!I78*1000	
29		ch5	0.595	1.26	=D29+((E29-D29)/100)*E3*100	0.333	0	='GFM to UZ Raw Data'!I79*1000	
30		ch6	0.595	1.26	=D30+((E30-D30)/100)*E3*100	0.333	0	='GFM to UZ Raw Data'!I80*1000	
31		pp4	0.569	1.13	=D31+((E31-D31)/100)*E3*100	0.3	0	='GFM to UZ Raw Data'!I81*1000	
32		pp3	0.569	1.13	=D32+((E32-D32)/100)*E3*100	0.3	0	='GFM to UZ Raw Data'!I82*1000	
33		pp2	0.8145	1.38	=D33+((E33-D33)/100)*E3*100	0.2545	0	='GFM to UZ Raw Data'!I83*1000	
34									

INTENTIONALLY LEFT BLANK

ATTACHMENT III

DOCUMENTATION OF THE DIMENSIONLESS PULSE RESPONSE CALCULATION

INTENTIONALLY LEFT BLANK

This attachment documents a Mathcad calculation to develop the dimensionless pulse response used in the analytical ventilation calculations. The electronic copy of the Mathcad calculation, Dimensionless Pulse Response.mcd, and the text output files DIMPULSE1.txt and DIMPULSE2.txt are contained in the zipped file Dimensionless Pulse.zip (DTN: MO0307MWDAC8MV.000).

Develop a calculation of the dimensionless wall-temperature response due to a pulse for a region bounded internally by a cylinder for an arbitrary radius and thermal physical properties. Using Equation 6-57:

$$F(\xi,\tau) := -\left(1 - e^{-\xi^2\cdot\tau}\right)\cdot\frac{\left[\left(J0(\xi)\right)\cdot Y1(\xi) - Y0(\xi)\cdot J1(\xi)\right]}{\xi^2\cdot\left(J1(\xi)^2 + Y1(\xi)^2\right)}$$

Estimate the range of dimensionless time (τ):

$$\alpha := 20\cdot\frac{m^2}{yr}$$

$$a := 10\cdot m$$

$$t := 1\cdot yr$$

$$\tau := \frac{\alpha\cdot t}{a^2}$$

$$\tau = 0.2$$

$$\alpha := 30\cdot\frac{m^2}{yr}$$

$$a := 2.\cdot m$$

$$t := 1000\cdot yr$$

$$\tau := \frac{\alpha\cdot t}{a^2}$$

$$\tau = 7.5\times 10^3$$

Use a values of τ as 10, 20, 50, 100, 200, 400, 1000, 5000, which lie within the previously established bounds of τ = 0.2 to 7500.

$$\xi := 0, 0.1 .. 100$$

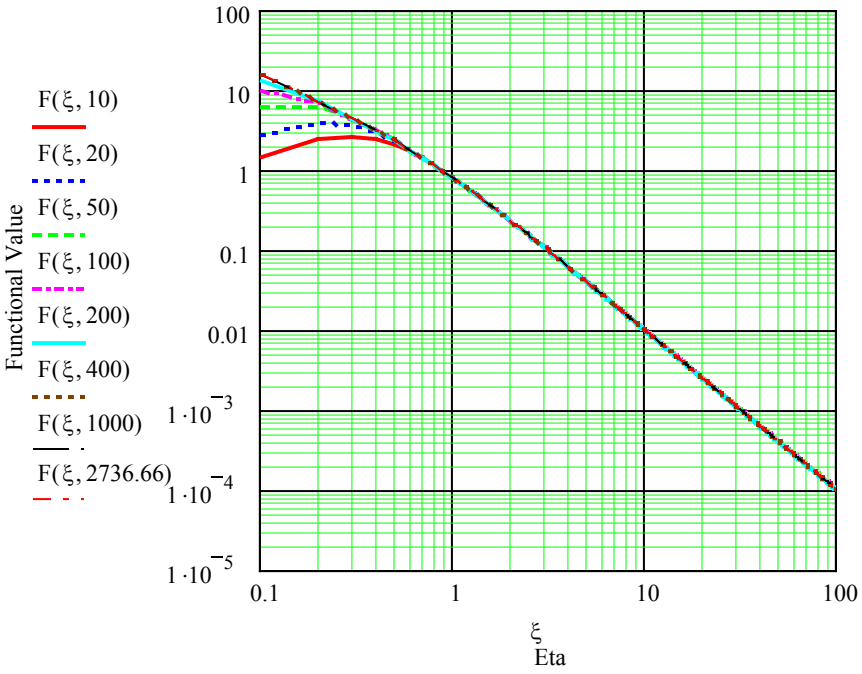

$$\Theta(\tau) := \frac{2}{\pi} \cdot \int_0^{\infty} F(\xi, \tau)\, d\xi$$

$$\tau := .01 , .02 .. 10.0$$

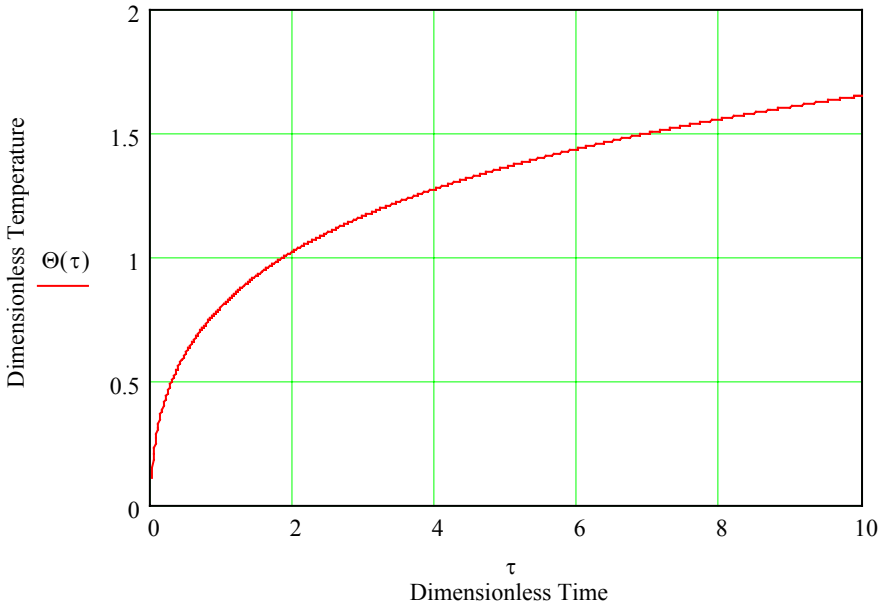

This is the relationship presented by Carslaw and Jaeger (1959, p. 338).

$$\tau := 1, 2 .. 7500.($$

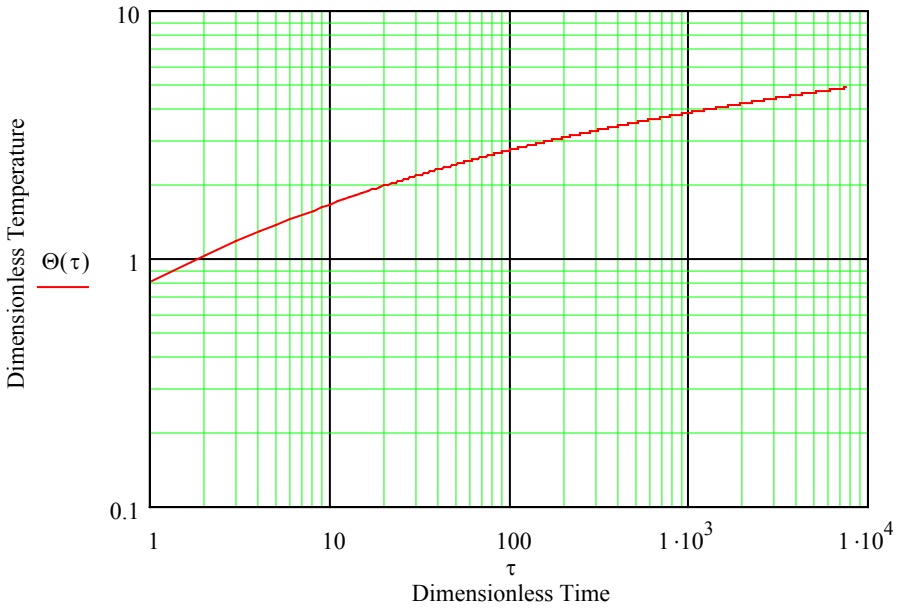

Define an interpolation array and an interpolation function for the “working” equation.

$$i := 1 .. 100$$

$$\tau_i := 0.0 + (i - 1)\cdot 0.1$$

$$Kv_{i,1} := \tau_i$$

$$Kv_{i,2} := \Theta(\tau_i)$$

$$i := 1, 2 .. 15000$$

$$\tau_i := 10.0 + (i - 1)\cdot 0.5$$

$$Kv1_{i,1} := \tau_i$$

$$Kv1_{i,2} := \Theta(\tau_i)$$

$$A := \text{stack}(Kv, Kv1)$$

WRITEPRN("DIMPULSE1.TXT") := A

A =

	0	1	2
0	0	0	0
1	0	0	0
2	0	0.1	0.314
3	0	0.2	0.424
4	0	0.3	0.502
5	0	0.4	0.565
6	0	0.5	0.617
7	0	0.6	0.662
8	0	0.7	0.702
9	0	0.8	0.739
10	0	0.9	0.772
11	0	1	0.802
12	0	1.1	0.83
13	0	1.2	0.857
14	0	1.3	0.881
15	0	1.4	0.905

Write out a pulse to 10000 years every year.

$$i := 1, 2 .. 10000$$

$$\tau_i := i$$

$$Kv2_{i,1} := \tau_i$$

$$Kv2_{i,2} := \Theta(\tau_i)$$

$$B := Kv2$$

WRITEPRN ("DIMPULSE2.TXT") := B

ATTACHMENT IV

DOCUMENTATION OF THE ANSYS-LA-COARSE VENTILATION MODEL (INPUTS AND OUTPUTS)

INTENTIONALLY LEFT BLANK

This attachment documents the ANSYS-LA-Coarse ventilation model which was developed using the ANSYS software and spreadsheet methods. The input and output files, and Microsoft Excel spreadsheet are contained in the file ANSYS-LA-Coarse.zip (DTN: MO0306MWDASLCV.001). Table IV-1 is a description of the input and output files, and the worksheets contained in the spreadsheet ANSYS-LA-Coarse.xls. Further documentation of the cell formulas and referencing are found within the electronic copy of the file.

Table IV-1. Contents of ANSYS-LA-Coarse.zip

ANSYS Input and Output Files	
File	**Description**
decay_data.input	ANSYS input file containing the waste package heat decay
th_data.input	ANSYS input file containing the thermal properties of the repository layers and the EBS components
la800.dat	ANSYS input file which generates the mesh and assigns thermal properties to each cell within the mesh
la800.db	ANSYS output file
la800.grph	ANSYS output file
la800.sub	ANSYS output file
la800.out	ANSYS output file
air_temp_c0 through air_temp_c10	ANSYS input files containing the inlet air temperature of the specified segment (from ANSYS-LA-Coarse.xls)
dr_h_c0 through dr_h_c10	ANSYS input file containing the drift wall convection coefficients for the specified segment (from ANSYS-LA-Coarse.xls)
wp_h_c0 through wp_h_c10	ANSYS input files containing the waste package convection coefficients for the specified segment (from ANSYS-LA-Coarse.xls)
la800c0 through la800c10	Main ANSYS input files
la800c0.db through la800c10.db	ANSYS output files
la800c0.grph through la800c10.grph	ANSYS output files
la800c0.dsub through la800c10.dsub	ANSYS output files
la800c0.mntr through la800c10.mntr	ANSYS output files
la800c0.osav through la800c10.osav	ANSYS output files
la800c0.rth through la800c10.rth	ANSYS output files
la800c0.stat through la800c10.stat	ANSYS output files
la800c0.s01 to .s21 through la800c10.s01 to .s21	ANSYS output files
la800c0.out through la800c10.out	Main ANSYS output files
result_c0 through result_c10	Temperature results that are cut from the end of the .out files and imported to ANSYS-LA-Coarse.xls
ANSYS-LA-Coarse.xls	
Worksheet	Description.
0-800m data	Contains the calculations of the heat removal by convection for each segment given the waste package, drift wall, and air temperatures, and waste package and drift wall convection coefficients. Calculates the exit air temperatures for the inlet conditions of the next segment.
Transposed 0-800m data	Contains the waste package, drift wall, and air temperature and efficiencies copied from worksheet 0-800m data into a more usable format.
Efficiency data	Contains the integrated ventilation efficiency calculation for 600 m and 800 m.

Efficiency vs. Time	Plots the ventilation efficiency versus time.
Efficiency vs. Length	Plots the ventilation efficiency versus distance from the drift inlet.
WP Temp vs. Length	Plots the waste package temperature versus distance from the drift inlet for each time step.
DW Temp vs. Length	Plots the drift wall temperature versus distance from the drift inlet for each time step.
Inlet Air Temp vs. Length	Plots the air temperature versus distance from the drift inlet for each time step.
0m through 800m	Plots the waste package, drift wall, and air temperatures versus time.
c0-t0-19 through c10-t0-19	Contains the temperature results from the result_c0 through result_c10 ANSYS output files. Performs a circumferential weighted average given the temperatures of each element of the drift wall and waste package.
c0-h through c10-h	Contains the calculation of convection heat transfer coefficients using the Mixed Convection Correlation (Attachment IX).
Matl prop and constants	Contains the inputs needed to calculate mixed convection heat transfer coefficients. These inputs are obtained from Table 4-24 and Table 4-26.

ATTACHMENT V

DOCUMENTATION OF THE ANSYS-LA-FINE VENTILATION MODEL (INPUTS AND OUTPUTS)

INTENTIONALLY LEFT BLANK

This attachment documents the ANSYS-LA-Fine ventilation model which was developed using the ANSYS software and spreadsheet methods. The input and output files, and Microsoft Excel spreadsheet are contained in the file ANSYS-LA-Fine.zip (DTN: MO0306MWDALAFV.000). Table V-1 is a description of the input and output files, and the worksheets contained in the spreadsheet ANSYS-LA-Fine.xls. Further documentation of the cell formulas and referencing are found within the electronic copy of the file.

Table V-1. Contents of ANSYS-LA-Fine.zip

ANSYS Input and Output Files	
File	**Description**
decay_data.input	ANSYS input file containing the waste package heat decay
th_data.input	ANSYS input file containing the thermal properties of the repository layers and the EBS components
la600.dat	ANSYS input file which generates the mesh and assigns thermal properties to each cell within the mesh
la600.db	ANSYS output file
la600.grph	ANSYS output file
la600.sub	ANSYS output file
la600.out	ANSYS output file
air_temp_c0 through air_temp_c24	ANSYS input files containing the inlet air temperature of the specified segment (from ANSYS-LA-Coarse.xls)
dr_h_c0 through dr_h_c24	ANSYS input file containing the drift wall convection coefficients for the specified segment (from ANSYS-LA-Coarse.xls)
wp_h_c0 through wp_h_c24	ANSYS input files containing the waste package convection coefficients for the specified segment (from ANSYS-LA-Coarse.xls)
la600c0 through la600c24	Main ANSYS input files
la600c0.db through la600c24.db	ANSYS output files
la600c0.grph through la600c24.grph	ANSYS output files
la600c0.dsub through la600c24.dsub	ANSYS output files
la600c0.mntr through la600c24.mntr	ANSYS output files
la600c0.osav through la600c24.osav	ANSYS output files
la600c0.rth through la600c24.rth	ANSYS output files
la600c0.stat through la600c24.stat	ANSYS output files
la600c0.s01 to .s21 through la600c24.s01 to .s21	ANSYS output files
la600c0.out through la600c24.out	Main ANSYS output files
result_c0 through result_c24	Temperature results that are cut from the end of the .out files and imported to ANSYS-LA-Coarse.xls
ANSYS-LA-Coarse.xls	
Worksheet	Description.
0-600m data	Contains the calculations of the heat removal by convection for each segment given the waste package, drift wall, and air temperatures, and waste package and drift wall convection coefficients. Calculates the exit air temperatures for the inlet conditions of the next segment.
Transposed 0-600m data	Contains the waste package, drift wall, and air temperature and efficiencies copied from worksheet 0-800m data into a more usable format.
Efficiency data	Contains the integrated ventilation efficiency calculation.
Efficiency vs. Time	Plots the ventilation efficiency versus time.

Efficiency vs. Length	Plots the ventilation efficiency versus distance from the drift inlet.
WP Temp vs. Length	Plots the waste package temperature versus distance from the drift inlet for each time step.
DW Temp vs. Length	Plots the drift wall temperature versus distance from the drift inlet for each time step.
Inlet Air Temp vs. Length	Plots the air temperature versus distance from the drift inlet for each time step.
0m through 600m	Plots the waste package, drift wall, and air temperatures versus time.
c0-t0-19 through c24-t0-19	Contains the temperature results from the result_c0 through result_c24 ANSYS output files. Performs a circumferential weighted average given the temperatures of each element of the drift wall and waste package.
c0-h through c24-h	Contains the calculation of convection heat transfer coefficients using the Mixed Convection Correlation (Attachment IX).
Matl prop and constants	Contains the inputs needed to calculate mixed convection heat transfer coefficients. These inputs are obtained from Table 4-24 and Table 4-26.

ATTACHMENT VI

DOCUMENTATION OF THE ANALYTICAL-LA-COARSE VENTILATION MODEL (SPREADSHEET METHODS)

INTENTIONALLY LEFT BLANK

This attachment documents the Analytical-LA-Coarse ventilation model which was developed using spreadsheet methods. The Microsoft Excel spreadsheet model is contained in the file Analytical-LA-Coarse-800m.xls (DTN: MO0307MWDAC8MV.000). Table VI-1 is a description of each worksheet contained in the spreadsheet Analytical-LA-Coarse.xls. Further documentation of the cell formulas and referencing are found within the electronic copy of the file.

Table VI-1. Contents of Analytical-LA-Coarse-800m.xls

Worksheet	Description
Input	Contains the inputs needed for other worksheets to calculate the ventilation efficiency and the preclosure temperatures of the waste package, drift wall, and in-drift air. These inputs are obtained from Section 4 and 6.5 of this report. More specific references to subsections of Section 4 and 6.5 are documented in Column G. The input values listed in Column E are cell referenced throughout the spreadsheet. No calculations are made in this worksheet.
WP Decay	Contains the power source (waste package) decay history for the preclosure period obtained from Table 4-20. This information is used if the Waste Emplacement Power History Flag ('Input!E25') is set to 2.
3 Component Exponential WP Decay	Fits the waste package power decay to a 3 component exponential equation by defining pre-exponential power constants and exponential decay constants.
Mixed Convection Inputs	Contains the inputs needed to calculate mixed convection heat transfer coefficients. These inputs are obtained from Table 4-24 and Table 4-26.
Thermal Model	Contains the calculation of the bulk thermal conductivity (which takes into account solids, and air and water filled voids) which is linear function of the water saturation of the rock. Also contains the a calculation of volumetric heat capacity and associated effective bulk density.
Dimensionless Pulse Calculation	Contains the output of the MathCad file, Dimensionless Pulse Response.mcd. The MathCad file generates a text file, DIMPULSE2.txt, which is copied into this worksheet.
Cylinder Pulse	Contains the calculation of the drift wall temperature response due to a dimensionless pulse (worksheet Dimensionless Pulse Response) for a region bounded internally by a cylinder. This worksheet uses the drift dimensions and the thermal physical properties listed in worksheet Input. The mathematical equations for this calculation are also documented in Section 6.4.2.4.1.
Slab Pulse	Contains the calculation of the drift wall temperature response due to a dimensionless pulse (worksheet Dimensionless Pulse Response) applied at the surface of a semi-infinite homogeneous slab. The mathematical equations for this calculation are also documented in Section 6.4.2.4.2.
Composite Pulse	Builds the drift wall temperature response which is a composite of the Cylinder Pulse and the Slab Pulse worksheets.
CSTR Analysis	Contains preparatory or initial calculations used in the CSTR01 through CSTR08 worksheets. These calculations use the inputs listed on worksheet Input to calculate Eq. 6-18, Eq. 6-45, Eq. 6-32, Eq. 6-31, Eq. 6-38, Eq. 6-29, Eq. 6-30, and Eq. 6-56. This worksheet also contains a summary of the convection heat transfer coefficients used in the CSTR01 through CSTR08 worksheets. A user-defined heat transfer coefficient, or the mixed convection correlation, (described in Attachment VIII) may be used here, depending on the value of a flag set on worksheet Input.
CSTR01	Contains the heat transfer analysis for the first 100-m section. These calculations use the results of the CSTR Analysis worksheet and iterative calculations of Eq. 6-18, Eq. 6-45, Eq. 6-32, Eq. 6-31, Eq. 6-38, Eq. 6-29, Eq. 6-30, Eq. 6-56, and Eq. 6-39. The methodology is described in Section 6.4.2. The output of this worksheet includes waste package, drift wall, and drift air temperatures, an energy balance, and initial conditions for CSTR02.

CSTR01-h	Contains the calculation of convection heat transfer coefficients using the Mixed Convection Correlation (Attachment VIII) for CSTR01.
CSTR02	Contains the heat transfer analysis for the second 100-m section (200-m). These calculations use the results of the CSTR01 worksheet and iterative calculations of Eq. 6-18, Eq. 6-45, Eq. 6-32, Eq. 6-31, Eq. 6-38, Eq. 6-29, Eq. 6-30, Eq. 6-56, and Eq. 6-39. The methodology is described in Section 6.4.2. The output of this worksheet includes waste package, drift wall, and drift air temperatures, an energy balance, and initial conditions for CSTR03.
CSTR02-h	Contains the calculation of convection heat transfer coefficients using the Mixed Convection Correlation (Attachment VIII) for CSTR02.
CSTR03	Contains the heat transfer analysis for the third 100-m section (300-m). These calculations use the results of the CSTR02 worksheet and iterative calculations of Eq. 6-18, Eq. 6-45, Eq. 6-32, Eq. 6-31, Eq. 6-38, Eq. 6-29, Eq. 6-30, Eq. 6-56, and Eq. 6-39. The methodology is described in Section 6.4.2. The output of this worksheet includes waste package, drift wall, and drift air temperatures, an energy balance, and initial conditions for CSTR04.
CSTR03-h	Contains the calculation of convection heat transfer coefficients using the Mixed Convection Correlation (Attachment VIII) for CSTR03.
CSTR04	Contains the heat transfer analysis for the fourth 100-m section (400-m). These calculations use the results of the CSTR03 worksheet and iterative calculations of Eq. 6-18, Eq. 6-45, Eq. 6-32, Eq. 6-31, Eq. 6-38, Eq. 6-29, Eq. 6-30, Eq. 6-56, and Eq. 6-39. The methodology is described in Section 6.4.2. The output of this worksheet includes waste package, drift wall, and drift air temperatures, an energy balance, and initial conditions for CSTR05.
CSTR04-h	Contains the calculation of convection heat transfer coefficients using the Mixed Convection Correlation (Attachment VIII) for CSTR04.
CSTR05	Contains the heat transfer analysis for the fifth 100-m section (500-m). These calculations use the results of the CSTR04 worksheet and iterative calculations of Eq. 6-18, Eq. 6-45, Eq. 6-32, Eq. 6-31, Eq. 6-38, Eq. 6-29, Eq. 6-30, Eq. 6-56, and Eq. 6-39. The methodology is described in Section 6.4.2. The output of this worksheet includes waste package, drift wall, and drift air temperatures, an energy balance, and initial conditions for CSTR06.
CSTR05-h	Contains the calculation of convection heat transfer coefficients using the Mixed Convection Correlation (Attachment VIII) for CSTR05.
CSTR06	Contains the heat transfer analysis for the sixth 100-m section (600-m). These calculations use the results of the CSTR05 worksheet and iterative calculations of Eq. 6-18, Eq. 6-45, Eq. 6-32, Eq. 6-31, Eq. 6-38, Eq. 6-29, Eq. 6-30, Eq. 6-56, and Eq. 6-39. The methodology is described in Section 6.4.2. The output of this worksheet includes waste package, drift wall, and drift air temperatures, and an energy balance, and initial conditions for CSTR07.
CSTR06-h	Contains the calculation of convection heat transfer coefficients using the Mixed Convection Correlation (Attachment VIII) for CSTR06.
CSTR07	Contains the heat transfer analysis for the seventh 100-m section (500-m). These calculations use the results of the CSTR06 worksheet and iterative calculations of Eq. 6-18, Eq. 6-45, Eq. 6-32, Eq. 6-31, Eq. 6-38, Eq. 6-29, Eq. 6-30, Eq. 6-56, and Eq. 6-39. The methodology is described in Section 6.4.2. The output of this worksheet includes waste package, drift wall, and drift air temperatures, an energy balance, and initial conditions for CSTR08.
CSTR07-h	Contains the calculation of convection heat transfer coefficients using the Mixed Convection Correlation (Attachment VIII) for CSTR07.
CSTR08	Contains the heat transfer analysis for the eighth 100-m section (600-m). These calculations use the results of the CSTR07 worksheet and iterative calculations of Eq. 6-18, Eq. 6-45, Eq. 6-32, Eq. 6-31, Eq. 6-38, Eq. 6-29, Eq. 6-30, Eq. 6-56, and Eq. 6-39. The methodology is described in Section 6.4.2. The output of this worksheet includes waste package, drift wall, and drift air temperatures, and an energy balance.

CSTR08-h	Contains the calculation of convection heat transfer coefficients using the Mixed Convection Correlation (Attachment VIII) for CSTR06.
CSTR01 Plot	Plots the waste package, drift wall, and drift air temperature results versus time for CSTR01.
CSTR02 Plot	Plots the waste package, drift wall, and drift air temperature results versus time for CSTR02.
CSTR03 Plot	Plots the waste package, drift wall, and drift air temperature results versus time for CSTR03.
CSTR04 Plot	Plots the waste package, drift wall, and drift air temperature results versus time for CSTR04.
CSTR05 Plot	Plots the waste package, drift wall, and drift air temperature results versus time for CSTR05.
CSTR06 Plot	Plots the waste package, drift wall, and drift air temperature results versus time for CSTR06.
CSTR07 Plot	Plots the waste package, drift wall, and drift air temperature results versus time for CSTR07.
CSTR08 Plot	Plots the waste package, drift wall, and drift air temperature results versus time for CSTR08.
Ventilation Efficiency	Contains the calculations of both integrated and instantaneous ventilation efficiency described by Eq. 6-6 and Eq. 6-5.

INTENTIONALLY LEFT BLANK

ATTACHMENT VII

DOCUMENTATION OF DELTA METHOD USING THE ANALYTICAL VENTILATION MODEL (SPREADSHEET METHODS)

This attachment documents the use of the Delta Method (Section 6-11) to quantify the sensitivity of the integrated ventilation efficiency to uncertainties in key input parameters. The Delta Method uses the analytical or spreadsheet approach to ventilation. The electronic copy of this Microsoft Excel spreadsheet is contained in the file Analytical-LA-Coarse-Delta-Method.xls (DTN: MO0306MWDLACVD.000) and Analytical-LA-Coarse-Delta-Method-800m.xls (DTN: MO0307MWDAC8VD.000). Table VII-1 and Table VII-2 are descriptions of each worksheet contained in the spreadsheets. Further documentation of the cell formulas and referencing are found within the electronic copy of the file.

Table VII-1. Contents of Analytical-LA-Coarse-Delta-Method.xls

Worksheet	Description
Input	Contains the inputs needed for other worksheets to calculate the ventilation efficiency and the preclosure temperatures of the waste package, drift wall, and in-dirft air. These inputs are obtained from Sections 4 and 6.5 of this report. More specific references to subsections of Sections 4 and 6.5 are documented in Column G. The input values listed in Column E are cell referenced throughout the spreadsheet. This worksheet also contains the key input parameters and their respective standard deviations used for the Delta Method (Table 6-9). No calculations are made in this worksheet.
Delta Method	Contains the calculation to determine the mean system performance (i.e., mean integrated ventilation efficiency) and its standard deviation based on the means and standard deviations of the component variables (key input parameters). This worksheet manually implements Eq. 6-89 and Eq. 6-90 described in Section 6.11.
Plot Delta Method	Qualitatively plots the results of the Delta Method to show the influence of the key input parameters on the mean and standard deviation of the integrated ventilation efficiency.
WP Decay	Contains the power source (waste package) decay history for the preclosure period obtained from Table 4-20. This information is used if the Waste Emplacement Power History Flag ('Input!E25') is set to 2.
3 Component Exponential WP Decay	Fits the waste package power decay to a 3 component exponential equation by defining pre-exponential power constants and exponential decay constants.
Mixed Convection Inputs	Contains the inputs needed to calculate mixed convection heat transfer coefficients. These inputs are obtained from Tables 4-24 and 4-26.
Thermal Model	Contains the calculation of the bulk thermal conductivity (which takes into account solids, and air and water filled voids) which is linear function of the water saturation of the rock. Also contains the a calculation of volumetric heat capacity and associated effective bulk density.
Dimensionless Pulse Calculation	Contains the output of the MathCad file, Dimensionless Pulse Response.mcd. The MathCad file generates a text file, DIMPULSE2.txt, which is copied into this worksheet.
Cylinder Pulse	Contains the calculation of the drift wall temperature response due to a dimensionless pulse (worksheet Dimensionless Pulse Response) for a region bounded internally by a cylinder. This worksheet uses the drift dimensions and the thermal physical properties listed in worksheet Input. The mathematical equations for this calculation are also documented in Section 6.4.2.4.1.

Slab Pulse	Contains the calculation of the drift wall temperature response due to a dimensionless pulse (worksheet Dimensionless Pulse Response) applied at the surface of a semi-infinite homogeneous slab. The mathematical equations for this calculation are also documented in Section 6.4.2.4.2.
Composite Pulse	Builds the drift wall temperature response which is a composite of the Cylinder Pulse and the Slab Pulse worksheets.
CSTR Analysis	Contains preparatory or initial calculations used in the CSTR01 through CSTR06 worksheets. These calculations use the inputs listed on worksheet Input to calculate Eq. 6-18, Eq. 6-45, Eq. 6-32, Eq. 6-31, Eq. 6-38, Eq. 6-29, Eq. 6-30, and Eq. 6-56. This worksheet also contains a summary of the convection heat transfer coefficients used in the CSTR01 through CSTR06 worksheets. A user-defined heat transfer coefficient, or the mixed convection correlation, (described in Attachment VIII) may be used here, depending on the value of a flag set on worksheet Input.
CSTR01	Contains the heat transfer analysis for the first 100-m section. These calculations use the results of the CSTR Analysis worksheet and iterative calculations of Eq. 6-18, Eq. 6-45, Eq. 6-32, Eq. 6-31, Eq. 6-38, Eq. 6-29, Eq. 6-30, Eq. 6-56, and Eq. 6-39. The methodology is described in Section 6.4.2. The output of this worksheet includes waste package, drift wall, and drift air temperatures, an energy balance, and initial conditions for CSTR02.
CSTR01-h	Contains the calculation of convection heat transfer coefficients using the Mixed Convection Correlation (Attachment VIII) for CSTR01.
CSTR02	Contains the heat transfer analysis for the second 100-m section (200-m). These calculations use the results of the CSTR01 worksheet and iterative calculations of Eq. 6-18, Eq. 6-45, Eq. 6-32, Eq. 6-31, Eq. 6-38, Eq. 6-29, Eq. 6-30, Eq. 6-56, and Eq. 6-39. The methodology is described in Section 6.4.2. The output of this worksheet includes waste package, drift wall, and drift air temperatures, an energy balance, and initial conditions for CSTR03.
CSTR02-h	Contains the calculation of convection heat transfer coefficients using the Mixed Convection Correlation (Attachment VIII) for CSTR02.
CSTR03	Contains the heat transfer analysis for the third 100-m section (300-m). These calculations use the results of the CSTR02 worksheet and iterative calculations of Eq. 6-18, Eq. 6-45, Eq. 6-32, Eq. 6-31, Eq. 6-38, Eq. 6-29, Eq. 6-30, Eq. 6-56, and Eq. 6-39. The methodology is described in Section 6.4.2. The output of this worksheet includes waste package, drift wall, and drift air temperatures, an energy balance, and initial conditions for CSTR04.
CSTR03-h	Contains the calculation of convection heat transfer coefficients using the Mixed Convection Correlation (Attachment VIII) for CSTR03.
CSTR04	Contains the heat transfer analysis for the fourth 100-m section (400-m). These calculations use the results of the CSTR03 worksheet and iterative calculations of Eq. 6-18, Eq. 6-45, Eq. 6-32, Eq. 6-31, Eq. 6-38, Eq. 6-29, Eq. 6-30, Eq. 6-56, and Eq. 6-39. The methodology is described in Section 6.4.2. The output of this worksheet includes waste package, drift wall, and drift air temperatures, an energy balance, and initial conditions for CSTR05.
CSTR04-h	Contains the calculation of convection heat transfer coefficients using the Mixed Convection Correlation (Attachment VIII) for CSTR04.
CSTR05	Contains the heat transfer analysis for the fifth 100-m section (500-m). These calculations use the results of the CSTR04 worksheet and iterative calculations of Eq. 6-18, Eq. 6-45, Eq. 6-32, Eq. 6-31, Eq. 6-38, Eq. 6-29, Eq. 6-30, Eq. 6-56, and Eq. 6-39. The methodology is described in Section 6.4.2. The output of this worksheet includes waste package, drift wall, and drift air temperatures, an energy

	balance, and initial conditions for CSTR06.
CSTR05-h	Contains the calculation of convection heat transfer coefficients using the Mixed Convection Correlation (Attachment VIII) for CSTR05.
CSTR06	Contains the heat transfer analysis for the sixth 100-m section (600-m). These calculations use the results of the CSTR05 worksheet and iterative calculations of Eq. 6-18, Eq. 6-45, Eq. 6-32, Eq. 6-31, Eq. 6-38, Eq. 6-29, Eq. 6-30, Eq. 6-56, and Eq. 6-39. The methodology is described in Section 6.4.2. The output of this worksheet includes waste package, drift wall, and drift air temperatures, and an energy balance.
CSTR06-h	Contains the calculation of convection heat transfer coefficients using the Mixed Convection Correlation (Attachment VIII) for CSTR06.
CSTR01 Plot	Plots the waste package, drift wall, and drift air temperature results versus time for CSTR01.
CSTR02 Plot	Plots the waste package, drift wall, and drift air temperature results versus time for CSTR02.
CSTR03 Plot	Plots the waste package, drift wall, and drift air temperature results versus time for CSTR03.
CSTR04 Plot	Plots the waste package, drift wall, and drift air temperature results versus time for CSTR04.
CSTR05 Plot	Plots the waste package, drift wall, and drift air temperature results versus time for CSTR05.
CSTR06 Plot	Plots the waste package, drift wall, and drift air temperature results versus time for CSTR06.
Ventilation Efficiency	Contains the calculations of both integrated and instantaneous ventilation efficiency described by Eq. 6-6 and Eq. 6-5.

Table VII-2. Contents of Analytical-LA-Coarse-Delta-Method-800m.xls

Worksheet	Description
Input	Contains the inputs needed for other worksheets to calculate the ventilation efficiency and the preclosure temperatures of the waste package, drift wall, and in-dirft air. These inputs are obtained from Sections 4 and 6.5 of this report. More specific references to subsections of Sections 4 and 6.5 are documented in Column G. The input values listed in Column E are cell referenced throughout the spreadsheet. This worksheet also contains the key input parameters and their respective standard deviations used for the Delta Method (Table 6-9). No calculations are made in this worksheet.
Delta Method	Contains the calculation to determine the mean system performance (i.e., mean integrated ventilation efficiency) and its standard deviation based on the means and standard deviations of the component variables (key input parameters). This worksheet manually implements Eq. 6-89 and Eq. 6-90 described in Section 6-11.
Plot Delta Method	Qualitatively plots the results of the Delta Method to show the influence of the key input parameters on the mean and standard deviation of the integrated ventilation efficiency.
WP Decay	Contains the power source (waste package) decay history for the preclosure period obtained from Table 4-20. This information is used if the Waste Emplacement Power History Flag ('Input!E25') is set to 2.
3 Component Exponential WP Decay	Fits the waste package power decay to a 3 component exponential equation by defining pre-exponential power constants and exponential decay constants.
Mixed Convection Inputs	Contains the inputs needed to calculate mixed convection heat transfer coefficients. These inputs are obtained from Tables 4-24 and 4-26.

Thermal Model	Contains the calculation of the bulk thermal conductivity (which takes into account solids, and air and water filled voids) which is linear function of the water saturation of the rock. Also contains the a calculation of volumetric heat capacity and associated effective bulk density.
Dimensionless Pulse Calculation	Contains the output of the MathCad file, Dimensionless Pulse Response.mcd. The MathCad file generates a text file, DIMPULSE2.txt, which is copied into this worksheet.
Cylinder Pulse	Contains the calculation of the drift wall temperature response due to a dimensionless pulse (worksheet Dimensionless Pulse Response) for a region bounded internally by a cylinder. This worksheet uses the drift dimensions and the thermal physical properties listed in worksheet Input. The mathematical equations for this calculation are also documented in Section 6.4.2.4.1.
Slab Pulse	Contains the calculation of the drift wall temperature response due to a dimensionless pulse (worksheet Dimensionless Pulse Response) applied at the surface of a semi-infinite homogeneous slab. The mathematical equations for this calculation are also documented in Section 6.4.2.4.2.
Composite Pulse	Builds the drift wall temperature response which is a composite of the Cylinder Pulse and the Slab Pulse worksheets.
CSTR Analysis	Contains preparatory or initial calculations used in the CSTR01 through CSTR06 worksheets. These calculations use the inputs listed on worksheet Input to calculate Eq. 6-18, Eq. 6-45, Eq. 6-32, Eq. 6-31, Eq. 6-38, Eq. 6-29, Eq. 6-30, and Eq. 6-56. This worksheet also contains a summary of the convection heat transfer coefficients used in the CSTR01 through CSTR06 worksheets. A user-defined heat transfer coefficient, or the mixed convection correlation, (described in Attachment VIII) may be used here, depending on the value of a flag set on worksheet Input.
CSTR01	Contains the heat transfer analysis for the first 100-m section. These calculations use the results of the CSTR Analysis worksheet and iterative calculations of Eq. 6-18, Eq. 6-45, Eq. 6-32, Eq. 6-31, Eq. 6-38, Eq. 6-29, Eq. 6-30, Eq. 6-56, and Eq. 6-39. The methodology is described in Section 6.4.2. The output of this worksheet includes waste package, drift wall, and drift air temperatures, an energy balance, and initial conditions for CSTR02.
CSTR01-h	Contains the calculation of convection heat transfer coefficients using the Mixed Convection Correlation (Attachment VIII) for CSTR01.
CSTR02	Contains the heat transfer analysis for the second 100-m section (200-m). These calculations use the results of the CSTR01 worksheet and iterative calculations of Eq. 6-18, Eq. 6-45, Eq. 6-32, Eq. 6-31, Eq. 6-38, Eq. 6-29, Eq. 6-30, Eq. 6-56, and Eq. 6-39. The methodology is described in Section 6.4.2. The output of this worksheet includes waste package, drift wall, and drift air temperatures, an energy balance, and initial conditions for CSTR03.
CSTR02-h	Contains the calculation of convection heat transfer coefficients using the Mixed Convection Correlation (Attachment VIII) for CSTR02.
CSTR03	Contains the heat transfer analysis for the third 100-m section (300-m). These calculations use the results of the CSTR02 worksheet and iterative calculations of Eq. 6-18, Eq. 6-45, Eq. 6-32, Eq. 6-31, Eq. 6-38, Eq. 6-29, Eq. 6-30, Eq. 6-56, and Eq. 6-39. The methodology is described in Section 6.4.2. The output of this worksheet includes waste package, drift wall, and drift air temperatures, an energy balance, and initial conditions for CSTR04.
CSTR03-h	Contains the calculation of convection heat transfer coefficients using the Mixed Convection Correlation (Attachment VIII) for CSTR03.
CSTR04	Contains the heat transfer analysis for the fourth 100-m section (400-m). These calculations use the results of the CSTR03 worksheet and iterative calculations of Eq. 6-18, Eq. 6-45, Eq. 6-32, Eq. 6-31, Eq. 6-38, Eq. 6-29, Eq. 6-30, Eq. 6-56, and Eq. 6-39. The methodology is described in Section 6.4.2. The output of this worksheet includes waste package, drift wall, and drift air temperatures, an energy balance, and initial conditions for CSTR05.
CSTR04-h	Contains the calculation of convection heat transfer coefficients using the Mixed

	Convection Correlation (Attachment VIII) for CSTR04.
CSTR05	Contains the heat transfer analysis for the fifth 100-m section (500-m). These calculations use the results of the CSTR04 worksheet and iterative calculations of Eq. 6-18, Eq. 6-45, Eq. 6-32, Eq. 6-31, Eq. 6-38, Eq. 6-29, Eq. 6-30, Eq. 6-56, and Eq. 6-39. The methodology is described in Section 6.4.2. The output of this worksheet includes waste package, drift wall, and drift air temperatures, an energy balance, and initial conditions for CSTR06.
CSTR05-h	Contains the calculation of convection heat transfer coefficients using the Mixed Convection Correlation (Attachment VIII) for CSTR05.
CSTR06	Contains the heat transfer analysis for the sixth 100-m section (600-m). These calculations use the results of the CSTR05 worksheet and iterative calculations of Eq. 6-18, Eq. 6-45, Eq. 6-32, Eq. 6-31, Eq. 6-38, Eq. 6-29, Eq. 6-30, Eq. 6-56, and Eq. 6-39. The methodology is described in Section 6.4.2. The output of this worksheet includes waste package, drift wall, and drift air temperatures, and an energy balance, and initial conditions for CSTR07.
CSTR06-h	Contains the calculation of convection heat transfer coefficients using the Mixed Convection Correlation (Attachment VIII) for CSTR06.
CSTR07	Contains the heat transfer analysis for the seventh 100-m section (500-m). These calculations use the results of the CSTR06 worksheet and iterative calculations of Eq. 6-18, Eq. 6-45, Eq. 6-32, Eq. 6-31, Eq. 6-38, Eq. 6-29, Eq. 6-30, Eq. 6-56, and Eq. 6-39. The methodology is described in Section 6.4.2. The output of this worksheet includes waste package, drift wall, and drift air temperatures, an energy balance, and initial conditions for CSTR08.
CSTR07-h	Contains the calculation of convection heat transfer coefficients using the Mixed Convection Correlation (Attachment VIII) for CSTR07.
CSTR08	Contains the heat transfer analysis for the eighth 100-m section (600-m). These calculations use the results of the CSTR07 worksheet and iterative calculations of Eq. 6-18, Eq. 6-45, Eq. 6-32, Eq. 6-31, Eq. 6-38, Eq. 6-29, Eq. 6-30, Eq. 6-56, and Eq. 6-39. The methodology is described in Section 6.4.2. The output of this worksheet includes waste package, drift wall, and drift air temperatures, and an energy balance.
CSTR08-h	Contains the calculation of convection heat transfer coefficients using the Mixed Convection Correlation (Attachment VIII) for CSTR06.
CSTR01 Plot	Plots the waste package, drift wall, and drift air temperature results versus time for CSTR01.
CSTR02 Plot	Plots the waste package, drift wall, and drift air temperature results versus time for CSTR02.
CSTR03 Plot	Plots the waste package, drift wall, and drift air temperature results versus time for CSTR03.
CSTR04 Plot	Plots the waste package, drift wall, and drift air temperature results versus time for CSTR04.
CSTR05 Plot	Plots the waste package, drift wall, and drift air temperature results versus time for CSTR05.
CSTR06 Plot	Plots the waste package, drift wall, and drift air temperature results versus time for CSTR06.
CSTR07 Plot	Plots the waste package, drift wall, and drift air temperature results versus time for CSTR07.
CSTR08 Plot	Plots the waste package, drift wall, and drift air temperature results versus time for CSTR08.
Ventilation Efficiency	Contains the calculations of both integrated and instantaneous ventilation efficiency described by Eq. 6-6 and Eq. 6-5.

ATTACHMENT VIII

DOCUMENTATION OF THE EFFECT OF WATER SATURATION ON THE INTEGRATED VENTILATION EFFICIENCY USING THE ANALYTICAL VENTILATION MODEL (SPREADSHEET METHODS)

This attachment documents the use of the effect of water saturation on the integrated ventilation efficiency (Section 6.9.2). The electronic copy of this Microsoft Excel spreadsheet is contained in the file Analytical-LA-Coarse-Wet-vs-Dry-kth.xls (DTN: MO0306MWDRTCCV.000). Table VIII-1 is a description of each worksheet contained in the spreadsheet Analytical-LA-Coarse-Delta-Method.xls. Further documentation of the cell formulas and referencing are found within the electronic copy of the file.

Table VIII-1. Contents of Analytical-LA-Coarse-Wet-vs-Dry-kth.xls

Worksheet	Description
Input	Contains the inputs needed for other worksheets to calculate the ventilation efficiency and the preclosure temperatures of the waste package, drift wall, and in-drift air. These inputs are obtained from Sections 4 and 6.5 of this report. More specific references to subsections of Sections 4 and 6.5 are documented in Column G. The input values listed in Column E are cell referenced throughout the spreadsheet. This worksheet also contains the key input parameters and their respective standard deviations used for the Delta Method (Table 6-9). No calculations are made in this worksheet.
Wet vs. Dry	Contains the results of varying the water saturation on the integrated ventilation efficiency and waste package, drift wall, and drift air temperatures. This calculation is made by changing the water saturation input on worksheet Input and manually pasting the results into the Wet vs. Dry worksheet.
WP Decay	Contains the power source (waste package) decay history for the preclosure period obtained from Table 4-20. This information is used if the Waste Emplacement Power History Flag ('Input!E25') is set to 2.
3 Component Exponential WP Decay	Fits the waste package power decay to a 3 component exponential equation by defining pre-exponential power constants and exponential decay constants.
Mixed Convection Inputs	Contains the inputs needed to calculate mixed convection heat transfer coefficients. These inputs are obtained from Tables 4-24 and 4-26.
Thermal Model	Contains the calculation of the bulk thermal conductivity (which takes into account solids, and air and water filled voids) which is linear function of the water saturation of the rock. Also contains the a calculation of volumetric heat capacity and associated effective bulk density.
Dimensionless Pulse Calculation	Contains the output of the MathCad file, Dimensionless Pulse Response.mcd. The MathCad file generates a text file, DIMPULSE2.txt, which is copied into this worksheet.
Cylinder Pulse	Contains the calculation of the drift wall temperature response due to a dimensionless pulse (worksheet Dimensionless Pulse Response) for a region bounded internally by a cylinder. This worksheet uses the drift dimensions and the thermal physical properties listed in worksheet Input. The mathematical equations for this calculation are also documented in Section 6.4.2.4.1.
Slab Pulse	Contains the calculation of the drift wall temperature response due to a dimensionless pulse (worksheet Dimensionless Pulse Response) applied at the surface of a semi-infinite homogeneous slab. The mathematical equations for this calculation are also documented in Section 6.4.2.4.2.
Composite Pulse	Builds the drift wall temperature response which is a composite of the Cylinder Pulse and the Slab Pulse worksheets.

CSTR Analysis	Contains preparatory or initial calculations used in the CSTR01 through CSTR06 worksheets. These calculations use the inputs listed on worksheet Input to calculate Eq. 6-18, Eq. 6-45, Eq. 6-32, Eq. 6-31, Eq. 6-38, Eq. 6-29, Eq. 6-30, and Eq. 6-56. This worksheet also contains a summary of the convection heat transfer coefficients used in the CSTR01 through CSTR06 worksheets. A user-defined heat transfer coefficient, or the mixed convection correlation, (described in Attachment VIII) may be used here, depending on the value of a flag set on worksheet Input.
CSTR01	Contains the heat transfer analysis for the first 100-m section. These calculations use the results of the CSTR Analysis worksheet and iterative calculations of Eq. 6-18, Eq. 6-45, Eq. 6-32, Eq. 6-31, Eq. 6-38, Eq. 6-29, Eq. 6-30, Eq. 6-56, and Eq. 6-39. The methodology is described in Section 6.4.2. The output of this worksheet includes waste package, drift wall, and drift air temperatures, an energy balance, and initial conditions for CSTR02.
CSTR01-h	Contains the calculation of convection heat transfer coefficients using the Mixed Convection Correlation (Attachment VIII) for CSTR01.
CSTR02	Contains the heat transfer analysis for the second 100-m section (200-m). These calculations use the results of the CSTR01 worksheet and iterative calculations of Eq. 6-18, Eq. 6-45, Eq. 6-32, Eq. 6-31, Eq. 6-38, Eq. 6-29, Eq. 6-30, Eq. 6-56, and Eq. 6-39. The methodology is described in Section 6.4.2. The output of this worksheet includes waste package, drift wall, and drift air temperatures, an energy balance, and initial conditions for CSTR03.
CSTR02-h	Contains the calculation of convection heat transfer coefficients using the Mixed Convection Correlation (Attachment VIII) for CSTR02.
CSTR03	Contains the heat transfer analysis for the third 100-m section (300-m). These calculations use the results of the CSTR02 worksheet and iterative calculations of Eq. 6-18, Eq. 6-45, Eq. 6-32, Eq. 6-31, Eq. 6-38, Eq. 6-29, Eq. 6-30, Eq. 6-56, and Eq. 6-39. The methodology is described in Section 6.4.2. The output of this worksheet includes waste package, drift wall, and drift air temperatures, an energy balance, and initial conditions for CSTR04.
CSTR03-h	Contains the calculation of convection heat transfer coefficients using the Mixed Convection Correlation (Attachment VIII) for CSTR03.
CSTR04	Contains the heat transfer analysis for the fourth 100-m section (400-m). These calculations use the results of the CSTR03 worksheet and iterative calculations of Eq. 6-18, Eq. 6-45, Eq. 6-32, Eq. 6-31, Eq. 6-38, Eq. 6-29, Eq. 6-30, Eq. 6-56, and Eq. 6-39. The methodology is described in Section 6.4.2. The output of this worksheet includes waste package, drift wall, and drift air temperatures, an energy balance, and initial conditions for CSTR05.
CSTR04-h	Contains the calculation of convection heat transfer coefficients using the Mixed Convection Correlation (Attachment VIII) for CSTR04.
CSTR05	Contains the heat transfer analysis for the fifth 100-m section (500-m). These calculations use the results of the CSTR04 worksheet and iterative calculations of Eq. 6-18, Eq. 6-45, Eq. 6-32, Eq. 6-31, Eq. 6-38, Eq. 6-29, Eq. 6-30, Eq. 6-56, and Eq. 6-39. The methodology is described in Section 6.4.2. The output of this worksheet includes waste package, drift wall, and drift air temperatures, an energy balance, and initial conditions for CSTR06.
CSTR05-h	Contains the calculation of convection heat transfer coefficients using the Mixed Convection Correlation (Attachment VIII) for CSTR05.
CSTR06	Contains the heat transfer analysis for the sixth 100-m section (600-m). These calculations use the results of the CSTR05 worksheet and iterative calculations of Eq. 6-18, Eq. 6-45, Eq. 6-32, Eq. 6-31, Eq. 6-38, Eq. 6-29, Eq. 6-30, Eq. 6-56, and Eq. 6-39. The methodology is

	described in Section 6.4.2. The output of this worksheet includes waste package, drift wall, and drift air temperatures, and an energy balance.
CSTR06-h	Contains the calculation of convection heat transfer coefficients using the Mixed Convection Correlation (Attachment VIII) for CSTR06.
CSTR01 Plot	Plots the waste package, drift wall, and drift air temperature results versus time for CSTR01.
CSTR02 Plot	Plots the waste package, drift wall, and drift air temperature results versus time for CSTR02.
CSTR03 Plot	Plots the waste package, drift wall, and drift air temperature results versus time for CSTR03.
CSTR04 Plot	Plots the waste package, drift wall, and drift air temperature results versus time for CSTR04.
CSTR05 Plot	Plots the waste package, drift wall, and drift air temperature results versus time for CSTR05.
CSTR06 Plot	Plots the waste package, drift wall, and drift air temperature results versus time for CSTR06.
Ventilation Efficiency	Contains the calculations of both integrated and instantaneous ventilation efficiency described by Eq. 6-6 and Eq. 6-5.

ATTACHMENT IX

DOCUMENTATION OF THE MIXED CONVECTION METHODOLOGY

SYMBOLS

a	coefficient in Fourier series for $q''(x,\theta)$
b	coefficient in Fourier series for $q''(x,\theta)$
c	Nusselt number coefficient for laminar natural convection
$\overline{C}$	Nusselt number coefficient for turbulent natural convection
D	diameter
D_h	hydraulic diameter D_o - D_i
e*	dimensionless eccentricity, $2\varepsilon/(D_o - D_i)$, positive upward
g	gravitational acceleration
$h(x,\theta)$	local convective heat transfer coefficient
$\overline{h}(x)$	effective circumferential convective heat transfer coefficient
h_{cond}	overall conductive heat transfer coefficient for the combined concrete and insulation.
$\tilde{h}$	error in convection coefficient
k	thermal conductivity of the fluid
L_i	combined length of the waste packages
m	exponent for blending laminar and turbulent forms for Nusselt numbers
M	value of the second derivative of y with respect to x somewhere in (x_0, x_1)
$\overline{Nu}(x)$	effective circumferential Nusselt number, $\overline{h}(x)(D_o - D_i)/k$
Nu_{conv}	Nusselt number for overall natural convection between the cylinders, $\frac{D_i\overline{q}''}{k(\overline{T}_i - \overline{T}_o)}$
Nu_i'	Kuehn-Goldstein Nusselt number, $\overline{h}_i D_i/k$
Nu_{ii}	forced-convection Nusselt number of inner cylinder when it alone is heated
Nu_{oo}	forced-convection Nusselt number of outer cylinder when it alone is heated
Nu_o'	Kuehn-Goldstein Nusselt number for the outer cylinder, $\overline{h}_o D_o/k$
Pr	Prandtl number, ν/α
$q''(x,\theta)$	convective heat flux (positive into the fluid)
$\overline{q}''(x)$	circumferential average convective heat flux (positive into the fluid)
$\overline{q}''_{rad,i}(x)$	circumferential average radiative flux from the waste packages at location x
q_{in}	24-hour average power generated in the waste packages
r^*	ratio of the diameters, D_i/D_o
R_n	eigenfunction for nth harmonic of axial variation in heat flux on one wall (the next subscript is the affected wall; the last subscript is the heated wall)
$Ra(x)$	Rayleigh number, $\frac{g\beta D^3}{\nu\alpha}\left\lvert\overline{T}(x) - T_f(x)\right\rvert$
Re	dimensionless Reynolds number, $\frac{u_m(D_o - D_i)}{\nu}$
Re_0	Reynolds number at the lower end of an interpolation interval
Re_1	Reynolds number at the upper end of an interpolation interval

Re_M	equivalent Reynolds number for mixed convection
Re_N	equivalent Reynolds number for natural convection
$T(x,\theta)$	surface temperature
$\overline{T}(x)$	circumferential average surface temperature
$\overline{\overline{T^4}}(x)$	24-hour and circumferential average of the 4th power of the absolute temperature
$T_f(x)$	mean fluid temperature
$u\ (x)$	standard uncertainty in a predicted value x
$u_c\ (y)$	combined standard uncertainty in a predicted value y
u_m	mean axial fluid velocity
x	longitudinal coordinate along the cylinder in the direction of flow or input variable for an interpolation
x_0	lower boundary of an interpolation interval
x_1	upper boundary of an interpolation interval
$y\ (x)$	surrogate for any parameter being interpolated in a table

Greek Symbols

α	thermal diffusivity
β	fluid coefficient of thermal expansion
ε	distance between the central axes of the cylinders
ε_i	measured emissivity of the waste package
ε_o	measured emissivity of the concrete pipe
$\overline{\Phi}_b$	average dimensionless fluid temperature
ϕ	angle between the vertical direction and the direction of forced flow
ν	kinematic viscosity
$\tau(x)$	dimensionless temperature parameter, $\frac{\overline{T}_i(x) - T_f(x)}{\overline{T}_o(x) - T_f(x)}$
θ	angle from the zenith relative to the axis of a cylinder
σ	Stefan-Boltzmann constant
θ^*	influence coefficient in forced-convection correlation

Subscripts

a	average external ambient
b	bottom
F	forced convection
i	inner cylinder surface
L	laminar
l	left
M	mixed convection
N	natural convection
n	harmonic of Fourier expansion
o	outer cylinder surface
r	right
T	turbulent
t	top

IX. DOCUMENTATION OF THE MIXED CONVECTION METHODOLOGY

Heat transfer coefficients are classically predicted by the use of equations that are called correlations. The use of equations or correlations for the prediction not only of heat transfer coefficients, but also for mass and momentum transfer, is commonly accepted engineering practice that has been in successful use for over 50 years. The terminology of correlations or equations is not universal (for an example of the use of the word "correlation" as it refers to heat transfer, see Ebadian and Dong [1998, p. 5.26, Table 5.11]). However, Kern (1950, pp. 43 to 57) appears to use the words "correlation," "equation," and "evaluation" interchangeably. Thus, even though various word usages will appear in the text-book literature when referring to correlations, equations, and evaluations, the meanings are all the same.

Obtaining a heat-transfer correlation thus is common practice in the process industry, and usually involves a very limited set of data for a particular configuration of the heat transfer surfaces. The reason a "very limited set of data" is available is because it is not practical to have measurements of heat transfer (or mass or momentum) for every combination of independent variables. However, the final heat-transfer correlation is not based on just any equation form, but is based on the correlating parameters of Reynolds number, Prandtl number, and a few other dimensionless groups (Kern 1950, pp. 38 to 40). The fact that these correlating parameters do work is based on dimensional analysis and experience.

The test that follows evaluates heat transfer coefficients and results in a correlation for the case of mixed convection in an internally heated pipe. Mixed convection is the situation where the forced flow rate is so small that natural convection does contribute to the overall rate of heat transfer. It must be emphasized that the relative importance to the overall rate of heat transfer does not always depend on just the heat transfer coefficients, but also on what is on the other side of the surface where the heat transfer coefficient is being applied.

The efficiency of the ventilating air can be defined as the percentage of the total energy generated from the waste packages that is removed by the ventilating air. The energy is transferred to the ventilating air by a combination of forced and natural convection, defined as mixed convection. A temperature-dependent correlation of the mixed convection within the emplacement drifts has been developed. The correlation provides a measure of the convection heat transfer occurring at the waste package and drift wall surfaces in the form of a parameter equal to the dimensionless temperature gradient, the Nusselt number. From the Nusselt number, convective heat transfer coefficients dependent on temperatures of the waste package, the emplacement drift wall, and the ventilation air due to the decay of the nuclear waste can be determined.

Section IX.1 of this attachment describes the development of the mixed-convection methodology. Sections IX.2 and IX.3 present a sensitivity study and a discussion of the uncertainty associated with the methodology. Section IX.4 examines the methodology for YMP specific conditions using experimental data from the EBS Ventilation Test Series.

Results of the following activities are included:

- Development of a methodology to calculate the effective heat transfer coefficients for convection within the EBS based on mixed convection.
- Determine the sensitivity of the methodology to each of its parameters.
- Estimate the uncertainty in the heat transfer coefficients predicted by the methodology.
- Comparison of methodology results with data from the ventilation tests.

IX.1 METHODOLOGY DEVELOPMENT

As a means of general introduction, the next few sections (IX.1.1 through IX.1.3) provide an overview of mixed convection, including:

- A conceptual picture of the processes involved
- Definitions of dimensionless groups used in describing the processes
- Underlying engineering principles.

Prior to developing a mathematical methodology to quantitatively define mixed convection, a literature search was performed to determine if any applicable models appropriate for mixed convection in the YMP emplacement drifts existed. None was found, although a general methodology for combining forced and natural convection models into a mixed-convection methodology was documented. Sections IX.1.4 through IX.1.6 summarize the results of the literature search, first covering correlations for natural convection, then for forced convection, and finally the methodology for mixed convection. The summary includes correlations and methods that were not used and the rationale for not selecting them. The discussion also details the idealizations inherent in the correlations chosen for the methodology. This section refers to Section 4 for information about inputs.

IX.1.1 Concept for Mixed Convection

A concept for mixed convection can be constructed by determining the flow patterns that will be established within the emplacement drifts.

In the absence of forced ventilation, and when the inner cylinder is hotter than the outer, air adjacent to the inner cylinder will be heated, expanding and rising from buoyancy effects. When it reaches the outer cylinder, it will begin to cool as it transfers heat. The density of the air will increase as it falls along the outer wall, continuing to transfer heat to the outer cylinder. Figure IX-1a shows the resulting two-dimensional flow pattern from pure natural convection.

At sufficiently high ventilation speeds, forced convection will dominate. The flow will be exclusively axial, as shown in Figure IX-1b.

At low ventilation speeds, the forced flow is modified by the buoyancy effect. If there were no significant radiation to the outer cylinder, so that its temperature remained below the air temperature, the flow would be as in Figure IX-1c. Heat transfer from this flow pattern is called

mixed convection. The mixed flow velocity at many locations is approximately the vector sum of the natural convection flow velocity and the forced convection flow velocity.

At the temperatures anticipated in the EBS, radiation causes the outer cylinder to be hotter than the fluid, which will modify the mixed-convection flow patterns described above. Buoyancy effects will tend to make the air rise in the boundary layer along the outer wall as well as along the inner cylinder. The return downward flow must occur away from the walls, within the annulus. This mixed-convection flow, suggested by Figure IX-1d, is reflective of the YMP emplacement drifts.

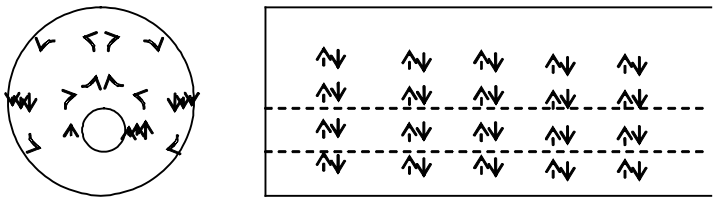

(a) Flow in natural convection

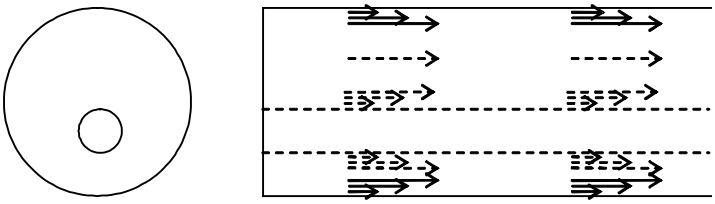

(b) Flow in forced convection

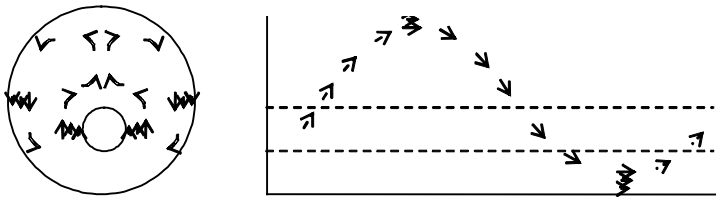

(c) Flow in mixed convection without significant radiation

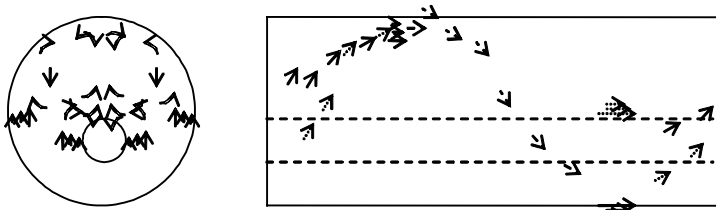

(d) Flow in mixed convection with outer wall hotter than fluid

Figure IX-1. Flow Patterns for Various Modes of Convection (Boundary Layer Thickness Exaggerated.

IX.1.2 Dimensionless Groups

Papers in refereed journals usually express correlations of experimental heat transfer data as relationships between certain dimensionless groups, such as the Reynolds, Nusselt, Prandtl and

Rayleigh numbers. The definitions of the dimensionless groups are not uniform in the literature. This section presents the definitions used in this attachment.

The driver for forced convection is the mean axial fluid velocity, u_m (m/s). Its surrogate is the dimensionless Reynolds number, *Re*, a measure of the ratio of inertial to viscous forces. It is usually defined for the opening between cylinders as (Ebadian and Dong 1998, p. 5.3, Eq. 5.3):

$$Re = \frac{u_m (D_o - D_i)}{v} \qquad \text{(Eq. IX-1)}$$

where v is the kinematic viscosity (m^2/s), D_o the outer cylinder diameter, and D_I the inner cylinder diameter.

The dimensionless surrogate for the heat transfer coefficient is the Nusselt number. Corresponding to each convection coefficient $\overline{h}(x)$ is the effective circumferential Nusselt number, $\overline{Nu}(x)$, defined in this attachment by (Kays and Leung 1963, p. 537).

$$\overline{Nu_i}(x) = \overline{h_i}(x)(D_o - D_i)/k \qquad \text{(Eq. IX-2)}$$

$$\overline{Nu_o}(x) = \overline{h_o}(x)(D_o - D_i)/k \qquad \text{(Eq. IX-3)}$$

where k is the thermal conductivity of the fluid and the subscripts indicate the inner or outer cylinder. Here the arbitrary distance parameter has been chosen as the hydraulic diameter, equal to four times the ratio of the orifice area to its perimeter (Ebadian and Dong 1998).

Another dimensionless group is the Prandtl number, which is a property of the fluid, defined by:

$$Pr = v/\alpha \qquad \text{(Eq. IX-4)}$$

where α is the thermal diffusivity (m^2/s) (Raithby and Hollands 1998, pp. 4.83 to 4.86). The methodology documented here is limited to $Pr = 0.7$.

Natural convection is driven by buoyancy forces, which are caused by temperature gradients in the fluid. The Rayleigh number, Ra, includes the ratio of buoyancy to viscous forces. The Rayleigh numbers for the cylinders are conventionally defined by (Raithby and Hollands 1998, p. 4.21, Figure 4.16a):

$$Ra_i(x) = \frac{g\beta D_i^{\,3}}{v\alpha}\left|\overline{T}_i(x) - T_f(x)\right| \qquad \text{(Eq. IX-5)}$$

$$Ra_o(x) = \frac{g\beta D_o^{\,3}}{v\alpha}\left|\overline{T}_o(x) - T_f(x)\right| \qquad \text{(Eq. IX-6)}$$

where g is the gravitational acceleration (m/s^2) and β is the fluid coefficient of thermal expansion (K^{-1}). For gases such as air, β is evaluated as $1/T_f$, as for a perfect gas (Raithby and Hollands 1998, p. 4.2).

The mixed-convection methodology documented here considers each cylinder separately. It does not attempt to predict the Nusselt number for radial convective heat transfer at each position on a surface. Rather, it predicts a circumferential average at each axial location. That is, it predicts an effective circumferential Nusselt number at each axial location that is directly related to the effective circumferential heat transfer coefficient for radial convection (Equation IX-2 or IX-3). That heat transfer coefficient is defined in terms of the following properties of that axial location:

- The mean surface temperature
- The mean heat flux
- The cross-sectional mean fluid temperature.

Therefore, the predicted Nusselt number and the two average temperatures are sufficient to predict the circumferential average heat flux (by definition).

IX.1.3 Underlying Engineering Principles

Incropera and DeWitt (1985, p. 296) describe two approaches to determine convection coefficients, one theoretical and one empirical. The empirical approach involves performing heat transfer measurements under controlled conditions and correlating the data in terms of appropriate dimensionless parameters. The theoretical approach involves solving the boundary layer equations for the particular geometry. No completely theoretical solution is available for turbulent flow in an annulus; the mathematical methodology documented here incorporates empirical correlations.

The available correlations are for experiments in which the boundary conditions are uniform over the circumference of each cylinder. The correlations apply to the total or mean heat flux on each surface. They do not provide information on the variation of heat flux with position around the circumference.

The fluid temperature away from the boundary layers is sufficiently uniform such that any central temperature is a good approximation to the mean fluid temperature. A user of the methodology can obtain the average heat fluxes from the predicted Nusselt numbers and the average temperatures.

Because the Nusselt number is dimensionless, it must depend on dimensionless groups (Cho et al. 1998, p. 1.24). The methodology documented here is based on correlations of experimental data that relate the Nusselt number to the Reynolds number, the Rayleigh number, the Prandtl number, and temperature ratios.

The mixed-convection concept suggests that the mixed flow velocity at any point be approximated as the vector sum of the natural convection flow velocity and the forced convection flow velocity. For horizontal ventilation, ignoring end effects, the forced flow is

always orthogonal to the natural flow. Therefore, the square of the mixed velocity would be the sum of the squares of the natural and forced components. Rather than make such a postulation explicitly, the mathematical methodology documented here uses the method of Morgan (1975).

IX.1.4 Natural Convection

The Kuehn-Goldstein (1978) correlation is the basis for the natural convection correlation documented here. A search of the engineering literature regarding natural convection in an annulus determined that the Kuehn-Goldstein correlation is generally accepted as the best available. For example, Raithby and Hollands (1998, p. 4.59) discuss their own correlation, but recommend the Kuehn-Goldstein correlation if turbulence effects may be important. Kuehn and Goldstein (1978, p. 639) report that it fits the data better than the general correlation given in their earlier paper (Kuehn and Goldstein 1976).

The Kuehn-Goldstein correlation is for idealized configurations that differ from the EBS in the following respects. The correlation is:

- For situations in which the outer cylinder is colder than the air (Figures IX-1a and IX-1c).
- For cylinders that each have a uniform temperature (are isothermal).
- For a configuration with concentric cylinders.
- For a configuration in which the inner cylinder extends the full length of the outer cylinder (coextensive).
- For cylinders with fully insulated ends.

For local natural convection at the inner and outer cylinders, the Kuehn-Goldstein correlation is:

$$Nu_i' = \frac{2}{\ln\left[1 + \frac{2}{\left[\left(c_i Ra_i^{1/4}\right)^m + \left(\overline{C}_i Ra_i^{1/3}\right)^m\right]^{\frac{1}{m}}}\right]} \qquad \text{(Eq. IX-7)}$$

$$Nu_o' = \frac{-2}{\ln\left[1 - \frac{2}{\left[\left(c_o Ra_o^{1/4}\right)^m + \left(\overline{C}_o Ra_o^{1/3}\right)^m\right]^{\frac{1}{m}}}\right]} \qquad \text{(Eq. IX-8)}$$

where $Nu_i' = \overline{h}_i D_i / k$, $Nu_o' = \overline{h}_o D_o / k$, the constants are listed in Table IX-1, and the parameters are taken to be independent of x. These Nusselt numbers use the cylinder diameters as the arbitrary distance parameters instead of the hydraulic diameter chosen for this mixed-convection

methodology. To restate the correlation in terms of the Nusselt numbers defined in Equations IX-2 and IX-3, the parameter r^* (defined as D_i/D_o) is used, so that:

$$D_h = D_o - D_i = D_o\left(1 - r^*\right) = D_i\left(1/r^* - 1\right) \quad \text{(Eq. IX-9)}$$

$$\overline{Nu_{Ni}}(x) = \frac{2\left(1/r^* - 1\right)}{\ln\left[1 + \frac{2}{\left(\left\{c_i\left[Ra_i(x)\right]^{1/4}\right\}^m + \left\{\overline{C_i}\left[Ra_i(x)\right]^{1/3}\right\}^m\right)^{\frac{1}{m}}}\right]} \quad \text{(Eq. IX-10)}$$

$$\overline{Nu_{No}}(x) = \frac{-2\left(1 - r^*\right)}{\ln\left[1 - \frac{2}{\left(\left\{c_o\left[Ra_o(x)\right]^{1/4}\right\}^m + \left\{\overline{C_o}\left[Ra_o(x)\right]^{1/3}\right\}^m\right)^{\frac{1}{m}}}\right]} \quad \text{(Eq. IX-11)}$$

Table IX-1. Values of Constants for Large Ra in the Correlations of Kuehn and Goldstein

Constant	Value (dimensionless)
c_i	0.5
$\overline{C}_i$	0.12
c_o	1
$\overline{C}_o$	0.12
m	15

Source: Kuehn and Goldstein 1978

The effects of the idealized configuration of the Kuehn-Goldstein correlation when applied to the more complex YMP geometry are considered in the uncertainty analysis presented later in this attachment.

IX.1.5 Forced Convection

For forced convection, the Kays-Leung (1963) correlation underlies the methodology presented in this attachment. The correlation is specific for fully developed turbulent forced convection through an annulus and makes extensive use of theoretical solutions. The results cover a wide range of annulus radius ratio and Reynolds number. Their paper is cited by Ebadian and Dong (1998, p. 5.51 and Table 5.27).

Some modelers have used the Dittus-Boelter correlation rather than the Kays-Leung correlation. The Dittus-Boelter formula gives the asymptotic Nusselt number for fully developed turbulent

flow (Re > 10,000) in circular tubes (r^* = 0). For air (Pr = 0.70), and the tube hotter than the fluid, the correlation is (Incropera and DeWitt 1985, p. 394, Eq. 8.58)

$$Nu = 0.020 Re^{0.8} \quad \text{(Eq. IX-12)}$$

This formula was used for the Nusselt number at the outer wall in earlier ventilation model calculations with fully developed turbulent. Incropera and DeWitt (1985, p. 400) consider the Dittus-Boelter equation to be a first approximation, in which the inner and outer convection coefficients are assumed to be equal.

For concentric circular cylinders with a uniform heat rate on each cylinder, Kays and Leung (1963, p. 539, Eq. 15-16) derived the following expressions:

$$\overline{Nu}_i(x) = \frac{Nu_{ii}(x)}{1 - \theta_i^*(x)(q_o''/q_i'')} \quad \text{(Eq. IX-13)}$$

$$\overline{Nu}_o(x) = \frac{Nu_{oo}(x)}{1 - \theta_o^*(x)(q_i''/q_o'')} \quad \text{(Eq. IX-14)}$$

where

$Nu_{ii}(x)$ = the Nusselt number of the inner cylinder when it alone is heated

$Nu_{oo}(x)$ = the Nusselt number of the outer cylinder when it alone is heated

$\theta_i^*(x)$ and $\theta_o^*(x)$ = influence coefficients

Using empirical velocity and eddy distribution profiles, Kays and Leung (1963) evaluated the parameters by obtaining asymptotic solutions of the energy differential equations, using fluid properties evaluated at $T_f(x)$ and empirical equations for turbulent region diffusivity.

Kays and Leung (1963, Table 1) tabulated the asymptotic values of the parameters, θ_i^*, θ_o^*, Nu_{ii}, and Nu_{oo} as functions of r^*, the Reynolds number, and the Prandtl number. Table IX-2 contains the values for Pr=0.7 and r^* of 0.2 and 0.5, which are used in Section IX.1.6. The methodology is limited to values of r^* between 0.2 and 0.5, which includes the design value for the EBS.

Table IX-2. Parameters for Forced Convection Correlation for Fully Developed Flow and Pr = 0.7

r^*:	0.2				
Re:	10000	30000	100000	300000	1000000
Nu_{ii}:	38.6	79.8	196	473	1270
θ_I:	0.412	0.338	0.286	0.260	0.235
Nu_{oo}:	29.4	64.3	165	397	1070
θ_o:	0.063	0.055	0.049	0.044	0.040
r^*:	0.5				
Re:	10000	30000	100000	300000	1000000
Nu_{ii}:	30.9	66	166	400	1080
θ_I:	0.3	0.258	0.225	0.206	0.185
Nu_{oo}:	28.3	62	158	380	1040
θ_o:	0.137	0.119	0.107	0.097	0.090

Source: Kays and Leung 1963, Table 1

However, Equations IX-13 and IX-14 do not provide an explicit form for the calculation of heat transfer coefficients for models that have known boundary temperatures rather than known fluxes. In convective processes involving heat transfer from a boundary surface exposed to a relatively low-velocity fluid stream, it is convenient to introduce a local convective heat transfer coefficient, $h(x,\theta)$ (W/m^2·K), defined implicitly by Newton's law of cooling, which is:

$$q''(x,\theta) = h(x,\theta)\left[T(x,\theta) - T_f(x)\right] \quad \text{(Eq. IX-15)}$$

where $q''(x,\theta)$ is the convective heat flux (W/m^2) (positive into the fluid) and $T(x,\theta)$ is the surface temperature (K) (Incropera and DeWitt 1985, p. 8, Eq. 1.3). If the temperature difference is zero, then $q''(x,\theta)$ is zero, and $h(x,\theta)$ is not defined.

Because the methodology does not permit heat transfer coefficients that vary around the circumference, a nominal value, the "effective circumferential" convective heat transfer coefficient $\overline{h}(x)$ (W/m^2·K), is defined such that:

$$\overline{q}''(x) = \overline{h}(x)\left[\overline{T}(x) - T_f(x)\right] \quad \text{(Eq. IX-16)}$$

where $\overline{q}''(x)$ is the circumferential average convective heat flux (W/m^2) and $\overline{T}(x)$ is the circumferential average surface temperature (K). If the cylinder has a uniform temperature around its circumference, then $\overline{h}(x)$ is the circumferential average of $h(x,\theta)$, but if the temperature varies around the circumference, $\overline{h}(x)$ may differ from the average of $h(x,\theta)$.

From Equations IX-16, IX-2, and IX-3, the ratio of heat fluxes is:

$$\frac{\overline{q}_i''(x)}{\overline{q}_o''(x)} = \frac{\overline{Nu}_i(x)}{\overline{Nu}_o(x)}\tau(x) \quad \text{(Eq. IX-17)}$$

where

$$\tau(x) = \frac{\overline{T}_i(x) - T_f(x)}{\overline{T}_o(x) - T_f(x)} \quad \text{(Eq. IX-18)}$$

Substituting for the ratio in Equations IX-13 and IX-14, using the asymptotic values of the parameters, yields the following two solutions for the asymptotic Nusselt numbers:

$$\overline{Nu}_i(x) = \frac{Nu_{ii}}{1 - \frac{\theta_i^*}{\tau(x)} \frac{\overline{Nu}_o(x)}{\overline{Nu}_i(x)}} \quad \text{(Eq. IX-19)}$$

$$\overline{Nu}_o(x) = \frac{Nu_{oo}}{1 - \theta_o^* \frac{\overline{Nu}_i(x)}{\overline{Nu}_o(x)} \tau(x)} \quad \text{(Eq. IX-20)}$$

The forced-convection correlation is valid only for fully developed flows. This permits replacing the asymptotic limits with the local values. Solving the above simultaneous equations yields the following formulas for explicit calculation of the effective circumferential Nusselt numbers from the temperatures:

$$\overline{Nu_{Fi}}(x) = \frac{Nu_{ii}(Re) + Nu_{oo}(Re)\theta_i^*(Re)/\tau(x)}{1 - \theta_o^*(Re)\theta_i^*(Re)} \quad \text{(Eq. IX-21)}$$

$$\overline{Nu_{Fo}}(x) = \frac{Nu_{oo}(Re) + Nu_{ii}(Re)\theta_o^*(Re)\tau(x)}{1 - \theta_o^*(Re)\theta_i^*(Re)} \quad \text{(Eq. IX-22)}$$

In comparing experimental data with their correlations, Kays and Leung (1963, pp. 544-545, Figure 6-8) did not correct the experimental data for *Re* effects of natural convection. Because the flow was vertically upward, so that buoyancy effects were longitudinal rather than transverse, the effects of natural convection are minimized.

The Kays-Leung correlations are for idealized configurations that differ from the EBS in that the cylinders are concentric. The effects of this idealization are considered in the uncertainty analysis presented later in this attachment.

IX.1.6 Mixed Convection

Review of the literature shows little research has been completed for mixed convection conditions, and no information was found for configurations similar to the YMP drifts. For internal flows, Incropera and DeWitt (1985, p. 445) and Raithby and Hollands (1998, pp. 4.78 to 4.79) limit consideration of mixed convection to laminar flows within heated cylinders. Earlier ventilation model calculations neglected natural convection, using only a model for forced convection. The method used for mixed convection in the methodology documented here is based on the method of Morgan (1975, p. 244, Eq. 21).

The literature search found no published correlations of experimental data for the flow pattern of Figure IX-1d. In order to use published correlations, the following statements need to be true:

- Mixed-convection in the EBS configuration is approximately the same as mixed-convection in an idealized configuration in which a hotter cylinder is inside a cooler cylinder.

- The effective circumferential Nusselt number at each surface is related to the Reynolds number and dimensionless temperature difference across the boundary layer, but is independent of the conditions at the other surface. This relation is given by the correlation of Kays and Leung (1963, p. 539, Eq. 15-16) for natural convection.

- Natural convection in the EBS may be predicted by the correlation of Kuehn and Goldstein (1978, p. 639, Eq. 1). In particular, the Kuehn-Goldstein correlation must remain valid when the outer surface is hotter than the air.

- The effective Reynolds number for natural convection at a surface depends only on the circumferential Nusselt number at that surface, as predicted by the Kuehn-Goldstein correlation. In particular, the effective Reynolds number is approximately the same as the Reynolds number for the particular forced flow at that surface that would give the same effective Nusselt number.

- As proposed by Morgan (1975) for configurations in which the direction for natural convection is 90º from the direction for forced convection, the effective Reynolds number for mixed convection is the square root of the sum of the square of the Reynolds number for forced convection and the square of the effective Reynolds number for natural convection.

The validity of these statements is demonstrated in comparison of the methodology to experimental data.

IX.1.6.1 Methodology

Morgan (1975) proposed a method for calculating the Nusselt number when both natural and forced modes of convection are present. He considered an equivalent Reynolds number for natural convection, Re_N, such that the Nusselt number for natural convection would be equal to the Nusselt number for a forced convection that had a Reynolds number of Re_N.

In other words, for the forced-convection flow pattern of Figure IX-1b, equations IX-21 and IX-22 provide relationships among the Reynolds number and the two effective circumferential Nusselt numbers. The Morgan approach applies these relationships to the natural-convection flow pattern of Figure IX-1a to obtain effective Reynolds numbers for natural convection. The equations are similar, with the Nusselt numbers and Reynolds number replaced by $\overline{Nu_{Ni}}(x)$, $\overline{Nu_{Ni}}(x)$, Re_{Ni}, and Re_{No}.

For the natural-convection flow pattern of Figure IX-1a, the two surfaces need not have the same effective Reynolds number. By conservation of mass, the mass flow rates must be related, but

the channel widths are not known. For example, the flow speed may be higher when the air is rising past the inner cylinder, because the motion is in the direction of buoyancy. At the outer cylinder the flow may be slower and occupy a wider channel. Therefore, in applying Equations IX-21 and IX-22 to natural convection (or mixed convection) each equation uses the Reynolds number appropriate to the surface.

For steady pure natural convection, with or without radiation, energy conservation requires that the ratio of the convective fluxes at the two surfaces be related to the inverse of their circumferences. This additional relationship might have permitted simultaneous solution of Equations IX-21 and IX-22 in the case of natural convection. However, the appearance of an additional variable, the second Reynolds number, precludes solving the equations simultaneously. Therefore, each surface must be treated separately.

Once the effective Reynolds number for natural convection at a surface is available, the Morgan procedure defines the effective Reynolds number for the mixed flow to be Re_M, such that (Morgan 1975, p. 244, Eq. 21):

$$\left(Re_M\right)^2 = \left(Re_N\right)^2 + \left(Re\right)^2 + 2\left(Re_N\right)\left(Re\right)\cos\phi \qquad \text{(Eq. IX-23)}$$

where Re is the Reynolds number for forced convection and ϕ is the angle between the direction of gravity and the direction of forced flow. The total heat transfer is found by using Re_M in place of Re in the forced convection correlation. Section IX.1.6.2 uses Equation IX-23, in the special case that $\phi = 90^o$, ($\cos\phi = 0$), for prediction of mixed convection in the EBS during ventilation.

Morgan (1975) applied the mixed-convection technique to predict the effective Reynolds number for mixed convection in external horizontal flow that is transverse to a horizontal cylinder. He compared the predicted ratio of effective Nusselt number to forced-flow Nusselt number to the experimental values from two data sets (Morgan 1975, p. 249, Figure 10). Section IX.3.5 uses this comparison as a sound basis for estimating the additional uncertainty that arises when Equation 5-28 is used.

The mixed-convection methodology incorporates correlations of experimental data. The correlations are for idealized configurations that are not the same as the EBS configuration. With one exception, methodology development recognizes that the idealizations are not true and considers their effects in the uncertainty analysis (Section IX.3). The one exception applies to natural convection when the outer surface is hotter than the air. During forced ventilation, the ventilating air removes heat. Because the outer cylinder is heated by thermal radiation from the inner cylinder, the outer surface will be hotter than the air. As discussed in Section 5, the development of the mixed-convection methodology assumes that the Kuehn-Goldstein correlation remains valid when the outer surface is hotter than the air.

IX.1.6.2 Mathematical Methodology

The methodology documented here combines the natural and forced convection formulas into mixed convection formulas. The following formulas give the effective circumferential Nusselt number for mixed convection at each surface:

$$\overline{Nu_{Mi}}(x) = \frac{Nu_{ii}(Re_{Mo}(x)) + Nu_{oo}(Re_{Mo}(x))\theta_i^*(Re_{Mo}(x))/\tau(x)}{1-\theta_o^*(Re_{Mo}(x))\theta_i^*(Re_{Mo}(x))} \quad \text{(Eq. IX-24)}$$

$$\overline{Nu_{Mo}}(x) = \frac{Nu_{oo}(Re_{Mi}(x)) + Nu_{ii}(Re_{Mi}(x))\theta_o^*(Re_{Mi}(x))\tau(x)}{1-\theta_o^*(Re_{Mi}(x))\theta_i^*(Re_{Mi}(x))} \quad \text{(Eq. IX-25)}$$

where the parameters are interpolated linearly between Reynolds numbers and values of r^* in Table IX-2,

$$Re_{Mi}(x) = \sqrt{Re^2 + [Re_{Ni}(x)]^2} \quad \text{(Eq. IX-26)}$$

$$Re_{Mo}(x) = \sqrt{Re^2 + [Re_{No}(x)]^2} \quad \text{(Eq. IX-27)}$$

The Morgan procedure entails finding the equivalent natural-convection Reynolds numbers, Re_{Ni} and Re_{No}, such that Equations IX-24 and IX-25 are satisfied with the subscript $_M$ replaced by the subscript $_N$. To simplify the implicit equations to be solved, the methodology documented here makes the following approximations:

$$\overline{Nu_{Ni}}(x) = \mathrm{Nu}_{ii}(Re_{Ni}(x)) \quad \text{(Eq. IX-28)}$$

$$\overline{Nu_{No}}(x) = \mathrm{Nu}_{oo}(Re_{No}(x)) \quad \text{(Eq. IX-29)}$$

with $\overline{Nu_{Ni}}(x)$ and $\overline{Nu_{No}}(x)$ given by Equations IX-10, IX-11 and Table IX-1 and with linear interpolations with respect to Reynolds number and r^* in Table IX-2. The uncertainty analysis of Section IX.3.5 includes the effects of these approximations.

Equations IX-10 and IX-11 are appropriate to the flow patterns of Figures IX-1a and IX-1c. The methodology documented here applies those correlations to the general case, including the flow pattern of Figure IX-1d.

An application of the methodology may be represented as an algorithm, with a preparation phase to establish the dimensionless groups that are input to the methodology, a Nusselt number prediction phase that accords with the methodology, and a phase for interpretation of the calculated Nusselt numbers. The *preparation* phase consists of the following steps:

Step P1. (Geometry) Calculate D_i/D_o, which is r^*. Also calculate the hydraulic diameter, D_o-D_i.

Step P2. (Reynolds Number) Choose the axial position of interest, x. Determine the mass flow rate, $u_m(x)$, and the mean fluid temperature, $T_f(x)$. Calculate Re, using Equation IX-1.

Step P3. (Rayleigh Numbers) Estimate the local value of *g*. Determine the circumferential average temperature on each surface, $\overline{T}_i(x)$ and $\overline{T}_o(x)$. Calculate $\overline{T}_i(x) - T_f(x)$ and $\overline{T}_o(x) - T_f(x)$. Calculate $\tau(x)$ using Equation IX-18. Calculate $Ra_i(x)$ and $Ra_o(x)$, using Equations IX-5 and IX-6.

The following steps apply the methodology to predict the mixed-convection *Nusselt* numbers:

Step N1. (Forced-Convection Parameters) Using linear interpolation for r^* in Table IX-2, establish tables for $\mathrm{Nu}_{\mathrm{ii}}$, $\mathrm{Nu}_{\mathrm{oo}}$, θ_i^*, and θ_o^* as functions of *Re*.

Step N2. (Natural Convection) Using Equations IX-10 and IX-11 with Table IX-1, calculate $\overline{Nu_{Ni}}(x)$ and $\overline{Nu_{No}}(x)$. Using the table created in Step N1, and using linear dependence on *Re* between table values, find $Re_{Ni}(x)$ to satisfy Equation IX-28 and $Re_{No}(x)$ to satisfy Equation IX-29.

Step N3. (Inner-Surface Nusselt Number) Using Equation IX-26, calculate $Re_{Mi}(x)$. Using linear interpolation in the table created in Step N1, look up the values of $Nu_{ii}(Re_{Mi}(x))$, $Nu_{oo}(Re_{Mi}(x))$, $\theta_i^*(Re_{Mi}(x))$, and $\theta_o^*(Re_{Mi}(x))$. Using Equation IX-24, calculate $\overline{Nu_{Mi}}(x)$.

Step N4. (Outer-Surface Nusselt Number) Using Equation IX-27, calculate $Re_{Mo}(x)$. Using linear interpolation in the table created in Step N1, look up the values of $Nu_{ii}(Re_{Mo}(x))$, $Nu_{oo}(Re_{Mo}(x))$, $\theta_i^*(Re_{Mo}(x))$, and $\theta_o^*(Re_{Mo}(x))$. Using Equation IX-25, calculate $\overline{Nu_{Mo}}(x)$.

The development of the methodology supports the following *interpretation* of the mixed-convection Nusselt numbers:

Step I1. Using Equations IX-2 and IX-3, calculate $\overline{h_i}(x)$ and $\overline{h_o}(x)$.

Step I1. Using Equation IX-16, calculate the two circumferential average heat fluxes and apply them uniformly over each surface.

Attachment X contains an Excel spreadsheet that may be used for this algorithm.

IX.1.6.3 Methodology Limitations

This section summarizes the limitations of the ventilation methodology discussed in the above sections of the attachment. The impacts of these limitations are addressed in Section IX.3. Sentences describing the limitations appear in italics.

Although forced ventilation is proposed during the preclosure period, the anticipated flow rate is low enough that both natural and forced convection play a significant role in the transfer of

energy. This combination increases the complexity of predicting heat transfer. Review of the literature showed little research has been completed for mixed convection conditions, with no information found for configurations similar to the YMP drifts.

The available correlations are based on measurements of stationary processes. Therefore, the mixed-convection methodology documented here applies only when the temperatures at the surfaces are varying so slowly with time that the convective processes are nearly stationary. The ventilating fluid must be air, and its velocity and other properties at every location must be varying slowly enough that processes are nearly stationary.

Also, the methodology documented here uses a forced-convection correlation that is valid only for fully developed flows. Therefore, the methodology is limited to situations in which the flow is fully developed over most of the length of the drift.

The EBS drift configuration is similar to a horizontal cylindrical cylinder (the drift) with an interior cylindrical solid (the train of waste packages), as shown in Figure IX-2. The methodology documented here is limited to configurations in which the waste packages are spaced in the drift such that the heat generation per unit length will be nearly uniform throughout the drift.

The cylinders are neither concentric nor of equal length (coextensive). The diameters of the inner and outer cylinders are D_i and D_o, respectively. Because the core of the methodology uses only dimensionless parameters, any consistent system of units is acceptable. The applications discussed in this attachment use SI units, so the diameters are in meters. To improve readability, this attachment indicates the SI units for each variable.

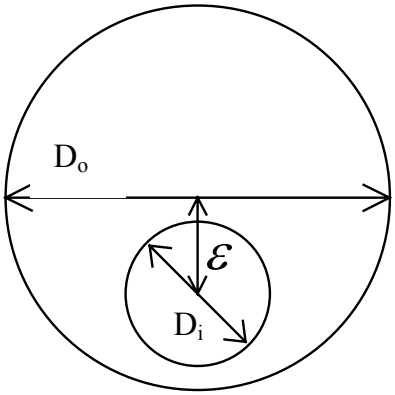

Figure IX-2. Configuration Treated by Methodology of Mixed-Convection Heat Transfer

The parameter r^* is the ratio of the diameters, D_i/D_o. *The methodology documented here has the limitation that* $0.5 \geq r^* \geq 0.2$.

The distance between the central axes of the cylinders is ε. The dimensionless eccentricity, e^*, is $2\varepsilon/(D_o - D_i)$, positive upward. *Another methodology limitation is that* $0 \geq e^* > -2/3$. That is the range covered by the experimental data for natural convection.

The driver for forced convection is the mean axial fluid velocity, u_m (m/s). Its surrogate is the dimensionless Reynolds number, *Re*, a measure of the ratio of inertial to viscous forces. *A limitation of the mixed convection methodology is that the Reynolds number be at least 15,000 (turbulent)*. This is the range in which both the natural convection correlation and the forced convection correlation are valid.

The coordinate pair (x, θ_o) specifies positions on the inner surface of the outer cylinder, with x being the longitudinal coordinate along the cylinder in the direction of flow and θ_o being the angle from the vertically upward direction (zenith) relative to the axis of the outer cylinder. Similarly, (x, θ_i) specifies positions on the outer surface of the inner cylinder, with θ_i being the angle from the zenith relative to the axis of the inner cylinder. If a statement applies to either surface, the subscript on θ is omitted.

A thermal boundary layer must develop whenever the surface temperature differs from the fluid free-stream temperature (Incropera and DeWitt 1985, p. 251). At each longitudinal position along the annulus, the central region of the fluid has a mean temperature $T_f(x)$ (K). *The current methodology is limited to air, with a Prandtl number of 0.7 and all other properties evaluated at* $T_f(x)$.

In convective processes involving heat transfer from a boundary surface exposed to a relatively low-velocity fluid stream, it is convenient to introduce a local convective heat transfer coefficient, $h(x,\theta)$ (W/m^2·K), defined implicitly by *Newton's law of cooling*, Equation IX-15.

The mixed-convection methodology documented here addresses the heat transfer coefficients used to predict convection in the EBS and in scaled tests of EBS designs. *Therefore, another limitation of the methodology is that the inner cylinder be hotter than the outer cylinder.*

The methodology does not predict local heat transfer coefficients. Rather, it leads to an effective circumferential convective heat transfer coefficient $\overline{h}(x)$ (W/m^2·K), defined by Equation IX-16.

IX.2 SENSITIVITY STUDY

Table IX-3 presents the results of a simple sensitivity study for the algorithm, Steps N1 through N3. The table shows how the values of the two Nusselt numbers change as each of the five inputs are varied. Each sensitivity for each input is the ratio of the change in Nusselt number to the change in the dimensionless input.

Attachment X contains the Excel spreadsheet that produced this sensitivity study.

Table IX-3. Sensitivity Study

Case		Ra_i	Ra_o	τ	Re	r^*	Nu_{Mi}	Nu_{Mo}	Sensitivity Nu_{Mi}	Sensitivity Nu_{Mo}
Base Values		1.E+08	7.E+08	6	45,000	0.3	165	202		
Re	low	1.E+08	7.E+08	6	15,000	0.3	145	177	1E-03	1E-03
	high	1.E+08	7.E+08	6	150,000	0.3	285	348		
τ	low	1.E+08	7.E+08	3	45,000	0.3	171	169	-9E-01	1E+01
	high	1.E+08	7.E+08	15	45,000	0.3	161	301		
Ra_i	low	5.E+07	7.E+08	6	45,000	0.3	144	202	3E-07	
	high	2.E+08	7.E+08	6	45,000	0.3	195	202		
Ra_o	low	1.E+08	2.E+08	6	45,000	0.3	165	168		4E-08
	high	1.E+08	2.E+09	6	45,000	0.3	165	243		
r^*	low	1.E+08	7.E+08	6	45,000	0.2	253	203	-5E+02	-5E+01
	high	1.E+08	7.E+08	6	45,000	0.5	103	189		

IX.3 UNCERTAINTY ANALYSIS

Both the forced and the natural convection correlations used in developing the mixed convection methodology are empirical or semi-empirical in nature. Thus, there is some inherent uncertainty associated with each correlation separately. Combining these equations into a mixed convection equation further increases the uncertainty. This section describes a comprehensive analysis of the overall uncertainty in the mixed convection equations.

This analysis discusses the uncertainty in the predictions without reference to any particular application. Therefore, it does not consider uncertainties in the dimensionless groups that are inputs to the methodology. Those uncertainties must be addressed by making use of the sensitivity study of Section IX.2. Section IX.4 provides examples of quantifying uncertainty from all sources using data from the EBS Ventilation Test Series.

IX.3.1 Definitions

There is no standard for the expression of uncertainty in predictions made with algorithms. However, algorithms are used to predict measurements. The treatment of uncertainty in this attachment is based on ANSI/NCSL Z540-2-1997, *American National Standard for Calibration — U.S. Guide to the Expression of Uncertainty in Measurement*. The following are adapted from definitions that appear in the standard:

1. The **measurand** is the particular quantity subject to measurement and therefore to prediction. Its definition may require specification of the conditions under which the quantity is measured. The standard avoids the phrase “true value of the measurand” because the word “true” is viewed as redundant. The “true value of the measurand” is simply the value of the measurand (ANSI/NCSL Z540-2-1997, p. 41).

2. The **measurement error** is the result of the measurement minus the value of the measurand. The **prediction error** is the result of the prediction minus the value of the measurand (ANSI/NCSL Z540-2-1997, p. 34).

3. A **random component** of prediction error is an effect that, for multiple predictions with varying inputs, produces a mean error that is small relative to the standard deviation of the error from that effect. An example of a random component is the residual error after a formula has been adjusted to correlate with data.

4. A **systematic component** of prediction error is an effect that is not a random component.

5. If the systematic component of prediction error includes a systematic effect that is quantifiable, one may add a **correction** to the prediction to compensate for that effect. However, the necessary correction may not be practical in the intended application of the prediction.

6. The **uncertainty** of the result of a prediction is an estimate of the likelihood of nearness to the best value that is consistent with presently available knowledge (adapted from ANSI/NCSL Z540-2-1997, p. 41). Components of uncertainty include estimates of random error, uncertainties in corrections, and estimates of uncorrected or unrecognized systematic effects.

7. **Standard uncertainty** *u (x)*, of a predicted value *x* is the uncertainty of the result of a prediction expressed as a standard deviation. It does not correspond to a high level of confidence.

8. A **Type A evaluation** of uncertainty is an evaluation by statistical analysis of a series of observations. A **Type B evaluation** of uncertainty is an evaluation by any other method. A Type B evaluation is founded on an *a priori* distribution of the possible values (ANSI/NCSL Z540-2-1997, p. 3).

9. If the result of a prediction is a function of the values of a number of other quantities, the standard uncertainty in the prediction is the **combined standard uncertainty**.

10. For contributions to uncertainty that are independent, the **law of propagation of uncertainty** (ANSI/NCSL Z540-2-1997, p. 19) determines the combined standard uncertainty. For $y = f(x_i \ldots, x_n)$, the combined standard uncertainty $u_c(y)$ is given by:

$$u_c^2(y) = \sum_{i=1}^{N} \left(\frac{\delta f}{\delta x_i} \right)^2 u^2(x_i) \qquad \text{(Eq. IX-30)}$$

11. In some applications, it may be necessary to have a measure of uncertainty that encompasses a large fraction of the values that one could reasonably attribute to the measurand. If necessary, the user may multiply the standard uncertainty by a **coverage factor** to obtain an **expanded uncertainty**. In general, the coverage factor will be in the range 2 to 3 (ANSI/NCSL Z540-2-1997, p. 24). This attachment uses a coverage factor of 2 to approximate a 95% confidence interval (ASME PTC 19.1-1998, p. 95).

12. The **relative combined standard uncertainty** in a predicted positive value y is $u_c\,(y)/y$ (ANSI/NCSL Z540-2-1997, p. 25, Sect. 7.2.1).

13. For non-zero values of the x_i, Equation IX-30 may be rewritten for propagation of relative uncertainty:

$$\left[\frac{u_c(y)}{y}\right]^2 = \sum_{i=1}^{N}\left(\frac{x_i}{y}\frac{\partial f}{\partial x_i}\right)^2\left[\frac{u(x_i)}{x_i}\right]^2 \qquad \text{(Eq. IX-31)}$$

IX.3.2 Interpolation Errors

The uncertainty analysis considers errors arising from interpolation in Table IX-2.

Consider one variable at a time. Let x be the variable and y be a parameter defined by $f(x)$. The error in linear interpolation for y is (Conte and de Boor 1972, p. 212, Example 4.5):

$$\frac{(x-x_1)(x-x_2)}{2}f''(\xi)$$

where x is the input variable, (x_1, x_2) is the interpolation interval, and $f''(\xi)$ is a value of the second derivative of y with respect to x at some point ξ in the interval (x_1, x_2). The relative error is:

$$\frac{(x-x_1)(x-x_2)}{2}M'$$

The maximum value of $(x-x_1)(x-x_2)/2$ in the interval (x_1, x_2) is $(x_2-x_1)^2/8$. Therefore, the maximum relative error in the interval is $(x_2-x_1)^2 M'/8$.

Suppose the interpolation interval is not at the edge of the table, so that for $x_0 < x_1 < x_2 < x_3$ we have the values y_0, y_1, y_2, and y_3. By the mean value theorem for derivatives (Conte and de Boor 1972, p. 23, Theorem 1.6), there is x_a in (x_0, x_1) where

$$f'(x_a) = \frac{y_1 - y_0}{x_1 - x_0} \qquad \text{(Eq. IX-32)}$$

Similarly, there is x_b in (x_2, x_3) where

$$f'(x_b) = \frac{y_3 - y_2}{x_3 - x_2} \qquad \text{(Eq. IX-33)}$$

Applying the mean value theorem for derivatives one more time, there is x_m in (x_a, x_b) where

$$f''(x_m) = \frac{f'(x_b) - f'(x_a)}{x_b - x_a} \qquad \text{(Eq. IX-34)}$$

Because the smallest possible value of $x_b - x_a$ is $x_2 - x_1$,

$$\left|\frac{\mathrm{d}^2 y}{\mathrm{d}x^2}(x_m)\right| \le \frac{\left|\frac{y_3 - y_2}{x_3 - x_2} - \frac{y_1 - y_0}{x_1 - x_0}\right|}{x_2 - x_1} \qquad \text{(Eq. IX-35)}$$

so that the right hand side is a high estimate of the second derivative somewhere in (x_0, x_3). We use it as though it were a high estimate of the magnitude of $f''(\xi)$. Therefore, a high estimate for the magnitude of *M'* is:

$$\frac{1}{(x_2 - x_1)\mathrm{Min}(y_1, y_2)}\left|\frac{y_3 - y_2}{x_3 - x_2} - \frac{y_1 - y_0}{x_1 - x_0}\right|$$

where Min (y_1, y_2) is the minimum value of y between x_1 and x_2.

We now address interpolation with respect to r^*. Table IX-4 provides the parameter table for r^* values of 0.1, 0.2, 0.5, and 0.8 (Kays and Leung 1963, pp. 552 to 554) and the calculation of *M'*. All calculations in this attachment were performed to many significant digits, with the results being rounded for presentation in tables.

Consider, for example, the parameter Nu_{ii} as a function of r^*, with *Re* fixed at 10,000. The values of x_0, x_1, x_2, and x_3 are 0.1, 0.2, 0.5, and 0.8. The values of y_0, y_1, y_2, and y_3 are 48.5, 38.6, 30.9, and 28.5. At some unknown location x_a between 0.1 and 0.2, the derivative of the function is (38.6-48.5)/(0.2-0.1), which is -99. Similarly, there is a location x_b between 0.5 and 0.8 where the derivative of the function is (28.5-30.9)/(0.8-0.5), or -8.0.

Therefore, there is some x_m between x_a and x_b, where the second derivative is [-8.0-(-99]/(x_b-x_a), or 91/(x_b-x_a). We do not know the value of either x_a or x_b, but we know that one is not larger than 0.2 and the other is no smaller than 0.5, so that their difference must be at least 0.3. Therefore, we know that there is some point between 0.1 and 0.8 where the second derivative is less than 303 (about 91 divided by 0.3).

If the function is sufficiently smooth, x_m will be between x_1 and x_2. To get a high estimate of *M'*, we divide by the smallest value of y between x_1 and x_2, which is 30.9. Therefore, the high estimate of *M'* is 9.8 (303 divided by 30.9). In fact, this is the largest value for any function in Table IX-4, so for interpolation with respect to r^*, we take the upper bound on *M'* to be 10.

Table IX-4. High Estimate of Second Derivative with Respect to r^*

Re	10,000				
	r^*	Nu_{ii}	θ_i	Nu_{oo}	θ_o
	0.1	48.5	0.512	29.8	0.032
	0.2	38.6	0.412	29.4	0.063
	0.5	30.9	0.300	28.3	0.137
	0.8	28.5	0.224	28.0	0.192
	$\delta y/\delta x(x_a)$	-99.0	-1.0	-4.0	0.3
	$\delta y/\delta x(x_b)$	-8.0	-0.3	-1.0	0.2
	$\delta^2 y/\delta x^2(x_m)$	303.3	2.5	10.0	0.4
	M'	9.8	8.296	0.4	6.702
Re	30,000				
	r^*	Nu_{ii}	θ_i	Nu_{oo}	θ_o
	0.1	98.0	0.407	66.0	0.028
	0.2	79.8	0.338	64.3	0.055
	0.5	66.0	0.258	62.0	0.119
	0.8	62.3	0.212	61.0	0.166
	$\delta y/\delta x(x_a)$	-182.0	-0.7	-17.0	0.3
	$\delta y/\delta x(x_b)$	-12.3	-0.2	-3.3	0.2
	$\delta^2 y/\delta x^2(x_m)$	565.6	1.8	45.6	0.4
	M'	8.6	6.934	0.7	6.869
Re	100,000				
	r^*	Nu_{ii}	θ_i	Nu_{oo}	θ_o
	0.1	235.0	0.338	167.0	0.024
	0.2	196.0	0.286	165.0	0.049
	0.5	166.0	0.225	158.0	0.107
	0.8	157.0	0.186	156.0	0.150
	$\delta y/\delta x(x_a)$	-390.0	-0.5	-20.0	0.3
	$\delta y/\delta x(x_b)$	-30.0	-0.1	-6.7	0.1
	$\delta^2 y/\delta x^2(x_m)$	1200.0	1.3	44.4	0.4
	M'	7.2	5.778	0.3	7.256

Now consider interpolation with respect to Reynolds numbers. For each interval (Re_n, Re_{n+1}) in the table, Re_{n+1} is approximately $3Re_n$. Therefore, the maximum relative error, $(Re_{n+1} - Re_n)^2 M'/8$, is $0.5(Re_n)^2 M'$.

For the EBS Ventilation Test Series, the inner and outer diameters were 40.64 cm and 1.37 m (BSC 2003f, Sections 2.2.2.1 and 2.2.2.2), so that $r^* = 0.297$. Table IX-5 contains the parameter table after interpolation to $r^* = 0.297$. In order to have four values of *Re*, we take the values for 300,000 from Kays and Leung (1963, pp. 552 to 554).

Table IX-5 shows the derivation of *M'* and the values of $0.5(Re_1)^2 M'$. Again consider the calculation for the parameter Nu_{ii}, this time as a function of *Re*, with r^* fixed at 0.297. Now the

values of x_0, x_1, x_2, and x_3 are 10,000, 30,000, 100,000, and 300,000, and the values of y_0, y_1, y_2, and y_3 are 36.1, 75.4, 186.3, and 449.5. At some unknown Reynolds number x_a between 10,000 and 30,000, the derivative of the function is (75.4-36.1)/(30000-10000), which is 1.96×10^{-3}. Similarly, there is Reynold number x_b between 100,000 and 300,000 where the derivative of the function is (449.5-186.3)/(300000-100000), or 1.32×10^{-3}.

Therefore, there is some x_m between x_a and x_b, where the second derivative is $(1.32\times10^{-3}-1.96\times10^{-3})/(x_b-x_a)$, or $-6.4\times10^{-4}/(x_b-x_a)$. We do not know the value of either x_a or x_b, but we know that one is not larger than 30,000 and the other is no smaller than 100,000, so that their difference must be at least 70,000. Therefore, we know that there is some Reynolds number between 10,000 and 300,000 where the magnitude of the second derivative is less than 9.23×10^{-9} (about 6.4×10^{-4} divided by 70,000).

If the function is sufficiently smooth, x_m will be between x_1 and x_2. To get a high estimate of M', we divide by the smallest value of y between x_1 and x_2, which is 75.4. Therefore, the high estimate of M' is 1.22×10^{-10} (about 9.2×10^{-9} divided by 75.4) and the maximum relative error for Reynolds numbers between 30,000 and 100,000 is 5.5%, which is $0.5\times(30{,}000)^2\times1.22\times10^{-10}$. The results in Table IX-5 indicate that the relative error should be no more than about 7%.

Table IX-5. High Estimate of Second Derivative with Respect to *Re*

r^* 0.297					
	Re	Nu_{ii}	θ_i	Nu_{oo}	θ_o
	10,000	36.1	0.376	29.0	0.087
	30,000	75.4	0.312	63.6	0.076
	100,000	186.3	0.266	162.7	0.068
	300,000	449.5	0.243	391.5	0.061
	$\delta y/\delta x\,(x_a)$	1.96E-03	-3.18E-06	1.73E-03	-5.61E-07
	$\delta y/\delta x\,(x_b)$	1.32E-03	-1.19E-07	1.14E-03	-3.31E-08
	$\delta^2 y/\delta x^2\,(x_m)$	9.23E-09	4.38E-11	8.31E-09	7.54E-12
	M'	1.22E-10	1.64E-10	1.31E-10	1.11E-10
	$0.5M'(30{,}000)^{\wedge}2$	5.5%	7.4%	5.9%	5.0%
	$\delta x/\delta y\,(y_a)$	5.10E+02		5.79E+02	
	$\delta x/\delta y\,(y_b)$	7.60E+02		8.74E+02	
	$\delta^2 x/\delta y^2\,(y_m)$	2.26E+00		2.97E+00	
	M'	7.52E-05		9.90E-05	
	$M'(y_2-y_1)^2/8$	11.6%		12.2%	

At the bottom of Table IX-5 is an error analysis for the reverse interpolation for $Re_{Ni}(x)$ or $Re_{No}(x)$, starting from Nu_{ii} or Nu_{oo}. The roles of the variables are reversed.

For example, the first derivative of *Re* with respect to Nu_{ii}, at some value of Nu_{ii} between 36.1 and 75.4, is 510 (30,000-10,000)/(75.4-36.1). Similarly, the value of the derivative is 760 somewhere between 186 and 450.

Therefore, the value of the second derivative is less than (760-510)/(186.3-75.4), which is about 2.26, at some value of Nu_{ii} between 36.1 and 450. Dividing by the smallest value of Re in the intermediate interval, 30,000, yields 7.5×10^{-5} as a high estimate for *M'*.

Therefore, the relative error should be no more than 11.6%, which is the result of $M'\times(186.3-75.4)^2/8$. Table IX-5 shows that a similar analysis for reverse interpolation from Nu_{oo} gives 12.2% as a high estimate of the relative error.

IX.3.3 Uncertainty in Nusselt Numbers from the Natural Convection Methodology

This section evaluates the following sources of uncertainty in effective circumferential Nusselt numbers calculated from the natural convection correlation:

1. The extent to which measured Nusselt numbers for concentric, coextensive, isothermal cylinders deviate from the effective circumferential Nusselt numbers predicted by the correlation.

2. The uncertainty arising from applying a correlation for a diameter ratio of 0.38 to configurations with other diameter ratios in the range 0.2 to 0.5.

3. Uncertainty in the effective circumferential Nusselt numbers arising from temperature variation along the lengths of the cylinders.

This section also discusses the following sources of uncertainty, which must be evaluated for each particular application:

1. The uncertainty in effective circumferential Nusselt numbers for coextensive, isothermal cylinders arising from eccentric location of the inner cylinder.

2. The uncertainty in effective circumferential Nusselt numbers for isothermal cylinders arising from unequal cylinder lengths.

3. Uncertainty in the effective circumferential Nusselt numbers arising from temperature variation along the circumferences of the cylinders.

This uncertainty analysis does not estimate the error from applying the natural convection correlation to situations in which the outer surface is hotter than the air (Figure IX-1d).

IX.3.3.1 Deviations in Measured $\overline{Nu_N}$ for Concentric, Coextensive, Isothermal Cylinders

This section estimates the uncertainty inherent in the Kuehn-Goldstein correlation, even when applied to idealized configurations.

One definition of a Nusselt number for *overall* convection between the two cylinders is:

$$\overline{Nu}_{conv} = \frac{D_i \overline{q}_i''}{k\left(\overline{T}_i - \overline{T}_o\right)} \qquad \text{(Eq. IX-36)}$$

As suggested by Kuehn and Goldstein (1978, p. 639), the three Nusselt numbers are related by:

$$\overline{Nu}_{conv}(x) = \left(\frac{1}{Nu_i'} + \frac{1}{Nu_o'} \right)^{-1} = \left[\frac{\left(1/r^* - 1 \right)}{\overline{Nu}_i(x)} + \frac{\left(1 - r^* \right)}{\overline{Nu}_o(x)} \right]^{-1} \quad \text{(Eq. IX-37)}$$

Kuehn and Goldstein (1978) correlated results of 40 tests for which *Pr* was 0.7, r^* was 0.38, and the Rayleigh number ranged widely. After correcting test data for end losses and radiation, they determined that their correlation fit $\overline{Nu}_{conv}$ for *Ra* > 5,000 (33 tests) with a standard deviation of 1.7% (Kuehn and Goldstein 1978, p. 639).

However, a fit to $\overline{Nu}_{conv}$ does not require a fit to each of the values of $\overline{Nu_{Ni}}$ and $\overline{Nu_{No}}$. For example, $\overline{Nu_{Ni}}$ could be too large and $\overline{Nu_{No}}$ too small. These could combine to produce the correct value of $\overline{Nu}_{conv}$, but the predicted value of T_f would be too large.

Kuehn and Goldstein (1978, p. 636) define an average dimensionless fluid temperature, $\overline{\Phi}_b$, by

$$\overline{\Phi}_b = \left(T_f - \overline{T}_o \right) / \left(\overline{T}_i - \overline{T}_o \right) \quad \text{(Eq. IX-38)}$$

They report that the dimensionless average fluid temperature near the center of the gap obtained from the correlation agrees "fairly well" with the experimental results. They give only one example, for which the experimental result is 0.25 compared to 0.28 given by the correlation (Kuehn and Goldstein 1978, p. 639).

In steady natural convection, the total heat flux at the two cylinders must be equal and opposite. That is:

$$\overline{q_i''}\ D_i = -\overline{q_0''}\ D_0 \quad \text{(Eq. IX-39)}$$

The average dimensionless fluid temperature, $\overline{\Phi}_b$, is related to the ratio $\overline{Nu}_{conv} / \overline{Nu_0}$, or alternatively to the ratio $\overline{Nu}_{conv} / \overline{Nu_i}$. A derivation of the relationship between $\overline{\Phi}_b$ and $\overline{Nu}_{conv} / \overline{Nu_0}$ starts with Equation IX-28, first substitutes for the temperature differences from Equations IX-16 and IX-36, and then uses Equations IX-39 and IX-3 to simplify. The resulting expression can be converted to use $\overline{Nu}_{conv} / \overline{Nu_i}$ by applying Equation IX-37. The result is:

$$\overline{\Phi}_b = \frac{-\overline{q_o''} / \overline{h}_o}{D_i \overline{q}_i'' / k \overline{Nu}_{conv}} = \frac{\left(D_o - D_i \right) \overline{Nu}_{conv}}{D_0 \overline{Nu}_o} = \left(1 - r^* \right) \frac{\overline{Nu}_{conv}}{\overline{Nu}_o} = 1 - \left(\frac{1}{r^*} - 1 \right) \frac{\overline{Nu}_{conv}}{\overline{Nu}_i} \quad \text{(Eq. IX-40)}$$

Therefore, if $\overline{Nu_{\text{conv}}}$ is relatively accurate, an error of +12% in $\overline{\phi}_b$ corresponds to a value of $\overline{Nu_{Ni}}$ that is about 12% too high and a value of $\overline{Nu_{No}}$ that is about 12% too low.

This attachment uses an *a priori* normal distribution for a Type B evaluation of the uncertainty inherent in the Kuehn-Goldstein correlation. This analysis assigns a relative standard uncertainty of 12% to predictions of $\overline{Nu_{Ni}}$ and $\overline{Nu_{No}}$ for concentric, coextensive, isothermal cylinders with $r^* = 0.38$. The smaller error for $\overline{Nu}_{conv}$ indicates that the errors in $\overline{Nu_{Ni}}$ and $\overline{Nu_{No}}$ tend to be equal and opposite. With only one data point available, this uncertainty analysis treats the error as random rather than systematic.

IX.3.3.2 Uncertainty in $\overline{Nu_N}$ from Diameter Ratio

For $Ra > 10^8$, $Pr = 0.7$, and $r^* = 0.33$ or 0.5, the agreement between the Kuehn-Goldstein correlation for natural convection was within 5% the experimental data (Kuehn and Goldstein 1976, Figure 2). Kuehn and Goldstein (1978, p. 639, Eq. 1) presented a modified correlation for the same data which provided an even better fit. Therefore, this attachment neglects any additional uncertainty for r^* between 0.2 and 0.5.

IX.3.3.3 Uncertainty in $\overline{Nu_N}$ from Longitudinal Temperature Variation

In natural convection, there should be no longitudinal gradient. To the extent that there are longitudinal gradients in a natural convection test, they are considered to be the result of end effects, and the test results are corrected for these effects. Therefore, there is no uncertainty associated with longitudinal temperature gradients in natural convection.

In mixed convection, there is a longitudinal gradient that is expected from forced convection. In this attachment, any effects on the natural convection Nusselt number from a longitudinal temperature gradient are included in the uncertainties inherent in combining the two correlations into a mixed convection model.

IX.3.3.4 Uncertainty in $\overline{Nu_N}$ from Eccentricity

Kuehn and Goldstein (1978, p. 637) reported the effects of eccentricity on heat transfer coefficients. The *overall* heat transfer coefficients tend to increase by 10 percent as the inner cylinder is moved downward from the concentric position to an e^* of -2/3.

The methodology is limited to values between 0 and –2/3 (Section IX.1.6.3). This attachment uses that information for a Type B evaluation of uncertainty by assuming that the error is linear with the eccentricity. That is, the use of the concentric correlation systematically underestimates the heat transfer coefficients. The fractional error is about $-0.15 \left| e^* \right|$, so that it would be zero if the cylinders were concentric and is -0.1 when the value of e^* is -2/3.

IX.3.3.5 Uncertainty in $\overline{Nu_N}$ from Unequal Cylinder Lengths

In a particular configuration, the outer cylinder may be longer than the inner cylinder. The inner cylinder may be a series of waste packages with gaps between them, reducing the heated length of the inner cylinder. The additional area of the outer cylinder may permit more convective heat transfer from the air to the outer cylinder. Therefore, the air temperature may be closer to the

temperature of the outer cylinder than it would be if the inner cylinder extended the entire length of the outer cylinder.

The contribution to uncertainty from the length difference may be neglected if the following conditions hold:

1. The greater length of the outer cylinder does not cause a qualitative change in the flow from natural convection other than mild divergence and convergence along the axis.

2. The change in the Rayleigh numbers appearing in the correlation, caused by the change in air temperature, properly account for most of the changes in the circumferential average Nusselt numbers.

3. The remaining effects of the longer outer cylinder are not significant compared to the other contributions to uncertainty.

IX.3.3.6 Uncertainty in $\overline{Nu_N}$ from Circumferential Temperature Variation

It may be that heat transfer by thermal conductivity within one or both cylinders is not sufficient to maintain a cylinder at nearly uniform temperature. In such a case, one must consider how accurately the natural convection correlation predicts an effective circumferential Nusselt number.

Kuehn and Goldstein (1978, p. 637) observed that moving a heated inner cylinder below its concentric position results in more uniform local coefficients on the outer cylinder. However, this uncertainty analysis uses results for concentric cylinders.

Because the inner cylinder is hotter than the outer cylinder and the flow develops as shown in Figure IX-1a, natural convection cools the bottom of the inner cylinder more effectively than the top and transfers heat to the top of the outer cylinder more effectively than to the bottom. Therefore, both cylinders are hotter at the top than at the bottom. For pure natural convection, in which T_f is between the temperatures of the cylinders, the magnitude of the temperature difference between the inner cylinder and the fluid is smallest at the bottom. For the outer cylinder, on the other hand, the difference is smallest at the top.

Kuehn and Goldstein (1978) obtained temperature distributions and local heat transfer coefficients using time-averaged interferograms. For four Rayleigh numbers, they plotted local equivalent conductivities (which are proportional to the local heat transfer coefficients) for isothermal cylinders as a function of angular position numbers (Kuehn and Goldstein 1978, Figure 8).

First, consider the inner cylinder. Because the inner cylinder is hotter than the outer cylinder and the flow develops as shown in Figure IX-1a, natural convection cools the bottom of the inner cylinder more effectively than the top. Therefore, if conduction within the cylinder is not sufficient to maintain a uniform temperature, the inner cylinder is hotter at the top than at the bottom. The magnitude of the temperature difference between the inner cylinder and the fluid is *smallest* at the bottom.

For four Rayleigh numbers, Kuehn and Goldstein (1978, Figure 8) plotted local heat transfer coefficients for concentric isothermal cylinders as a function of angular position. Their plot shows that h_i is smallest at the top of the cylinder, may increase by a factor of five or more at the sides, and stays within 50% of that value along the bottom half of the cylinder.

To estimate the effect of deviations from temperature uniformity around the inner cylinder, we use the approximation that the heat transfer coefficients are not affected. We let h_T be the heat transfer coefficient around the top quarter of the cylinder and assign $5h_T$ as the heat transfer coefficient around the rest of the circumference.

For an isothermal inner cylinder, the effective circumferential heat transfer coefficient is the same as the average, which is $4h_t$. For varying temperatures at the top, left, bottom, and right, each representing the average over one-quarter of the circumference, we have:

$$\overline{h}_i[\overline{T}_i - T_f] = \frac{h_t[T_t - T_f] + 5h_t[T_l - T_f] + 5h_t[T_r - T_f] + 5h_t[T_b - T_f]}{4} \qquad \text{(Eq. IX-41)}$$

Adding and subtracting $h_t\,[T_t - T_f]$ on the right and letting $\overline{T}_i$ be the average of the four temperatures, we obtain:

$$\overline{h}_i[\overline{T}_i - T_f] = 5h_t[\overline{T}_i - T_f] - h_t[T_t - T_f] \qquad \text{(Eq. IX-42)}$$

$$\overline{h}_i = 5h_t - \frac{h_t[T_t - T_f]}{[\overline{T}_i - T_f]} = 4h_t + \frac{h_t[\overline{T}_i - T_f]}{[\overline{T}_i - T_f]} - \frac{h_t[T_t - T_f]}{[\overline{T}_i - T_f]} \qquad \text{(Eq. IX-43)}$$

$$\overline{h}_i = 4h_t - \frac{h_t[T_t - \overline{T}_i]}{[\overline{T}_i - T_f]} \qquad \text{(Eq. IX-44)}$$

The error from using the average,

$$\widetilde{h}_i = \frac{h_t + 5h_t + 5h_t + 5h_t}{4} = 4h_t \qquad \text{(Eq. IX-45)}$$

is

$$\widetilde{h}_i - \overline{h}_i = \frac{\overline{h}_i[T_t - \overline{T}_i]}{[\overline{T}_i - T_f]} = +0.25\frac{\widetilde{h}_i[T_t - \overline{T}_i]}{[\overline{T}_i - T_f]} \qquad \text{(Eq. IX-46)}$$

so that the relative error is about $+0.25[T_t - \overline{T}_i]/[\overline{T}_i - T_f]$. This is also the relative error in the inner-cylinder Nusselt number.

Now, consider the outer cylinder. As shown in Figure IX-1a, natural convection transfers heat to the top of the outer cylinder more effectively than to the bottom. Therefore, if conduction within the cylinder is not sufficient to maintain a uniform temperature, the outer cylinder is hotter at the top than at the bottom. For pure natural convection, in which T_f is between the temperatures of

the cylinders, the magnitude of the temperature difference between the inner cylinder and the fluid is *smallest* at the top.

The Kuehn and Goldstein chart (1978, Figure 8) shows that h_o is largest at the top of the outer cylinder, drops by a factor of three or more at the sides, and drops to zero along the bottom of the cylinder.

To estimate the effect of deviations from temperature uniformity around the outer cylinder, we again use the approximation that the heat transfer coefficients are not affected. We let h_t be the heat transfer coefficient around the top quarter of the cylinder and assign $h_t/3$ as the heat transfer coefficient at the sides. As in the application to the EBS tests, we exclude the bottom quarter from the analysis.

For an isothermal outer cylinder, the effective circumferential heat transfer coefficient is the same as the average of the three coefficients, which is $5h_t/9$. For varying temperatures at the top, left, and right, each representing the average over one-quarter of the circumference, and using the relative heat transfer coefficients from the previous paragraph, we have

$$\overline{h}_o[T_f - \overline{T}_o] = \frac{h_t[T_f - T_t] + \frac{1}{3}h_t[T_f - T_l] + \frac{1}{3}h_t[T_f - T_R]}{3} \qquad \text{(Eq. IX-47)}$$

In this case, we subtract and add $\frac{2}{9}h_t\left[T_f - T_t\right]$ on the right and let $\overline{T}_o$ be the average of these temperatures to obtain

$$\overline{h}_o[T_f - \overline{T}_o] = \frac{1}{3}h_t[T_f - \overline{T}_o] + \frac{2}{9}h_t[T_f - T_t] \qquad \text{(Eq. IX-48)}$$

$$\overline{h}_o = \frac{1}{3}h_t + \frac{2}{9}h_t\frac{[T_f - T_t]}{[T_f - \overline{T}_o]} = \frac{5}{9}h_t - \frac{2}{9}h_t\frac{[T_f - \overline{T}_o]}{[T_f - \overline{T}_o]} + \frac{2}{9}h_t\frac{[T_f - T_t]}{[T_f - \overline{T}_o]} \qquad \text{(Eq. IX-49)}$$

$$\overline{h}_o = \frac{5}{9}h_t - \frac{2}{9}h_t\frac{[T_t - \overline{T}_o]}{[T_f - \overline{T}_o]} \qquad \text{(Eq. IX-50)}$$

The error from using the average,

$$\widetilde{h}_o = \frac{h_t + \frac{1}{3}h_t + \frac{1}{3}h_t}{3} = \frac{5}{9}h_t \qquad \text{(Eq. IX-51)}$$

is

$$\widetilde{h}_o - \overline{h}_o = +\frac{2}{9}\frac{h_t[T_t - \overline{T}_o]}{[T_f - \overline{T}_o]} = +\frac{2}{5}\frac{\widetilde{h}_o[T_t - \overline{T}_o]}{[T_f - \overline{T}_o]} \qquad \text{(Eq. IX-52)}$$

so that the relative error is about $+0.4[T_t - \overline{T}_o]/[T_f - \overline{T}_o]$. This is also the relative error in the outer-cylinder Nusselt number.

IX.3.4 Uncertainty in Nusselt Numbers from the Forced Convection Correlation

This uncertainty analysis evaluates the following sources of uncertainty in effective circumferential Nusselt numbers calculated from the forced convection correlation:

1. Uncertainty in the Nusselt numbers arising from flux variation along the lengths of the cylinders.

2. Uncertainty in the effective circumferential Nusselt numbers arising from flux variation along the circumferences of the cylinders.

This section also discusses the following sources of uncertainty, which must be evaluated for each particular application:

1. The extent to which measured Nusselt numbers for fully developed flow in concentric, coextensive, uniform-flux cylinders deviate from the Nusselt numbers predicted by the correlation.

2. Uncertainty from linear interpolation of the Kays-Leung parameters to the diameter ratio of 0.3.

3. Uncertainty from linear interpolation of the Kays-Leung parameters to the appropriate Reynolds number.

4. The uncertainty in effective circumferential Nusselt numbers for fully developed flow in uniform-flux cylinders arising from unequal cylinder lengths.

5. The uncertainty in effective circumferential Nusselt numbers for fully developed flow in coextensive, uniform-flux cylinders arising from eccentric location of the inner cylinder.

6. Uncertainty arising from deviations from fully developed flow.

IX.3.4.1 Uncertainty in Measured $\overline{Nu_F}$ from Flux Variation Along the Lengths of the Cylinders

The methodology documented here is limited to configurations in which the waste packages are spaced in the drift such that the heat generation will be roughly constant per unit length of drift. Therefore, the surface flux should vary sufficiently slowly in the axial direction that the flow at each location is approximately the same as if that flux were uniform over the length of the cylinder. Consequently, this analysis neglects that source of error.

IX.3.4.2 Uncertainty in Measured $\overline{Nu_F}$ from Flux Variation Along the Circumferences of the Cylinders

In pure forced convection with uniform boundary conditions, there is no dependence on the angle θ. Sutherland and Kays (1964, p. 1189) considered fully developed flow in a concentric annulus with heat flux varying circumferentially, but not axially. They represented the heat fluxes at each surface as a Fourier series of the form:

$$q''(\theta) = \sum_{n=0}^{\infty} \left[a_n \sin(n\theta) + b_n \cos(n\theta) \right] \qquad \text{(Eq. IX-53)}$$

Neglecting thermal conduction in the walls, they derived (Sutherland and Kays 1964, p. 1189, Eqs. 3a and 3b):

$$\begin{aligned} T_i(\theta) - T_f &= \frac{D_o - D_i}{k} \sum_{n=0}^{\infty} R_{n_{ii}} \left[a_{n_i} \sin(n\theta) + b_{n_i} \cos(n\theta) \right] \\ &+ \frac{D_o - D_i}{k} \sum_{n=0}^{\infty} R_{n_{io}} \left[a_{n_o} \sin(n\theta) + b_{n_o} \cos(n\theta) \right] \end{aligned} \qquad \text{(Eq. IX-54)}$$

$$\begin{aligned} T_0(\theta) - T_f &= \frac{D_o - D_i}{k} \sum_{n=0}^{\infty} R_{n_{oi}} \left[a_{n_i} \sin(n\theta) + b_{n_i} \cos(n\theta) \right] \\ &+ \frac{D_o - D_i}{k} \sum_{n=0}^{\infty} R_{n_{oo}} \left[a_{n_o} \sin(n\theta) + b_{n_o} \cos(n\theta) \right] \end{aligned} \qquad \text{(Eq. IX-55)}$$

where the R_n are the eigenfunctions when only one wall is heated. The index n indicates the harmonic of the Fourier expansion, its first subscript is the affected wall, and its second subscript is the heated wall.

Integration of those equations over θ (over 2π) yields:

$$\overline{q}_i'' = 2\pi b_{0i} \qquad \text{(Eq. IX-56)}$$

$$\overline{q}_o'' = 2\pi b_{0_0} \qquad \text{(Eq. IX-57)}$$

$$\frac{k(\overline{T}_i - T_f)}{D_o - D_i} = R_{0_{ii}} 2\pi b_{0_i} + R_{0_{io}} 2\pi b_{0_o} = R_{0_{ii}} \overline{q}_i'' + R_{0_{io}} \overline{q}_o'' \qquad \text{(Eq. IX-58)}$$

$$\frac{k(\overline{T}_0 - T_f)}{D_o - D_i} = R_{0_{oi}} 2\pi b_{0_i} + R_{0_{oo}} 2\pi b_{0_o} = R_{0_{oi}} \overline{q}_i'' + R_{0_{oo}} \overline{q}_o'' \qquad \text{(Eq. IX-59)}$$

Therefore, the relationships between the mean heat fluxes and the mean temperatures are independent of any axial variation. Consequently this attachment neglects the uncertainty arising from flux variation around the circumference.

IX.3.4.3 Deviations in Measured $\overline{Nu_F}$ for Concentric, Coextensive, Uniform-Flux Cylinders

The concentric tubes were mounted vertically with airflow from the bottom upward (Reynolds et al. 1963, p. 489). The reported experimental data reflect correction for radiative heat transfer (Kays and Leung 1963, p. 540). Correction for the effects of natural convection were not necessary (as explained previously). They reported measurement uncertainties of about 3% in Nu_{ii} and Nu_{oo} after correction for radiative heat transfer (Kays and Leung 1963, p. 541). They presented the asymptotic Nusselt numbers, both analytical and experimental, for various values of r^*, including 0.255, 0.376, and 0.5 (Kays and Leung 1963, pp. 544-545, Figures 6 to 8).

The measurements were consistently within 3% of the correlation, except that Nu_{ii} tended to deviate from the experimental data at Reynolds numbers below 20,000. At Re = 15,000 and r^* = 0.255, for instance, the correlation predicts a value for Nu_{ii} that is about 10% high (the two labels for "Present analysis" in their Figure 8 having been transposed inadvertently). The mixed-convection methodology is limited to Reynolds numbers greater than 15,000 (Section IX.1.6.3).

Because the contributions of natural convection to the experimental results can be neglected (Section IX.1.5), this attachment uses an *a priori* normal distribution for a Type B evaluation of the uncertainty inherent in the Kays-Leung correlation. For concentric, coextensive, uniform-flux cylinders, this attachment assigns a relative uncertainty of 3% as the random component and an additional systematic error in $\overline{Nu_{Fi}}(x)$ that decreases linearly from 10% to zero as Re increases from 15,000 to 20,000.

IX.3.4.4 Uncertainty in $\overline{Nu_F}$ from Linear Interpolation in Diameter Ratio

The error in linear interpolation for y is (Conte and de Boor 1972, p. 212, Example 4.5).

$$(x - x_0)(x - x_1)M / 2$$

where x is the input variable, (x_0, x_1) is the interpolation interval, and M is a value of the second derivative of y with respect to x somewhere in (x_0, x_1). The analysis in Section IX.3.2 suggests that the absolute value of M is no more than 10 times the value of the parameters. For $0.5 \geq r^* \geq 0.2$, and letting the worst case value of M correspond to the 95% confidence limit, one may take:

$$5(r^* - 0.2)(0.5 - r^*)$$

as the upper 95% confidence limit in the relative error caused by interpolation in r^*, so that the standard relative uncertainty would be one-half of that value.

IX.3.4.5 Uncertainty in $\overline{Nu_F}$ from Linear Interpolation in Reynolds Number

The maximum error in an interpolation interval is (Conte and de Boor 1972, p. 212, Example 4.5):

$$(x_1 - x_0)^2 M / 8$$

where x is the input variable, (x_0, x_1) is the interpolation interval, and M is a value of the second derivative of y with respect to x somewhere in (x_0, x_1). For the Kays-Leung tables, in which $Re_1 = 3Re_0$, the maximum error is $0.5(Re_0)^2 M$. Section IX.3.2 provides an example demonstrating the evaluation of M from the table developed in Step P2. One may take $0.5(Re_0)^2 M$ as the upper 95% confidence limit in the error caused by interpolation in Re.

IX.3.4.6 Uncertainty in $\overline{Nu_F}$ from Eccentric Location of the Inner Cylinder

Here we estimate the error caused by using a correlation developed for concentric cylinders to predict forced-convection Nusselt numbers for eccentric configurations. Our analysis is based on a review of experimental results for the turbulent flow of air in an eccentric annulus with fully developed constant heat rate (Kays and Perkins 1973, pp. 7-109 to 7-110, Figures 89 and 90).

Although the Nusselt number is uniform around the cylinder for the concentric configuration, eccentricity introduces circumferential variation in the Nusselt numbers. The cited charts provide the ratio of the local Nusselt number to the concentric value, as a function of positive eccentricity, for two opposite locations on the cylinder and two values of r^*. For pure forced convection, there is no difference between positive and negative eccentricity. The locations where the cylinders are most separated (labeled A in the figures) correspond to the tops of the cylinders in a configuration with negative eccentricity.

First, we consider the inner cylinder. We take the effect on Nu_{ii} as an estimate of the effect on $\overline{Nu_{Fi}}(x)$. We consider only the effect at the bottom, where the local heat transfer coefficient may be greater by about a factor of 5 (from natural convection, see Kuehn and Goldstein 1978, Figure 8). For the two values of r^*, with heating from the inner surface and the outer surface insulated, piecewise linear fits (by inspection) to the data in the region of interest (Kays and Perkins 1973, pp. 7-109, Figure 89, "B") result in the following approximations:

$$\frac{\overline{Nu_{Fi}}(x)}{\mathrm{Nu}_{ii}(Re)} = 1 + 0.15e^*, \quad r^* = 0.255,\ 0 \geq e^* \geq -0.67 \qquad \text{(Eq. IX-60)}$$

$$\frac{\overline{Nu_{Fi}}(x)}{\mathrm{Nu}_{ii}(Re)} = 1, \quad r^* = 0.5,\ 0 \geq e^* \geq -0.27 \qquad \text{(Eq. IX-61)}$$

$$\frac{\overline{Nu_{Fi}}(x)}{\mathrm{Nu}_{ii}(Re)} = 1 + 0.5(e^* + 0.27), \quad r^* = 0.5,\ -0.27 \geq e^* \geq -0.67 \qquad \text{(Eq. IX-62)}$$

The following general form for the relative error, $1-\frac{\overline{Nu_{Fi}}(x)}{\mathrm{Nu}_{ii}(Re)}$, covers the range $0.5 \geq r^* \geq 0.2$ and matches the above equations at $r^* = 0.255$ and $r^* = 0.5$:

$$1-\frac{\overline{Nu_{Fi}}(x)}{\mathrm{Nu}_{ii}(Re)} = -\frac{r^*-0.15}{0.7}e^*, \quad 0.3 \geq r^* \geq 0.2,\ 0 \geq e^* \geq -0.67 \qquad \text{(Eq. IX-63)}$$

$$1-\frac{\overline{Nu_{Fi}}(x)}{\mathrm{Nu}_{ii}(Re)} = 0, \quad 0.5 \geq r^* \geq 0.3,\ 0 \geq e^* \geq 0.405\text{-}1.35r^* \qquad \text{(Eq. IX-64)}$$

$$1-\frac{\overline{Nu_{Fi}}(x)}{\mathrm{Nu}_{ii}(Re)} = -\frac{r^*-0.15}{0.7}\left(e^*+1.35r^*-0.405\right),$$

$$0.5 \geq r^* \geq 0.3,\ 0.405\text{-}1.35r^* \geq e^* \geq -0.67 \qquad \text{(Eq. IX-65)}$$

For the outer cylinder, we take the effect on Nu_{oo} as representative of the effect on $\overline{Nu_{Fo}}(x)$. We consider only the effect at the top, because the local heat transfer coefficient may drop to zero at the bottom (from natural convection, see Section IX.3.3). For the two values of r^*, with heating from the outer surface and the inner surface insulated, the ratio is approximately (Kays and Perkins 1973, p. 7-110, Figure 90, "A"):

$$\frac{\overline{Nu_{Fo}}(x)}{\mathrm{Nu}_{oo}(Re)} = 1, \quad r^* = 0.255,\ 0 \geq e^* \geq -0.4 \qquad \text{(Eq. IX-66)}$$

$$\frac{\overline{Nu_{Fo}}(x)}{\mathrm{Nu}_{oo}(Re)} = 1+0.15\left(e^*+0.4\right), \quad r^* = 0.255,\ -0.4 \geq e^* \geq -0.67 \qquad \text{(Eq. IX-67)}$$

$$\frac{\overline{Nu_{Fo}}(x)}{\mathrm{Nu}_{oo}(Re)} = 1, \quad r^* = 0.5,\ 0 \geq e^* \geq -0.53 \qquad \text{(Eq. IX-68)}$$

$$\frac{\overline{Nu_{Fo}}(x)}{\mathrm{Nu}_{oo}(Re)} = 1+0.35\left(e^*+0.53\right), \quad r^* = 0.5,\ -0.53 \geq e^* \geq -0.67 \qquad \text{(Eq. IX-69)}$$

The following is the linear form for the relative error, $1-\frac{\overline{Nu_{Fo}}(x)}{\mathrm{Nu}_{oo}(Re)}$, $0.5 \geq r^* \geq 0.2$, that matches the above equations at $r^* = 0.255$ and $r^* = 0.5$:

$$1-\frac{\overline{Nu_{Fo}}(x)}{\mathrm{Nu}_{oo}(Re)} = 0, \quad 0.5 \geq r^* \geq 0.2,\ 0 \geq e^* \geq -\frac{26r^*+12.97}{49} \qquad \text{(Eq. IX-70)}$$

$$1-\frac{\overline{Nu_{Fo}}(x)}{\mathrm{Nu}_{oo}(Re)}=-\frac{r^*-0.07125}{1.225}\left(e^*+\frac{26r^*+12.97}{49}\right),\quad 0.5\ge r^*\ge 0.2,$$

$$-\frac{26r^*+12.97}{49}\ge \mathrm{e}^*\ge -0.67 \qquad \text{(Eq. IX-71)}$$

This is, the error in $\overline{Nu_{Fi}}(x)$ is positive, with a formula that depends on the value of r^*. If $0.3\ge r^*\ge 0.2$ and $0\ge \mathrm{e}^*\ge -0.67$, Equation IX-63 shows that there is a systematic relative error in $\overline{Nu_{Fi}}(x)$ of about $\left(-\mathrm{e}^*\right)\frac{r^*-0.15}{0.7}$.

For $0.5\ge r^*\ge 0.3$, the error in $\overline{Nu_{Fi}}(x)$ is not significant if $0\ge \mathrm{e}^*\ge 0.405-1.35r^*$; otherwise, there is a systematic relative error in $\overline{Nu_{Fi}}(x)$ of about (Equation IX-65) $+\left(-\mathrm{e}^*+0.405-1.35r^*\right)\frac{r^*-0.15}{0.7}$.

The error in $\overline{Nu_{Fo}}(x)$ is negligible if $0\ge \mathrm{e}^*\ge -\frac{26r^*+12.97}{49}$. Otherwise, Equation IX-71 shows that there is a systematic relative error in $\overline{Nu_{Fo}}(x)$ of about $+\frac{r^*-0.07125}{1.225}\left(-\mathrm{e}^*-\frac{26r^*+12.97}{49}\right)$.

IX.3.4.7 Uncertainty in Measured $\overline{Nu_F}$ from Unequal Cylinder Lengths

As in natural convection, any additional area in the outer cylinder may permit more convective heat transfer from the air to the outer cylinder. Also, where the inner cylinder is not present, the orifice area increases from $\pi\ (D_o - D_i)^2/4$ to $\pi\ \mathrm{D_o}^2/4$, by a factor of $1/(1\text{-}r^*)^2$. Because the mass flow rate must be the same and density does not change significantly, air velocity must drop by a factor of $(1\text{-}r^*)^2$. If the additional length of the cylinder is sufficiently small, the contribution to uncertainty from the length difference may be neglected. Alternatively, if r^* is sufficiently small, the effect of the greater length of the outer cylinder may be accounted for by applying the predicted Nusselt number to the additional area.

IX.3.4.8 Uncertainty in Measured $\overline{Nu_F}$ from Deviations from Fully Developed Flow

Kays and Leung also considered thermally developing annular flow. They presented non-dimensional fluid temperatures, including parameters labeled θ_{ii} and θ_{oo}, for thermally developing annular flow with r^*=0.255 (Kays and Leung 1963, p. 542, Figure 2). The parameters Nu_{ii} and $\mathrm{Nu_{oo}}$ are approximately the inverses of θ_{ii} and θ_{oo}, respectively. The Nusselt numbers start out at about twice their asymptotic value but decay to within 10% of their asymptote in a distance of about ten hydraulic diameters. For $x \le 11\ (D_o\text{-}D_i)$, this uncertainty

analysis assigns systematic errors in predictions of $\overline{Nu_{Fi}}(x)$ and $\overline{Nu_{Fo}}(x)$, based on a linear fit to the errors at x = 0 and x = 10 (D_o-D_i), that amount to

$$+\left[1-\frac{x}{11(D_o-D_i)}\right]100\%$$

IX.3.5 Uncertainty in Nusselt Numbers from the Mixed Convection Methodology

The uncertainty in the mixed-convection methodology is affected by the uncertainties in natural convection and forced convection in accordance with the Law of Propagation of Uncertainty (ANSI/NCSL Z540-2-1997, p. 19). Because the preliminary steps are not part of the methodology, this section considers only the uncertainties in Steps N1 through N4. In addition to the uncertainty contributed by the underlying convection correlations, this uncertainty analysis considers two sources of uncertainty in the mixed convection methodology. One is the error from using an approximation to the forced convection correlation (Equations IX-28 and IX-29) to find the equivalent Reynolds number for natural convection. The second source of uncertainty is the variation of measured mixed convection results from the Morgan approximation.

As noted at the beginning of Section IX.3, uncertainties in the input dimensionless groups must be evaluated by using the sensitivity analysis of Section IX.2. In addition, the uncertainty inherent in the methodology depends on the input parameters. Therefore, the prediction uncertainty is not quantified in this section. Section IX.4 provides examples of the evaluation of uncertainty in specific applications.

Step N1 uses interpolation in r^* to create a table of forced-convection parameters that are functions of *Re* only. As discussed in Section IX.3.4, the standard relative uncertainty is

$$2.5(r^*-0.2)(0.5-r^*)$$

Step N2 produces the equivalent Reynolds numbers for natural convection, $Re_{Ni}(x)$ and $Re_{No}(x)$. The uncertainty in each of these equivalent Reynolds numbers is a combined relative uncertainty, composed of the following contributions:

1. Relative uncertainty in the appropriate Nusselt number for natural convection, calculated in accordance with Section IX.3.3.

2. Relative uncertainty in the values for $\mathrm{Nu}_{\mathrm{ii}}$ and $\mathrm{Nu}_{\mathrm{oo}}$ produced by Step N1, calculated as described above.

3. Relative uncertainty in the reverse linear interpolation to get $Re_{Ni}(x)$ and $Re_{No}(x)$, calculated in accordance with the discussion of forward interpolation in Section IX.3.4.

4. Relative uncertainty introduced by the approximations represented by Equations IX-28 and IX-29.

The errors from using Equation IX-28 for $Re_{Ni}(x)$ and Equation IX-29 for $Re_{No}(x)$, instead of Equations IX-24 and IX-25, depend on the value of $\tau(x)$ and must therefore be evaluated separately for each application.

In Step N3, the equivalent Reynolds number for inner surface natural convection combines with the Reynolds number for forced convection to produce an equivalent Reynolds numbers for mixed convection. The uncertainty in $Re_{Ni}(x)$ propagates through Equation IX-23 (specialized to the inner surface by adding the subscript *i*). Taking the partial derivative of that equation with respect to $Re_{Ni}(x)$ and multiplying by $Re_{Ni}(x)/Re_{Mi}(x)$ yields:

$$\frac{Re_{Ni}(x)}{Re_{Mi}(x)}\frac{\partial Re_{Mi}(x)}{\partial Re_{Ni}(x)} = \left(\frac{Re_{Ni}(x)}{Re_{Mi}(x)}\right)^2 \qquad \text{(Eq. IX-72)}$$

This factor, applied to the relative uncertainty in $Re_{Ni}(x)$, produces its contribution to the combined relative uncertainty in $Re_{Mi}(x)$ (see Equation IX-31).

Next, Step N3 produces the Nusselt number for the inner surface. There are three contributors to the uncertainty in the Nusselt number:

1. The uncertainty in $Re_{Mi}(x)$, propagated according to the Law of Propagation of Uncertainty and making use of the sensitivity study (Section IX.2)
2. The uncertainty in the forced convection methodology when the input Reynolds number is known, calculated in accordance with Section IX.3.4
3. The uncertainty in mixed-convection Nusselt numbers inherent in the Morgan approximation.

Morgan (1975, p. 249, Figure 10) compared the experimental values from two data sets to the predicted ratio of effective Nusselt number to forced-flow Nusselt number. The experimental value for the ratio was consistently within 15% of the theoretical value. Taking 15% as the 95% confidence limit of an *a priori* normal distribution for a Type B evaluation of the uncertainty, this attachment assigns a standard uncertainty of 7.5% as the relative error inherent in the Morgan approximation for mixed convection.

Step N4 is the same as Step N3, except that it applies to the outer surface. The uncertainty considerations are the same as those for Step N3.

IX.4 COMPARISON OF METHODOLOGY RESULTS TO TEST DATA

This section evaluates the methodology under YMP specific conditions by corroboration of methodology results with data acquired from the EBS Ventilation Test series. Uncertainties in both the measurements and the predictions are considered.

The calculated uncertainties in the previous section determine the accuracy of the predictions for the EBS forced ventilation test configuration, taking into consideration that the cylinders in the EBS model were of different lengths, were not held to either constant temperature or constant flux conditions, and were not concentric. However, the invert and waste package support systems make the EBS test geometry more complex than that for which the uncertainty was evaluated. To determine how appropriate the methodology is for the EBS configuration, it was applied to the EBS ventilation tests. A description of how this was done and the overall results are given below.

IX.4.1 Prediction of Nusselt numbers

This section describes the prediction of Nusselt numbers for the EBS Ventilation Tests, in accordance with the algorithm of Section IX.1.6.

Step P1. (Geometry) For D_i = 0.4064 m and D_o = 1.37 m (Tables 4-27 and 4-29), r^* = 0.297. The predictions ignore the effect of the invert, so that they use a hydraulic diameter of 0.96 m. The effect of the invert would be to reduce the hydraulic diameter to about 0.93 m.

Step P2. (Reynolds Number) To minimize the influence of end effects, the axial position of interest is the most centrally located measurement station (Station 3). The cross-sectional area is 1.34 m^2. For each test, the mean fluid temperature at Station 3, T_f, is the average of the two reported measurements (Tables 4-35 through 4-37). Table 4-24 contains the properties of air at temperatures relevant to the EBS Ventilation Test Series. For each test, Table IX-6 or IX-7 shows the value of T_f, the kinematic viscosity, ν, of air at T_f, linearly interpolated in Table 4-24, the average of the two reported flow rates (Tables 4-33 and 4-34), the mean axial flow velocity calculated by dividing the flow rate by the annulus cross-sectional area, and the value of *Re* calculated using Equation IX-1.

Step P3. (Rayleigh Numbers) The value for g is 9.8 m/s^2 (Table 4-28). For each test (at Station 3), Table IX-8 or IX-9 gives the circumferential average temperature on each surface, based on the measurements in Tables 4-35 through Table 4-37. On the inner surface (the waste package), $\overline{T}_i$ is the average of the four reported measurements. However, because the bottom of the outer surface is covered by the invert, the circumferential average temperature on the outer surface, $\overline{T}_o$, is the average of only the top and side measurements. Tables IX-8 and IX-9 also show the amount that each average differs from its associated T_f , as well as the Rayleigh numbers calculated from Equations IX-5 and IX-6 and the relevant air properties.

Step N1. (Forced-Convection Parameters) Table IX-10 contains the forced-convection parameters as a function of *Re*, for *Pr*=0.7 and r^*=0.297, linearly interpolated from Table IX-2.

Step N2. (Natural Convection) For each test (at Station 3), Table IX-11 or IX-12 gives the effective circumferential Nusselt numbers for natural convection, on the inner and

outer surfaces. The tables also show the equivalent Reynolds numbers, calculated in accordance with Equations IX-28 and IX-29.

Step N3. (Inner-Surface Nusselt Number) Tables IX-13 and IX-14 report the mixed-convection Reynolds number at the inner surface for each test, calculated in accordance with Equation IX-26. These tables also report the forced-convection parameters associated with each such Reynolds number, from interpolation in Table IX-6. The last column contains the effective circumferential Nusselt number convection at the inner surface, from the mixed-convection methodology, Equation IX-24.

Step N4. (Outer-Surface Nusselt Number) Tables IX-15 and IX-16 report the mixed-convection Reynolds number at the outer surface for each test, calculated in accordance with Equation IX-27. These tables also report the forced-convection parameters associated with each such Reynolds number, from interpolation in Table IX-6. The last column contains the effective circumferential Nusselt number for mixed convection at the outer surface, from the mixed-convection methodology, Equation IX-25.

Table IX-6. Reynolds Numbers for EBS Ventilation Test Series, Phase 1

Location	T_f (ºC)	T_f (K)	ν (m^2/s)	V (m^3/s)	u_m (m/s)	Re (Thousands)
Test 1, Station 3	27.60	300.75	1.597E-05	0.999	0.74	44.8
Test 2, Station 3	31.40	304.55	1.635E-05	0.498	0.37	21.8
Test 3, Station 3	29.25	302.40	1.613E-05	1.007	0.75	44.7
Test 4, Station 3	27.00	300.15	1.591E-05	1.990	1.48	89.7
Test 5, Station 3	31.00	304.15	1.631E-05	0.522	0.39	22.9
Test 6, Station 3	21.70	294.85	1.543E-05	3.050	2.27	141.7

Table IX-7. Reynolds Numbers for EBS Ventilation Test Series, Phase 2

Location	T_f (ºC)	T_f (K)	ν (m^2/s)	V (m^3/s)	u_m (m/s)	Re (Thousands)
Test 1, Station 3	27.40	300.55	1.595E-05	0.996	0.74	44.8
Test 2, Station 3	36.80	309.95	1.689E-05	1.012	0.75	42.9
Test 3, Station 3	46.85	320.00	1.790E-05	1.035	0.77	41.4
Test 4, Station 3	46.60	319.75	1.788E-05	1.028	0.76	41.2
Test 5, Station 3	29.75	302.90	1.618E-05	1.006	0.75	44.6
Test 6, Station 3	39.50	312.65	1.716E-05	1.023	0.76	42.7
Test 7, Station 3	48.90	322.05	1.811E-05	1.032	0.77	40.8
Test 8, Station 3	48.85	322.00	1.810E-05	1.034	0.77	40.9
Test 9, Station 3	31.60	304.75	1.637E-05	0.511	0.38	22.4
Test 10, Station 3	40.35	313.50	1.725E-05	0.548	0.41	22.8
Test 11, Station 3	49.65	322.80	1.818E-05	0.542	0.40	21.4
Test 12, Station 3	36.15	309.30	1.683E-05	0.550	0.41	23.4
Test 13, Station 3	43.95	317.10	1.761E-05	0.552	0.41	22.5
Test 14, Station 3	53.35	326.50	1.856E-05	0.545	0.41	21.1
Test 15, Station 3	34.50	307.65	1.666E-05	0.993	0.74	42.7
Test 16, Station 3	34.20	307.35	1.663E-05	0.991	0.74	42.7

Table IX-8. Rayleigh Numbers for EBS Ventilation Test Series, Phase 1

Location	Avg T_i (ºC)	Avg T_o (ºC)	(T_i-T_f) (ºC)	(T_o-T_f) (ºC)	τ	α (m^2/s)	Ra_i (Millions)	Ra_o (Millions)
Test 1, Station 3	42.33	30.17	14.73	2.567	5.74	2.26E-05	89	596
Test 2, Station 3	46.28	33.27	14.88	1.867	7.97	2.32E-05	85	408
Test 3, Station 3	55.40	33.33	26.15	4.083	6.40	2.29E-05	154	923
Test 4, Station 3	50.03	29.93	23.03	2.933	7.85	2.25E-05	141	687
Test 5, Station 3	57.33	34.23	26.33	3.233	8.14	2.31E-05	151	711
Test 6, Station 3	41.30	23.53	19.60	1.833	10.69	2.18E-05	130	465

Table IX-9. Rayleigh Numbers for EBS Ventilation Test Series, Phase 2

Location	Avg T_i (ºC)	Avg T_o (ºC)	(T_i-T_f) (ºC)	(T_o-T_f) (ºC)	τ	α (m^2/s)	Ra_i (Millions)	Ra_o (Millions)
Test 1, Station 3	44.85	30.53	17.45	3.133	5.57	2.26E-05	106	730
Test 2, Station 3	53.48	38.63	16.68	1.833	9.10	2.40E-05	87	368
Test 3, Station 3	62.88	48.27	16.03	1.417	11.31	2.55E-05	72	245
Test 4, Station 3	62.40	47.90	15.80	1.300	12.15	2.54E-05	72	225
Test 5, Station 3	56.03	33.97	26.28	4.217	6.23	2.29E-05	154	945
Test 6, Station 3	65.38	43.43	25.88	3.933	6.58	2.44E-05	130	758
Test 7, Station 3	73.63	51.63	24.73	2.733	9.05	2.58E-05	108	458
Test 8, Station 3	73.63	51.47	24.78	2.617	9.47	2.58E-05	109	439
Test 9, Station 3	49.10	34.93	17.50	3.333	5.25	2.32E-05	99	726
Test 10, Station 3	57.30	42.80	16.95	2.450	6.92	2.45E-05	84	466
Test 11, Station 3	65.85	50.83	16.20	1.183	13.69	2.59E-05	70	196
Test 12, Station 3	62.43	40.60	26.28	4.450	5.90	2.39E-05	139	902
Test 13, Station 3	69.50	47.17	25.55	3.217	7.94	2.50E-05	120	580
Test 14, Station 3	78.00	55.50	24.65	2.150	11.47	2.64E-05	101	338
Test 15, Station 3	60.53	38.13	26.03	3.633	7.16	2.36E-05	141	756
Test 16, Station 3	60.38	37.63	26.18	3.433	7.62	2.36E-05	143	718

Table IX-10. Parameters for Annular Forced Convection at Pr = 0.7 and $r^* = 0.297$

Re:	10000	30000	100000	300000	1000000
Nu_{ii}:	36.1	75.4	186.3	449.5	1208.8
θ_i:	0.376	0.312	0.266	0.243	0.219
Nu_{oo}:	29.0	63.6	162.7	391.5	1060.3
θ_o:	0.087	0.076	0.068	0.061	0.056

Table IX-11. Natural Convection Nusselt Numbers for EBS Ventilation Test Series, Phase 1

Location	Nu_{Ni}	Nu_{No}	Re_{Ni} (Thousands)	Re_{No} (Thousands)
Test 1, Station 3	131	109	65	62
Test 2, Station 3	129	99	64	55
Test 3, Station 3	156	122	81	71
Test 4, Station 3	152	113	78	65
Test 5, Station 3	155	114	80	66
Test 6, Station 3	148	103	76	58

Table IX-12. Natural Convection Nusselt Numbers for EBS Ventilation Test Series, Phase 2

Location	Nu_{Ni}	Nu_{No}	Re_{Ni} (Thousands)	Re_{No} (Thousands)
Test 1, Station 3	139	115	70	66
Test 2, Station 3	130	97	65	53
Test 3, Station 3	123	87	60	47
Test 4, Station 3	123	85	60	45
Test 5, Station 3	156	123	81	72
Test 6, Station 3	148	116	76	67
Test 7, Station 3	139	102	70	57
Test 8, Station 3	140	101	71	57
Test 9, Station 3	136	115	68	66
Test 10, Station 3	129	103	64	58
Test 11, Station 3	122	83	59	43
Test 12, Station 3	151	121	78	71
Test 13, Station 3	144	108	73	62
Test 14, Station 3	137	95	69	52
Test 15, Station 3	152	116	78	67
Test 16, Station 3	152	114	79	66

Table IX-13. Predicted Inner-Surface Nusselt Numbers for EBS Ventilation Test Series, Phase 1

Location	Re_{Mi} (Thousands)	$Nu_{ii}(Re_{Mi})$	$Nu_{oo}(Re_{Mi})$	$\theta_i(Re_{Mi})$	$\theta_o(Re_{Mi})$	Nu_{Mi}
Test 1, Station 3	79	153	133	0.280	0.070	163
Test 2, Station 3	68	135	117	0.288	0.071	142
Test 3, Station 3	92	174	152	0.271	0.069	184
Test 4, Station 3	119	211	184	0.264	0.067	221
Test 5, Station 3	83	160	139	0.277	0.070	168
Test 6, Station 3	161	266	232	0.259	0.066	276

Table IX-14. Predicted Inner-Surface Nusselt Numbers for EBS Ventilation Test Series, Phase 2

Location	Re_{Mi} (thousands)	$Nu_{ii}(Re_{Mi})$	$Nu_{oo}(Re_{Mi})$	$\theta_i(Re_{Mi})$	$\theta_o(Re_{Mi})$	Nu_{Mi}
Test 1, Station 3	83	159	139	0.278	0.070	170
Test 2, Station 3	78	151	131	0.281	0.070	158
Test 3, Station 3	73	143	124	0.284	0.071	150
Test 4, Station 3	73	143	124	0.284	0.071	149
Test 5, Station 3	92	174	152	0.271	0.069	184
Test 6, Station 3	87	166	144	0.275	0.069	175
Test 7, Station 3	81	157	136	0.279	0.070	164
Test 8, Station 3	82	157	137	0.278	0.070	164
Test 9, Station 3	72	141	123	0.285	0.071	151
Test 10, Station 3	68	135	117	0.288	0.071	143
Test 11, Station 3	63	128	110	0.291	0.072	133
Test 12, Station 3	81	156	136	0.279	0.070	166
Test 13, Station 3	77	149	130	0.282	0.070	157
Test 14, Station 3	72	142	123	0.285	0.071	148
Test 15, Station 3	89	169	147	0.273	0.069	178
Test 16, Station 3	89	170	148	0.273	0.069	178

Table IX-15. Predicted Outer-Surface Nusselt Numbers for EBS Ventilation Test Series, Phase 1

Location	Re_{Mo} (thousands)	$Nu_{ii}(Re_{Mo})$	$Nu_{oo}(Re_{Mo})$	$\theta_i(Re_{Mo})$	$\theta_o(Re_{Mo})$	Nu_{Mo}
Test 1, Station 3	77	149	130	0.282	0.070	194
Test 2, Station 3	59	122	105	0.293	0.072	179
Test 3, Station 3	84	161	140	0.277	0.069	216
Test 4, Station 3	111	201	175	0.265	0.067	286
Test 5, Station 3	70	138	120	0.286	0.071	204
Test 6, Station 3	153	256	223	0.260	0.066	411

Table IX-16. Predicted Outer-Surface Nusselt Numbers for EBS Ventilation Test Series, Phase 2

Location	Re_{Mo} (thousands)	$Nu_{ii}(Re_{Mo})$	$Nu_{oo}(Re_{Mo})$	$\theta_i(Re_{Mo})$	$\theta_o(Re_{Mo})$	Nu_{Mo}
Test 1, Station 3	80	155	134	0.279	0.070	198
Test 2, Station 3	69	136	118	0.287	0.071	211
Test 3, Station 3	62	127	110	0.291	0.072	217
Test 4, Station 3	61	125	108	0.292	0.072	222
Test 5, Station 3	84	162	141	0.277	0.069	215
Test 6, Station 3	79	154	134	0.280	0.070	209
Test 7, Station 3	70	139	121	0.286	0.071	215
Test 8, Station 3	70	138	120	0.286	0.071	218
Test 9, Station 3	70	138	120	0.286	0.071	175
Test 10, Station 3	62	126	109	0.291	0.072	175
Test 11, Station 3	48	104	90	0.300	0.074	199
Test 12, Station 3	74	146	127	0.283	0.071	191
Test 13, Station 3	66	132	114	0.289	0.072	193
Test 14, Station 3	56	117	101	0.295	0.073	202
Test 15, Station 3	79	154	134	0.280	0.070	215
Test 16, Station 3	79	152	132	0.280	0.070	218

IX.4.2 Uncertainty in Predicted Nusselt Numbers

This section evaluates the sources of uncertainty that have a quantitative dependence on the configuration or environment. These are the sources for which Section IX.3 does not provide a numerical uncertainty. The sources of uncertainty, both those evaluated here and those evaluated in Section IX.3, become inputs to the combined uncertainty.

IX.4.2.1 Uncertainty in the Predicted Nusselt Numbers for Natural Convection

For natural convection, Section IX.3.3 evaluates the deviation of measured Nusselt numbers from the Kuehn-Goldstein correlation of those measurements. The Type B evaluation gives a random relative standard uncertainty of 12%. It also finds that the contribution from the effects of diameter ratio are negligible for the value in the EBS Ventilation Test Series, $r^* = 0.3$.

This section evaluates the following sources of uncertainty for the particular configuration and conditions of the EBS Ventilation Tests, based on the discussions in Section IX.3.3:

1. The uncertainty in predicted effective circumferential Nusselt numbers for coextensive, isothermal cylinders arising from eccentric location of the inner cylinder

2. The uncertainty in predicted effective circumferential Nusselt numbers for isothermal cylinders arising from unequal cylinder lengths

3. Uncertainty in the effective circumferential Nusselt numbers arising from temperature variation along the circumferences of the cylinders.

As described in Section IX.3.3, the use of the concentric correlation for natural convection systematically underestimates the natural convection heat transfer by $-0.15|e^*|$. For the EBS Ventilation Test Series configuration, with an *e** of -0.42, this source of uncertainty causes a systematic error of about –6%.

The use of data from Station 3 minimizes the effects of the extra length of wall beyond the ends of the waste package train. As suggested in Section IX.3.3, this analysis neglects the error caused by those extensions and by the gaps between the waste packages, because the following conditions hold:

1. The greater length of the outer cylinder does not cause a qualitative change in the flow from natural convection other than mild divergence and convergence along the axis.

2. The changes in the Rayleigh numbers appearing in the correlation, caused by the change in air temperature, account for most of the changes in the circumferential average Nusselt numbers.

3. The remaining effects of the longer outer cylinder are not significant compared to the other contributions to uncertainty.

The following is an evaluation of the effects of the circumferential temperature variations in the EBS Ventilation Tests. From Section IX.3.3, the relative error in the inner-cylinder Nusselt number is about $+0.25[T_t - \overline{T}_i]/[\overline{T}_i - T_f]$ and the relative error in the outer-cylinder Nusselt number is about $+0.4[T_t - \overline{T}_o]/[T_f - \overline{T}_o]$.

Table IX-17 provides an evaluation of the errors for each test in the EBS Ventilation Test Series. The average is a Type A evaluation of the effects of the circumferential temperature variations. The predictions for $\overline{Nu_{Ni}}(x)$ have a systematic error of +8% with a random standard uncertainty that is 0.5% of $\overline{Nu_{Ni}}(x)$.

At the outer surface, the values are negative, because unlike the situation for pure natural convection, the ventilation tests have $\overline{T}_o > T_f$. The negative error is reasonable because the magnitude of the temperature difference is *largest* at the top. The predictions have a systematic error of –3% in $\overline{Nu_{No}}(x)$ with a random standard uncertainty of 2%.

Table IX-17. Errors in $\overline{Nu_N}(x)$ for EBS Ventilation Test Series

	Location	Nu_{Ni} Error	Nu_{No} Error
Phase 1	Test 1, Station 3	8.6%	-5.2%
	Test 2, Station 3	8.9%	-7.1%
	Test 3, Station 3	7.6%	-4.6%
	Test 4, Station 3	8.0%	0.5%
	Test 5, Station 3	7.9%	-4.5%
	Test 6, Station 3	8.5%	2.9%
Phase 2	Test 1, Station 3	8.1%	-3.4%
	Test 2, Station 3	8.7%	-3.6%
	Test 3, Station 3	8.6%	-3.8%
	Test 4, Station 3	8.7%	-3.1%
	Test 5, Station 3	7.4%	-3.4%
	Test 6, Station 3	7.9%	-3.7%
	Test 7, Station 3	7.9%	-2.4%
	Test 8, Station 3	7.8%	-2.0%
	Test 9, Station 3	8.7%	-4.4%
	Test 10, Station 3	9.1%	-3.3%
	Test 11, Station 3	9.0%	-5.6%
	Test 12, Station 3	8.3%	-3.6%
	Test 13, Station 3	8.3%	3.3%
	Test 14, Station 3	8.2%	-1.9%
	Test 15, Station 3	7.8%	-2.9%
	Test 16, Station 3	7.9%	-3.1%
	mean	8.3%	-3.0%
	std dev	0.5%	2.46%

In all of the EBS ventilation tests, the outer surface was hotter than the air (Tables IX-8 and IX-9). Therefore, the flow patterns were more like Figure IX-1d than Figure IX-1c. There may be an unknown error from applying the Kuehn-Goldstein correlation to the flow pattern of Figure IX-1d.

Table IX-18 presents the contributions to $\overline{Nu_N}$ uncertainty from other causes and their combined standard uncertainty. Systematic effects are shown as corrections, which have the opposite signs from the errors. The 95% confidence interval for $\overline{Nu_{Ni}}(x)$ is from –26% to +22%. At the outer surface, the systematic effects are in the same direction, so that the 95% confidences limit is from –15% to +33%. Of the effects considered in Table IX-18, the dominant source of uncertainty is the deviation of measured Nusselt numbers reported by Kuehn and Goldstein (1976) from their correlation of those measurements.

Table IX-18. Uncertainty Budget, Predicted $\overline{Nu_N}$

Source of Uncertainty	Relative Standard Uncertainties from Random Effects		Corrections for Systematic Effects	
	Type A Evaluation	Type B Evaluation	Type A Evaluation	Type B Evaluation
Correlation for concentric, coextensive, isothermal cylinders		12%		
Eccentricity				+6%
Circumferential temperature variation	$\overline{Nu_{Ni}}$: 0.6% $\overline{Nu_{No}}$: 2%			$\overline{Nu_{Ni}}$: -8% $\overline{Nu_{No}}$: +3%

NOTES: $\overline{Nu_{Ni}}$: Correction for systematic effects: -2%
Combined standard uncertainty from random effects: 12%
95% confidence interval: -26% to +22%

$\overline{Nu_{No}}$: Correction for systematic effects: +9%
Combined standard uncertainty from random effects: 12%
95% confidence interval: -15% to +33%

IX.4.2.2 Uncertainty in the Predicted Nusselt Numbers for Forced Convection

For forced convection, Section IX.3.4 finds that the contribution from the effects of flux variations along the lengths and the circumferences of the cylinder are negligible. This section evaluates the following sources of uncertainty for the particular configuration and conditions of the EBS Ventilation Tests, based on the discussions in Section IX.3.4:

1. The extent to which measured circumferential average Nusselt numbers for fully developed flow in concentric, coextensive, uniform-flux cylinders deviate from the circumferential average Nusselt numbers predicted by the correlation.

2. Uncertainty from linear interpolation of the Kays-Leung parameters to the diameter ratio of 0.3.

3. Uncertainty from linear interpolation of the Kays-Leung parameters to the appropriate Reynolds number.

4. The uncertainty in effective circumferential Nusselt numbers for fully developed flow in uniform-flux cylinders arising from unequal cylinder lengths.

5. The uncertainty in effective circumferential Nusselt numbers for fully developed flow in coextensive, uniform-flux cylinders arising from eccentric location of the inner cylinder.

6. Uncertainty arising from deviations from fully developed flow.

For the uncertainty inherent in the Kays-Leung correlation, the Type B evaluation in Section IX.3.4 assigns a relative uncertainty of 3% as the random component. Because all of the ventilation tests had *Re* greater than 20,000, the systematic component is negligible.

For $0.2 < r^* < 0.5$, one may take $5(r^* - 0.2)(0.5 - r^*)$ as the upper 95% confidence limit in the relative error caused by interpolation of r^* (Section IX.3.4). For interpolation to r^*=0.3, the 95% confidence limit is 10%. This attachment uses an *a priori* normal distribution for a Type B evaluation of the uncertainty, with a standard uncertainty of 5%, for the relative error caused by interpolation in r^*.

The maximum error in an interpolation in *Re* is $0.5(Re_0)^2 M$, where Re_0 is the value at the lower end of the interval and *M* is a second derivative (Section IX.3.2). The analysis in Section IX.3.2 indicates that for $r^* = 0.3$, the relative error should be no more than 7%. Taking 7% as the 95% confidence limit of an *a priori* normal distribution for a Type B evaluation of the uncertainty, this attachment assigns a standard uncertainty of 3.5% as the relative error caused by interpolation in *Re*.

Section IX.3.4 derived expressions for the relative systematic errors in the Nusselt numbers arising from the eccentricity of the configuration. For the configuration of the EBS Ventilation Test Series, $r^* = 0.3$ and $e^* = -0.4$. Applying these values to the expressions, the relative systematic errors for the inner and outer Nusselt numbers are:

$$1 - \frac{\overline{Nu_{Fi}}(x)}{\mathrm{Nu}_{ii}(Re)} = +8.6\% \qquad \text{(Eq. IX-73)}$$

and

$$1 - \frac{\overline{Nu_{Fo}}(x)}{\mathrm{Nu}_{oo}(Re)} = 0 \qquad \text{(Eq. IX-74)}$$

As suggested in Section IX.3.4, this analysis neglects the error caused by the difference in total lengths of the cylinders, because the necessary conditions hold. That is, the additional length of the cylinder is sufficiently small.

Section IX.3.4 provides an estimate of the systematic error arising from applying Nusselt numbers predicted for fully developed flow to regions of thermally developing flow. According to that estimate, the systematic error becomes negligible at a distance of 10 (D_i - D_o) into the flow. For the EBS Ventilation Test configuration, that distance is 10 m. Because Station 3 is about 20 m from the inlet (BSC 2003f, Section 2), this analysis neglects that source of uncertainty.

Table IX-19 presents the contributions to $\overline{Nu_F}$ uncertainty from various causes and the combined standard uncertainty. Systematic effects are shown as corrections and therefore have opposite signs. There are three major random effects that are approximately equal in significance, causing the 95% confidence limit for $\overline{Nu_{Fo}}$ to range from –14% to +14%. $\overline{Nu_{Fi}}$

also has a systematic effect from eccentricity, so that its 95% confidence limit extends from –23% to +5%.

Table IX-19. Uncertainty Budget, Predicted $\overline{Nu_F}$

Source of Uncertainty	Relative Uncertainties from Random Effects		Corrections for Systematic Effects	
	Type A Evaluation	Type B Evaluation	Type A Evaluation	Type B Evaluation
Correlation for fully-developed flow in concentric, coextensive, uniform-flux cylinders		3%		
Linear interpolation in r^*		5%		
Linear interpolation in *Re*		3.5%		
Eccentricity				$\overline{Nu_{Fi}}$: -9%

NOTES: Correction for systematic effects, $\overline{Nu_{Fi}}$ only: -9%
Combined standard uncertainty from random effects: 7%
$\overline{Nu_{Fi}}$ 95% confidence interval: -23% to +5%
$\overline{Nu_{Fo}}$ 95% confidence interval: -14% to +14%

IX.4.2.3 Uncertainty in the Predicted Nusselt Numbers for Mixed Convection

This section evaluates the uncertainties in the predicted Nusselt numbers by propagating uncertainty through the calculations of Step N1 through Step N3 that were reported in Section IX.4.1. The uncertainty analysis reflects the discussion in Section IX.3.5. Uncertainties in measured temperatures and flow rates are neglected.

Step N1 uses interpolation in r^* to create Table IX-10, in which the forced-convection parameters are functions of *Re* only. As discussed above, the standard uncertainty in each interpolated parameter, such as Nu_{ii} or Nu_{oo}, is 5%.

Step N2 begins with the calculation of the two natural convection Nusselt numbers, $\overline{Nu_{Ni}}(x)$ and $\overline{Nu_{No}}(x)$, reported in Tables IX-11 and IX-12. As reported in Table IX-18, each is missing a correction for systematic effects and has a combined standard uncertainty of 12% from random effects. These combine with the 5% standard uncertainties in Nu_{ii} and Nu_{oo} to produce the total uncertainty in the Nusselt numbers that $Re_{Ni}(x)$ and $Re_{No}(x)$ are supposed to represent. That is, the total uncertainty before the reverse interpolation consists of a combined standard uncertainty of 13% from random effects, as well as a systematic error. This does not include the error arising from having the flow pattern of Figure IX-1d instead of the pattern of Figure IX-1c.

The factor for propagating relative uncertainty is $(Nu_{ii}/Re)\partial Re/\partial Nu_{ii}$ or $(Nu_{oo}/Re)\partial Re/\partial Nu_{oo}$ (see Equation IX-31). For the interval between *Re* of 30,000 and *Re* of 100,000 in Table IX-10, for example, the last two weighting factors are both about 1.3. Taking 1.3 as a representative

propagation factor, the uncertainty in Nu_N contributes 17% to the random standard uncertainty in Re_N from random effects. The corrections of -2% and +9% in the $\overline{Nu_{Ni}}(x)$ and $\overline{Nu_{No}}(x)$ become corrections of -3% and +12% in $Re_{Ni}(x)$ and $Re_{No}(x)$, respectively.

Another source of uncertainty in $Re_{Ni}(x)$ and $Re_{No}(x)$ is the interpolation in Reynolds number. The analysis in Section IX.3.2 shows that the error may range up to 12%. That result is the basis for a Type B evaluation of the uncertainty and an assignment of 6% as the standard relative uncertainty from the reverse interpolation. Together with the 17% of the previous paragraph, this yields 18% as the combined standard uncertainty from random effects (applying Equation IX-30).

A final source of uncertainty in $Re_{Ni}(x)$ and $Re_{No}(x)$ is the use of the approximations represented by Equations IX-28 and IX-29. For purposes of this attachment, Tables IX-20 and IX-21 present the values of $Re_{Ni}(x)$ and $Re_{No}(x)$ that would have been obtained without the approximation. These "correct" values are the result of applying the bisection method (Conte and de Boor 1972, p. 28, Algorithm 2.1) until the interval in Re was less than 50.0.

Tables IX-20 and IX-21 also contain the percentage corrections that are implied for the values of $Re_{Ni}(x)$ and $Re_{No}(x)$ appearing in Tables IX-11 and IX-12, the random uncertainties, and the 95% confidence limits. For the confidence limits, the percentage of random uncertainty was applied *after* the correction. For Test 1 of Phase 1, for example, the correction is –15%, the random standard uncertainty is 14%, and the lower confidence limit of –39% is the value of the expression (100% - 28%) (100% - 15%) – 100%. The confidence limits do not include the error from the approximation that the effects of the Figure IX-1d flow pattern are negligible.

Of the evaluated sources of uncertainty in $Re_{Ni}(x)$ the dominant source is the uncertainty in $\overline{Nu_{Ni}}(x)$, which stems from the deviation of measured Nusselt numbers reported by Kuehn and Goldstein (1976) from their correlation of those measurements. The dominant contribution to the evaluated uncertainty in $Re_{No}(x)$ is the approximation represented by Equation IX-29.

Table IX-20. Combined Uncertainty in Re_{Ni} and Re_{No} for EBS Ventilation Test Series, Phase 1

Location	Re_N from Eq. IX-28 or IX-29 (Simplified) (Thousands)	Re_N from Eq. IX-24 or IX-25 (Not Simplified) (Thousands)	To Correct for Simplified Equation	Correction for Systematic Effect in Nu_N	Combined Correction for Systematic Effects	Standard Uncertainty from Random Effects	95% Confidence Interval	
							Lower	Upper
Re_{Ni}								
Test 1, Station 3	65	60	-8%	-3%	-11%	18%	-43%	21%
Test 2, Station 3	64	60	-7%	-3%	-10%	18%	-42%	22%
Test 3, Station 3	81	76	-7%	-3%	-10%	18%	-42%	23%
Test 4, Station 3	78	74	-6%	-3%	-9%	18%	-42%	24%
Test 5, Station 3	80	76	-6%	-3%	-9%	18%	-42%	24%
Test 6, Station 3	76	72	-5%	-3%	-8%	18%	-41%	25%
Re_{No}								
Test 1, Station 3	62	35	-44%	12%	-32%	18%	-56%	-7%
Test 2, Station 3	55	25	-54%	12%	-42%	18%	-63%	-21%
Test 3, Station 3	71	39	-45%	12%	-33%	18%	-57%	-9%
Test 4, Station 3	65	31	-52%	12%	-40%	18%	-62%	-19%
Test 5, Station 3	66	31	-54%	12%	-42%	18%	-63%	-21%
Test 6, Station 3	58	22	-62%	12%	-50%	18%	-68%	-32%

Table IX-21. Combined Uncertainty in Re_{Ni} and Re_{No} for EBS Ventilation Test Series, Phase 2

Location	Re_N from Eq. IX-28 or IX-29 (Simplified) (Thousands)	Re_N from Eq. IX-24 or IX-25 (Not Simplified) (Thousands)	To Correct for Simplified Equation	Correction for Systematic Effect in Nu_N	Combined Correction for Systematic Effects	Standard Uncertainty from Random Effects	95% Confidence Interval	
							Lower	Upper
Re_{Ni}								
Test 1, Station 3	70	65	-8%	-3%	-11%	18%	-43%	21%
Test 2, Station 3	65	61	-7%	-3%	-10%	18%	-42%	23%
Test 3, Station 3	60	57	-6%	-3%	-9%	18%	-42%	24%
Test 4, Station 3	60	57	-5%	-3%	-8%	18%	-41%	26%
Test 5, Station 3	81	75	-8%	-3%	-11%	18%	-43%	21%
Test 6, Station 3	76	71	-7%	-3%	-10%	18%	-42%	23%
Test 6, Station 3	76	71	-7%	-3%	-10%	18%	-42%	23%

Table IX-21. Combined Uncertainty in Re_{Ni} and Re_{No} for EBS Ventilation Test Series, Phase 2

Location	Re_N from Eq. IX-28 or IX-29 (Simplified) (Thousands)	Re_N from Eq. IX-24 or IX-25 (Not Simplified) (Thousands)	To Correct for Simplified Equation	Correction for Systematic Effect in Nu_N	Combined Correction for Systematic Effects	Standard Uncertainty from Random Effects	95% Confidence Interval	
Test 6, Station 3	76	71	-7%	-3%	-10%	18%	-42%	23%
Test 7, Station 3	70	66	-6%	-3%	-9%	18%	-42%	23%
Test 8, Station 3	71	67	-6%	-3%	-9%	18%	-42%	24%
Test 9, Station 3	68	63	-8%	-3%	-11%	18%	-43%	21%
Test 10, Station 3	64	60	-7%	-3%	-10%	18%	-42%	23%
Test 11, Station 3	59	57	-5%	-3%	-8%	18%	-41%	25%
Test 12, Station 3	78	72	-7%	-3%	-10%	18%	-43%	22%
Test 13, Station 3	73	69	-6%	-3%	-9%	18%	-42%	24%
Test 14, Station 3	69	65	-5%	-3%	-8%	18%	-41%	25%
Test 15, Station 3	78	74	-6%	-3%	-9%	18%	-42%	24%
Test 16, Station 3	79	74	-6%	-3%	-9%	18%	-42%	23%
Re_{No}								
Test 1, Station 3	66	39	-42%	12%	-30%	18%	-55%	-5%
Test 2, Station 3	53	23	-58%	12%	-46%	18%	-65%	-26%
Test 3, Station 3	47	16	-66%	12%	-54%	18%	-70%	-37%
Test 4, Station 3	45	15	-68%	12%	-56%	18%	-72%	-40%
Test 5, Station 3	72	41	-44%	12%	-32%	18%	-56%	-7%
Test 6, Station 3	67	36	-47%	12%	-35%	18%	-58%	-12%
Test 7, Station 3	57	24	-58%	12%	-46%	18%	-65%	-26%
Test 8, Station 3	57	23	-59%	12%	-47%	18%	-66%	-28%
Test 9, Station 3	66	40	-40%	12%	-28%	18%	-54%	-2%
Test 10, Station 3	58	29	-50%	12%	-38%	18%	-60%	-15%
Test 11, Station 3	43	12	-72%	12%	-60%	18%	-74%	-45%
Test 12, Station 3	71	40	-43%	12%	-31%	18%	-56%	-7%
Test 13, Station 3	62	29	-54%	12%	-42%	18%	-63%	-21%
Test 14, Station 3	52	18	-65%	12%	-53%	18%	-70%	-36%
Test 15, Station 3	67	34	-49%	12%	-37%	18%	-60%	-15%
Test 16, Station 3	66	32	-51%	12%	-39%	18%	-61%	-18%

Steps N3 and N4 begin with calculations of $Re_{Mi}(x)$ and $Re_{Mo}(x)$, for which the only uncertainty is from the uncertainty in $Re_{Ni}(x)$ and $Re_{No}(x)$. As explained in Section IX.3.5, the relative uncertainty propagates in Re_N propagates into Re_M with a factor of $[Re_N/Re_M]^2$. Tables IX-22 and IX-23 show that propagation for the EBS Ventilation Test Series, still omitting the error from the qualitatively different flow pattern.

Finally, steps N3 and N4 calculate $\overline{Nu_{Mi}}(x)$ and $\overline{Nu_{Mo}}(x)$. Tables IX-22 and IX-23 show the factor $(Re_M/Nu_M)\partial Nu_M/\partial Re_M$ by which the relative uncertainty in Re_M propagates into $\overline{Nu_M}$. For purposes of this attachment, the derivatives were estimated by taking a small increment in Re_M and evaluating $\overline{Nu_M}$ again.

Table IX-22. Combined Uncertainty in Re_{Mi} and Re_{Mo} for EBS Ventilation Test Series, Phase 1

Location	$(Re_N/Re_M)^2$	Combined Correction for Systematic Effects	Standard Uncertainty from Random Effects	(Re_M/Nu_M) Times Partial of Nu_M with Respect to Re_M
Re_{Mi}				
Test 1, Station 3	0.68	-8%	12%	0.80
Test 2, Station 3	0.90	-9%	16%	0.78
Test 3, Station 3	0.77	-7%	14%	0.80
Test 4, Station 3	0.43	-4%	8%	0.74
Test 5, Station 3	0.92	-8%	17%	0.81
Test 6, Station 3	0.22	-2%	4%	0.79
Re_{Mo}				
Test 1, Station 3	0.66	-21%	12%	0.78
Test 2, Station 3	0.86	-36%	16%	0.74
Test 3, Station 3	0.72	-24%	13%	0.78
Test 4, Station 3	0.34	-14%	6%	0.70
Test 5, Station 3	0.89	-37%	16%	0.76
Test 6, Station 3	0.14	-7%	3%	0.74

Table IX-23. Combined Uncertainty in Re_{Mi} and Re_{Mo} for EBS Ventilation Test Series, Phase 2

Location	$(Re_N/Re_M)^2$	Combined Correction for Systematic Effects	Standard Uncertainty from Random Effects	(Re_M/Nu_M) Times Partial of Nu_M with Respect to Re_M
Re_{Mi}				
Test 1, Station 3	0.71	-8%	13%	0.81
Test 2, Station 3	0.69	-7%	12%	0.80
Test 3, Station 3	0.68	-6%	12%	0.80
Test 4, Station 3	0.68	-5%	12%	0.80
Test 5, Station 3	0.77	-8%	14%	0.80
Test 6, Station 3	0.76	-8%	14%	0.82
Test 7, Station 3	0.75	-7%	13%	0.81
Test 8, Station 3	0.75	-6%	13%	0.81
Test 9, Station 3	0.90	-10%	16%	0.79
Test 10, Station 3	0.89	-9%	16%	0.78
Test 11, Station 3	0.89	-7%	16%	0.77
Test 12, Station 3	0.92	-9%	17%	0.81
Test 13, Station 3	0.91	-8%	16%	0.80
Test 14, Station 3	0.91	-8%	16%	0.79
Test 15, Station 3	0.77	-7%	14%	0.82
Test 16, Station 3	0.77	-7%	14%	0.82
Re_{Mo}				
Test 1, Station 3	0.69	-21%	12%	0.79
Test 2, Station 3	0.61	-28%	11%	0.75
Test 3, Station 3	0.56	-30%	10%	0.74
Test 4, Station 3	0.55	-31%	10%	0.73
Test 5, Station 3	0.72	-23%	13%	0.79
Test 6, Station 3	0.71	-25%	13%	0.78
Test 7, Station 3	0.66	-30%	12%	0.76
Test 8, Station 3	0.66	-31%	12%	0.75
Test 9, Station 3	0.90	-25%	16%	0.77
Test 10, Station 3	0.86	-33%	16%	0.75
Test 11, Station 3	0.80	-48%	14%	0.70
Test 12, Station 3	0.90	-28%	16%	0.78
Test 13, Station 3	0.88	-37%	16%	0.75
Test 14, Station 3	0.86	-46%	15%	0.73
Test 15, Station 3	0.71	-26%	13%	0.78
Test 16, Station 3	0.70	-28%	13%	0.77

The other contributors to the uncertainty in each mixed-convection Nusselt number are:

1. The uncertainty in the forced convection correlation when the input Reynolds number is known, which is a correction of -9% for systematic effects, at the inner surface only, and a standard uncertainty of 7% from random effects at both surfaces (Table IX-19).

2. The 7.5% standard uncertainty in mixed-convection Nusselt numbers inherent in the Morgan approximation (Section IX.3.5).

Tables IX-24 and IX-25 present the combined uncertainties in $\overline{Nu_{Mi}}(x)$ and $\overline{Nu_{Mo}}(x)$, with the various contributors to those uncertainties. As before, this does not include the effect of the qualitatively different flow pattern.

Of the evaluated sources of uncertainty in each mixed-convection Nusselt number, the dominant source is the uncertainty in the effective Reynolds number. For the inner surface Nusselt number, the root source is the deviation of measured Nusselt numbers reported by Kuehn and Goldstein (1976) from their correlation of those measurements. At the outer surface, the root source is the approximation represented by Equation IX-29.

Table IX-24. Uncertainty in Predicted $\overline{Nu_M}$ for EBS Ventilation Test Series, Phase 1

Location	From Uncertainty in Re_M		From Nu_F Uncertainty		From Morgan Approx.	Combined Uncertainty		95% Confidence Interval	
	Correction for Systematic Effects	Random Standard Uncert.	Correction for Systematic Effects	Random Standard Uncert.	Random Standard Uncert.	Correction for Systematic Effects	Random Standard Uncert.	Lower	Upper
					Nu_{Mi}				
Test 1, Station 3	-6%	10%	-9%	7%	7.5%	-15%	14%	-39%	9%
Test 2, Station 3	-7%	13%	-9%	7%	7.5%	-16%	16%	-43%	11%
Test 3, Station 3	-6%	11%	-9%	7%	7.5%	-15%	15%	-41%	11%
Test 4, Station 3	-3%	6%	-9%	7%	7.5%	-12%	12%	-33%	9%
Test 5, Station 3	-7%	14%	-9%	7%	7.5%	-16%	17%	-44%	13%
Test 6, Station 3	-1%	3%	-9%	7%	7.5%	-10%	11%	-30%	9%
					Nu_{Mo}				
Test 1, Station 3	-16%	9%	0%	7%	7.5%	-16%	14%	-39%	7%
Test 2, Station 3	-27%	12%	0%	7%	7.5%	-27%	15%	-50%	-5%
Test 3, Station 3	-19%	10%	0%	7%	7.5%	-19%	14%	-42%	5%
Test 4, Station 3	-10%	4%	0%	7%	7.5%	-10%	11%	-30%	10%
Test 5, Station 3	-28%	12%	0%	7%	7.5%	-28%	16%	-51%	-5%
Test 6, Station 3	-5%	2%	0%	7%	7.5%	-5%	10%	-25%	14%

Table IX-25. Uncertainty in Predicted $\overline{Nu_M}$ for EBS Ventilation Test Series, Phase 2

Location	From Uncertainty in Re_M		From Nu_F Uncertainty		From Morgan Approx.	Combined Uncertainty		95% Confidence Interval	
	Correction for Systematic Effects	Random Standard Uncert.	Correction for Systematic Effects	Random Standard Uncert.	Random Standard Uncert.	Correction for Systematic Effects	Random Standard Uncert.	Lower	Upper
					Nu_{Mi}				
Test 1, Station 3	-6%	10%	-9%	7%	7.5%	-15%	15%	-40%	10%
Test 2, Station 3	-5%	10%	-9%	7%	7.5%	-14%	14%	-39%	10%
Test 3, Station 3	-5%	10%	-9%	7%	7.5%	-14%	14%	-38%	11%
Test 4, Station 3	-4%	10%	-9%	7%	7.5%	-13%	14%	-38%	11%
Test 5, Station 3	-7%	11%	-9%	7%	7.5%	-16%	15%	-41%	10%
Test 6, Station 3	-6%	11%	-9%	7%	7.5%	-15%	15%	-41%	11%
Test 7, Station 3	-6%	11%	-9%	7%	7.5%	-15%	15%	-40%	11%

Table IX-25. Uncertainty in Predicted $\overline{Nu_M}$ for EBS Ventilation Test Series, Phase 2 (Continued)

Location	From Uncertainty in Re_M		From Nu_F Uncertainty		From Morgan Approx.	Combined Uncertainty		95% Confidence Interval	
	Correction for Systematic Effects	Random Standard Uncert.	Correction for Systematic Effects	Random Standard Uncert.	Random Standard Uncert.	Correction for Systematic Effects	Random Standard Uncert.	Lower	Upper
Test 8, Station 3	-5%	11%	-9%	7%	7.5%	-14%	15%	-40%	11%
Test 9, Station 3	-8%	13%	-9%	7%	7.5%	-17%	16%	-44%	10%
Test 10, Station 3	-7%	13%	-9%	7%	7.5%	-16%	16%	-43%	12%
Test 11, Station 3	-5%	12%	-9%	7%	7.5%	-14%	16%	-42%	13%
Test 12, Station 3	-8%	13%	-9%	7%	7.5%	-17%	17%	-45%	11%
Test 13, Station 3	-7%	13%	-9%	7%	7.5%	-16%	17%	-44%	13%
Test 14, Station 3	-6%	13%	-9%	7%	7.5%	-15%	17%	-43%	13%
Test 15, Station 3	-6%	11%	-9%	7%	7.5%	-15%	15%	-41%	11%
Test 16, Station 3	-6%	11%	-9%	7%	7.5%	-15%	15%	-41%	11%
Nu_{Mo}									
Test 1, Station 3	-16%	10%	0%	7%	7.5%	-16%	14%	-40%	8%
Test 2, Station 3	-21%	8%	0%	7%	7.5%	-21%	13%	-42%	0%
Test 3, Station 3	-22%	7%	0%	7%	7.5%	-22%	13%	-42%	-2%
Test 4, Station 3	-23%	7%	0%	7%	7.5%	-23%	13%	-42%	-3%
Test 5, Station 3	-18%	10%	0%	7%	7.5%	-18%	14%	-42%	6%
Test 6, Station 3	-19%	10%	0%	7%	7.5%	-19%	14%	-42%	4%
Test 7, Station 3	-23%	9%	0%	7%	7.5%	-23%	14%	-44%	-2%
Test 8, Station 3	-23%	9%	0%	7%	7.5%	-23%	14%	-44%	-3%
Test 9, Station 3	-20%	13%	0%	7%	7.5%	-20%	16%	-46%	6%
Test 10, Station 3	-25%	12%	0%	7%	7.5%	-25%	16%	-48%	-1%
Test 11, Station 3	-34%	10%	0%	7%	7.5%	-34%	14%	-53%	-15%
Test 12, Station 3	-22%	13%	0%	7%	7.5%	-22%	16%	-47%	3%
Test 13, Station 3	-28%	12%	0%	7%	7.5%	-28%	16%	-51%	-5%
Test 14, Station 3	-33%	11%	0%	7%	7.5%	-33%	15%	-53%	-13%
Test 15, Station 3	-21%	10%	0%	7%	7.5%	-21%	14%	-43%	2%
Test 16, Station 3	-21%	10%	0%	7%	7.5%	-21%	14%	-44%	1%

IX.4.3 Measurement of Nusselt Numbers

This attachment follows the practice in the open literature on convective heat transfer, such as Kuehn and Goldstein (1978). "Measured" circumferential average Nusselt numbers are based on measured heat input and measured temperatures, with corrections for non-convective mechanisms, such as radiative heat transfer and conductive heat transfer. At the Rayleigh numbers and Reynolds numbers in the EBS Ventilation Test Series, conduction to the air is not a significant mechanism.

Therefore, a measured value for circumferential average convective heat flux from the inner surface at a central location (Station 3) is:

$$\overline{q_i''}(x) = \frac{q_{in}}{\pi D_i L_i} - \overline{q''_{rad,i}}(x) \qquad \text{(Eq. IX-75)}$$

where q_{in} is the 24-hour average power generated in the waste packages, L_i is the combined length of the waste packages, and $\overline{q''_{rad,i}}(x)$ is the circumferential average radiative flux from the waste packages at location x. For each ventilation test, Table 4-33 or 4-34 gives the value of the average line load, $\frac{q_{in}}{L_i}$.

For transparent air between concentric cylinders (Incropera and DeWitt 1985, p. 647, Eq. 13.25):

$$\overline{q''_{rad,i}}(x) = \frac{\sigma\left[\overline{\overline{T^4}}_i(x) - \overline{\overline{T^4}}_o(x)\right]}{\frac{1}{\varepsilon_i} + \frac{1-\varepsilon_o}{\varepsilon_o} r^*} \qquad \text{(Eq. IX-76)}$$

where σ is the Stefan-Boltzmann constant (Table 4-28), ε_i and ε_o are the measured emissivity of the waste package steel and concrete pipe (Tables 4-27 and 4-29), and each $\overline{\overline{T^4}}(x)$ is the 24-hour and circumferential average of the fourth power of the absolute temperature (K). This attachment approximates the averages of the fourth powers from the 24-hour averages, $\overline{T}(x)$, of absolute temperatures (K) at the top (t), left (l), bottom (b), and right (r) positions on the surfaces as follows:

$$\overline{\overline{T^4}}_i(x) \cong \left\{\overline{\overline{T}}_i(x)\right\}^4 = \left\{\left[\overline{T}_{ti}(x) + \overline{T}_{bi}(x) + \overline{T}_{li}(x) + \overline{T}_{ri}(x)\right]/4\right\}^4 \qquad \text{(Eq. IX-77)}$$

$$\overline{\overline{T^4}}_o(x) \cong \left\{\overline{\overline{T}}_o(x)\right\}^4 = \left\{\left[\overline{T}_{to}(x) + \overline{T}_{lo}(x) + \overline{T}_{ro}(x)\right]/3\right\}^4 \qquad \text{(Eq. IX-78)}$$

Because the bottom of the concrete pipe is covered by the invert, its bottom temperature is not included for radiation.

By factoring, Equation IX-78 may be put in the form:

$$\overline{q''_{rad,i}}(x) \cong \frac{\sigma}{\frac{1}{\varepsilon_i} + \frac{1-\varepsilon_o}{\varepsilon_o} r^*} \left\{ \left[\overline{\overline{T_i}}(x)\right]^3 + \left[\overline{\overline{T_i}}(x)\right]^2 \left[\overline{\overline{T_o}}(x)\right] + \left[\overline{\overline{T_i}}(x)\right] \left[\overline{\overline{T_o}}(x)\right]^2 + \left[\overline{\overline{T_o}}(x)\right]^3 \right\} \left[\overline{\overline{T_i}}(x) - \overline{\overline{T_o}}(x)\right]$$

$$= \frac{0.5\sigma}{\frac{1}{\varepsilon_i} + \frac{1-\varepsilon_o}{\varepsilon_o} r^*} \left\{ \left[\overline{\overline{T_i}}(x) + \overline{\overline{T_o}}(x)\right]^3 \left[\overline{\overline{T_i}}(x) - \overline{\overline{T_o}}(x)\right] + \left[\overline{\overline{T_i}}(x) + \overline{\overline{T_o}}(x)\right] \left[\overline{\overline{T_i}}(x) - \overline{\overline{T_o}}(x)\right]^3 \right\}$$

(Eq. IX-79)

Ignoring the term containing the cube of the temperature difference, the approximation becomes:

$$\overline{q''_{rad,i}}(x) \cong \frac{0.5\sigma}{\frac{1}{\varepsilon_i} + \frac{1-\varepsilon_o}{\varepsilon_o} r^*} \left[\overline{\overline{T_i}}(x) + \overline{\overline{T_o}}(x)\right]^3 \left[\overline{\overline{T_i}}(x) - \overline{\overline{T_o}}(x)\right] \qquad \text{(Eq. IX-80)}$$

For each ventilation test, Table IX-26 or IX-27 shows $\overline{q''_{rad,i}}(x)$ calculated in accordance with Equation IX-80, the measured $\overline{q''_i}(x)$, the value of $\overline{h_i}(x)$ from Equation IX-16, and the value of $\overline{Nu_i}(x)$ from Equation IX-2, using k = 0.0263 W/mK.

Table IX-26. Inner-Surface Nusselt Number Measurements, EBS Ventilation Test Series, Phase 1

Location	$q_{in}/\pi D_i L$ (W/m^2)	$q''_{rad,i}$ (W/m^2)	q''_i (W/m^2)	Effective h_i (W/m^{2}K)	Effective Nu_i
Test 1, Station 3	143	64	78	5.32	195
Test 2, Station 3	140	71	69	4.65	170
Test 3, Station 3	281	126	155	5.94	218
Test 4, Station 3	284	110	174	7.54	276
Test 5, Station 3	284	134	150	5.70	209
Test 6, Station 3	285	90	195	9.94	364

Table IX-27. Inner-Surface Nusselt Number Measurements, EBS Ventilation Test Series, Phase 2

Location	$q_{in}/\pi D_i L$ (W/m^2)	$q''_{rad,i}$ (W/m^2)	q''_i (W/m^2)	Effective h_i (W/m^{2}K)	Effective Nu_i
Test 1, Station 3	171	77	94	5.39	198
Test 2, Station 3	171	86	85	5.08	186
Test 3, Station 3	169	92	77	4.79	175
Test 4, Station 3	168	91	77	4.87	178
Test 5, Station 3	282	127	155	5.91	217
Test 6, Station 3	281	137	144	5.55	204
Test 7, Station 3	280	148	131	5.31	194
Test 8, Station 3	280	149	131	5.29	194
Test 9, Station 3	168	79	89	5.11	187
Test 10, Station 3	168	87	81	4.79	175
Test 11, Station 3	169	98	72	4.42	162
Test 12, Station 3	282	133	149	5.66	208
Test 13, Station 3	282	145	137	5.36	196
Test 14, Station 3	283	157	125	5.08	186
Test 15, Station 3	282	134	148	5.69	209
Test 16, Station 3	285	136	150	5.71	209

At the outer surface, heat arrives by radiation and leaves by conduction into the wall and by convection into the air. Therefore, the measured value for circumferential average convective flux is:

$$\overline{q_o''}(x) = r^* \overline{q''_{rad,i}}(x) - h_{cond}\left[\overline{\overline{T}_o}(x) - \overline{\overline{T}_a}(x)\right] \qquad \text{(Eq. IX-81)}$$

where the radiative flux at the waste package has been multiplied by r^* to reflect the larger circumference at the outer wall, h_{cond} is the overall conductive heat transfer coefficient for the combined thickness of concrete and insulation and $\overline{\overline{T}_a}(x)$ is an average ambient temperature external to the insulation, defined by

$$\overline{\overline{T}_a}(x) = \left[\overline{T}_{ta}(x) + \overline{T}_{la}(x) + \overline{T}_{ra}(x)\right]/3 \qquad \text{(Eq. IX-82)}$$

The two natural convection tests conducted at the end of Phase 1 establish a value for h_{cond}. Because there is no heat removed by ventilating air in the natural convection tests, conduction through the wall must be equal to the heat input. That is, neglecting end effects,

$$r^* \frac{q_{in}}{\pi D_i L_i} = h_{cond}\left[\overline{\overline{T}_o}(x) - \overline{\overline{T}_a}(x)\right] \qquad \text{(Eq. IX-83)}$$

where the flux from the heat source has been multiplied by r^* to reflect the larger circumference at the outer wall. Table IX-28 shows that the calculation of h_{cond} from data in Table 35 for the

two natural convection tests gives an average value of 1.99 W/m^{2}K, with a standard deviation of less than 1%.

For each ventilation test, Table IX-29 or IX-30 shows the measured $\overline{q_o''}(x)$, the value of $\overline{h}_o(x)$ from Equation IX-16, and the value of $\overline{Nu_o}(x)$ from Equation IX-3, with k = 0.0263 W/mK.

For the direct measurements taken during the EBS Ventilation Test Series, the uncertainties are small. Averaging 96 measurements to get a 24-hour average reduces further the effects of random errors. For example, the uncertainty in the average heat input is only 2.6 W out of a total input of 4 kW or more (BSC 2003f, Tables 3-15 and 3-16).

The major uncertainty in the measured Nusselt numbers is in the approximation for radiative heat transfer. One source of uncertainty is the absence of measured temperatures below the center of the concrete pipe. Other sources are the approximations that underlie the radiation formula, including:

- Concentric cylinders
- Isothermal surfaces
- Transparent air
- No end effects

The effort documented here did not include a literature search for data regarding deviations from these approximations. This attachment does not provide numerical uncertainties for the measured Nusselt numbers.

Table IX-28. Determination of Conductive Heat Transfer Coefficient from Natural Convection Tests Conducted During EBS Ventilation Test Series

Location	q_{in}/L (W/m)	Source at Wall (W/m^2)	Avg. T_a (ºC)	Avg. T_o (ºC)	Avg. (T_o-T_a) (ºC)	h_{cond} (W/m^{2}ºC)
Test NC1, Station 3	120	27.9	27.97	45.83	17.87	1.561
Test NC2, Station 3	242	56.2	32.53	68.77	36.23	1.552
					average	1.556
					std. dev.	0.006

Table IX-29. Outer-Surface Nusselt Number Measurements, EBS Ventilation Test Series, Phase 1

Location	r^*q"$_{rad,i}$ (W/m^2)	Avg T_a (ºC)	q_{cond} (W/m^2)	q"$_o$ (W/m^2)	Effective h_o (W/m^{2}K)	Effective Nu_o
Test 1, Station 3	19.0	28.57	2.5	16.6	6.45	236
Test 2, Station 3	21.1	28.27	7.8	13.3	7.12	261
Test 3, Station 3	37.4	26.73	10.3	27.1	6.63	243
Test 4, Station 3	32.6	26.23	5.8	26.9	9.16	336
Test 5, Station 3	39.6	23.90	16.1	23.5	7.28	267
Test 6, Station 3	26.8	20.63	4.5	22.3	12.16	445

Table IX-30. Outer-Surface Nusselt Number Measurements, EBS Ventilation Test Series, Phase 2

Location	$r^* q''_{rad,i}$ (W/m^2)	Avg T_a (°C)	q_{cond} (W/m^2)	q''_o (W/m^2)	Effective h_o (W/m^{2}K)	Effective Nu_o
Test 1, Station 3	22.7	28.43	3.3	19.5	6.21	228
Test 2, Station 3	25.5	29.20	14.7	10.8	5.92	217
Test 3, Station 3	27.4	36.33	18.6	8.9	6.26	229
Test 4, Station 3	27.1	36.07	18.4	8.7	6.71	246
Test 5, Station 3	37.6	30.53	5.3	32.2	7.64	280
Test 6, Station 3	40.8	36.67	10.5	30.2	7.69	282
Test 7, Station 3	44.0	37.97	21.3	22.8	8.33	305
Test 8, Station 3	44.3	37.20	22.2	22.1	8.46	310
Test 9, Station 3	23.5	32.67	3.5	19.9	5.98	219
Test 10, Station 3	25.9	36.13	10.4	15.5	6.33	232
Test 11, Station 3	28.9	39.63	17.4	11.5	9.72	356
Test 12, Station 3	39.5	35.30	8.2	31.2	7.02	257
Test 13, Station 3	43.0	34.77	19.3	23.7	7.37	270
Test 14, Station 3	46.7	38.47	26.5	20.2	9.40	345
Test 15, Station 3	39.7	29.50	13.4	26.3	7.23	265
Test 16, Station 3	40.2	27.73	15.4	24.8	7.22	265

IX.4.4 Corroboration of Predicted Results With Test Data

Figures IX-3 through IX-6 compare "measured" and predicted Nusselt numbers at Station 3 for the Phase 1 and Phase 2 tests in the EBS Ventilation Test Series. When the prediction agrees with the measurement, the point lies on the diagonal line. These plots show the 95% confidence limits for the predictions. In some cases, because of systematic errors that are not corrected in the methodology, the predicted value is outside of the confidence limits.

The "measured" values of $\overline{Nu_i}$ agree with the predicted values to within the uncertainty (Figures IX-3 and IX-4). However, the "measured" values for $\overline{Nu_o}$ are consistently higher than the predicted values (Figures IX-5 and IX-6).

The predicted values of $\overline{Nu_o}$ (Figures IX-5 and IX-6) could be brought within their own 95% confidence limits by solving Equation IX-25 implicitly, thereby eliminating the systematic error caused by the approximation of Equation IX-29. For each case, one could evaluate the right hand side of Equation IX-25 for two or three values of *Re*, then interpolate in the resulting small table. However, this would not improve the agreement with the measured values.

A striking feature of Figure IX-6, in particular, is that the measured values of $\overline{Nu_o}$ span a factor of three, while the predicted values are relatively constant. Most of the variation in measured $\overline{Nu_o}$ occurred in tests at the lowest flow rate, 0.5 m^3/s. Table IX-31 is a summary of the measured values of $\overline{Nu_o}$ for all tests that had controlled inlet air conditions and a nominal flow

rate of 0.5 m^3/s. There appears to be a strong dependence on air inlet temperature that was not seen at higher flow rates. At the lower flow rates, natural convection has a greater influence. The natural convection correlation is based on the flow pattern of Figure IX-1c, but the actual circulation near the outer surface is in the opposite direction, as shown in Figure IX-1d. Because the temperature of the outer surface is near the temperature of the air (Table IX-11 and IX-12), details of the flow pattern may be sensitive to the inlet temperature.

Table IX-31 also contains the predicted Nusselt numbers and the values that would result from the Dittus-Boelter formula. The Dittus-Boelter predictions are the result of applying Equation IX-12, using Reynolds numbers from Table IX-7. Although the predictions are low, the Dittus-Boelter values are even lower, by about a factor of three.

Concentrating attention on the Nusselt numbers tends to exaggerate the significance of the errors with respect to overall energy transfer in the EBS Ventilation Tests. To provide another perspective, an energy balance can be represented by expressing the various components of energy transfer as percentages of the total input energy. A certain percentage was convected from the inner wall to the air, a percentage was convected from the outer wall to the air, and a percentage was conducted through the outer wall. Using measured data, these percentages must sum to 100%.

Figures IX-7 and IX-8 show an energy balance using the methodology for convection to the air and measured conduction losses. All of these plots are based on a vertical section at the center of the configuration (Station 3) and contain no adjustment for longitudinal effects other than the airflow. The figures show the sum, $\pi D_i \overline{q}_i'' + \pi D_o \left(\overline{q}_o'' + q_{\text{cond}}\right)$, as a percentage of the average line load given in Table 4-33 or 4-34. In forming the sum, q_{cond} is from Table IX-29 or IX-30. The convective heat flux at each surface is:

$$\overline{q}'' = \frac{k\,\overline{Nu}\left(\overline{T} - T_f\right)}{D_o - D_i} \qquad \text{(Eq. IX-84)}$$

The Nusselt numbers are from Tables IX-13 through IX-16, each temperature is from Table IX-8 or IX-9, and k is 0.0263 W/m K.

The percentages cluster around 85%. Of the energy convected, 75-85% was directly from the waste package, with the remaining 15-25% being convected from the drift wall. From this perspective, the effects of errors in $\overline{Nu_o}$ are limited because $\overline{T}_o - T_f$ is small. Considered in terms of the effects of the errors in ventilation model that conserves total energy, the surface temperatures might have to rise enough to remove an additional 10% of the energy. For the ventilation tests, for example, a ventilation model that used the mixed-convection methodology might predict a waste package temperature that was too high by about 2°C and a wall temperature that was too high by about 0.3ºC.

In summary, the results of the EBS Ventilation Tests support the mixed convection methodology for prediction of the Nusselt number at the waste package, which is the dominant source for heat transfer to the air. They also support the use of the methodology, rather than a forced convection

formula, at the drift wall. The determination of accuracy and precision followed conventional scientific standards, and used sensitivity analyses and bounding techniques, as appropriate.

This attachment accounts for uncertainties and variabilities in parameter values and provides for the technical basis for parameter ranges, probability distributions, or bounding values that may be used in predictions. Also, this attachment considers alternative conceptual models of processes that are consistent with available data and current scientific understanding and evaluates the effects that alternative conceptual models have on the predictions.

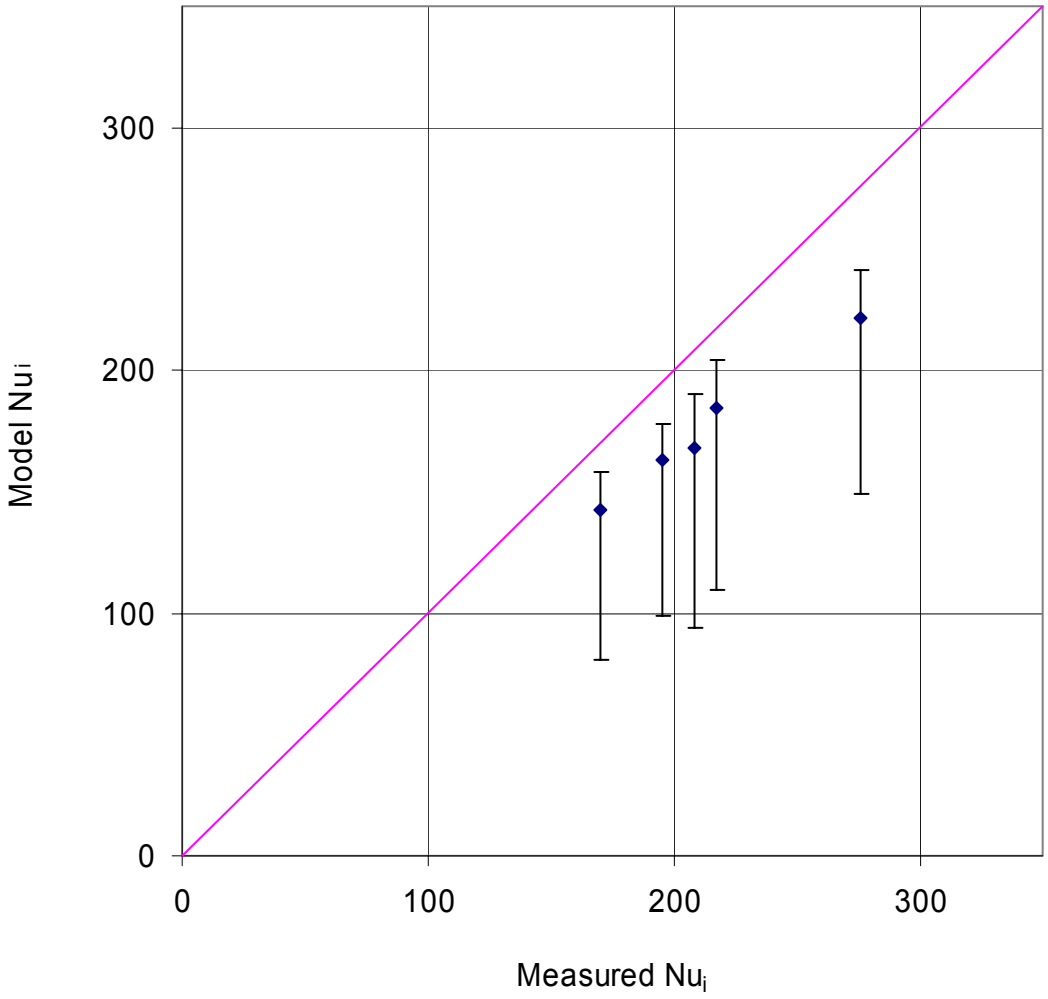

Figure IX-3. Comparison of "Measured" and Model Inner Surface Nusselt Numbers for Phase 1 Ventilation Tests.

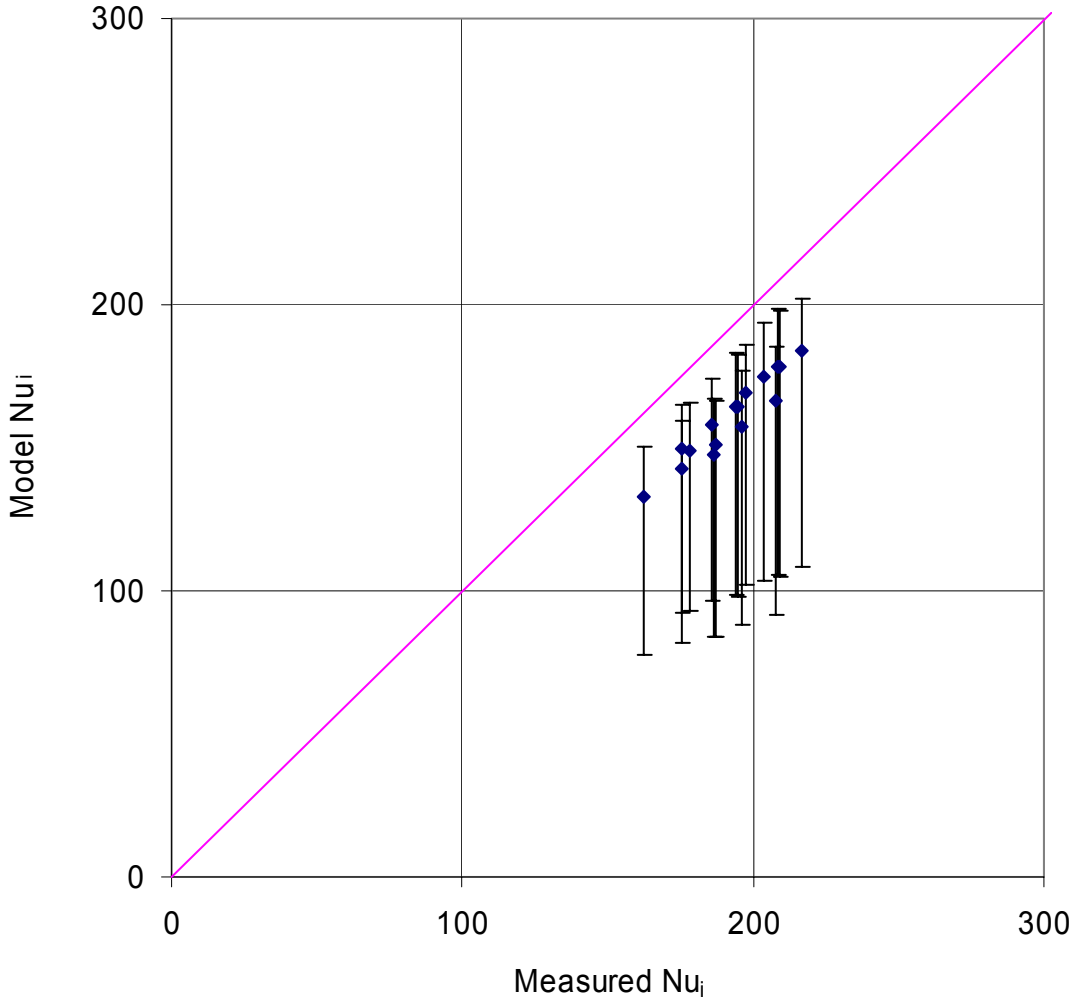

Figure IX-4. Comparison of "Measured and Model Inner Surface Nusselt Numbers for Phase 2 Ventilation Tests

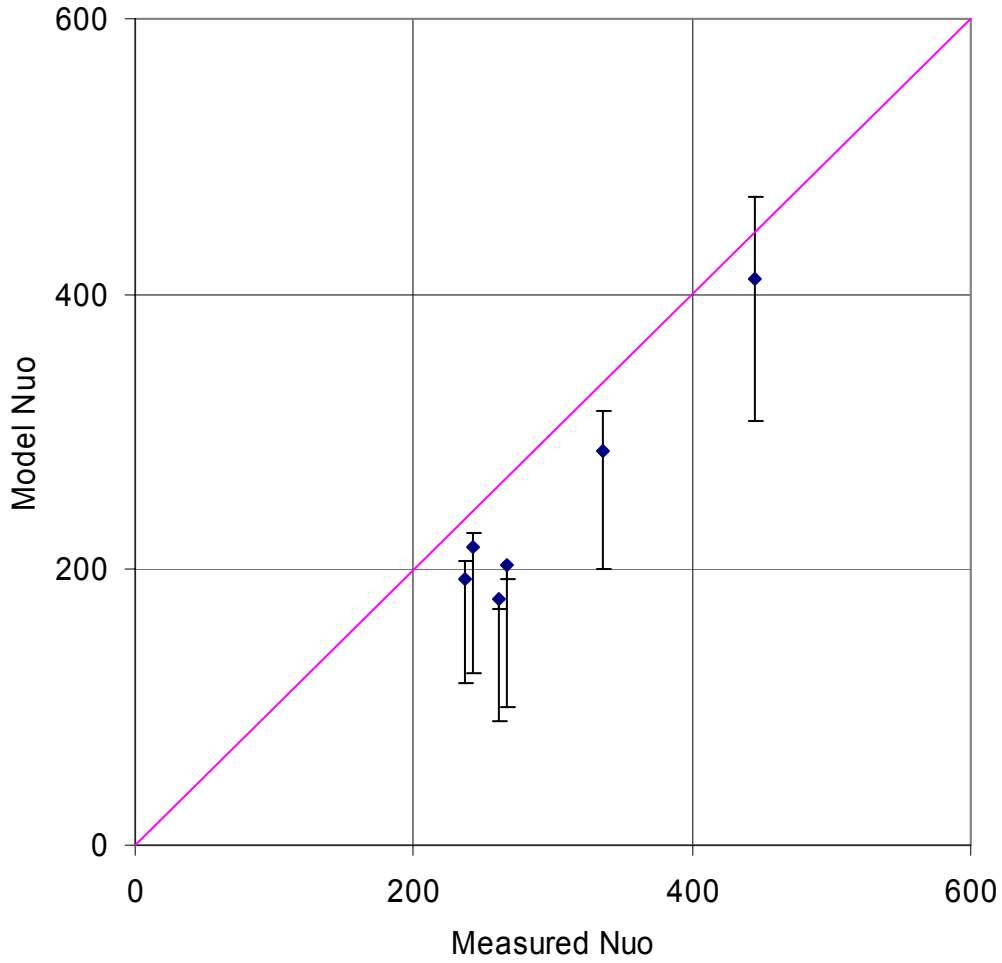

Figure IX-5. Comparison of "Measured" and Model Outer Surface Nusselt Numbers for Phase 1 Ventilation Tests

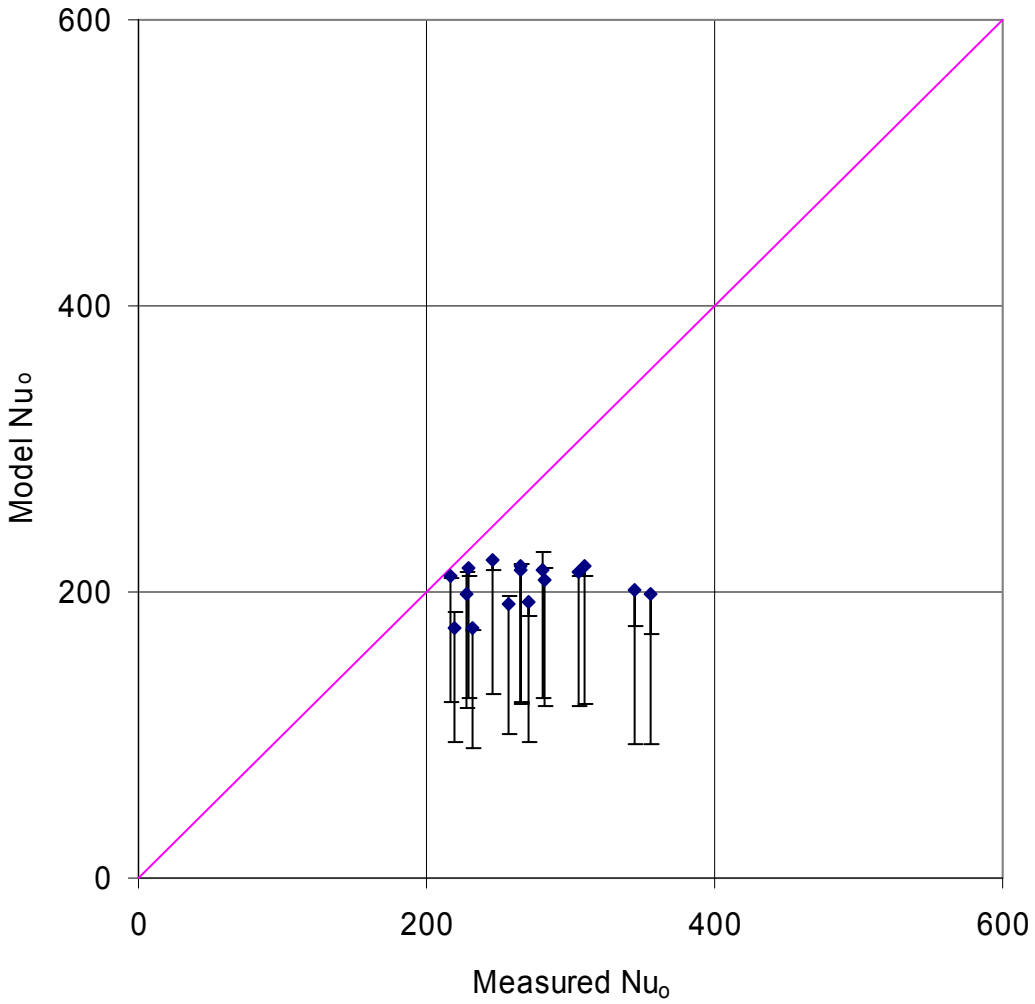

Figure IX-6. Comparison of "Measured" and Model Outer Surface Nusselt Numbers for Phase 2 Ventilation Tests

Table IX-31. Outer-Surface Nusselt Number Measurements for Flow Rate of 0.5 m^3/s

Phase	Test	Nominal Line Load (W/m)	Inlet Air Temperature (C)	Inlet Air Relative Humidity (%)	Measured Nu_o	Predicted Nu_o	*Dittus-Boelter* Nu_o
2	9	220	25	30	219	175	60
2	10	220	35	17	232	175	61
2	11	220	45	10	356	199	58
2	12	360	25	30	257	191	63
2	13	360	35	17	270	193	61
2	14	360	45	10	345	202	58

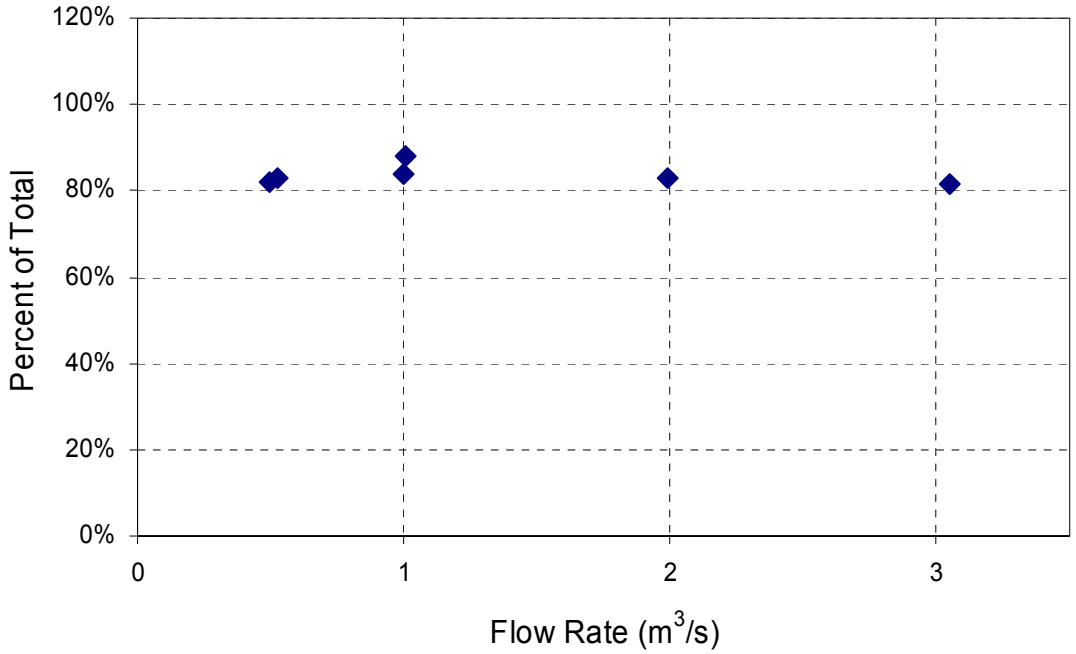

Figure IX-7. Energy Balance Using Convection Model for Phase 1 Tests (Heat Convected to Air, Augmented by Heat Conducted Through Concrete, as a Percentage of Input Energy)

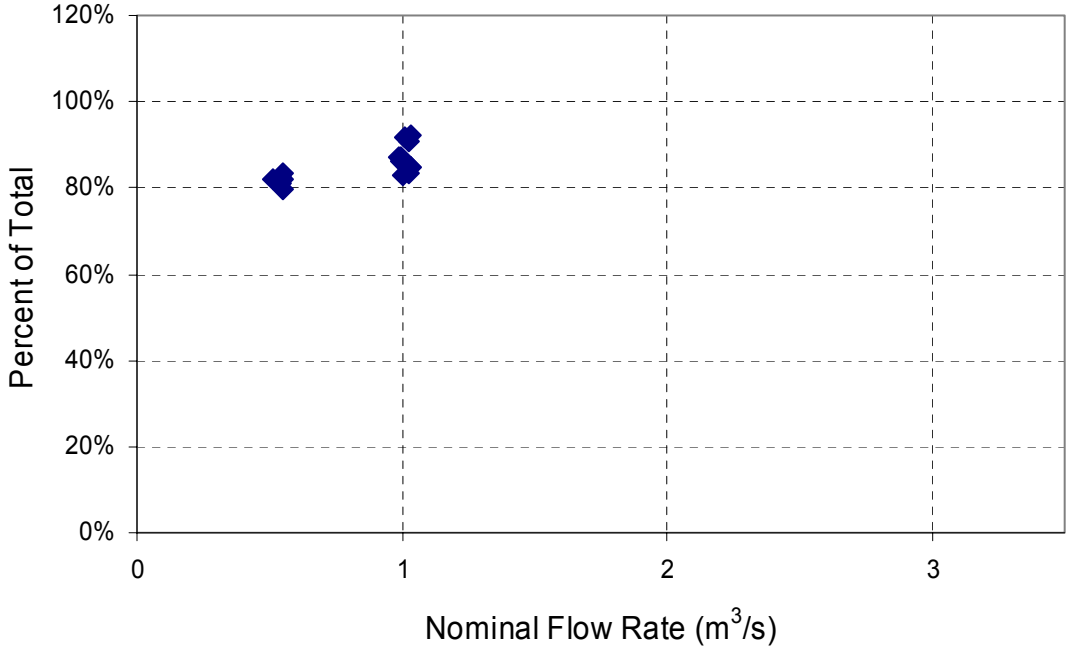

Figure IX-8. Energy Balance Using Convection Model for Phase 2 tests (Heat Convected to Air, Augmented by Heat Conducted Through Concrete, as a Percentage of Input Energy)

ATTACHMENT X

VERIFICATION CALCUATIONS IN SUPPORT OF THE MIXED CONVECTION CORRELATION (ATTACHMENT IX)

INTENTIONALLY LEFT BLANK

This attachment documents the spreadsheets calculations used in Attachment IX. The electronic copies of these Microsoft Excel spreadsheets are contained in Mixed Convection.zip (DTN: MO0306MWDMXCNV.000). Table summarizes the contents of the spreadsheets. Further documentation of the cell formulas and referencing are found within the electronic copy of the file.

Table X-1. Contents of Spreadsheet used in the Mixed Convection Methodology of Attachment IX

File Name (.xls)	Contents
Phase 1 Supporting Calculations for Mixed Convection	Mixed Convection model applied to the EBS Ventilation Test Series, Phase I; Evaluation of uncertainty for EBS Ventilation Tests Series, Phase I; Determination of measured Nusselt numbers for EBS Ventilation Test Series, Phase I; Calculated Energy Balance for Phase I.
Phase 2 Supporting Calculations for Mixed Convection	Mixed Convection model applied to the EBS Ventilation Test Series, Phase II; Evaluation of uncertainty for EBS Ventilation Tests Series, Phase II; Determination of measured Nusselt numbers for EBS Ventilation Test Series, Phase II; Calculated Energy Balance for Phase II.
h-cond from NC tests	Evaluation of effective heat transfer coefficient for conduction
Mixed Convection Sensitivity	Sensitivity of Mixed Convection model to input parameters

INTENTIONALLY LEFT BLANK

ATTACHMENT XI

ANALYSIS OF THE VENTILATION TEST PHASE II DATA IN SUPPORT OF THE CALCULATIONS PERFORMED IN ATTACHMENT X

INTENTIONALLY LEFT BLANK

The Phase II Ventilation Test Data Report was not available to reference and thus could not be included in this report. Data used to validate the mixed convection correlation in Attachment IX is developed below, the raw data taken from DTN: SN0208F3409100.009. This data is contained in Vent-Test Phase-II.zip (DTN: MO0306MWDVTPH2.000).

There is one file for each test (*Phase II Test 1_Q.xls, Phase II Test 2_Q.xls, Phase II Test 3_Q.xls, Phase II Test 4_Q.xls, Phase II Test 5_Q.xls, Phase II Test 6_Q.xls, Phase II Test 7_Q.xls, Phase II Test 8_Q.xls, Phase II Test 9_Q.xls, Phase II Test 10_Q.xls, Phase II Test 11_Q.xls, Phase II Test 12_Q.xls, Phase II Test 13_Q.xls, Phase II Test 14_Q.xls, Phase II Test 15_Q.xls, and Phase II Test 16_Q.xls*) that contains:

- The data recorded by the datalogger and entered into the Technical Data Management System - sheet name "*raw data*." This sheet also contains simple statistical analysis (average, standard deviation, maximum and minimum) for a defined time period. The time period was chosen as a 24-hour period over which data is representative of steady state conditions where the ventilating air was at or near the desired temperature and relative humidity.

  The sheet is organized as follows:

  - Cell A14: DTN associated with the data
  - Time period chosen for averaging data: Cells C1 and C2
  - Rows 4 and 5: addresses corresponding to chosen time period for statistical analysis
  - Rows 7, 8, 9 and 10: resulting statistical analysis (average, standard deviation, maximum and minimum) for the chosen time period
  - Row 24: Starting row for the data pulled from the Technical Data Management System

- The calculated total power input (summation of the five stations) and line load (total power input divided by the heated length). – sheet name "*power.*"

  The sheet is organized as follows:

  - Columns A through F: Summary of the power data, including the time stamp and recorded power data for the five power stations (taken directly from the "raw data" worksheet)
  - Column H: Summation of the five recorded power inputs for each time stamp
  - Column I: Calculated average line load for the test train, defined as the total power input (column H) divided by the total heated length (111' 4" (33.9 m), calculated by adding the recorded distance to the leading edge of waste package 25 (98' 2 1/2" + 105 1/2") plus the recorded length of waste package 25 (52") (BSC 2003f, p. 2.3).

- The calculated volumetric and mass flow rates– sheet name "*flow*." The flow rates for each test were calculated based on air velocity probe differential pressure, relative humidity, barometric pressure, and air temperature measurements. Complete details of the calculation can be found in *Testing to Provide Data for Ventilation System Design: Phase 1* (BSC 2003f, Section 5.2.1). As a summary, the measured differential pressure was converted to an air velocity. Properties of the ventilating fluid (e.g., the mixture of air and water vapor) were determined using measured relative humidities and temperatures. The air velocity was then combined with the cross-sectional area of the ducting to determine a volume flow rate.

  The sheet is organized as follows:

  - Column A through J: Summary of the data required to calculate flow. At station A, there were two differential pressure gauges (VA-VEL-01 and VA-VEL-02), two relative humidity gauges (VA-HUM-H1 and VA-HUM-H2), and nine RTDs measuring air temperature (VA-RTD-01 through VA-RTD-09), that were used in calculating the flow. Each set of measurements was averaged to create the differential pressure, relative humidity, and air temperature needed for the flow calculations. The flow at station D was calculated using measurements from one differential pressure gauge at station D (VD-VEL-01), two relative humidity gauges at station C (VC-HUM-H1 and VC-HUM-H2), and two RTD air temperature gauges at station C (VC-RTD-01 and VC-RTD-02).

  - Columns L through AD: Calculations of flow rates for Station A

  - Column AI through AY: Calculations of flow rate for Station D

- All constants and dimensions used in the calculation are given in a sheet named "*properties*." References for these properties are provided.

ATTACHMENT XII

DOCUMENTATION OF THE VENTILATION PHASE I POST-TEST ANSYS ANALYSES FOR MODEL VALIDATION (INPUTS AND OUTPUTS)

This attachment documents the Ventilation Test Phase I post test ANSYS modeling for validation purposes, which was developed using the Ventilation Test Phase I data, ANSYS software and spreadsheet methods. The input and output files, and Microsoft Excel spreadsheets are contained in DTN: MO0209MWDANS30.017.

ATTACHMENT XIII

ANALYTICAL SOLUTION USING MATHCAD FOR THE CONTRIBUTION OF LATENT HEAT TO THE IN-DRIFT AIR OF A VENTILATED EMPLACEMENT DRIFT USING A SOLUTION FOR STEADY STATE UNSATURATED FLOW TO MOISTURE POTENTIAL BOUNDARY AT THE DRIFT WALL

INTENTIONALLY LEFT BLANK

Steady State Solution Summary Unsaturated Flow to a Drift Subject to a Moisture Potential Boundary Condition at the Drift Surface

Note that the symbol := used throughout this attachment means to assign the right hand value or expression to the left hand variable.

Develop a steady solution for radial unsaturated flow to the specified moisture potential conditions. Neglect the gravity component of flow, and consider the Van Genuchten constitutive relationships. *Soil Physics* (Jury et al. 1991, Section 3.4) develops the solution for radial flow under saturated conditions. In the case of steady state flow under saturated conditions, the water conservation equation for a cylindrical coordinate geometry is given by:

$$\frac{1}{r} \cdot \frac{d}{dr}\left(r \cdot J_r\right) = 0 \qquad \text{Eq. XIII-1}$$

where

r = Radial Coordinate
J_r = Darcy Flux in the Radial Direction

Equation XIII-1 can be integrated once to produce the result:

$$r \cdot J_r = \phi = cons\,tan\,t = \frac{Q}{2\pi \cdot z_0} \qquad \text{Eq. XIII-2}$$

where

Q = Steady state moisture flow
z_0 = Drift length

The radial flux under Darcy's Law is given by:

$$J_r = -K_s \cdot \frac{dp}{dr} \qquad \text{Eq. XIII-3}$$

where

K_S = Saturated Hydraulic Conductivity
p = Pressure or Pressure Head Depending on convention adopted for Darcy's Law

Writing Darcy's Law for radial flow to the tunnel surface:

$$-K_s \cdot \frac{dp}{dr} = \frac{Q}{2\pi \cdot z_0 \cdot r} \qquad \text{Eq. XIII-4}$$

This equation can be integrated after placing all factors explicitly for r on the same side of the equation:

$$dp = \frac{-Q}{2\pi \cdot K_s \cdot z_0} \cdot \frac{dr}{r} \qquad \text{Eq. XIII-5}$$

Since $p(R_1) = p_1$ and $p(R_2) = p_2$ are specified at the boundary then:

$$\int_{p_1}^{p_2} dp = \frac{-Q}{2\pi \cdot K_s \cdot z_0} \int_{R_1}^{R_2} \frac{dr}{r} \qquad \text{Eq. XIII-6}$$

from which we calculate:

$$Q = \frac{2\pi \cdot K_s \cdot z_0 \cdot (p_1 - p_2)}{ln\left(\frac{R_2}{R_1}\right)} \qquad \text{Eq. XIII-7}$$

This expression agrees with the formulation presented in *Soil Physics* (Jury et al. 1991, p. 113 Equation 3.92).

Now consider the unsaturated flow case. The pressure gradient becomes a moisture potential gradient. For unsaturated flow, the unsaturated hydraulic conductivity is a strong nonlinear function of the moisture potential $\overline{\psi}$.

Neglecting the elevation head:

$$H_1 = \frac{p_1}{\gamma_w g} + 0 = -\psi_1 \qquad \text{Eq. XIII-8}$$

$$H_2 = \frac{p_2}{\gamma_w g} + 0 = -\psi_2 \qquad \text{Eq. XIII-9}$$

where

H_1	=	Total Potential at the Drift Surface R1
H_2	=	Total Potential at the Outer Boundary R2
ψ_1	=	Moisture Potential at Radius R1 Set by the RH in the Drift
ψ_2	=	Moisture Potential at Radius R2 Set by Undisturbed State of Capillary Equilibrium
γ_w	=	Unit Weight of Water
g	=	gravitational constant

Writing Darcy's Law for unsaturated radial flow:

$$-K(\psi) \cdot \frac{dH}{dr} = \frac{Q}{2\pi \cdot z_0 \cdot r} \qquad \text{Eq. XIII-10}$$

Noting that if we neglect the elevation head:

$$H \approx \psi$$

$$-K(\psi)\cdot\frac{d\psi}{dr}=\frac{Q}{2\pi\cdot z_0\cdot r} \qquad \text{Eq. XIII-11}$$

The convention is adopted that moisture potential is in units of head (Jury et al. 1991, p. 51). Now the Van Genuchten constitutive relation can be invoked. From *Contaminant Hydrogeology* (Fetter 1993, p. 182), the constitutive relation is:

$$K(\psi)=\frac{K_s\left\{1-(\alpha\psi)^{n-1}\left[1+(\alpha\psi)^n\right]^{-m}\right\}^2}{\left[1+(\alpha\psi)^n\right]^{\frac{m}{2}}} \qquad \text{Eq. XIII-12}$$

where

n	=	1/(1-m)
α	=	Van Genuchten alpha
m	=	Van Genuchten fitting parameter

Substituting in the constitutive relation into Darcy's Law:

$$\frac{K_s\left\{1-(\alpha\psi)^{n-1}\left[1+(\alpha\psi)^n\right]^{-m}\right\}^2}{\left[1+(\alpha\psi)^n\right]^{\frac{m}{2}}}\cdot\frac{d\psi}{dr}=\frac{Q}{2\pi\cdot z_0\cdot r} \qquad \text{Eq. XIII-13}$$

Equation XIII-13 can be integrated in the same manner:

$$\int_{\psi_1}^{\psi_2}\frac{K_s\left\{1-(\alpha\psi)^{n-1}\left[1+(\alpha\psi)^n\right]^{-m}\right\}^2}{\left[1+(\alpha\psi)^n\right]^{\frac{m}{2}}}\cdot d\psi=\frac{Q}{2\pi\cdot z_0}\int_{R_1}^{R_2}\frac{dr}{r}=\frac{Q}{2\pi\cdot z_0}\cdot ln\left(\frac{R_2}{R_1}\right) \qquad \text{Eq. XIII-14}$$

Note that the sign convention in the constitutive law is positive while in Darcy's Law it is negative. Note that ψ_1 and ψ_2 are expressed in units of head consistent with sign convention presented by *Soil Physics* (Jury et al. 1991, p. 151). Substituting in the definition of hydraulic conductivity (Fetter 1993, p. 181):

$$K_s=\frac{\rho g k}{\mu} \qquad \text{Eq. XIII-15}$$

where

k	=	intrinsic permeability (m^2)
μ	=	fluid viscosity ($N\cdot s/m^2$)

$$Q = \frac{-2\pi \cdot z_0 \cdot \frac{\rho g k}{\mu} \cdot \int_{\psi_1}^{\psi_2} \frac{\left\{1-(\alpha\psi)^{n-1}\left[1+(\alpha\psi)^n\right]^{-m}\right\}^2}{\left[1+(\alpha\psi)^n\right]^{\frac{m}{2}}} \cdot d\psi}{ln\left(\frac{R_2}{R_1}\right)} \qquad \text{Eq. XIII-16}$$

Now consider the boundary conditions, and the geometry for the problem. Use an RH of 30 percent (Section 4.1.1.3) in the ventilated drift and use the Kelvin Equation to calculate moisture potential (Jury et al. 1991, p. 60):

$$RH = exp\left(\frac{M_w \psi_1}{\rho_w RT}\right) \qquad \text{Eq. XIII-17}$$

Input properties for analysis. The properties for water are obtained from Section 4.1.3.6 at 350 K:

$$\rho_w = 973.7 \text{ kg/m}^3 = 0.9737 \text{ gm/cm}^3$$

From Table 4-28:

M_w = 18 gm/mol
R = 8.315 J/mol·K

Substituting into Equation XIII-17:

$$\psi(RH,T) = \frac{\rho_w RT}{M_w} \cdot ln\left(\frac{RH}{100}\right)$$

$$\psi(30\%,350K) = -1.896 \cdot 10^8 \frac{kg}{m \cdot s^2}$$

The moisture potential is expressed in pressure. Calculate the moisture potential in units of head:

$$\psi_1 = \frac{|\psi(30\%,350K)|}{\rho_w g} = \frac{\left|-1.896 \cdot 10^8 \frac{kg}{m \cdot s^2}\right|}{\left(973.7 \frac{kg}{m^3}\right) \cdot \left(9.81 \frac{m}{s^2}\right)} = 1.985 \cdot 10^4 m = 1.985 \cdot 10^6 cm$$

From Table 4-13 and Table 4-16, the hydrologic properties for the repository host rock unit surrounding the drift (Tptpll or tsw35) are:

Matrix permeability = $k_m = 4.48 \cdot 10^{-18}$ m^2
Matrix porosity = $\phi_m = 0.1486$

Van Genuchten matrix alpha = $\alpha = 1.08 \cdot 10^{-5}$ Pa^{-1}
Van Genuchten matrix fitting parameter = $m = 0.216$
Residual matrix saturation = $\theta_r = s_{lrm} \cdot \phi_m = 0.0178$
Satiated matrix saturation = $\theta_s = s_{lsm} \cdot \phi_m = 0.1486$

From Table 4-25 at 350 K:

$$\mu_w = 3.65 \cdot 10^{-4} \text{ N} \cdot \text{s/m}^2$$

To convert α from Pa^{-1} to cm^{-1}, multiply by $\rho_w g$:

$$\alpha = \left(\frac{1.08 \cdot 10^{-5}}{Pa}\right)\left(\frac{1Pa}{1\frac{N}{m^2}}\right)\left(\frac{1N}{1\frac{kg \cdot m}{s^2}}\right)\left(973.7\frac{kg}{m^3}\right)\left(9.81\frac{m}{s^2}\right) = 0.1032m^{-1} = 1.032 \cdot 10^{-3}cm^{-1}$$

The retention relationship (Fetter 1993, p. 172, Equation 4.9) is used to calculate the moisture potential:

$$\theta = \theta_r + \frac{\theta_s - \theta_r}{\left[1 + (\alpha\psi)^n\right]^m} \qquad \text{Eq. XIII-17}$$

where

$$n = \frac{1}{1-m} \qquad \text{Eq. XIII-18}$$

Solve Equation XIII-17 for moisture potential in terms of volumetric moisture content:

$$\psi = \frac{\left\{-1 + \left[\frac{-\left(-\theta_s + \theta_r\right)}{\theta - \theta_r}\right]^{\frac{1}{m}}\right\}^{\frac{1}{n}}}{\alpha} \qquad \text{Eq. XIII-19}$$

The average saturation of Tptpll (tsw35) given the saturations measured in USW SD-7, USW SD-9, USW NRG-6, USW NRG-7/7A, and USW UZ-7A in Table 4-11 is 0.74. The average volumetric moisture content is:

$$\theta = 0.76 \cdot \theta_s = 0.1100$$

Solving Equation XIII-19 then yields:

$$\psi = 2908 \text{ cm} = \psi_2$$

The radius of the drift, R_1, is 2.75 m (Table 4-23). Assume a radius of influence, R_2, of 6 m. The drift length, z_0, is 600 m. Calculate the steady state moisture flow at the drift wall by solving the integral in Equation XIII-16:

$$Q = 2.002 \cdot 10^{-8} \frac{m^3}{s}$$

The steady state moisture flow, expressed as a liquid flux toward the drift wall is:

$$\frac{Q}{2\pi \cdot R_1 \cdot z_0} = \frac{2.002 \cdot 10^{-8} \frac{m^3}{s}}{2\pi \cdot 2.75m \cdot 600m} \cdot \frac{31556926s}{1yr} \cdot \frac{1000mm}{1m} = 0.061 \frac{mm}{yr}$$

Calculate the latent heat transfer over the 50-year ventilation period by multiplying the flow by the latent heat of vaporization at 350 K (Table 4-25):

$$\left(2.002 \cdot 10^{-8} \frac{m^3}{s}\right) \cdot \left(973.7 \frac{kg}{m^3}\right) \cdot \left(2317 \frac{kJ}{kg}\right) \cdot \left(\frac{1000J}{1kJ}\right) \cdot (50yr) \cdot \left(\frac{31556926s}{1yr}\right) = 7.130 \cdot 10^{10} J$$

The total waste package heat input over 50 years and 600 meters is 8.60×10^{14} J (DTN: MO0307MWDAC8MV.000, worksheet "Ventilation Efficiency"). The contribution of latent heat expressed as a percentage of the total waste package heat input is:

$$\frac{7.130 \cdot 10^{10} J}{8.605 \cdot 10^{14} J} = 0.01\%$$

The calculation of the farfield moisture potential from the saturation on core measurements (Table 4-11) and the Van Genuchten retention relationship may be compared with measurements of water potential made in the ECRB Cross-Drift (Table 4-12). At a depth, R_2, of 5.62 m, the measured water potential, ψ_2, is 10 m. The potential at the drift wall was calculated previously to be $\psi_1(30\%,350K) = 1.985 \cdot 10^4$ m. The drift length, z_0, is again 600 m. Calculate the steady state moisture flow at the drift wall by solving the integral in Equation XIII-16:

$$Q = 9.1196 \cdot 10^{-8} \frac{\mathrm{m}^3}{\mathrm{s}}$$

The steady state moisture flow, expressed as a liquid flux toward the drift wall is:

$$\frac{Q}{2\pi \cdot R_1 \cdot z_0} = \frac{9.1196 \cdot 10^{-8} \frac{\mathrm{m}^3}{\mathrm{s}}}{2\pi \cdot 2.75\mathrm{m} \cdot 600\mathrm{m}} \cdot \frac{31556926\mathrm{s}}{1\mathrm{yr}} \cdot \frac{1000\mathrm{mm}}{1\mathrm{m}} = 0.278 \frac{\mathrm{mm}}{\mathrm{yr}}$$

Calculate the latent heat transfer over the 50-year ventilation period by multiplying the flow by the latent heat of vaporization at 350 K (Table 4-25):

$$\left(9.1196\cdot 10^{-8}\,\frac{\mathrm{m}^3}{\mathrm{s}}\right)\cdot\left(973.7\,\frac{\mathrm{kg}}{\mathrm{m}^3}\right)\cdot\left(2317\,\frac{\mathrm{kJ}}{\mathrm{kg}}\right)\cdot\left(\frac{1000\mathrm{J}}{1\mathrm{kJ}}\right)\cdot(50\mathrm{yr})\cdot\left(\frac{31556926\mathrm{s}}{1\mathrm{yr}}\right)=3.246\cdot 10^{11}\,\mathrm{J}$$

The total waste package heat input over 50-years and 600 meters is 8.60·1014 J (DTN: MO0307MWDAC8MV.000, worksheet "Ventilation Efficiency"). The contribution of latent heat expressed as a percentage of the total waste package heat input is:

$$\frac{3.246\cdot 10^{11}\,\mathrm{J}}{8.605\cdot 10^{14}\,\mathrm{J}}=0.04\%$$

INTENTIONALLY LEFT BLANK

ATTACHMENT XIV

DOCUMENTATION OF THE ANSYS-LA-COARSE-INSTANTANEOUS-EFFICIENCY-APPLICATION (INPUTS AND OUTPUTS)

INTENTIONALLY LEFT BLANK

This attachment documents the ANSYS-LA-Coarse-Instantaneous-Efficiency-Application model which was developed using the ANSYS software and spreadsheet methods. The input and output files, and Microsoft Excel spreadsheet are contained in the file ANSYS-LA-Coarse-Instantaneous-Efficiency-Application.zip (DTN: MO0306MWDCIEAP.000). Table XIV-1 is a description of the input and output files, and the worksheets contained in the spreadsheet ANSYS-LA-Coarse-Instantaneous-Efficiency-Application.xls. Further documentation of the cell formulas and referencing are found within the electronic copy of the file.

Table XIV-1. Contents of ANSYS-LA-Coarse-Instantaneous-Efficiency-Application.zip

ANSYS Input and Output Files	
File	**Description**
decay_data_c3.input	ANSYS input file containing the waste package heat decay for segment 3, reduced by the ventilation efficiency
decay_data_c8.input	ANSYS input file containing the waste package heat decay for segment 8, reduced by the ventilation efficiency
th_data.input	ANSYS input file containing the thermal properties of the repository layers and the EBS components
la800.dat	ANSYS input file which generates the mesh and assigns thermal properties to each cell within the mesh
la800.db	ANSYS output file
la800.grph	ANSYS output file
la800.sub	ANSYS output file
la800.out	ANSYS output file
air_temp_c3 and air_temp_c8	ANSYS input files containing the inlet air temperature of the specified segment (from ANSYS-LA-Coarse.xls)
dr_h_c3 and dr_h_c8	ANSYS input file containing the drift wall convection coefficients for the specified segment (from ANSYS-LA-Coarse.xls)
wp_h_c0 through wp_h_c10	ANSYS input files containing the waste package convection coefficients for the specified segment (from ANSYS-LA-Coarse.xls)
la800c3_ev1.dat and la800c8_ev1.dat	Main ANSYS input files
la800c3_ev1.db and la800c8_ev1.db	ANSYS output files
la800c3_ev1.grph and la800c8_ev1.grph	ANSYS output files
la800c3_ev1.dsub and la800c10.dsub	ANSYS output files
la800c3_ev1.mntr and la800c8_ev1.mntr	ANSYS output files
la800c3_ev1.osav and la800c8_ev1.osav	ANSYS output files
la800c3_ev1.rth and la800c8_ev1.rth	ANSYS output files
la800c3_ev1.stat and la800c8_ev1.stat	ANSYS output files
la800c3_ev1.s01 to .s21 and la800c8_ev1.s01 to .s21	ANSYS output files
la800c3_ev1.out and la800c8_ev1.out	Main ANSYS output files
result_c3_ev1 and result_c8_ev1	Temperature results that are cut from the end of the .out files and imported to ANSYS-LA-Coarse.xls

ANSYS-LA-Coarse-Instaneous-Efficiency-Application.xls	
Worksheet	**Description**
100m data	Contains the data from ANSYS-LA-Coarse.xls at 100 m (segment 3) used in the instantaneous ventilation efficiency application and the output of the ANSYS model.
Plot 100m	Plots the waste package and drift wall temperatures for ANSYS-LA-Coarse and ANSYS-LA-Coarse-Instantaneous-Efficiency-Application.
c3-t0-19	Contains the temperature results from the result_c3 ANSYS output files. Performs a circumferential weighted average given the temperatures of each element of the drift wall and waste package.
600m data	Contains the data from ANSYS-LA-Coarse.xls at 600 m (segment 8) used in the instantaneous ventilation efficiency application and the output of the ANSYS model.
Plot 600m	Plots the waste package and drift wall temperatures for ANSYS-LA-Coarse and ANSYS-LA-Coarse-Instantaneous-Efficiency-Application.
c8-t0-19	Contains the temperature results from the result_c8 ANSYS output files. Performs a circumferential weighted average given the temperatures of each element of the drift wall and waste package.

ATTACHMENT XV

DOCUMENTATION OF THE ANSYS-LA-COARSE-INSTANTANEOUS-EFFICIENCY-TWP-APPLICATION (INPUTS AND OUTPUTS)

INTENTIONALLY LEFT BLANK

This attachment documents the ANSYS-LA-Coarse-Instantaneous-Efficiency-Twp-Application model which was developed using the ANSYS software and spreadsheet methods. The input and output files, and Microsoft Excel spreadsheet are contained in the file ANSYS-LA-Coarse-Intstantaneous-Efficiency-Twp-Application.zip (DTN: MO0306MWDCIETA.000). Table XV-1 is a description of the input and output files, and the worksheets contained in the spreadsheet ANSYS-LA-Coarse-Intstantaneous-Efficiency-Twp-Application.xls. Further documentation of the cell formulas and referencing are found within the electronic copy of the file.

Table XV-1. Contents of ANSYS-LA-Coarse-Intstantaneous-Efficiency-Twp-Application.zip

ANSYS Input and Output Files	
File	**Description**
decay_data_c3.input	ANSYS input file containing the waste package heat decay for segment 3, reduced by the ventilation efficiency
decay_data_c8.input	ANSYS input file containing the waste package heat decay for segment 8, reduced by the ventilation efficiency
th_data.input	ANSYS input file containing the thermal properties of the repository layers and the EBS components
la800.dat	ANSYS input file which generates the mesh and assigns thermal properties to each cell within the mesh
la800.db	ANSYS output file
la800.grph	ANSYS output file
la800.sub	ANSYS output file
la800.out	ANSYS output file
air_temp_c3 and air_temp_c8	ANSYS input files containing the inlet air temperature of the specified segment (from ANSYS-LA-Coarse.xls)
dr_h_c3 and dr_h_c8	ANSYS input file containing the drift wall convection coefficients for the specified segment (from ANSYS-LA-Coarse.xls)
wp_h_c0 through wp_h_c10	ANSYS input files containing the waste package convection coefficients for the specified segment (from ANSYS-LA-Coarse.xls)
la800c3_ev2.dat and la800c8_ev2.dat	Main ANSYS input files
la800c3_ev2.db and la800c8_ev2.db	ANSYS output files
la800c3_ev2.grph and la800c8_ev2.grph	ANSYS output files
la800c3_ev2.dsub and la800c10.dsub	ANSYS output files
la800c3_ev2.mntr and la800c8_ev2.mntr	ANSYS output files
la800c3_ev2.osav and la800c8_ev2.osav	ANSYS output files
la800c3_ev2.rth and la800c8_ev2.rth	ANSYS output files
la800c3_ev2.stat and la800c8_ev2.stat	ANSYS output files
la800c3_ev2.s01 to .s21 and la800c8_ev2.s01 to .s21	ANSYS output files
la800c3_ev2.out and la800c8_ev2.out	Main ANSYS output files
result_c3_ev2 and result_c8_ev2	Temperature results that are cut from the end of the .out files and imported to ANSYS-LA-Coarse.xls

ANSYS-LA-Coarse-Instaneous-Efficiency-Application.xls	
Worksheet	**Description**
100m data	Contains the data from ANSYS-LA-Coarse.xls at 100 m (segment 3) used in the instantaneous ventilation efficiency application and the output of the ANSYS model.
Plot 100m	Plots the waste package and drift wall temperatures for ANSYS-LA-Coarse and ANSYS-LA-Coarse-Instantaneous-Efficiency-Application.
c3-t0-19	Contains the temperature results from the result_c3 ANSYS output files. Performs a circumferential weighted average given the temperatures of each element of the drift wall and waste package.
600m data	Contains the data from ANSYS-LA-Coarse.xls at 600 m (segment 8) used in the instantaneous ventilation efficiency application and the output of the ANSYS model.
Plot 600m	Plots the waste package and drift wall temperatures for ANSYS-LA-Coarse and ANSYS-LA-Coarse-Instantaneous-Efficiency-Application.
c8-t0-19	Contains the temperature results from the result_c8 ANSYS output files. Performs a circumferential weighted average given the temperatures of each element of the drift wall and waste package.

ATTACHMENT XVI

CALCULATION FOR ESTIMATING THE IN-DRIFT CROSS SECTIONAL AREA AVAILABLE FOR AIR FLOW

INTENTIONALLY LEFT BLANK

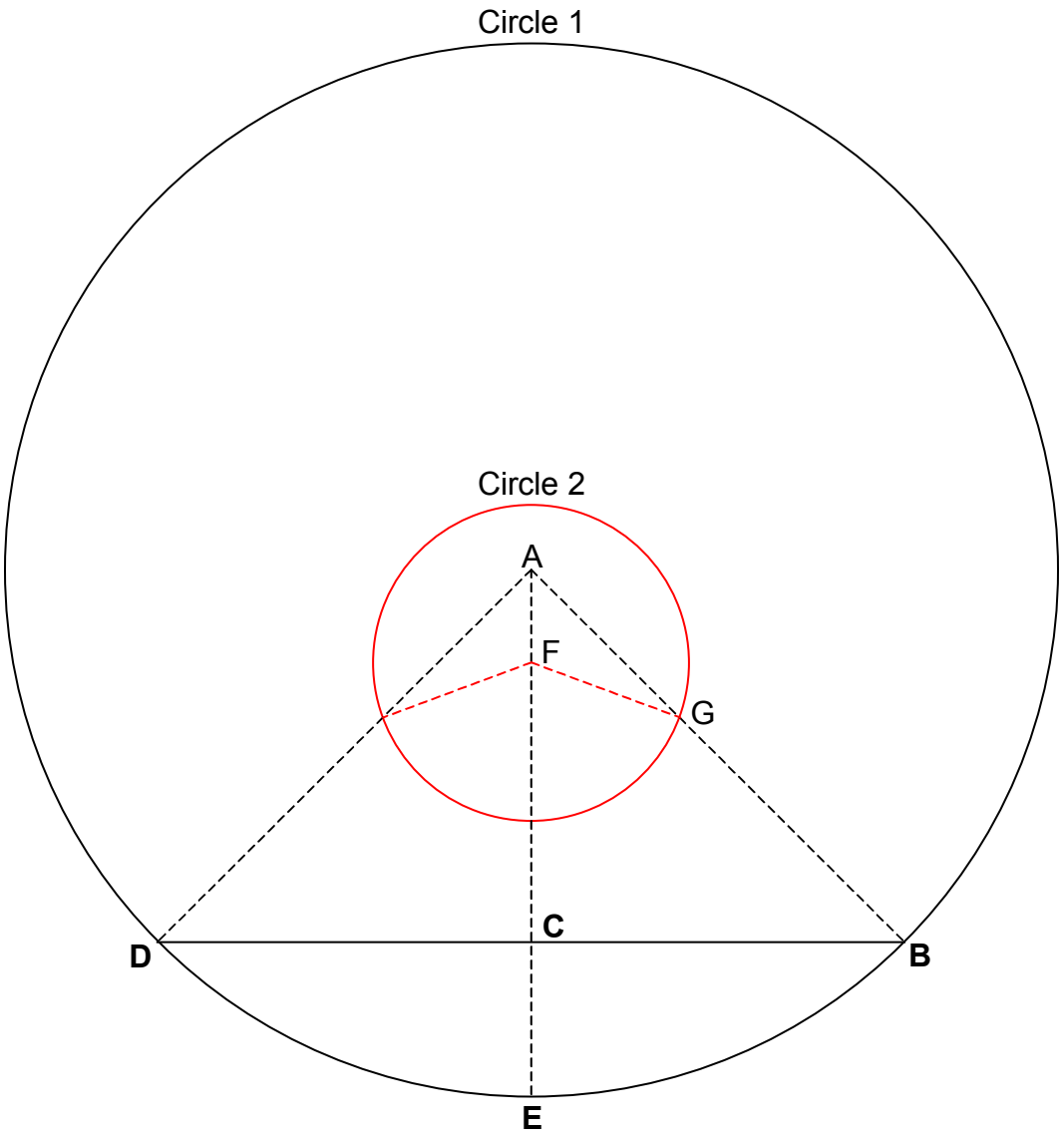

From Table 4-23:

$$AB = ACE = AD = \frac{5.5\text{m}}{2} = 2.75\text{m}$$

$$CE = 0.806\text{m}$$

From Table 4-22:

$$FG = \frac{1.644\text{m}}{2} = 0.822\text{m}$$

Using the Pythagorean Theorem:

$$AC^2 + BC^2 = AB^2$$

Then:

$$\mathrm{BC} = \sqrt{2.75^2 - (2.75 - 0.806)^2} = 1.945\mathrm{m}$$

$\angle$CAB is:

$$cos(\angle \mathrm{CAB}) = \frac{\mathrm{AC}}{\mathrm{AB}} = \frac{2.75 - 0.806}{2.75} = 0.707$$

Or:

$$\angle \mathrm{CAB} = cos^{-1}(0.707) = 45^\circ$$

Since ACE bisects BCD, $\angle$DAB is twice $\angle$CAB, or 90°. Since the sum of all internal angles emanating from the center of a circle is 360°, the pie shaped slice composed of points A, B, and D, and arc BED is ¼ the area of the Circle 1.

The area available for flow is: then the area of Circle 1; minus the area of the pie shaped slice composed of points A, B, and D, and arc BED; plus the area of the triangle composed of points ABCD; minus the area of the Circle 2.

The area of Circle 1 is:

$$\pi \mathrm{AB}^2 = \pi \cdot 2.75^2 = 23.758\mathrm{m}^2$$

The area of the pie shaped slice composed of points A, B, and D, and arc BED is:

$$\frac{1}{4}\pi \mathrm{AB}^2 = \frac{1}{4}\pi \cdot 2.75^2 = 5.940\mathrm{m}^2$$

The area of the triangle composed of points ABCD is:

$$\frac{1}{2} \cdot \mathrm{BCD} \cdot \mathrm{AC} = \frac{1}{2} \cdot 2 \cdot 1.945 \cdot (2.75 - 0.806) = 3.781\mathrm{m}^2$$

The area of Circle 2 is:

$$\pi \mathrm{FG}^2 = \pi \cdot 0.822^2 = 2.123\mathrm{m}^2$$

Therefore, the area available for flow is:

$$23.758 - 5.940 + 3.781 - 2.123 = 19.476\mathrm{m}^2$$

ATTACHMENT XVII

CALCULATION OF DITTUS-BOELTER HEAT TRANSFER COEFFICIENTS FOR THE VENTILATION TEST PHASE I CASES 1 THROUGH 5

INTENTIONALLY LEFT BLANK

Table XVII-1. Calculating the Convection Heat Transfer Coefficients for the Ventilation Test Phase 1 Cases 1 Through 5 Using the Dittus-Boelter Correlation for Fully Developed Turbulent Flow in a Smooth Cylinder

Input Parameter	Value	Source
Constant (pi), dimensionless	3.14	Universal Constant
Emplacement Drift Diameter (D), m	1.3716	Table 4-29 (convert in to m)
Waste Package Diameter (d), m	0.4064	Table 4-27 (convert in to m)
Wetted Perimeter (P), m	5.6	P=Pi · (D+d)
Cross Section Area (A), m^2	1.35	A=pi/4 · (D^2-d^2)
Hydraulic Diameter (Dh), m	0.9652	Dh=4A/P=D-d
Air Density (rho), kg/m^3	1.1614	Table 4-24 (for 300K)
Air Thermal Conductivity (k), W/m·K	0.0263	Table 4-24 (for 300K)
Air Specific Heat (Cp), J/kg-K	1007	Table 4-24 (for 300K)
Air Kinematic Viscosity (mu), kg/m-s	1.5890E-05	Table 4-24 (for 300K)
Air Prandtl Number (Pr), dimensionless	0.707	Table 4-24 (for 300K)
Case 3 and Case 5		
Air Flow Rate (Q), m^3/s per drift	0.5	Table 7-2
Air Flow Velocity (v), m/s	0.37	v=Q/A
Reynolds Number (Re), dimensionless	26170.15	Re=rho·v·Dh/mu (Incropera and DeWitt 1996, Section 8.1.2)
Nusselt Number (Nu), dimensionless	68.51	$Nu=0.023 \cdot Re^{0.8} \cdot Pr^{0.4}$ (Incropera and DeWitt 1996, Section 8.5)
Conv. Heat Transfer Coef. (h), $W/m^2 \cdot K$	1.9	h=k·Nu/Dh (Incropera and DeWitt 1996, Section 8.5)
Case 1 and Case 4		
Air Flow Rate (Q), m^3/s per drift	1	Table 7-2
Air Flow Velocity (v), m/s	0.74	v=Q/A
Reynolds Number (Re), dimensionless	52340.31	Re=rho · v · Dh/mu (Incropera and DeWitt 1996, Section 8.1.2)
Nusselt Number (Nu), dimensionless	119.28	$Nu=0.023 \cdot Re^{0.8} \cdot Pr^{0.4}$ (Incropera and DeWitt 1996, Section 8.5)
Conv. Heat Transfer Coef. (h), $W/m^2 \cdot K$	3.3	h=k·Nu/Dh (Incropera and DeWitt 1996, Section 8.5)
Case 2		
Air Flow Rate (Q), m^3/s per drift	2	Table 7-2
Air Flow Velocity (v), m/s	1.48	v=Q/A
Reynolds Number (Re), dimensionless	104680.62	Re=rho·v·Dh/mu (Incropera and DeWitt 1996, Section 8.1.2)
Nusselt Number (Nu), dimensionless	207.68	$Nu=0.023 \cdot Re^{0.8} \cdot Pr^{0.4}$ (Incropera and DeWitt 1996, Section 8.5)
Conv. Heat Transfer Coef. (h), $W/m^2 \cdot K$	5.7	h=k·Nu/Dh (Incropera and DeWitt 1996, Section 8.5)

INTENTIONALLY LEFT BLANK